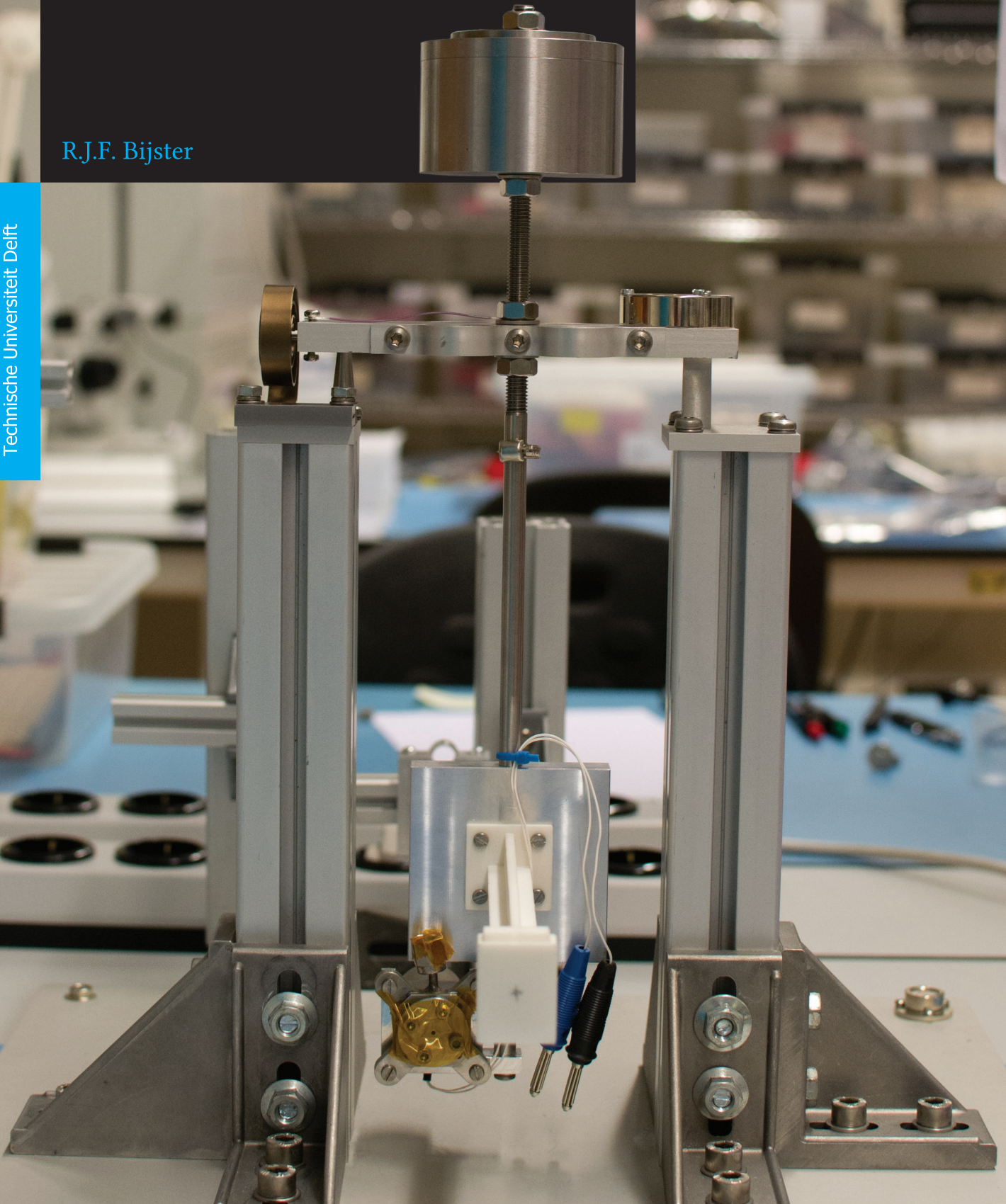


Design, Verification and Validation of a Micropropulsion Thrust Stand

R.J.F. Bijster

Technische Universiteit Delft



DESIGN, VERIFICATION AND VALIDATION OF A
MICROPROPULSION THRUST STAND

R.J.F. BIJSTER

(1506706)

AE5810 Master Thesis

Department of Space Engineering
Faculty of Aerospace Engineering
Delft University of Technology

April 2013 - January 2014
Final report



R.J.F. Bijster: *Design, verification and validation of a micropropulsion thrust stand*, AE5810 Master Thesis, © April 2013 - January 2014

GRADUATION COMMITTEE:

prof. dr. E.K.A. Gill (Space Systems Engineering, TU Delft)

ir. B.T.C. Zandbergen (Space Systems Engineering, TU Delft)

dr. R.M. Groves (Aerospace Structures and Materials, TU Delft)

dr. O. Sutherland (European Space Agency)

ir. J. Kuiper (MOOG Bradford Engineering B.V.)

"In the spirit of science, there really is no such thing as a 'failed experiment.' Any test that yields valid data is a valid test."

— **Adam Savage**

"A theory is something nobody believes, except the person who made it. An experiment is something everybody believes, except the person who made it."

— **Albert Einstein**

"If I have seen further it is by standing on ye sholders of Giants."

— **Sir Isaac Newton, in a letter to Robert Hooke (15 Feb. 1676)**

ABSTRACT

At the chair of Space Systems Engineering, students and staff work on the development of small propulsion systems in a wide thrust capability. Especially in recent years low thrust propulsion systems have gained an increased amount of interest in the entire department of Space Engineering. To support the development of these propulsion systems, there is a need for the testing of micropropulsion systems that provide a thrust in the 1 μN to 5 mN range. This capability complements the existing measurement equipment of the Delft Aerospace Rocket Thrust Stand facility of 0.5 mN to 1 N. To provide a solution to this need, the research question for this research is phrased as: "How can the DARTS facility be upgraded to measure thrust levels in the 1 μN to 5 mN range and impulse bits in the 1 μNs to 1 mNs range?".

Using numerical modelling the answer to that question is found in an upgraded design of the TB-2m thrust stand that was developed in 2010 by Perez-Grande. By introducing several improvements, amongst which are the replacement of the sensor system by a capacitive displacement sensor and the use of a segmented counter mass, the range of the TB-2m has been extended and the accuracy has been improved to meet the new requirements. A complementary calibration system is designed that allows an in situ calibration for the measurement of both the thrust and impulse bits. Where typical calibration actuators supply a force that is non-linear with engagement distance and have to rely on displacement measurements to linearize the calibration force, the new actuator is able to provide a force that is independent on the distance to the target. Using a specially designed solenoid that has a linearly varying turn-density along its length, the magnetic field is shaped to provide a constant magnetic gradient.

The thrust stand and calibration system are manufactured and tested. Using a previously tested cold gas thruster that is provided by Bradford Engineering, the complete thrust measurement system is validated with hardware-in-the-loop. This process has shown that the pendulum is in a state constant of oscillation. It is expected that this oscillation is removed by the introduction of a Foucault damper in the next design iteration. The validation process has shown that the thrust range is on par with the requirements. Also impulse bits can be measured, but the constant state of oscillation prohibited the detection of the smallest impulse bits of 1 μNs . Future experiments have to show whether the required and predicted accuracies are achieved.

LIST OF PUBLICATIONS

- [1] R.J.F. Bijster and B.T.C. Zandbergen. Integration of a Variable Turn-Density Coil Actuator in a Micropropulsion Thrust Stand. In *Space Propulsion 2014 (accepted)*, Cologne, Germany, 2014.

Copies of the publication(s) are available from the author and in [Appendix F](#).

"If I have seen further it is by standing on ye sholders of Giants."
— Sir Isaac Newton, in a letter to Robert Hooke (15 Feb. 1676)

ACKNOWLEDGEMENTS

Nine months of work have accumulated into the pinnacle of my master studies: the Master of Science thesis that lays before you. Although the thesis is an individual effort, it would not have been a success without the guidance, support and help of the organizations and people that made it possible. I would like to acknowledge the help and support that I have received during these months.

I would like to start by thanking ir. Barry Zandbergen for his role as my daily supervisor and his thought provoking questions and remarks. They have motivated me to look deeper in areas I wouldn't have and take a broader look in others. I would also like to thank the other members of the graduation committee: prof. dr. Eberhard Gill, dr. Roger Groves, dr. Orson Sutherland and ir. Johan Kuiper for taking the time to review my work and provide useful comments and directions along the way.

Gratitude goes to prof. dr. Cynthia M. Ross Friedman of the department of biological sciences and dr. Mark Paetkau of the department of physics of Thompson Rivers University for clarifying their work on Variable Turn-Density Coils; Daniel Perez-Grande MSc. for his comments on the AE-TB-2m, the thrust stand that formed the foundation of my work; Stef Janssens MSc. and Alessandro Migliaccio MSc. for their comments on the AE-TB-50m and the used calibration techniques. Their comments have provided me with additional insights that are much appreciated and were helpful in the design of the thrust stand.

It is due to the funding provided by the DelFFi programme and the Chair of Space Systems Engineering that the thrust stand could be manufactured and tested, for which I am very grateful. This allowed me to cover the entire process from conceptualization, design, manufacturing, integration, and verification and validation, which I believe is a process a student should have experienced in its totality before finishing his or her Master of Science degree. Special thanks go to MOOG Bradford Engineering for making their Proportional Micro Thruster available. The hardware in the loop validation of the thrust stand that was enabled in this way, deepens the confidence one can take in the final product. Additionally, I would like to acknowledge the practical support I got. The help and patience of Nuno Baltazar dos Santos is much appreciated and I am thankful for his insights

in the electric problems experienced during the verification and validation stage of the project. The insights of Ed Roessen and Hans Weerheim have benefitted the mechanical design and final test setup for which I am grateful.

Lastly, I would like to thank the people that helped in both technical and non-technical terms, either directly or indirectly during the thesis period. First, my friends and fellow students Thijs Arts, Dennis Dolkens, Saish Sridharan and John-John Boeva for their feedback and countless stress relieving coffee-breaks and many iterations of the Star Wars Cantina song. Especially John-John's experience with measurement devices, electronics and electro-magnetism have been very helpful and instructive. Secondly, I would like to thank Nina Ouddeken for her support along the way and proof reading this very document. Also I would like to thank Johan Bijster for his support. Their support was welcome during the many moments of frustration that inevitably come with both theoretical and (especially) experimental work. Lastly, I would like to thank my late mother, Francis Bijster, who motivated me ever since childhood to study and work hard, to pursue my dreams and never doubted I would.

Roy Bijster
Delft, December 2013

CONTENTS

1	INTRODUCTION	1
2	BACKGROUND AND DEFINITIONS	5
2.1	Thrust and impulse bit measurements	5
2.1.1	Hanging pendulum	5
2.1.2	Inverted pendulum	6
2.1.3	Folded pendulum	6
2.1.4	Torsion balance	6
2.1.5	Flexure	7
2.1.6	Resonant blade	8
2.2	Formal definitions	8
3	STAKEHOLDERS AND REQUIREMENT ANALYSIS	11
3.1	Stakeholders	11
3.2	Toplevel system requirements	13
3.3	Requirement rationale	14
4	THRUST STAND DESIGN	21
4.1	Thrust stand design option analysis	21
4.1.1	Analytical model	21
4.1.2	Sensor system and its accuracy	24
4.1.3	The effect of sensor tilt	28
4.1.4	Design feasibility	29
4.1.5	Counter mass selection	34
4.1.6	Impulse bits	34
4.1.7	Mass moment of inertia	35
4.2	Part design	36
4.2.1	Counter masses	36
4.2.2	Engine bracket	36
4.2.3	Sensor bracket	37
4.2.4	Sensor target and calibration mass	38
4.3	TB-2m and TB-5m compared	39
5	CALIBRATION ACTUATOR	43
5.1	Design options	43
5.1.1	Solenoid	45
5.1.2	Solenoid placed in a uniform magnetic field	45
5.1.3	Varying Turn-Density Coil	46
5.1.4	Anti-Helmholtz	47
5.1.5	Canted Helmholtz	47
5.1.6	Parallel plates	48
5.1.7	Electrostatic combs	48
5.1.8	Electrostatic fins	49
5.2	Design option trade-off	50
5.2.1	Solenoid	51
5.2.2	Solenoid placed in a uniform magnetic field	51

5.2.3	Varying Turn-Density Coil	52
5.2.4	Anti-Helmholtz	52
5.2.5	Canted Helmholtz	53
5.2.6	Parallel plates	53
5.2.7	Electrostatic combs and fins	53
5.2.8	Trade-off conclusion	54
5.3	Design of a Variable-Turn Density Coil based actuator	54
5.3.1	Mathematical model of Variable Turn-Density Coil based actuator	54
5.3.2	Magnetic moment of permanent magnet	56
5.3.3	Coil optimization	59
5.3.4	Actuator sizing	65
5.3.5	Mechanical design	67
5.4	Verification and Validation	73
5.5	Redesign of the calibration coil	74
6	VERIFICATION AND VALIDATION PLAN	79
6.1	Test conditions and equipment	79
6.1.1	System overview	80
6.1.2	Equipment used	80
6.1.3	Tested hardware	89
6.2	Test sequence and description	89
6.2.1	TEST-110: Force-current calibration	90
6.2.2	TEST-120: Impulse calibration	96
6.2.3	TEST-200: Feed system leak test	103
6.2.4	TEST-310: Characterization of environmentally induced noise	105
6.2.5	TEST-320: Characterization of feed system positioning	108
6.2.6	TEST-331: Natural frequency and damping ratio	110
6.2.7	TEST-332: Dynamic attenuation	112
6.2.8	TEST-411: Pendulum characterization - Sensitivity	114
6.2.9	TEST-412: Pendulum characterization - Drift	116
6.2.10	TEST-420: Characterization of the effect of the magnetic field of the Proportional Microthruster	118
6.2.11	TEST-430: Characterization of the effect of the center of gravity shift in the Proportional Microthruster	121
6.2.12	TEST-440: Characterization of the effect of changing vacuum pressure	123
6.2.13	TEST-450: Steady state thrust measurements	125
6.2.14	TEST-461: Thrust stand calibration for impulse bits	131
6.2.15	TEST-462: Impulse bit measurements	134
6.3	Full setup assembly and integration	135
6.3.1	Required equipment	136
6.3.2	Selection of arm lengths and counter masses	137

6.3.3	Placement and alignment of components	139
6.3.4	Connecting the gas feed system	141
7	EXPERIMENTAL RESULTS	145
7.1	Encountered hardware problems	145
7.1.1	Broken coil	145
7.1.2	Pressure transducers	145
7.1.3	Thermocouples	146
7.1.4	Data-acquisition system	146
7.2	Setup as calculated by program	148
7.3	Results	150
7.3.1	TEST-110: Force-current calibration	150
7.3.2	TEST-120: Impulse calibration	153
7.3.3	TEST-200: Feed system leak test	157
7.3.4	TEST-310: Characterization of environmentally induced noise	158
7.3.5	TEST-320: Characterization of feed system posi- tioning	164
7.3.6	TEST-331: Natural frequency and damping . . .	164
7.3.7	TEST-332: Dynamic attenuation	168
7.3.8	TEST-411: Pendulum characterization - Sensitivity	168
7.3.9	TEST-412: Pendulum characterization - Drift . .	169
7.3.10	TEST-420: Characterization of the effect of the magnetic field of the Proportional Microthruster	175
7.3.11	TEST-430: Characterization of the effect of the center of gravity shift in the Proportional Mi- crothruster	177
7.3.12	TEST-440: Characterization of the effect of chang- ing vacuum pressure	178
7.3.13	TEST-450: Steady state thrust measurements . .	179
7.3.14	TEST-461: Thrust stand calibration for impulse bits	187
7.3.15	TEST-462: Impulse bit measurements	187
7.3.16	Requirement validation	190
8	DESIGN CHANGES REQUIRED TO MEET DELFFI REQUIRE- MENTS	191
8.1	New requirements	191
8.2	Required design changes	191
8.2.1	Extension of the range	192
8.2.2	Sample size	193
8.2.3	Alignment issues	194
9	CONCLUSIONS AND RECOMMENDATIONS	195
9.1	Conclusions	195
9.2	Recommendations	196
9.2.1	Future research and development	196
9.2.2	Delft Aerospace Rocket Thrust Stand facility . .	198
9.2.3	Advise for future students	199

BIBLIOGRAPHY	201
A HELMHOLTZ AND ANTI-HELMHOLTZ SETUPS	211
A.1 Helmholtz	211
A.2 Anti-Helmholtz	212
B DETERMINATION OF THE SPRING CONSTANT	215
B.1 Measurement setup	215
B.2 Theoretical model	216
B.3 Measurement plan	217
B.3.1 Test overview	217
B.3.2 Procedure	218
B.4 Results and Discussion	218
B.5 Conclusions and Recommendations	219
C DETERMINATION OF THE MAGNETIC MOMENT USING A MAGNETIC PISTON	225
C.1 Measurement setup	225
C.2 Theoretical model	225
C.3 Measurement plan	227
C.3.1 Test overview	227
C.3.2 Procedure	228
C.4 Results and Discussion	228
D SAMPLE CALCULATIONS	231
D.1 Sensor system accuracy	231
E STATISTICS: SUMMARY OF USED RELATIONS	235
E.1 Unbiased estimators of the mean and variance	235
E.2 Expectation and variance of an average	235
E.3 Confidence intervals for the mean	235
E.4 Correlation coefficient	236
E.5 Standard Error of Estimation	236
E.6 Coefficient of Determination	237
E.7 Uncertainty in regression	237
F COPIES OF PUBLICATIONS	239
G PROGRAM CODES	241
H VIRTUAL INSTRUMENTS	243
I ENGINEERING DRAWINGS	247
J LIST OF USED DATA FILES	263
K HARDWARE QUOTATIONS AND INVOICES	269

LIST OF FIGURES

Figure 1	Sketches of pendulum type thrust stands. . . .	7
Figure 2	Sketches of torsion and flexure type thrust stands.	8
Figure 3	Relation between accuracy, precision, trueness and resolution.	9
Figure 4	Acceptable relative errors in specific impulse and thrust for the E-moth mission.	17
Figure 5	Acceptable relative errors in specific impulse and thrust for the DelFFi mission.	17
Figure 6	Allowable error in propellant-to-dry mass ratio as a function of propellant-to-dry mass ratio. .	18
Figure 7	Acceptance and goal requirements for the measurement accuracy.	19
Figure 8	Free-body diagram of the thrust stand as used in the preliminary design.	22
Figure 9	Error in full range estimate.	24
Figure 10	Flow diagram of how errors are added to the displacement measurement.	25
Figure 11	Relative error in displacement measurement due to tilting.	28
Figure 12	Free-body diagram of the simulated pendulum in preliminary design.	31
Figure 13	Sample data set for preliminary design.	31
Figure 14	Achievable accuracies for an updated TB-2m design.	32
Figure 15	Sensitivity of thrust accuracy to errors in counter mass and arm length.	33
Figure 16	Drawing of stacked masses forming the counter mass.	37
Figure 17	Drawing of engine bracket.	38
Figure 18	Drawing of sensor bracket.	39
Figure 19	Drawing of sensor target	40
Figure 20	Comparison of the AE-TB-2m and the AE-TB-5m	41
Figure 21	Design Option Tree for the calibration actuator.	43
Figure 22	Original design of a Varying Turn Density Coil.	47
Figure 23	Geometry of a canted Helmholtz coil.	48
Figure 24	Geometry of an electrostatic fin setup.	49
Figure 25	Simulated magnetic field for a 10 cm long ideal solenoid.	60
Figure 26	Simulation results for 10 cm and 100 cm ideal solenoids.	61
Figure 27	Geometry of the optimized VTDC.	63

Figure 28	Magnetic field at the geometric center line of the optimized VTDC.	64
Figure 29	Magnetic field in the xz-plane of the optimized VTDC.	65
Figure 30	Sketch of the coil holder of the calibration actuator.	68
Figure 31	Sketch of the calibration arm of the calibration actuator.	69
Figure 32	Magnetic field outside of the coil.	70
Figure 33	Magnetic field strength outside the coil.	70
Figure 34	Schematic drawing of simplified bending model.	71
Figure 35	Sketches of the magnet holders of the calibration actuator.	72
Figure 36	Calibration force as a function of engagement distance using a S-06-06-N magnet.	74
Figure 37	Magnetic field in the xz-plane of the redesigned VTDC.	75
Figure 38	Comparison between old and new actuator coil	77
Figure 39	System overview of the complete measurement chain.	81
Figure 40	Photo of feed system.	83
Figure 41	Photos of the vacuum transition flange.	85
Figure 42	Vacuum pumping pressure characteristic	86
Figure 43	Vacuum pressure leak characteristic	87
Figure 44	Required hardware for TEST-110	91
Figure 45	Electrical circuit diagram for TEST-110	94
Figure 46	Photos of TEST-110 procedure.	95
Figure 47	Resistor-Inductor representation of coil.	97
Figure 48	Coil response to a step input.	98
Figure 49	Circuit diagram for TEST-120.	99
Figure 50	Circuit diagram for TEST-200.	103
Figure 51	Photos of the setup in two orientations.	106
Figure 52	Circuit diagram for TEST-331, TEST-332 and TEST-411.	111
Figure 53	Cold junction compensation	117
Figure 54	Circuit diagram for TEST-420 and TEST-430.	119
Figure 55	Expected change in measured thrust due to center of gravity shift.	122
Figure 56	Expected vacuum chamber pressure increase caused by continuous engine thrusting.	124
Figure 57	Estimated pressure ratio of Proportional Micro Thruster.	127
Figure 58	Simulated thrust and specific impulse for Proportional Micro Thruster.	128
Figure 59	Modeled thrust compared to results of ESA ESTEC.	129

Figure 60	Required hardware for thrust stand assembly.	137
Figure 61	Photos of thrust stand assembly procedure. . .	144
Figure 62	Calibration curve for actuator using S-06-06-N magnet.	150
Figure 63	Calibration curve for actuator using two S-02-02-N magnet.	151
Figure 64	Calibration curve for an actuator that uses two S-1.5-0.5-N magnets.	152
Figure 65	Generated and measured pulses for impulse bit calibration.	153
Figure 66	Generated and measured pulses for impulse bit calibration (zoomed).	154
Figure 67	Comparison between methods to obtain current from transient voltage.	154
Figure 68	Generated impulse bit.	155
Figure 69	Photos of the leak fixes.	157
Figure 70	Ten second sample of noise measurement in first orientation.	158
Figure 71	Noise measurement in first orientation.	162
Figure 72	Noise measurement in second orientation.	163
Figure 73	Photos of the used feed system positioning.	164
Figure 74	Damping ratio as function of window length.	165
Figure 75	Damped natural frequency as function of window length.	166
Figure 76	Sample output for TEST-331.	167
Figure 77	Sample output for TEST-411.	168
Figure 78	Long-term drift results.	170
Figure 79	Log of thrust, pressure and mass flow (uncorrected).	173
Figure 80	Correlation between drift in thrust, mass flow and feed pressure.	174
Figure 81	Valve induced force readings (magnetic).	175
Figure 82	Linear fits for valve induced force readings (magnetic).	176
Figure 83	Valve induced force readings.	177
Figure 84	Linear fits for valve induced force readings.	179
Figure 85	Typical results for TEST-450.	181
Figure 86	Example of hysteresis in thrust measurements.	182
Figure 87	Log of thrust, pressure and mass flow (uncorrected) for hysteresis test.	183
Figure 88	Measured thrust compared to results of the model	184
Figure 89	Measured thrust compared to results of ESA ESTEC.	185
Figure 90	Determined specific impulse compared to results of ESA ESTEC.	185

Figure 91	Required coil current and pulse length for given impulse bit.	188
Figure 92	Response for a 1 mNs impulse.	189
Figure 93	Response for a 1 μ Ns impulse.	189
Figure 94	Achievable accuracies for an updated TB-5m design.	193
Figure A-1	Sketch of a Helmholtz setup.	212
Figure A-2	Field strength and field gradient of a Helmholtz setup.	213
Figure A-3	Field strength and field gradient of an Anti-Helmholtz setup.	213
Figure B-1	3D drawing of the TB-2m	215
Figure B-2	Photo of measurement setup with mass suspended from cross-beam.	216
Figure B-3	Measurement of the distance between the retainers of the gas canisters to determine the arm length.	219
Figure B-4	Measurement of rotation angle.	220
Figure B-5	Estimated spring constant based on given model and experimental data.	221
Figure C-1	Simple magnetic piston made of rolled plastic foil.	226
Figure C-2	Simple magnetic piston using a thin 3 mm drinking straw.	226
Figure H-1	Creation of data channels in Virtual Instruments.	244
Figure H-2	Taking measurements using the Virtual Instruments.	245
Figure H-3	Typical block diagram of the Labview Virtual Instrument for the test.	246

LIST OF TABLES

Table 1	Overview of the project stakeholders.	12
Table 2	TU Delft satellite mission propulsion requirements and characteristics.	16
Table 3	Impulse performance of thrusters.	19
Table 4	Required impulse bits for nanosatellite pointing.	20
Table 5	Accuracy parameters of the National Instruments PXI 6229	26
Table 6	Specifications and accuracies of the available capacitive sensor systems.	26
Table 7	Specifications and accuracies of the available capacitive sensor systems.	27
Table 8	Simulation parameters used in the calculation of accuracy and range for the preliminary design.	30
Table 9	Counter mass dimensions.	37
Table 10	Counter mass dimensions after production.	38
Table 11	Comparison between TB-2m. and TB-5m.	41
Table 12	Comparison of known calibration techniques.	44
Table 13	Trade-off table for calibration actuator.	51
Table 14	Specification of magnet magnetization class, dimensions, mass and strength.	58
Table 15	Simulation parameters for VTDC optimization.	62
Table 16	Required calibration force ranges and accuracies.	66
Table 17	Required electric current for calibration force of 1 μN to 45 μN range.	67
Table 18	Required electric current for calibration force of 45 μN to 420 μN range.	67
Table 19	Required electric current for calibration force of 200 μN to 5000 μN range.	67
Table 20	Gradation of vacuum level.	73
Table 21	Comparison between original VTDC design and the redesign.	76
Table 22	Required electric current for calibration force of 1 μN to 45 μN range with new coil.	78
Table 23	Required electric current for calibration force of 45 μN to 420 μN range with new coil.	78
Table 24	Required electric current for calibration force of 200 μN to 5000 μN range.	78
Table 25	Environmental conditions in the clean room.	79
Table 26	Used hardware components in the feed system.	82
Table 27	Used hardware components in the feed system.	84
Table 28	Overview of the used hardware components.	88
Table 29	TEST-110 required equipment	92

Table 30	TEST-120 required equipment	100
Table 31	TEST-200 required equipment	104
Table 32	Environmental and test conditions of facilities.	126
Table 33	Required equipment and hardware for full system assembly.	137
Table 34	Optimized setup parameters for measurements.	149
Table 35	Calibration parameters for calibration actuator	152
Table 36	Estimated deliverable impulse bit.	156
Table 37	Noise components in thrust signal.	159
Table 38	Estimated resonance frequencies of the building	161
Table 39	Found thrust stand sensitivities and spread. .	169
Table 40	Validations of requirements.	190
Table 41	Required electric current for calibration force of 2800 μN to 9500 μN range with current coil.	193
Table 42	Required electric current for calibration force of 2800 μN to 9500 μN range with new coil. . .	194
Table C-1	Specification of magnet magnetization class, dimensions, mass and quantity available.	228
Table C-2	Estimated magnetic moment for S-06-06-N magnets.	229
Table C-3	Estimated magnetic moment for S-04-04-N magnets.	229
Table C-4	Estimated magnetic moment for S-02-02-N magnets.	230
Table D-1	Accuracy parameters of the National Instruments PXI 6229	232
Table K-2	Costs incurred during the project.	270

LISTINGS

Listing 1 Calculation of the response of a RL network. . 241

ACRONYMS

CoG	Center of Gravity
DAQ	Data Acquisition System
DARTS	Delft Aerospace Rocket Thrust Stand
DOT	Design Option Tree
DUT	Delft University of Technology
EPL	Electric Propulsion Laboratory
ESC	Electrostatic Combs
ESD	Electrostatic Discharge
ESF	Electrostatic Fins
FBD	Free Body Diagram
FFT	Fast-Fourier Transform
FSO	Full Scale Output
ISO	International Organization for Standardization
JCGM	Joint Committee for Guides in Metrology
KNMI	Koninklijk Nederlands Meteorologisch Instituut / Royal Netherlands Meteorological Institute
LVDT	Linear Variable Displacement Transducers
MAX	National Instruments Measurement & Automation Explorer
MFC	Mass Flow Controller
MIB	Minimum Impulse Bit
MOP	Master Orientation Project
NPR	NASA Procedural Requirements
PMT	Proportional Micro Thruster
PSU	Power Supply Unit
SEE	Standard Error of Estimation
SSE	Space Systems Engineering
TRIM	Time Resolve Impulse Measurement

UHV Ultra High Vacuum

VI Virtual Instrument

VTDC Varying Turn-Density Coil

GLOSSARY

SYMBOL	UNIT	DESCRIPTION
A	m^2	Frontal area of electrodes of an electrostatic actuator that uses two parallel plates
A_{coil}	m	Cross-sectional area of a coil
A_{wire}	m	Cross-sectional area of a wire
A_e	m^2	Exit area of a nozzle
A_t	m^2	Throat area of a nozzle
\mathbf{B}	T	Magnetic field vector
B	T	Strength of a magnetic field
B_x	T	Component of magnetic field vector in the x-direction
B_y	T	Component of magnetic field vector in the y-direction
B_z	T	Component of magnetic field vector in the z-direction
C	-	Damping constant
c	m	Thickness of the fins in an electro-static fin actuator
c	$m\,s^{-1}$	Speed of light in vacuum
c_0	m^{-2}	Initial turn-density variation
D	m	Depth of the vacuum chamber
d	m	Depth of the fins in an electro-static fin actuator
D_{aero}	N	Aerodynamic drag force
D_{ant}	m	Diameter of a loop antenna
$d\mathbf{B}$	T	Infinitesimal contribution of a wire element to the magnetic field vector
D_{coil}	m	Diameter of a coil
D_i	m	Inner diameter of a rod
$d\mathbf{L}$	m	Infinitesimal wire element that is subject to an electric current
d_{max}	m	Measuring range of the sensor
d_{meas}	m	Measured displacement (including data-acquisition)

Continued on next page

Glossary – *Continued from previous page*

SYMBOL	UNIT	DESCRIPTION
D_o	m	Outer diameter of a rod
d_{real}	m	Real displacement
d_{sens}	m	Displacement as measured by the sensor
Δd_{sens}	m	Error introduced by the sensor to the displacement measurement
d_{wire}	m	Diameter of an electric wire
d_{work}	m	Working distance of the sensor
E	V m^{-1}	Induced electric field
F	N	Electromagnetic force vector
F	N	Force generated by an actuator
f	Hz	Tuned frequency of a loop antenna
G	-	Gain error
g	m s^{-2}	Gravitational acceleration at arbitrary altitude
g	m	Distance between the surfaces of two adjacent fins in an electro-static fin actuator
g_0	m s^{-1}	Gravitational acceleration at sea-level
H	m	Height of the vacuum chamber
\bar{I}	kg m^2	Effective mass moment of inertia
i	A	Electric current
I_{bit}	N s	Impulse bit
I_{sp}	s	Specific impulse
K	N m rad^{-1}	Spring stiffness of rotary spring
\bar{K}	N m rad^{-1}	Effective spring constant of pendulum
L_{coil}	m	Length of coil
l_{wire}	m	Length of a wire
L	m	Combined length of a solenoid and a suspended metallic core
l_{a1}	m	Distance between center of gravity of the top arm and the pivot
l_{a2}	m	Distance between center of gravity of the bottom arm and the pivot
l_b	m	Distance between center of gravity of the cross-beam and the pivot
L_c	H	Electric inductance of a coil

Continued on next page

Glossary – *Continued from previous page*

SYMBOL	UNIT	DESCRIPTION
l_c	m	Distance between center of gravity of counter mass and the pivot
l_{cg}	m	Distance between total center of gravity and the pivot
l_e	m	Distance between center of gravity of the engine and the pivot
l_m	m	Distance from the center of gravity of the added mass to the pivot
l_t	m	Distance between center of gravity of the sensor target and the pivot
M	$A\ m^{-1}$	Magnetization
M	$kg\ mol^{-1}$	Molar mass
m	$kg\ s^{-1}$	Mass flow
\hat{m}	kg	Added mass for mass moment of inertia calibration
m_0	kg	Mass of the gas that is initially present in the vacuum chamber prior to thrusting
M_{a_1}	kg	Mass of top arm of pendulum
M_{a_2}	kg	Mass of bottom arm of pendulum
M_{actual}	kg	Actual mass of a counter mass
M_b	kg	Mass of cross-beam
M_c	kg	Total counter mass
M_{design}	kg	Design mass of a counter mass
M_e	kg	Empty mass of spacecraft
M_e	kg	Total mass of engine
M_p	kg	Propellant mass
m_{sp}	$kg\ m^{-1}$	Specific mass of a rod
$m_{sp,corr}$	$kg\ m^{-1}$	Specific mass of a rod that is corrected for a hole drilled in the center of the rod
M_t	kg	Total mass of sensor target and calibration arm combined
ΔM	N m	Differential moment caused by a shift in the center of gravity of the thruster
N	-	Number of windings on a coil
n	m^{-1}	Turn-density
n	m^{-3}	Number density of magnetic moments per unit volume

Continued on next page

Glossary – *Continued from previous page*

SYMBOL	UNIT	DESCRIPTION
n_{cyc}	-	Number of cycles considered in the determination of the logarithmic decrement
N_{fins}	m	Total number of fins in an electro-static fin actuator
n_{sample}	-	Number of samples in a Monte Carlo simulation
N_x	N	Horizontal reaction force at pendulum support
N_y	N	Vertical reaction force at pendulum support
N_0	-	Initial number of turns
n_0	m^{-1}	Initial turn-density
p_a	Pa	Ambient pressure
p_c	Pa	Combustion chamber pressure of a thruster
p_e	Pa	Exhaust pressure of a thruster nozzle
P_s	Pa	Standard pressure
R	m	Radius of coil
R	m	Sensor full-scale range
R_{meas}	m	Radius of measurement area of sensor
R	$\text{J kg}^{-1} \text{K}^{-1}$	Specific gas constant
R	Ω	Electric resistance
R^2	-	Coefficient of determination
ΔR	m	Error in thrust range
R_c	Ω	Electric resistance of a coil
R_u	$\text{J mol}^{-1} \text{K}^{-1}$	Universal gas constant
S	V m^{-1}	Sensor sensitivity
s	s	Time variable in Laplace domain
S_f	VN^{-1}	Sensitivity of the thrust stand to thrust force
S_k	VK^{-1}	Sensitivity of a K-type thermocouple to a temperature difference across its terminals
s_β	-	Standard error of the slope
T	N	Thrust force
T	s	Period of oscillation

Continued on next page

Glossary – *Continued from previous page*

SYMBOL	UNIT	DESCRIPTION
t	s	Time variable in time domain
T_{gas}	K	Temperature of the gas in the vacuum chamber
t_{actual}	m	Actual thickness of a counter mass
T_c	K	Temperature in the combustion chamber
T_{daq}	K	Temperature of the data-acquisition system
t_{design}	m	Design thickness of a counter mass
T_i	K	Temperature of the sensing terminal of a thermocouple
T_R	N	Thrust range of thrust stand
T_{ref}	K	Temperature of a reference point
T_s	K	Standard temperature
\tilde{U}	V	Random noise in the displacement measurement signal that is introduced by the data-acquisition system
U_e	$m s^{-1}$	Exhaust velocity of a thruster nozzle
U_{meter}	V	Voltage over coil
U_{sens}	m	Output voltage of the sensor
V	m^3	Volume
\dot{V}	$m^3 s^{-1}$	Volume flow rate
V_{act}	V	Potential between two parts of an electrostatic actuator
$V_{chamber}$	V	Volume of the vacuum chamber
V_{ref}	m^3	Volume of a reference magnet
ΔV	$m s^{-1}$	Velocity increment due to an impulsive shot
W	m	Width of the vacuum chamber
W_t	N	Total weight of the pendulum
x	m	Coordinate in Cartesian coordinate system
\ddot{x}	$m s^{-2}$	Horizontal acceleration of center of gravity of the pendulum
x_0	m	Engagement distance in an electro-static fin actuator
δx	m	Sensor accuracy in linear displacement

Continued on next page

Glossary – *Continued from previous page*

SYMBOL	UNIT	DESCRIPTION
Δx	m	Average spacing between two consecutive turns on a coil
Δx_m	m	Distance over which a mass shifts to cause a differential moment on the thrust stand
y	m	Coordinate in Cartesian coordinate system
\ddot{y}	m s^{-2}	Vertical acceleration of center of gravity of the pendulum
z	m	Coordinate in Cartesian coordinate system
Γ	-	Vanderkerckhove-constant
γ	-	Ratio of specific heats
Δ_x	m	Error in displacement measurement due to sensor tilting
δ	-	Logarithmic decrement
$\delta()$	-	Dirac delta operator
ϵ_0	F m^{-1}	Permittivity of vacuum
ζ	-	Propellant-to-dry-mass ratio
Θ	rad	Tilting angle of sensor with respect to target
θ	rad	Canting angle of a canted Helmholtz setup
θ	rad	Rotation angle
$\dot{\theta}$	rad s^{-1}	Rotational rate
$\ddot{\theta}$	rad s^{-2}	Rotational acceleration
$\Theta(s)$	-	Rotation angle in Laplace domain
λ	m	Wavelength
μ	-	Average
μ	$\text{V s A}^{-1} \text{ m}^{-1}$	Magnetic permeability of a material
μ_0	$\text{V s A}^{-1} \text{ m}^{-1}$	Magnetic permeability of vacuum
μ_1	A m^2	Magnetic dipole moment
ρ	kg m^{-3}	Gas density
σ	-	Standard deviation
Φ	Wb	Magnetic flux density
χ	-	Attenuation factor
ω	rad s^{-1}	Rotational rate

Continued on next page

Glossary – *Continued from previous page*

SYMBOL	UNIT	DESCRIPTION
ω_{eff}	m s^{-1}	Effective exhaust velocity
ω_n	rad s^{-1}	Natural frequency
ω_n	rad s^{-1}	Damped natural frequency
$\mathcal{L}\{\}$	-	Laplace transform

INTRODUCTION

Design is an iterative process. What starts with an idea, goes through the stages of conceptualization, design, manufacturing, integration, assembly and testing. The latter one is a recurring activity: between iterations the current product is tested to determine its performance and check if it is working properly and as expected; models are verified and validated based on experimental results and once the product is finished it is tested at least one more time to verify that the delivered product meets the customer's requirement. Testing is an activity that comes back in every stage of the design of a rocket engine.

In the past century, rocket engineers and scientists have designed and developed rocket engines in all sorts and sizes: from enormous rocket engines that once propelled man to the moon to very small resistojets not larger than a dime. The last category of micropropulsion systems has received an increased amount of attention in the past 50 years and has been applied as the main source of propulsion for small satellites and for precise attitude control. Also at the Chair of Space Systems Engineering (SSE) of Delft University of Technology (DUT), these systems receive ample attention. Every year students graduate on the design and development of small propulsion systems that are to propel the in-house developed satellites. The increased attention for miniaturized space systems leads to the development of even smaller thrusters that provide lower levels of thrust that is sometimes not shy of just a few micronewtons. Continuous flow is no longer guaranteed and ideal rocket motor theory is no longer always sufficient. The development of thrusters at the chair is supported by the Delft Aerospace Rocket Thrust Stand (DARTS) facility that provides test stands to measure the force provided by the in-house developed thrusters. In the past years the DARTS facility has gained the capability to measure thrusts from 10 μN to 2 mN at an accuracy of $\leq 2 \mu\text{N}$ with the TB-2m, 0.5 mN to 50 mN at an accuracy of 0.5 mN with the TB-50m [39] and upto 1 N at an accuracy of 5 mN with the TB-1.1 [82, 71, 8, 72].

Commercial facilities such as ESA Electric Propulsion Laboratory (EPL) in the Netherlands, Ångström Space Technology Centre in Sweden and ONERA in France have the capability to extend their measurement range down into the μN regime. Great care is taken to reduce the environmentally induced noise to a minimum and to characterize

the setup to assure an accurate result. While tests at commercial facilities can cost up to €40.000 per week, an in-house facility gives quick and cost-effective access to test equipment and academic training.

Providing an accurate and precise thrust measurement in the micronewton to millinewton regime is not obvious. A sensitive system is required that is capable of detecting these small forces. The environmentally induced noise, however, is often in the same order of magnitude as the signal or larger [39] and the signal can get lost in the noise. Beside thrust measurement, also calibration of such small forces in a controlled and repeatable manner is a challenging matter as shown in prior investigations in thrust stand design at DUT. Especially at a severely constrained budget and schedule.

The research objective of the thesis can be summarized as

To enable thrust measurements in the 1 μ N to 5 mN range and impulse bits in the 1 μ Ns to 1 mNs range for the DARTS facility by one student in seven months within the available budget.

This objective is split into smaller sub-objectives that define the aims of the research effort:

1. to design a thrust stand that meets the required ranges, accuracy and any other imposed requirement;
2. to provide a calibration method that is capable of calibrating the developed thrust stand within the required ranges and accuracy;
3. to verify and validate the thrust stands and developed methods with hardware in the loop.

To fulfill the research objective the main research question is formulated as

How can the DARTS facility be upgraded to measure thrust levels in the 1 μ N to 5 mN range and impulse bits in the 1 μ Ns to 1 mNs range?

The problem is approached in a structured way. First the stakeholders and the requirements are analyzed. The results of which are used as input to the design process of the thrust stand. The thrust stand design is based on the AE-TB-2m. Using an analytical model, the design space is analyzed and design improvements are introduced. Second, as an integral part of the thrust measurement system, the calibration actuator is designed and manufactured. Lastly, the design is converted into a working lab model of the thrust measurement system and the design is verified and validated using a hardware-in-the-loop approach. The Proportional Micro Thruster (PMT) of Bradford Engineering has been tested before at two commercial facilities.

The obtained measurement data is compared to these two reference sources.

In this thesis, the development of the AE-TB-5m is described in detail. In [Chapter 2](#) thrust measurement systems and the terminology of basic metrology are introduced. In [Chapter 3](#) the stakeholders and the requirements are analyzed. Following the introductory chapters, the designs for the thrust stand and calibration system are described respectively in [Chapter 4](#) and [Chapter 5](#). The verification test, validation tests and the corresponding results are discussed in [Chapter 6](#) and [Chapter 7](#). Based on the results of the measurements, recommendations are made for changes in the design of the thrust stand to meet the renewed propulsion subsystem requirements of the DelFFi mission in [Chapter 8](#). The thesis is concluded with recommendations for future research in [Chapter 9](#).

BACKGROUND AND DEFINITIONS

Thrust measurement systems come in different varieties. In this chapter, the basic topologies for thrust stands are described and the basic terminology of metrology is introduced.

2.1 THRUST AND IMPULSE BIT MEASUREMENTS

The measurement techniques for micropropulsion systems are grouped based on their structural topology. Using this division, the thrust stands are grouped in hanging pendula, inverted pendula, torsion balances, swinging gates and folded pendula types. A secondary grouping is based on the location of the thruster: it can be mounted on the thrust stand itself - resulting in a direct measurement of thrust - or be mounted such that the exhaust plume hits the thrust stand - resulting in an indirect measurement of thrust. The mentioned types are discussed in this section, including examples, advantages and disadvantages, and shown performances. The dynamics of all mentioned types can be described accurately by a damped mass-spring system. The information in this section is also presented in the Master Orientation Project (MOP) [7].

2.1.1 *Hanging pendulum*

Hanging pendula are popular thrust stands due to their inherent stability and simplicity. However, high sensitivity inherently means relatively long pendulum arms. This renders the hanging pendula comparatively bulky and too large for most vacuum chambers [86]. A firing thruster creates a moment on the pendulum, that causes it to rotate. The thrust or impulse bit can be measured by a force transducer that is attached to the thrust stand or by measuring the movement of a reference point on the pendulum arm. A schematic drawing of a pendulum is given in [Figure 1a](#).

Hanging pendula are also popular for indirect thrust measurements. In that case the pendulum can be smaller and is free of ancillary forces due to wiring. Problems in indirect measurements are associated with unknown elasticity of the momentum exchange between the exhaust plume particles and the target [27, 28]. Research is currently ongoing in optimizing the shape of the target to minimize the effect of elastic momentum exchange [23].

The AE-TB-2m that was developed at Delft University of Technology by Perez-Grande [68] falls in the latter category. It is designed to provide a measurement range of $10\ \mu\text{N}$ to $2000\ \mu\text{N}$ at a resolution of $2\ \mu\text{N}$. The motion of the pendulum is measured using a laser triangulation sensor. Similar in design and performance is the ONERA Micro-Newton balance [66, 67]. This stand uses a capacitive sensor and an accelerometer to measure the dynamics. High sensitivities are obtained using laser interferometers to measure the displacements up to nanometer level. This allows the measurement of thrust levels of $5\ \mu\text{N} - 1\ \text{mN}$ [5].

Examples of hanging pendula with force transducers are the AE-TB-1.0, AE-TB-1.1 [93] and VAPHER [70].

2.1.2 *Inverted pendulum*

Inverted pendula are inherently unstable. This instability renders them very sensitive to small forces. The sensitivity can easily be tweaked by changing the stiffness of the flexures and load spring [86]. To achieve stability, actuators are added to the thrust stand design that forces the pendulum back to its equilibrium state, also known as null-type pendula.

The null-type inverted pendulum designed by Xu et al. [86] supports thrusters with a total mass of up to 250 kg and provides the ability of measuring loads between 1 mN and 5 N. The inverted pendulum is schematically drawn in Figure 1b.

2.1.3 *Folded pendulum*

The folded pendulum, also known as the Watts pendulum, consists of a horizontal bar that is supported by a hinged lever at one end and is suspended at the other end by a flat ribbon spring as depicted in Figure 1c. The center of mass of the horizontal bar moves in a straight line when it is excited. By moving the center of mass forward or aft, the period of the pendulum is controlled [14]. A long period allows the application of high frequency impulses without exciting any resonance with a small thrust stand. The counteracting stabilizing motion of the hanging pendulum and the instable motion of the inverted pendulum that support the horizontal bar result in a low effective stiffness and a high sensitivity to external loads [69, 78].

2.1.4 *Torsion balance*

Torsion balances have a restoring force that is independent of the thruster mass and provide high sensitivity. However, as for normal hanging pendula, the arms are relatively long and their placement

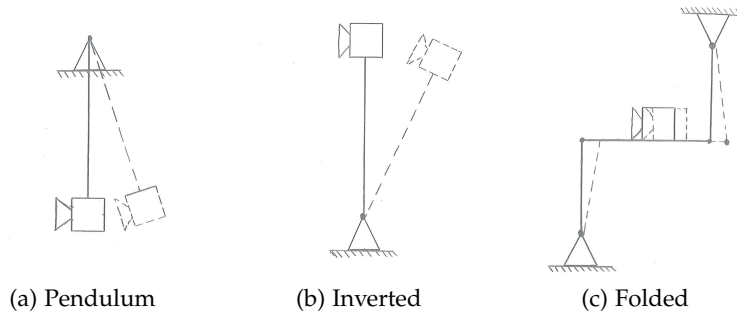


Figure 1: Sketches of pendulum type thrust stands.

render them often too large to fit in typical vacuum chambers when very high sensitivity is required [86]. Torsion balances come in different types. The most used type is the 'Swinging Gate Pendulum' in which the rotation axis is aligned with the local gravitational vector. This causes a restoring force to be completely independent from the thruster mass. Examples of this type are the AE-TB-50m developed at DUT [39, 93], NIBS [41], TASI [50] and other unnamed examples [42, 75, 89, 84].

The dynamics are determined using a force transducer or displacement transducer. For the latter option often Linear Variable Displacement Transducers (LVDT) or interferometers are used. All torsion balances have the following critical components: two arms, at least one supporting pivot, a torsion spring to provide the restoring force, a thruster and a counter weight. Often also a damper is included to reduce the settling time and to reduce noise.

Operation of a torsion balance is not limited to the horizontal plane. Motion in the vertical plane is also possible as depicted in Figure 2a. Examples of this are given by [19, 30, 48, 49]. Torsion balances can be used for both steady load and impulse bit measurements. The ranges are mainly dependent on the length of the arms and the accuracy of the dynamics measurement.

2.1.5 Flexure

To accurately measure impulse bits a more exotic thrust stand has been developed by Land [47]. The thruster is connected to the center of a flexure that vibrates upon firing of the thruster. A schematic drawing can be found in Figure 2b. The motion of the flexure is measured by a Michelson interferometer. From the dynamics of the flexure, the impulse bit can then be derived. The advantage of this type of thrust stand is its small size. This allows measurement in smaller vacuum chambers. Other advantages include the controllable sensitivity via flexure design and a high resonance frequency [47]. Flexures,

however, are designed for one specific thruster and are typically not readily available for a new thruster type.

2.1.6 Resonant blade

To measure impulse bits and average thrust of Pulsed Plasma Thrusters at low cost, a simple thrust stand was developed by Brito et al. [10]. The thruster is mounted on a blade with an eigenfrequency at the thruster activation frequency. This is schematically drawn in Figure 2c. It results in a forced vibration of the resonant blade that amplifies the motion that the blade would have after a single pulse. The resonant operation reduces the effect of environmental vibrations. This principle is also used for Torsion Balance operation by Lake et al. [75]. The advantage of this type of thrust stand lies in its relatively low cost. The disadvantage is that the thrust stand is limited to operation at the eigenfrequency of the resonant blade and therefore has to be redesigned for every thruster.

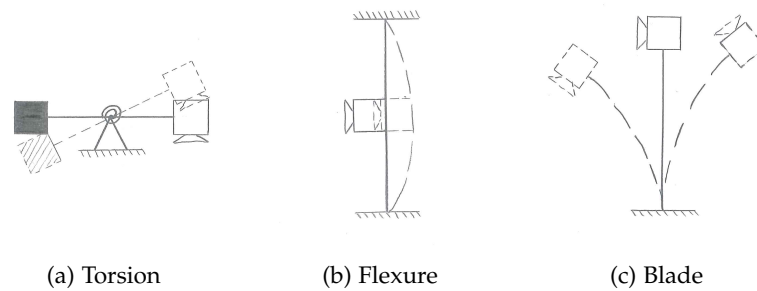


Figure 2: Sketches of torsion and flexure type thrust stands.

2.2 FORMAL DEFINITIONS

In this thesis, metrology related terminology is used often. For the remaining part of this report the conventions used by the International Organization for Standardization (ISO), NASA and the Joint Committee for Guides in Metrology (JCGM) are used. The used definitions are cited and explained below and a visual representation of the definitions is given in Figure 3.

ACCURACY

"The closeness of agreement between a test result and the accepted reference value." The accuracy is the combination of the trueness of a measurement and the precision.

TRUENESS

"The closeness of agreement between the average value obtained from

a large series of test results and an accepted reference." The trueness is not a quantity, but often characterized by a bias.

PRECISION

"The closeness of agreement between independent test results obtained under stipulated conditions." The precision is not a quantity. It is typically characterized by the standard deviation or variance of the spread of the set of results.

BIAS

"The difference between the expectation of the test results and an accepted reference value."

ACCEPTED REFERENCE VALUE

"A value that serves as an agreed-upon reference for comparison, and which is derived as: a) a theoretical or established value, based on scientific principles; b) an assigned or certified value, based on experimental work of some national or international organization; c) a consensus or certified value, based on collaborative experimental work under the auspices of a scientific or engineering group; d) when a), b) and c) are not available, the expectation of the (measurable) quantity, i.e. the mean of a specified population of measurements."

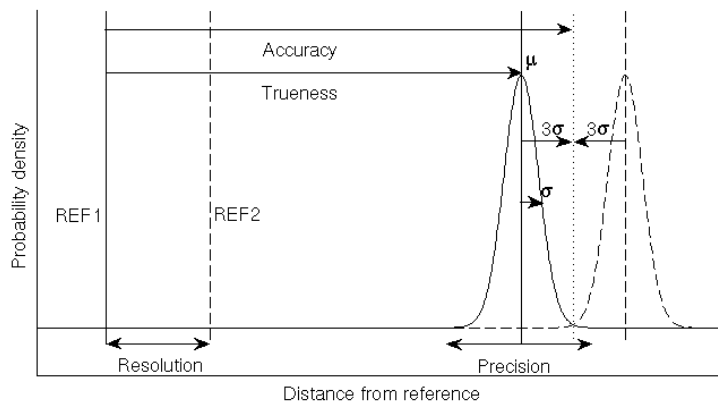


Figure 3: Relation between accuracy, precision, trueness and resolution according to ISO 5725-1:1994 [37].

The concepts of calibration, verification and validation are recurring subjects in metrology. The setup has to be calibrated to provide traceability of measurements to an (inter)national standard. Traceable measurements allow the verification and validation of the setup, as well as end-users to verify and validate their own products. Calibration is defined by JCGM [40] as follows:

CALIBRATION

"Operation that, under specified conditions, in a first step, establishes

a relation between the quantity values with measurement uncertainties provided by measurement standards and corresponding indications with associated measurement uncertainties and, in a second step, uses this information to establish a relation for obtaining a measurement result from an indication."

The latter two, verification and validation, are defined by NASA in its NASA Procedural Requirements (NPR) 7120.5D [57] as:

VERIFICATION

"Proof of compliance with design solution specifications and descriptive documents. May be determined by a combination of test, analysis, demonstration and inspection."

VALIDATION

"Proof that the product accomplishes the intended purpose based on stakeholder expectations. May be determined by a combination of test, analysis, demonstration and inspection."

STAKEHOLDERS AND REQUIREMENT ANALYSIS

Before embarking on the design of the thrust stand, the stakeholders, their requirements and derived requirements are discussed and explained. The requirements and their rationales are given and supported by (mathematical) modelling where necessary.

3.1 STAKEHOLDERS

For this project several stakeholders have been identified which are listed in [Table 1](#). The project supervisor, Barry Zandbergen, has been identified as the key stakeholder. As the manager of the [DARTS](#) facility, he is the prime customer and stakeholder for this thesis work and the corresponding requirements will largely influence the design effort.

Potential users, such as the DelFFi project, MSc and PhD students working on thruster design, and companies, dictate needs with respect to the thrust range and Minimum Impulse Bit ([MIB](#)). Stakeholder TNO is seeking collaboration with the [DARTS](#) facility and other facilities within the Netherlands and the rest of Europe to share measurement setups and is therefore considered a potential end-user [92].

ESA [EPL](#) and ONERA both provide measurement capabilities that are similar in range requirements as the designed upgrade of the [DARTS](#). Both have measured the performance of the Bradford Engineering [PMT](#) before and results obtained by these institutions can be used for validation. The measurement results are available for comparison with the hardware-in-the-loop measurement of the new thrust stand. In case the results of this study are published, both parties are a stakeholder in the publication and will have corresponding needs in terms of publication rights and non-disclosure of information.

The project is initially funded through the chair of [SSE](#) of the faculty of Aerospace Engineering of [DUT](#). The STW and NWO, both institutions that provide funding for academic research in the Netherlands, are potential funders of further research.

As can be seen in [Table 1](#), only the key stakeholder imposes requirements on the thrust accuracy. The requirement is cross-checked with possible requirements of potential end-users to verify the given numbers. As the accuracy is an important parameter for the design of the measurement equipment, the related top-level requirements are derived from general mission design and thruster design needs in [Section 3.3](#).

STAKEHOLDER	A/P	NEED
Roy Bijster	A	Needs to graduate with MSc. worthy project and learn in the process.
Barry Zandbergen 	A	Needs an upgraded DARTS facility, based on existing thrust stands, capable of measuring thrust from 1 μN – 5 mN and impulse bits with a minimum of 1 μN s. The stand should fit in the available vacuum chamber. Knowledge transfer on the thrust stand should be ensured between students and staff. Force accuracy of 1% in the 50 μN to 5000 μN range and 10% in the 1 μN to 50 μN range.
DelFFi	A	Need to measure thrust in the 1 mN to 10 mN range.
MSc. students	A	Need to measure in the 1 μN – 1 mN range. Need to determine specific impulse of thruster.
ESA EPL	A	EPL allows testing in their high vacuum facility. Thrust stand needs to fit in their tanks, do no damage to the equipment and comply with the available feed-through system. Also have a competitive system and have measured the thrust for the Bradford Engineering PMT before.
Bradford Engineering B.V.	A	BE lends their PMT thruster for validation of the thrust stand. They require that all measurement data is freely available to them and the corresponding data is covered by a non-disclosure agreement.
Chair of SSE	P	Provides a € 500 budget to cover any required expenses within the scope of the thesis. Wants to showcase the capabilities of the chair and its students.
STW/NWO	P	Potentially provide additional funding.
ISO	P	For ISO accreditation the facility and organization need to meet the requirements set by ISO 9001 and ISO 17025.
ONERA	P	Competitor that provides a competitive system and has measured thrust for the Bradford Engineering PMT before. In case results of the thrust stand validation are published, ONERA is a stakeholder in the publication.
TNO	A	Seeks possibilities for collaboration for thrust measurements within the Netherlands. Potential user.
CGG	A	Manufactures cold gas generators and thrusters that need qualification testing. Potential user.
Other users	A	Need to measure thrust or impulse bits in the available range.
Manufacturers	P	Need engineering drawings and/or specifications of the required parts.
Suppliers	P	Need to have specifications of the required parts.

Table 1: Overview of the project stakeholders and the stakeholder requirements. Stakeholders are identified as P(assive) or A(ctive) stakeholders.

3.2 TOPLEVEL SYSTEM REQUIREMENTS

From the stakeholder requirements the following toplevel requirements are derived. For every toplevel requirement the rationale is added. The requirements are labeled with identification tags for later reference. The tags are short-hand notations for words associated with the requirement: ACCUR for accuracy, DIMEN for dimensions, OPERA for operations, VACUU for vacuum conditions, SAMPL for sample related requirements, RESRC for the available resources and lastly CALIB for calibration.

RANGE-1 The measurement system shall provide a measurement range of $1 \mu\text{N} - 5 \text{mN}$ for steady state thrust.

Rationale: Stakeholder Barry Zandbergen requires sufficient overlap with the AE-TB-50m [39] thrust stand in the DARTS facility and an extension of the available measurement range into the micronewton regime.

RANGE-2 The measurement system shall provide a measurement range of $1 \mu\text{Ns} - 1 \text{mNs}$ for impulse bits.

Rationale: The possibility of impulse bit measurement has only been shown for the AE-TB-50m and not been verified [39]. To provide the DARTS facility with a useable capability this range of impulse bits has to be covered. See [Section 3.3](#) for details.

ACCUR-1 The measurement system shall provide a relative accuracy of 10% in the $1 \mu\text{N}$ to $10 \mu\text{N}$ range and a relative accuracy of 1% in the $10 \mu\text{N}$ to $5000 \mu\text{N}$ (threshold), an absolute accuracy of $0.1 \mu\text{N}$ over the $1 \mu\text{N}$ to $100 \mu\text{N}$ range and a relative accuracy of 0.1% over the $100 \mu\text{N}$ to $5000 \mu\text{N}$ range (goal).

Rationale: To provide sufficient accuracy that is required for specific impulse determination and to provide highly accurate measurements over the full range. For a more detailed rationale see [Section 3.3](#).

ACCUR-2 Impulse bits shall be measured with a relative accuracy of 10% (threshold), a relative resolution of 1% (goal) μNs .

Rationale: The smallest impulse bits are required for attitude control. For a more detailed rationale see [Section 3.3](#).

DIMEN-1 The thrust stand outer dimensions shall not exceed $52.9 \times 49.5 \times 48.9 \text{ cm}$ (D \times W \times H).

Rationale: The thrust stand needs to operate in the Heraeus Vacuotherm vacuum oven.

OPERA-1 A manual shall be provided in which the assembly and operation of the thrust stand and the calibration procedures are described and explained.

Rationale: The stand needs to be operated by students, staff and external parties without the need for specialized training.

OPERA-2 The measurement setup should be safe to operate and shall not harm the operator nor damage other equipment.

Rationale: Unexperienced users, such as new graduate students using the setup, need to be able to work with the stand without the risk of harming themselves or others.

VACUU-1 The measurement setup shall be able to operate at 1.5 mbar (threshold), Ultra-High Vacuum pressure (goal).

Rationale: Prior research has shown that detectors can be pressure sensitive or are not capable of vacuum operation. The setup should function correctly at pressure compliant with the Heraeus Vacuotherm vacuum oven. Preferably also at Ultra High Vacuum (UHV) so that it can be used at ESTEC's Propulsion Laboratory.

SAMPL-1 The measurement setup shall be able to measure thrust and impulse bits for thrusters with a maximum thruster mass of 0.3 kg. *Rationale: Analysis by Daniel Grande Perez [68] and Stef Janssens [39] has shown that this maximum sample mass is in line with small thrusters that have been developed in the past or are currently under development.*

RESRC-1 The budget is limited to € 500. For expenses that exceed this budget, approval from the project supervisor is required.

Rationale: The chair of Space Systems Engineering provides a € 500 budget for every master student. This budget is preliminary as other parties may provide additional funding or investments are justified.

RESRC-2 The project shall be completed within seven months from the kick-off meeting, on 14 December, 2013.

Rationale: The project started 1 April, 2013. The kick-off meeting was held on 14 May, 2013. The project shall be finished by 14 December, 2013.

CALIB-1 A calibration method shall be provided for steady state and impulse bit methods.

Rationale: The thrust stand needs to be calibrated.

CALIB-2 The calibration method shall allow in-situ calibration without manual interference of the operator.

Rationale: The operator needs to be able to calibrate the thrust stand when the thrust stand is in vacuum.

3.3 REQUIREMENT RATIONALE

The requirements for accuracy are derived from the stakeholder needs. One of those needs is the ability to determine engine specific impulse. Based on this need, the required relative accuracies in thrust and mass flow are calculated in this section. From this the requirements for the

measurement setup are derived.

The specific impulse is often used to estimate the propellant-to-dry mass ratio of a satellite or rocket. In mission design of small satellites that are propellant mass limited, a relative accuracy of 10% in this ratio is often acceptable [62, 92]. Using ideal rocket motor theory and Tsiolkovsky's equation, the relative error in the propellant-to-dry mass ratio ζ can be derived. The change in velocity due to an impulsive shot in vacuum is given by

$$\Delta V = I_{sp} g_0 \ln \left(\frac{M_e + M_p}{M_e} \right) \quad (1)$$

where I_{sp} is the specific impulse in s, g_0 the gravitational acceleration at sea level in m s^{-2} , M_e the empty mass in kg and M_p the propellant mass in kg. With the propellant-to-dry mass ratio defined as $\zeta = M_p/M_e$, this can be rewritten as

$$\zeta = \exp \left(\frac{\Delta V}{I_{sp} g_0} \right) - 1 \quad (2)$$

The absolute error in ζ can then be expressed using partial differentiation as

$$\delta \zeta = \left| \frac{\partial \zeta}{\partial \Delta V} \right| \delta \Delta V + \left| \frac{\partial \zeta}{\partial I_{sp}} \right| \delta I_{sp} + \left| \frac{\partial \zeta}{\partial g_0} \right| \delta g_0 \quad (3)$$

Working out the partial derivatives and dividing by (2) results in

$$\frac{\delta \zeta}{\zeta} = \frac{\Delta V}{I_{sp} g_0} \left(1 - \exp \left(\frac{-\Delta V}{I_{sp} g_0} \right) \right)^{-1} \left(\frac{\delta \Delta V}{\Delta V} + \frac{\delta I_{sp}}{I_{sp}} + \frac{\delta g_0}{g_0} \right) \quad (4)$$

Rewriting this for the relative error in I_{sp} results in an expression for the allowable error in I_{sp} as a function of allowable relative error in propellant-to-dry mass fraction, relative error in ΔV and relative error in gravitational acceleration:

$$\frac{\delta I_{sp}}{I_{sp}} = \frac{\Delta \zeta}{\zeta} \frac{I_{sp} g_0}{\Delta V} \left(1 - \exp \left(\frac{-\Delta V}{I_{sp} g_0} \right) \right) - \frac{\delta \Delta V}{\Delta V} - \frac{\delta g_0}{g_0} \quad (5)$$

With the gravitational acceleration $g_0 = 9.81 \text{ m s}^{-2}$ and the accuracy to which it is known $\delta g_0 \leq 0.005$, the relative error can be calculated to be $\delta g_0/g_0 \leq 5.1 \cdot 10^{-4}$ or equivalently $\leq 0.051\%$. The relative error in gravitational acceleration is thus very small and its contribution to the relative error in I_{sp} can be neglected.

Using ideal rocket motor theory the specific impulse of an engine can be expressed as

$$I_{sp} = \frac{\omega_{eff}}{g_0} = \frac{T}{m g_0} \quad (6)$$

where ω_{eff} is the effective exhaust velocity in m s^{-1} , T the thrust in N and m the mass flow in kg s^{-1} . In a similar fashion as for the propellant-to-dry mass ratio, the absolute error in the specific impulse can be found using partial differentiation

$$\Delta I_{sp} = \left| \frac{\partial I_{sp}}{\partial T} \right| \delta T + \left| \frac{\partial I_{sp}}{\partial m} \right| \delta m + \left| \frac{\partial I_{sp}}{\partial g_0} \right| \delta g_0 \quad (7)$$

Working out the partial derivatives, followed by division of this equation by (6) gives the relative error in specific impulse.

$$\frac{\delta I_{sp}}{I_{sp}} = \frac{\delta T}{T} + \frac{\delta m}{m} + \frac{\delta g_0}{g_0} \quad (8)$$

Rewriting this expression for the allowable relative error in thrust then gives

$$\frac{\delta T}{T} = \frac{\delta I_{sp}}{I_{sp}} - \frac{\delta m}{m} - \frac{\delta g_0}{g_0} \quad (9)$$

These error propagation relations can be used to estimate relative allowable errors for specific missions. As the **DARTS** facility is primarily used for TU Delft missions and thrusters, these serve as benchmarks for the requirements on resolution. Characteristic parameters used in mission design and propulsion system selection, such as velocity increment ΔV , thrust F and specific impulse I_{sp} , are listed in [Table 2](#). The listed mass flow rate is based on ideal rocket motor theory and calculated using the nominal thrust and specific impulse. The nominal values for the E-moth and DelFFi missions have been plugged into the derived relations and plotted in [Figure 4](#) and [Figure 5](#), respectively.

PARAMETER	E-MOTH	DELFFI ¹	OLFAR	DELFI-N ₃ X _T
$\Delta V(\text{m s}^{-1})$	4000	20 (ideal), 7 (conservative)	Not available	Not available
$T(\text{N})$	$840 \cdot 10^{-6}$	$9.5 \cdot 10^{-3}$	$1050 \cdot 10^{-6}$	$\approx 6 \cdot 10^{-3}$
$I_{sp}(\text{s})$	2500	70	2500	≥ 30
$m(\text{kg s}^{-1})$	$3.4 \cdot 10^{-8}$	$1.4 \cdot 10^{-5}$	$4.3 \cdot 10^{-8}$	$2.0 \cdot 10^{-5}$

Table 2: TU Delft satellite mission propulsion requirements and characteristics for E-moth [6], DelFFi [29], OLFAR [25] and Delfi-N₃X_T [92]. ¹: Based on estimates of April 2013.

Before the allowable errors can be estimated, the relative error in propellant-to-dry mass ratio that can be accepted needs to be estimated. The micropropulsion systems are primarily used for fine attitude control on bigger missions, and as the main propulsion system

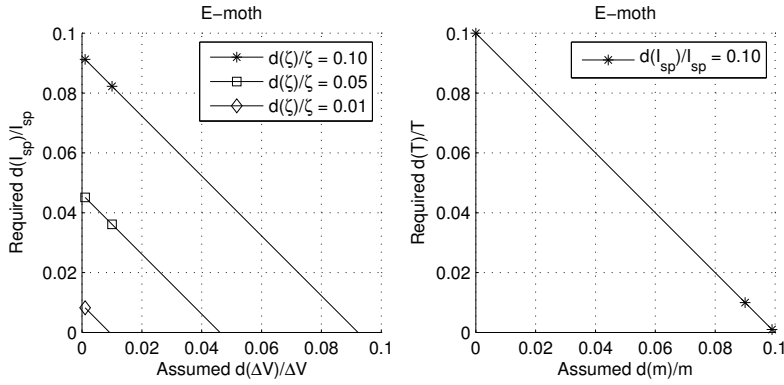


Figure 4: Acceptable relative errors in specific impulse and thrust for the E-moth mission.

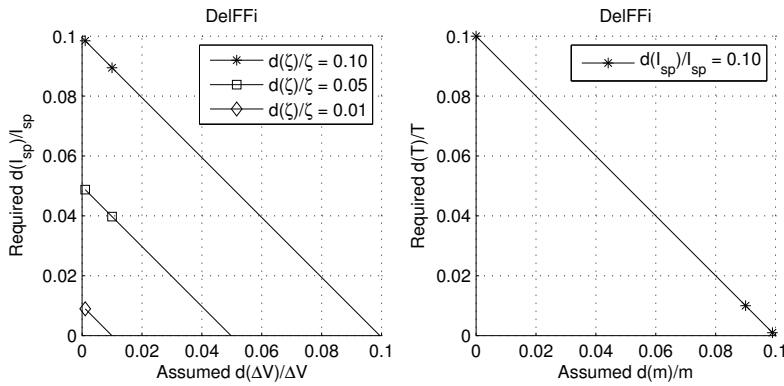


Figure 5: Acceptable relative errors in specific impulse and thrust for the DelFFi mission.

on micro- and nanosatellites. In this derivation, the focus is on the latter application. Assuming a cubesat such as Delfi-N₃Xt, with a total wet mass of 3 kg, several scenarios can be used. With a propellant-to-dry mass ratio of $\zeta = 2\%$, the propellant mass amounts to 59 g. In this case an error of 10 – 100% can be allowed, depending on the exact mission and design stage. If, however, $\zeta = 20\%$ the propellant mass equals 500 g. In that case an error of only 1 – 10% can be accepted. Following this line of thought, an indicative allowable error in propellant-to-dry mass ratio can be given. This envelope is depicted in Figure 6. The given numbers are provisional. Actual numbers should be related to the allowed design margins within the spacecraft design that are available for the propulsion system.

The allowable relative errors have been calculated for the E-moth and DelFFi missions. The corresponding results are depicted in Figure 4 and Figure 5. For an allowable relative error in propellant-to-dry mass ratio ζ of 10%, it is clear that a relative error slightly below 10% for specific impulse is allowed for both missions. Here it is assumed, that the required ΔV is known to 1%. This assumption has been verified by Noomen [62]. Both missions have completely different characteristics.

From
 $M_e + M_p = M_{wet}$
 and $\frac{M_p}{M_e} = \zeta$ one
 can derive that
 $M_p = \frac{\zeta}{1+\zeta} M_{wet}$.

A relative error in ζ of 10% could for example mean $\zeta = 0.18 \pm 0.018$.

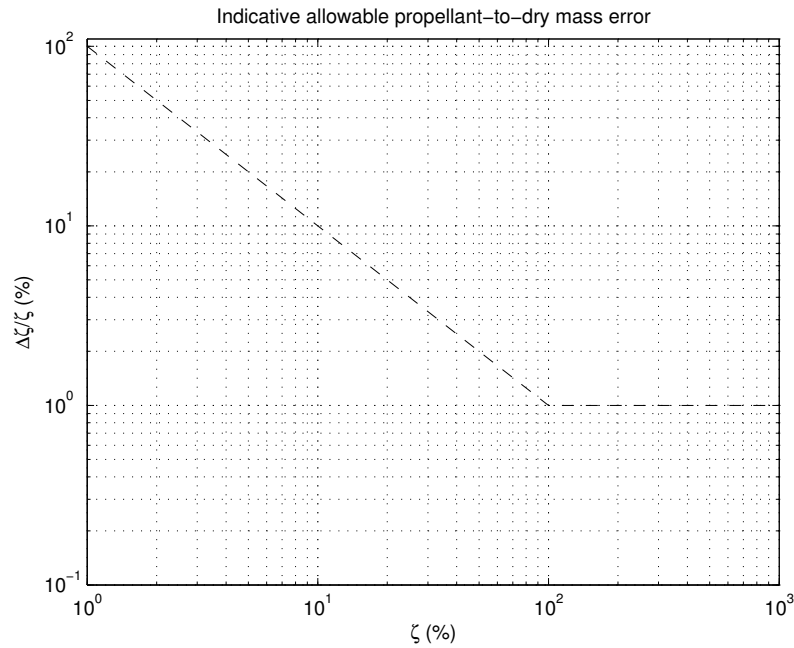


Figure 6: Indicative graph showing the allowable error in propellant-to-dry mass ratio $\Delta\zeta/\zeta$ as a function of ζ . Only allowable orders of magnitude are given. Depending on the mission or design stage, bigger or smaller errors may be acceptable.

E-moth uses electric propulsion for long durations and DelFFi uses cold gas thrusters for comparatively short amounts of time. Based on this comparison, it is assumed that a 10% relative error in specific impulse is acceptable for the TU Delft missions. To estimate the allowable relative error in steady thrust, the relative error in mass flow needs to be known. The mass flows required for DelFFi and Delfi-N₃Xt can be measured to 1% accurate [11]. For the E-moth mission and OLFAR mission no mass flow meter capable of measuring such low flow rates has been found. The mass flow rate could be obtained in different ways, such as measuring the changes in tank pressure and tank gas temperature over time. As this requires many more assumptions, this is left for now. It is assumed, that the mass flow rate can be measured up to an accuracy of 1%. In that case a relative error slightly below 10% in steady thrust is allowed. This is considered the acceptance level for the required accuracy. The literature survey [7], however, has shown that for many larger missions the thrust is required up to an accuracy of 0.1 μN . This is considered a goal for the absolute accuracy over the measurement range up to 100 μN . For higher thrust levels a 0.1% relative accuracy is used. A survey by Koopmans [43] has shown that 0.1% of relative accuracy is challenging, but has been shown before, e.g. by ESA EPL and Ångström Space Technology Centre in Sweden. The thrust requirements are summarized in Figure 7.

A line representing a 5% error is included for comparison in regions where the acceptance level is exceeded.

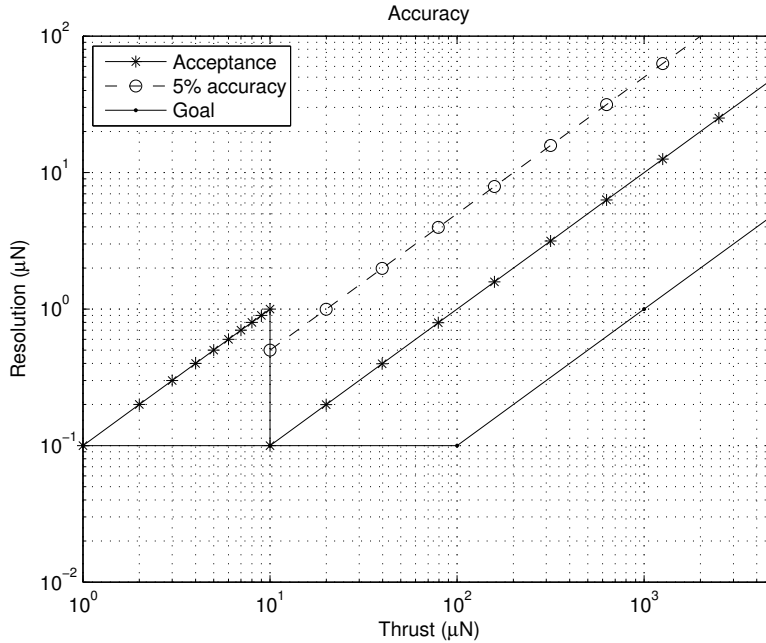


Figure 7: Acceptance and goal requirements for measurement accuracy.

For impulse bit measurements no requirements are given. For the bigger missions the required minimum impulse bit is often not specified. For control purposes, however, the MIB can be very important. A high specific impulse is often preferred to minimize propellant mass. For the micropropulsion systems used on the discussed missions, Hitt et al. [33] list typical values for both specific impulse and impulse bit. These values can be found in Table 3.

TYPE	SPECIFIC IMPULSE s	IMPULSE BIT μNs
Resistojet	45 – 100	100 – 1000
FEEP	17000	10 – 200
Microcolloid	450 – 1250	20 – 100
Micro-PPT	800 – 1000	0.1 – 10
Ion	1400 – 2000	0.1 – 10

Table 3: Typical values for Specific Impulse and Impulse Bit for micropropulsion systems [33].

Mueller et al. [56] have estimated the required impulse bits for micropropulsion systems used on nanosatellites for precise attitude control. For a cubic nanosatellite with a total mass of 1 – 20 kg and a mass moment of inertia of 0.017 kg m² to 0.533 kg m² the impulse bits have been calculated. The results are listed in Table 4. Comparison of the

available impulse bits listed in Table 3 and the requirements listed in Table 4 indicates that pointing accuracies of up to $1'$ can be achieved for the example microsattellites using micropropulsion systems. For more accurate pointing the engines will have to be improved. For this reason a measurement range of $1 \mu\text{Ns}$ to 1mNs is used.

POINTING ACCURACY	IMPULSE BIT Ns
1°	$10^{-5} - 10^{-3}$
$1'$	$10^{-7} - 10^{-5}$
$5''$	$10^{-8} - 10^{-6}$

Table 4: Estimated values for minimum impulse bit required for nanosatellite pointing for a cubic nanosatellite with a total mass of 1 kg to 20 kg and a mass moment of inertia of 0.017 kg m^2 to 0.533 kg m^2 [56].

THRUST STAND DESIGN

The new thrust stand will extend the capabilities of the [DARTS](#) facility into the micronewton regime, while re-using as much as of the available hardware from the AE-TB-2m (later called TB-2m) thrust stand as possible. A viable solution that achieves this with minimal changes to the original design is presented in this chapter. The design philosophy, important design decisions and background theory are outlined and explained in detail when required to support the design description.

4.1 THRUST STAND DESIGN OPTION ANALYSIS

A design based on the TB-2m is bound to be a pendulum design, which limits the design to two basic topologies: 1) the pendulum and 2) the inverted pendulum. An inverted pendulum is inherently unstable and therefore also very sensitive. Because the inverted pendulum will require a major redesign and the inclusion of actuators to achieve stability while maintaining high sensitivity, this design is not favored. A re-evaluation of the current design under minor design changes is preferred instead. This is aimed at keeping the design more robust and to allow reutilization of available hardware, while limiting the cost of ownership.

4.1.1 Analytical model

An analytical model is developed to calculate the achievable accuracy and range. Perez-Grande [68] performed a similar analysis, starting from the equations of steady state measurements. In the following analysis, however, the model is developed starting at the general equations of motion. This allows for the direct inclusion of the dynamics of the system and vibrations that are induced by the environment. The thrust stand is modeled as a lumped mass model. The corresponding Free Body Diagram (FBD) is depicted in [Figure 8](#). The thrust stand can be reduced to a cross-beam (M_b) that rests on a pair of pivots that allow the pendulum to rotate; a rotary spring connected to this cross-beam with stiffness K ; a pair of arms forming the pendulum (M_{a_1} and M_{a_2}); a counter mass (M_c); an engine (M_e); a sensor and/or sensor target (M_t); and possibly also other items connected to the arms required for calibration. In the figure N_x and N_y are the horizontal and vertical support forces respectively. The accelerations of the center of gravity in the used reference frame are indicated by

\ddot{x} , \ddot{y} and the product $l_{cg}\ddot{\theta}$. The accelerations \ddot{x} and \ddot{y} are linked to the vibrations that are induced by the environment and transferred via the baseplate and the suspension of the TB-2m .

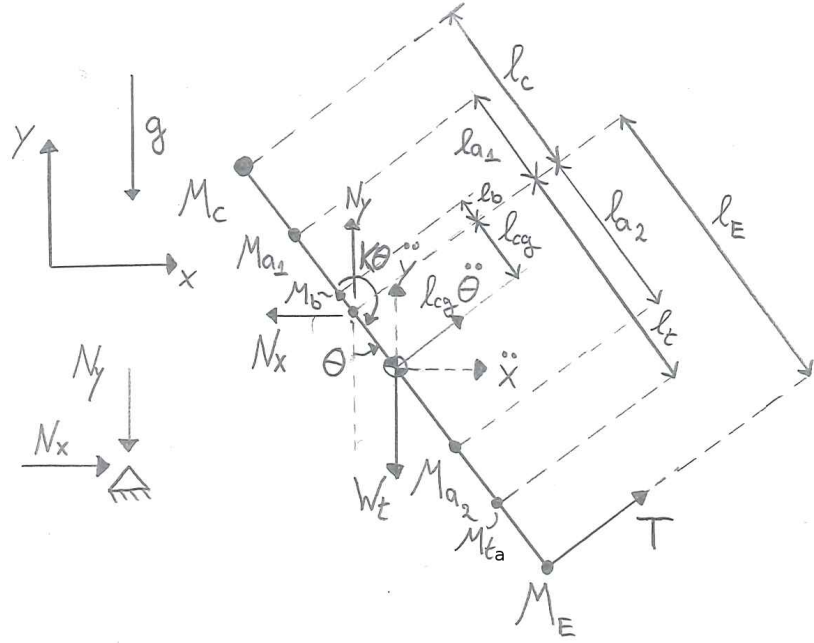


Figure 8: FBD of the thrust stand for the derivation of the analytical model that is used for the preliminary design phase.

The summation of forces along the vector $l_{cg}\ddot{\theta}$ results in the following equation of motion

$$(l_{cg}\ddot{\theta} + \ddot{x} \cos \theta + \ddot{y} \sin \theta) M_t = T - W_t \sin \theta + N_y \sin \theta - N_x \cos \theta \quad (10)$$

where W_t is the weight corresponding to the total mass of the pendulum. Summation of the moments about the center of gravity results in a second equation of motion

$$I_0\ddot{\theta} = (l_E - l_{cg}) T - K\theta - l_{cg}N_y \sin \theta + l_{cg}N_x \cos \theta \quad (11)$$

where I_0 is the mass moment of inertia about the center of gravity. Multiplication of (10) by l_{cg} and addition of the result to (11) results in

$$(I_0 + l_{cg}^2 M_t) \ddot{\theta} + (\ddot{x} \cos \theta + \ddot{y} \sin \theta) M_t l_{cg} = T l_{cg} - W_t l_{cg} \sin \theta + (l_E - l_{cg}) T - K\theta \quad (12)$$

This equation is nonlinear, but can easily be linearized by using small angle approximations. The rotation angle is assumed to stay small, causing $\cos \theta \approx 1$ and $\sin \theta \approx \theta$. Using these approximations finally yields the linearized equation of motion:

$$(I_0 + l_{cg}^2 M_t) \ddot{\theta} + (K + W_t l_{cg}) \theta = T l_E - (\ddot{x} + \ddot{y}\theta) M_t l_{cg} \quad (13)$$

A relation between the thrust and the rotation can be derived for a steady state condition ($\ddot{\theta} = 0$). Inaccuracies caused by uncertainty in the used lengths are neglected in this design stage. The rotation of the pendulum is sensed by a linear displacement sensor at a distance l_t from the pivot. The displacement Δx related to a small rotation $\Delta\theta$ is given by $\Delta\theta = \Delta x/l_t$. Rewriting (13) using these assumptions results in the required thrust ΔT to cause the sensed displacement Δx .

$$\Delta T = (K + W_t l_{cg}) \frac{\Delta x}{l_t l_E} + \left(\ddot{x} + \ddot{y} \frac{\Delta x}{l_t} \right) M_t \frac{l_{cg}}{l_E} \quad (14)$$

This equation can be used to estimate the thrust accuracy and thrust range that are measured by the thrust stand as a function of the geometry, environmental noise and sensor performance. To estimate the accuracy in thrust, Δx is the accuracy of the sensor system and the accuracy of the Data Acquisition System (DAQ). For accuracy estimation the second term on the right hand side of the equation has to be always positive, as disturbances will always lead to a lower accuracy (larger ΔT).

$$\delta T = (K + W_t l_{cg}) \frac{\delta x}{l_t l_E} + \left| \left(\ddot{x} + \ddot{y} \frac{\delta x}{l_t} \right) M_t \frac{l_{cg}}{l_E} \right| \quad (15)$$

In (15), δT is the thrust accuracy and δx is the accuracy of the sensor system and DAQ combined.

For range estimation, Δx represents half of the full sensor system range R . Only half of the full range can be used, because the full motion of the pendulum needs to be measured. The second term on the right hand side can be neglected. The thrust range T_R that can be measured is then given as

$$T_R = (K + W_t l_{cg}) \frac{R}{2l_t l_E} \quad (16)$$

This represents an ideal case; environmental vibrations may cause the pendulum to go out of range. This is neglected in this stage of the design, as the effects are in the order of magnitude of the thrust accuracy causing it to be much smaller than the full range. This assumption is confirmed by calculation of the error in range using

$$\Delta R = \left| \left(\ddot{x} + \ddot{y} \frac{\delta x}{l_t} \right) M_t \frac{l_{cg}}{l_E} \right| \quad (17)$$

An example of the error in the thrust range is printed in Figure 9. As can be seen from the figure, the error is dependent on arm length. When optimized, the effects of the noise are minimized, as well as on the error in the range.

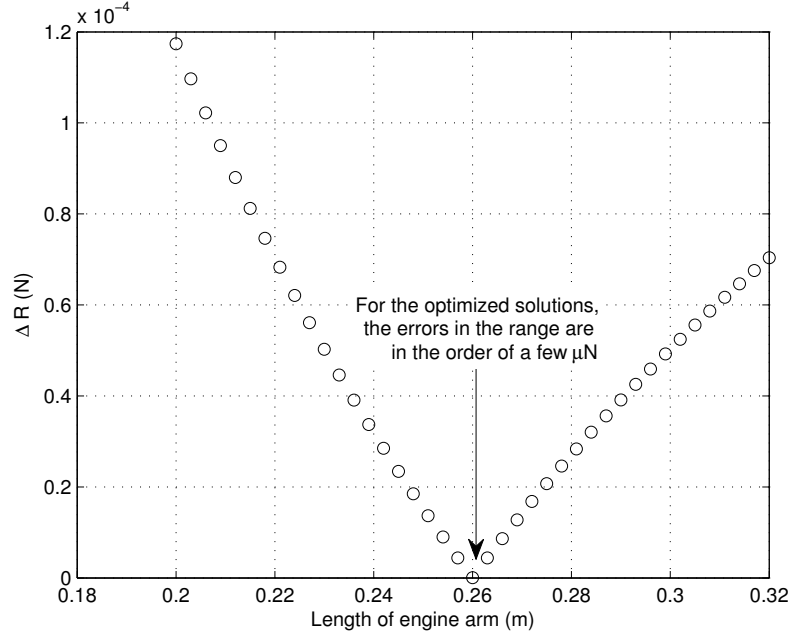


Figure 9: Error in full range estimate. $\Delta x = 1.15 \cdot 10^{-5} \text{ m}$, $R = 1.00 \cdot 10^{-3} \text{ m}$, $\ddot{x} = 2 \cdot 10^{-4} \text{ m s}^{-2}$, $\ddot{y} = 2 \cdot 10^{-5} \text{ m s}^{-2}$, $M_c = 1.20 \text{ kg}$, $l_c = l_1 - 0.025 \text{ m}$, $l_t = l_2 - 0.050 \text{ m}$ and $l_e = l_2 - 0.020 \text{ m}$.

4.1.2 Sensor system and its accuracy

In the MOP [7], the selection of potential sensor systems is reduced to displacement sensors that use either displacement induced eddy-currents or displacement induced changes in capacitance between parallel plates. These systems are vacuum compatible and compared to the other systems provide higher accuracies. Deliberations with the respective sensor manufacturer Micro-Epsilon have led to the selection of the capacitive displacement sensors. This decision is based on the higher resolutions and accuracies that can be achieved using this sensor system and the smaller required targets in comparison to the eddy-current systems. In the following section the uncertainties of the available sensor systems are estimated. A flow diagram that explains how errors are added is depicted in Figure 10.

The sensor measures the real displacement d_{real} at the location of the target. This displacement is caused by the rotation of the pendulum. The sensor and its controller both add an uncertainty to the sensed value through nonlinearity and non-repeatability. The sensed displacement can be labelled d_{sens} and is composed as

$$d_{\text{sens}} = d_{\text{real}} + \Delta d_{\text{sens}} \quad (18)$$

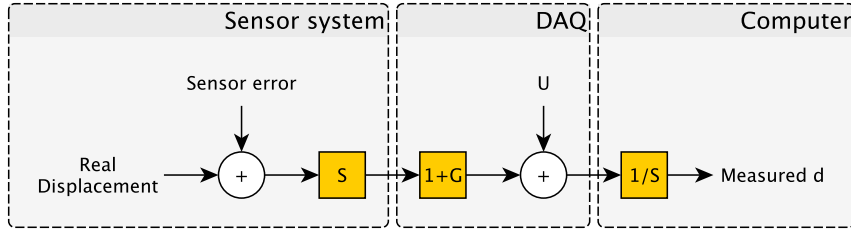


Figure 10: Flow diagram of how errors are added to the displacement measurement.

where Δd_{sens} is given as a percentage of the Full Scale Output (FSO). From the sensor controller, the displacement is translated into a voltage U_{sens} , given by

$$U_{sens} = d_{sens}S \quad (19)$$

where S is the sensitivity of the controller in $V m^{-1}$. The DAQ adds uncertainty in the form of a gain error and random noise.

$$U_{DAQ} = U_{sens} + U_{sens}G + \tilde{U} \quad (20)$$

where G is the gain error and \tilde{U} is the random noise on the voltage signal in $\mu Vrms$. In the calculations using these relations, the value for three standard deviations is used for \tilde{U} . The Gain Error G is calculated using

$$\begin{aligned} G = & \text{ResidualGainError} \\ & + \text{GainTempCo} \cdot (\text{TempChangeFromLastInternalCal}) \\ & + \text{ReferenceTempCo} \cdot (\text{TempChangeFromLastExternalCal}) \end{aligned} \quad (21)$$

where $\text{TempChangeFromLastExternalCal} = 10K$ and $\text{TempChangeFromLastInternalCal} = 1K$ as specified by National Instruments [58]. The coefficients are listed in Table 5 and depend on the voltage range setting of the DAQ. In data processing the measured U_{DAQ} is converted back into a displacement by division by the controller sensitivity S . The total uncertainty in the measured displacement introduced through the sensor, controller and DAQ is given by combining (18) - (20)

$$\Delta d = d_{meas} - d_{real} = d_{real}G + (1 + G)\Delta d_{sens} + \frac{\tilde{U}}{S} \quad (22)$$

The sensitivity of the sensor controller is easily found as the sensor FSO divided by the controller output voltage range. For the considered DT6530 and DT6200 the output voltage range is 0 V to 10 V. The DAQ voltage range is set to match this.

RANGE V POS- ITIVE SCALE	RESIDUAL GAIN ERROR (PPM OF READING)	GAIN TEM- PCO (PPM/C)	REFERENCE TEMPCO	RANDOM NOISE, σ (μVrms)
10	75	25	5	244
5	85	25	5	122
1	95	25	5	30
0.2	135	25	5	13

Table 5: Accuracy parameters of the National Instruments PXI 6229 [58].

The performance parameters of the sensor systems in combination with their required controllers are given in Table 7. The figures have been calculated using (22) and data from Table 6 and Table 7. This data is later combined with (15) and (16) to estimate the ideal measurement accuracy and range, respectively. A sample calculation is given in Section D.1.

PARAMETER	DT6530	DT6200 + DL6220
Static resolution (% F.S.O.)	$7.5\text{E}-5$	$4\text{E}-3$
Bandwidth digital output (kSa/s)	7.8	3.906
Linearity (% F.S.O.)	0.05	0.2
Maximum sensitivity deviation (% F.S.O.)	0.05	0.1
Repeatability (% F.S.O.)	0.0003	Not specified

Table 6: Sensor controller specifications for the DT6530 and DT6200 controller. The latter one is combined with a DL6220 pre-amplifier [53].

PARAMETER	cs005	cs02	cs05	cs08	cs1	cs2	cs3	cs5	cs10
Measuring range (m)	5E-5	2E-4	5E-4	8E-4	1E-3	2E-3	3E-3	5E-3	1E-2
Linearity (% F.S.O.)	0.2	0.2	0.05	0.05	0.05	0.05	0.05	0.05	0.05
Static resolution with DT6530 (m)	3.75E-11	1.5E-10	3.75E-10	6E-10	7.5E-10	1.5E-9	2.25E-9	3.75E-9	7.5E-9
Trueness incl. DAQ with DT6530 (m)	1.33E-7	5.30E-7	5.76E-7	9.21E-7	1.15E-6	2.30E-6	3.45E-6	5.76E-6	1.15E-5
Static resolution w/ DT6200+DL6220 (m)	2.00E-9	8.00E-9	2.00E-9	3.20E-8	4.00E-8	8.00E-8	1.20E-7	2.00E-7	4.00E-7
Trueness incl. DAQ w/ DT6200+DL6220 (m)	2.07E-7	8.30E-7	1.32E-6	2.12E-6	2.65E-6	5.30E-6	7.95E-6	1.32E-5	2.65E-5

Table 7: Specifications and accuracies of the available capacitive sensor systems. The static resolution is valid for oscillations at a frequency up to 2Hz. The resolutions and trueness are specified for two controllers: capaNCDT DT6530 and capaNCDT DT6200. Values of FSO and linearity have been obtained from Micro-Epsilon [53].

4.1.3 The effect of sensor tilt

When the sensor and sensor target are tilted with respect to each other, a measurement error is introduced that is caused by the fringing of the electric field between the two planes. The change in signal as a function of tilting angle Θ and engagement distance d_{work} is given by [53]

$$\Delta_x = d_{\text{work}} \left\{ \frac{1}{1 + \frac{R_{\text{meas}}^2}{4d_{\text{work}}^2} \tan^2 \Theta} - 1 \right\} \quad (23)$$

where R_{meas} is the measurement area radius in m, d_{work} the working distance between sensor and target in m, d_{max} the sensor measuring range and Θ the tilting angle in rad.

When the pendulum is in its equilibrium state and no thrust force is applied, the sensor is aligned such that $d_{\text{work}} = \frac{1}{2}d_{\text{max}}$. For that scenario, the relative reading error in the displacement signal can be estimated using (23) and the data of Table 7. The CS1 and CS10 have sensor radii of 5 mm and 30 mm, respectively. The relative errors are plotted in Figure 11. The maximum rotation angle is limited by geometric constraints. At the maximum angle indicated, the sensor and target touch.

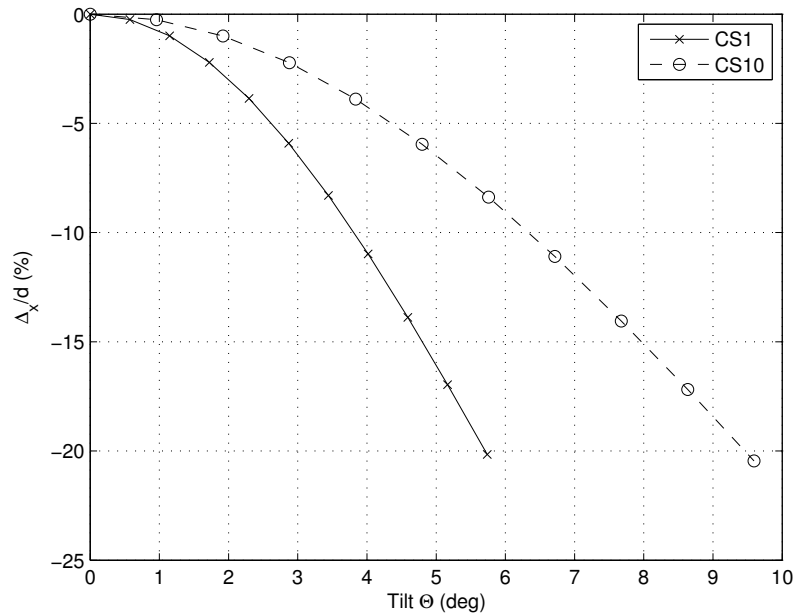


Figure 11: Relative error in displacement measurement due to tilting for the capaNCDDT CS1 and CS10 sensors.

The effect of misalignment of the sensor-target assembly on displacement measurement is removed through calibration, because the sensor response is measured as a function of applied calibrated force.

However, the sensitivity of the measurement and the measurement range depend on the alignment of the sensor-target assembly. From [Figure 11](#), it is concluded that an alignment of $\leq 1^\circ$ is required to minimize the effect.

4.1.4 Design feasibility

The feasibility of a design that is largely based on the TB-2m structure is tested by applying the model to the current design. For many configurations the accuracy and range are calculated using (15) and (16), respectively. For estimating the sensor system accuracy the data presented in [Table 7](#) are used. The configurations differ from one another in terms of the used sensor, torsional spring constant, arm lengths and installed counter mass.

In terms of sensors the CS1, CS5 and CS10 have been considered in this search. Initial calculations have shown that these would be the best candidates in terms of either resolution, range or both. The torsional spring constant was set to either 0 or $0.64 \text{ N m rad}^{-1}$ to represent cases in which the spring is disconnected or in which the spring of the TB-2m is used. The parameters used in the calculations are listed in [Table 8](#). The length of the bottom arm is simply calculated as $l_2 = l_a - l_1$. The center of mass of each of the two arms is assumed at half the arm length with respect to the pivot. The corresponding arm mass is calculated as a fraction of the total arm mass, proportional to its length:

$$M_{a_i} = \frac{l_i}{l_a} M_a \quad (24)$$

Furthermore, the relative positions of several components is fixed. The Center of Gravity (CoG) of the engine is assumed to be at 2 cm above the end of the bottom arm, the CoG of the target is assumed to be at 5 cm above the end of the bottom arm and the CoG of the counter mass is assumed to be at 2.5 cm below to the top of the top arm. These relative positions and lengths used in the calculations are also depicted in [Figure 12](#).

As will be shown later in [Section 4.1.7](#), the measurement of mass moment of inertia requires a removeable calibrated mass to be installed on the pendulum arm. For repeatability and user friendliness a holder shall be installed on the arm. For this feasibility analysis, it is assumed that the sensor target and calibration mass holder are combined into a single assembly with a total mass of 100 g.

A data set of accuracies and ranges is calculated for a set of a preset sensor and a preset spring constant. The counter mass and arm lengths are varied. For every data set the data points that do not meet requirements RANGE-1 and ACCUR-1 are discarded. An example of

The spring constant of $0.64 \text{ N m rad}^{-1}$ differs from the 0.3 N m rad^{-1} it was designed for. The experimental determination of the spring constant is described in [Appendix B](#).

PARAMETER	VALUE(S)	NOTE
Engine mass, M_e	0.1 0.2 0.3 kg	-
Torsional spring constant, K	0 0.64 N m rad ⁻¹	No spring or TB-2m spring.
Total arm length, l_a	0.37 m	TB-2m
Total arm mass, M_a	0.1556 kg	TB-2m
Distance to cross beam CoG, l_b	0.005 m	Assumed
Cross beam mass, M_b	0.225 kg	TB-2m
Target assembly mass, M_{ta}	0.100 kg	Assumed
Counter mass, M_c	0 kg to 2 kg	In steps of 0.05 kg
Top arm length, l_1	0.05 m to 0.29 m	In steps of 0.001 m
Horizontal accelerations, \ddot{x}	2E-4 m s ⁻²	In plane of rotation
Vertical accelerations, \ddot{y}	2E-5 m s ⁻²	-

Table 8: Simulation parameters used to calculate the accuracy and range of representative configurations of the TB-2m thrust stand with minor design changes.

a resulting data set is given in [Figure 13](#). In the figure, the accuracy after averaging, before averaging and the estimated range are shown as a function of arm length and counter mass. In total six different setups were evaluated for three distinct engine masses using either the TB-2m spring or no spring at all. The counter mass was varied from 0 kg to 2 kg in steps of 0.05 kg. The engine arm length was varied between 0.05 m to 0.29 m in steps of 0.001 m. This results in 9600 samples per setup and 57600 samples in total. The calculated data sets have been studied closely and three setups have been identified that jointly cover the full range as specified by RANGE-1 while being compliant with requirement ACCUR-1. The first range spans from 1 μ N to 45 μ N, providing an accuracy of $\approx 0.1 \mu$ N. In this range the CS1 sensor is used and the torsional spring is disconnected. The second range spans from 10 μ N to 420 μ N at an accuracy of 1 μ N. In addition to the CS1 sensor, the torsional spring with $K = 0.64 \text{ N m rad}^{-1}$ is connected. The last range covers from 1000 μ N to 5000 μ N at an accuracy of 10 μ N using the CS10 sensor and the torsional spring connected. The latter range can be extended down to 200 μ N when a relative error of 5% is accepted locally. In [Figure 14](#) the achievable accuracies are compared to the required accuracies as specified by ACCUR-1.

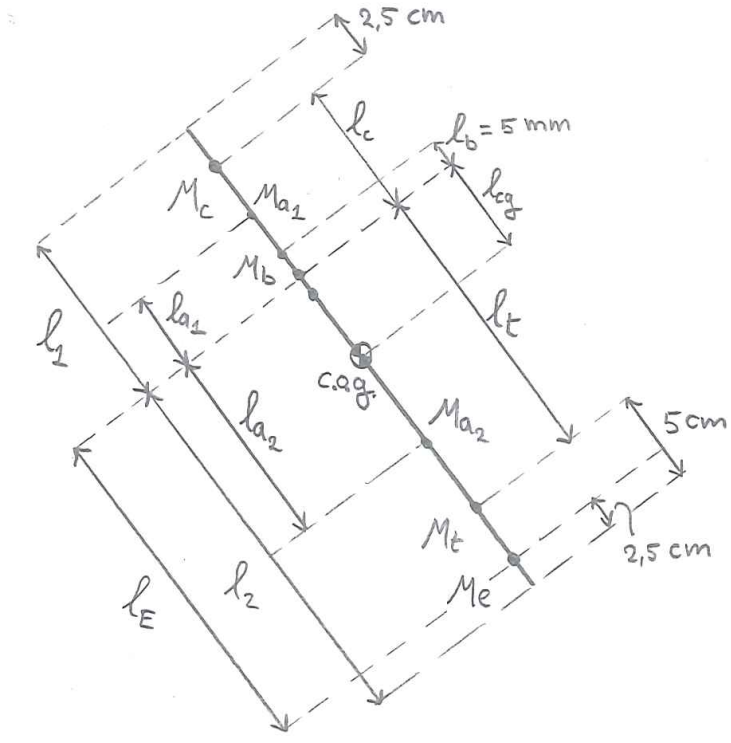


Figure 12: Free-body diagram of the thrust stand as modelled for the preliminary design. In the sketch the distance from the counter mass C_oG to the end of the top arm, the distance from the engine C_oG to the end of the bottom arm and the distance from the C_oG of the target to the end of the bottom arm have been fixed.

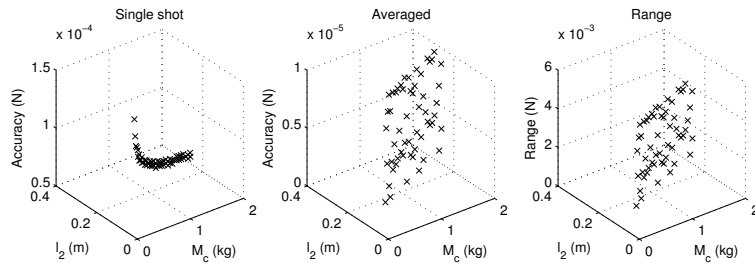


Figure 13: A sample data set for design feasibility analysis. Parameters: $M_e = 0.300\text{ kg}$, $K = 0.64\text{ Nm rad}^{-1}$. Data points have been selected to meet ACCUR-1 after averaging for the $1000\text{ }\mu\text{N}$ to $5000\text{ }\mu\text{N}$ range.

As can be seen in the figure the required relative accuracy of 1% is exceeded in the $45\text{ }\mu\text{N}$ to $100\text{ }\mu\text{N}$ range. Locally a relative error $\leq 2.23\%$ will be achieved, which is considered acceptable after deliberations with the key stakeholder. For the intended purpose of verification and validation of thrusters for the DelFFi mission among others, an accuracy of 2.5% is acceptable. A similar situation exists in the $420\text{ }\mu\text{N}$

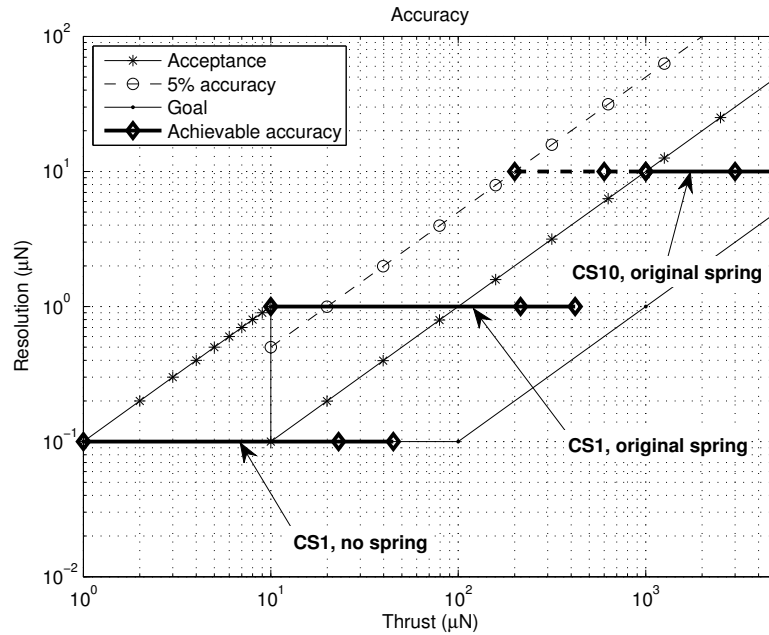


Figure 14: Achievable accuracies in preliminary design for an updated TB-2m design. The thrust range is split in three overlapping regions: 1 μN to 45 μN , 10 μN to 420 μN and 1000 μN to 5000 μN . The latter one can be extended down to 200 μN if locally an error of 5% is accepted. Assumed thruster mass of 300 g.

to 1000 μN range. To achieve these accuracies a lower arm length of 24 cm to 29 cm is required in combination with a 1.20 kg to 1.85 kg counter mass.

For the verification and validation of the setup the capaNCDT CS1 sensor and the capaNCDT DT6530 controller are used. This setup, including all supporting hardware costs € 7052 when purchased or € 176.30 per week (2.5% of total price per week) when rented. These amounts are based on the quotation that can be found in [Appendix K](#). The setup can be used free of charge for the first two weeks.

In [Figure 15](#), the sensitivities of the accuracy in the absence of noise are plotted on a logarithmic scale. As can be deduced from the figure, the solutions are (very) sensitive to changes. For example it was noted in the data analysis that a change in arm length of 1 mm could lead to a decrease in accuracy from 1 μN to 5 μN . The arm lengths and counter masses should be chosen such that the solutions lie in the areas of lowest sensitivities for the design to be robust. The partial derivative $\frac{\partial \delta T}{\partial M_c}$ varies between 10^{-7} and 10^{-2} , while the derivative $\frac{\partial \delta T}{\partial l_2}$ varies between 10^{-4} and 10^5 . Comparison of these values shows that the solutions are much more sensitive to changes in arm length than to changes in counter mass. In practice this means that the stand has to be set up in such a way that errors in the arm lengths are minimized as much as possible.

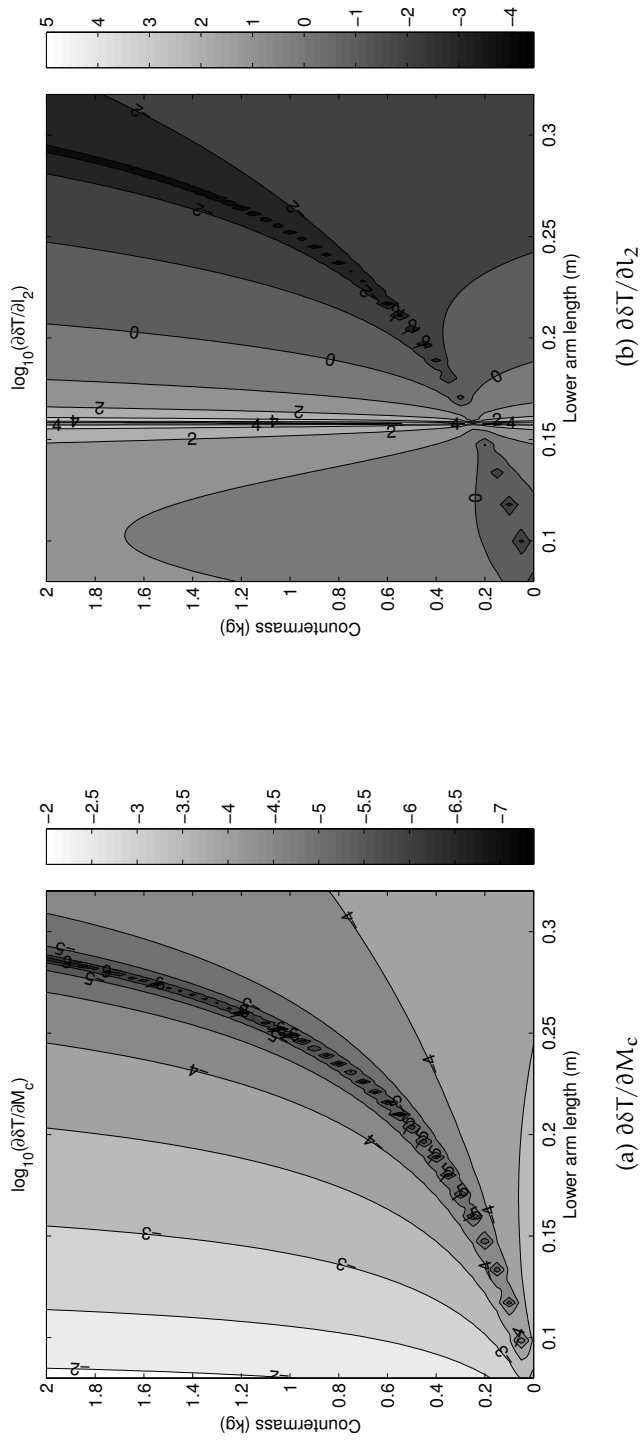


Figure 15: Sensitivity of thrust accuracy to errors in counter mass and arm length for the given geometry. The logarithm of base 10 has been used to indicate the magnitude of the partial derivatives. The partial derivative $\frac{\partial \delta T}{\partial M_c}$ varies between 10^{-7} and 10^{-2} , while the derivative $\frac{\partial \delta T}{\partial l_2}$ varies between 10^{-4} and 10^5 .

4.1.5 Counter mass selection

Based on analysis of the accuracy estimates after averaging, a total counter mass of 1.2 kg to 1.85 kg is required. To cover this full range, the counter mass is divided into five masses of respectively 0.05, 0.1, 0.2, 0.3 and 1.2 kg. This allows coverage over the entire range of required masses and tuning of the counter mass for a specific engine mass. After production, the actual masses are determined with a high precision scale that has a fixed absolute accuracy over its measurement range. The masses of 0.2 and 0.3 kg have been chosen over a larger set of masses of 0.1 kg to reduce the relative error in total mass. This will reduce the effects of the uncertainty in total mass on the thrust measurement.

*For example,
 $1 \times (300 \pm 0.1 \text{ g})$
 equates to a relative
 error of 0.033%; the
 same total mass
 composed of
 $3 \times (100 \pm 0.1 \text{ g})$
 equates to a relative
 error of 0.1%.*

4.1.6 Impulse bits

The equation of motion of the pendulum without damping and environmental noise can be given as

$$\tilde{I}\ddot{\theta} + \tilde{K}\theta = T(t) l_E$$

where the shorthand notations $\tilde{I} = I_0 + l_{cg}^2 M_t$ and $\tilde{K} = K + M_t g l_{cg}$ are used. To study the response of the pendulum to an ideal impulse, i.e. an impulse that is applied for an infinitesimally short time, this equation is transformed into the Laplace domain.

$$\mathcal{L}\{\tilde{I}\ddot{\theta} + \tilde{K}\theta\} = \mathcal{L}\{T(t) l_E\}$$

The thrust as a function of time is described by a Dirac delta function of magnitude I_{bit} :

$$T(t) = I_{bit} \delta(t) \quad (25)$$

Applying this transformation leads to

$$(\tilde{I}s^2 + \tilde{K}) \Theta(s) = I_{bit} l_E + \tilde{I}s\theta(0) + \tilde{I}\dot{\theta}(0) \quad (26)$$

where $\mathcal{L}\{\theta(t)\} = \Theta(s)$. The pendulum is assumed initially at rest before the impulse is applied, implying that $\theta(0) = \dot{\theta}(0) = 0$. Solving this equation for $\Theta(s)$ and rewriting it results in

$$\Theta(s) = \frac{I_{bit} l_E}{\tilde{I}} \frac{1}{s^2 + \left(\sqrt{\frac{\tilde{K}}{\tilde{I}}}\right)^2} \quad (27)$$

Using the inverse Laplace transformation, the result can be transformed back into time domain, the result of which is

$$\theta(t) = \frac{I_{bit} l_E}{\tilde{I} \omega_n} \sin(\omega_n t) \quad (28)$$

where the oscillation frequency or natural frequency of the pendulum is given by

$$\omega_n = \sqrt{\frac{\tilde{K}}{\tilde{I}}} \quad (29)$$

As can be seen, for an undamped system the impulse bit magnitude is hidden in the magnitude of the harmonic wave that results. It is apparent that all terms defining the magnitude of the wave can be measured: the mass moment of inertia about the point of rotation \tilde{I} , the oscillation frequency ω_n and the engine arm l_E . The accuracy at which these parameters can be measured directly determines the accuracy at which impulse bits can be measured.

4.1.7 Mass moment of inertia

For impulse bit measurements via the Time Resolve Impulse Measurement (TRIM) process [21] (as proposed by [68]) the mass moment of inertia needs to be known. A method for measuring the moment of inertia described here is based on a method by Zakrzwski et al. [89]. The derivation below serves to explain the method and give insight in the required parameters.

For an undamped pendulum the natural frequency is given by (29). When a mass \hat{m} is added to the pendulum at a known distance from the pivot l_m , the natural frequency changes to

$$\omega_n + \Delta\omega_n = \sqrt{\frac{\tilde{K} + \Delta\tilde{K}}{\tilde{I} + \Delta\tilde{I} + \hat{m}l_m^2}} \quad (30)$$

where $\Delta\tilde{I}$ is the mass moment of inertia of the calibration mass about its CoG and $\Delta\tilde{K}$ is the change in effective spring constant. This latter change can be written as

$$\Delta\tilde{K} = gl_m \hat{m} \quad (31)$$

The combination of (29), (30) and (31) results in an expression for the mass moment of inertia:

$$\tilde{I} = \frac{(\Delta\tilde{I} + l_m \hat{m}^2) (\omega_n + \Delta\omega_n)^2 - gl_m \hat{m}}{\omega_n^2 - (\omega_n + \Delta\omega_n)^2} \quad (32)$$

This conceptually simple method of determining the mass moment of inertia of the pendulum relies on accurate measurement of the added mass, the location of its CoG and measurement of the natural frequency.

4.2 PART DESIGN

In this section, the mechanical design of the parts that are discussed in [Section 4.1](#) is presented.

4.2.1 Counter masses

As described in [Section 4.1.5](#), the counter mass is divided over smaller discs of approximately 0.05, 0.1, 0.2, 0.3 and 1.2 kg respectively. To reduce manufacture time and costs, the discs are made out of steel rods that are readily available at the workshop of the faculty of Aerospace Engineering (hereafter referred to as the workshop). For each rod the specific mass is listed in a catalog in kg m^{-1} . These numbers need correction due to the hole that is drilled in each disc which is required for mounting on the pendulum arm. The corrected specific mass is given by

$$m_{\text{sp,corr}} = \frac{D_o^2 - D_i^2}{D_o^2} m_{\text{sp}} \quad (33)$$

where $m_{\text{sp,corr}}$ is the corrected specific mass, m_{sp} the listed specific mass in kg m^{-1} , D_o the outer diameter of the rod and D_i the diameter of the hole in m. The required thickness of the rod is then simply calculated by division of the total required mass by the corrected specific mass. Based on the catalog provided by the workshop and material availability, rods of 50 and 70 mm diameter were chosen. The required thicknesses can be found in [Table 9](#). The engineering drawings can be found in [Appendix I](#); a sketch of the combined counter mass is depicted in [Figure 16](#). After production the masses have been measured and weighed. The final dimensions are listed in [Table 10](#). As can be seen the masses differ from the design masses due to slight deviations in the thicknesses from the designed thicknesses and differences in actual specific mass. The masses have been determined using a Mettler Toledo AG245 whenever possible to provide the highest precision. The 1.2 kg and 0.3 kg masses, however, exceed the measurement range of the AG245. These masses have been measured to a lower precision using a Mettler Toledo PB8001.

4.2.2 Engine bracket

A custom engine bracket was designed to connect the MOOG Bradford Engineering PMT (see [Figure 17a](#)) to the thrust stand. As noted before, this engine will be used for hardware-in-the-loop validation. The bracket is produced from standard aluminum and made such that the holes on the bracket line up with the mounting holes on the engine. The bracket is bolted onto the arm using an M5 bolt. The fastener hole is tapered at the top, such that the bracket automatically

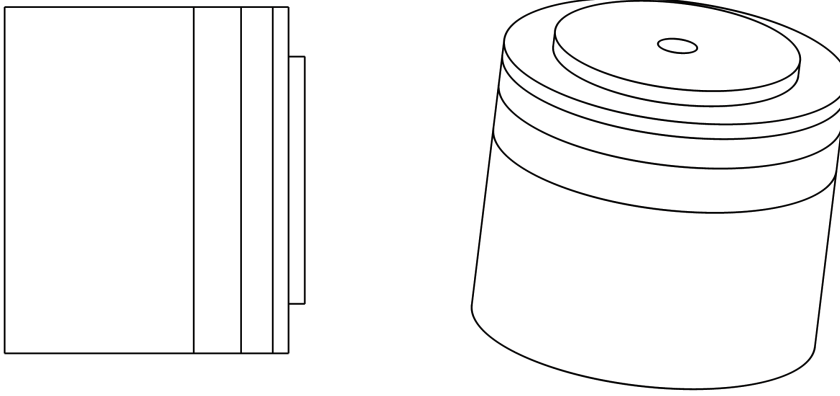


Figure 16: Drawing of stacked masses that form the counter mass. The masses can be combined to create a counter mass with a total mass of 1.2 kg to 1.85 kg.

aligns with the center of the arm. The engineering drawings can be found in [Appendix I](#); an isometric view of the bracket is depicted in [Figure 17b](#) to give an impression. After production the engine bracket was weighed. The mass of the bracket is 10.3755 g.

4.2.3 Sensor bracket

The sensor bracket, depicted in [Figure 18](#), is designed to hold the Micro-Epsilon capaNCDT CS1 and CS10 sensor heads. Using the bracket they can be mounted to a structure constructed of BOIKON profiles and brought into the right position and orientation with respect to the sensor target. The bracket is sized such that it can be mounted on a profile of 20 mm high. The engineering drawings can be found in [Appendix I](#).

MASS (kg)	D_o (mm)	$m_{sp,corr}$ (kg m^{-1})	t (mm)
1.2	70	31.29	38.3
0.3	70	31.29	9.6
0.2	70	31.29	6.4
0.1	70	31.29	3.2
0.05	50	15.34	3.3

Table 9: Counter mass dimensions. All counter masses are manufactured from circular rods and have a concentric hole of 8 mm.

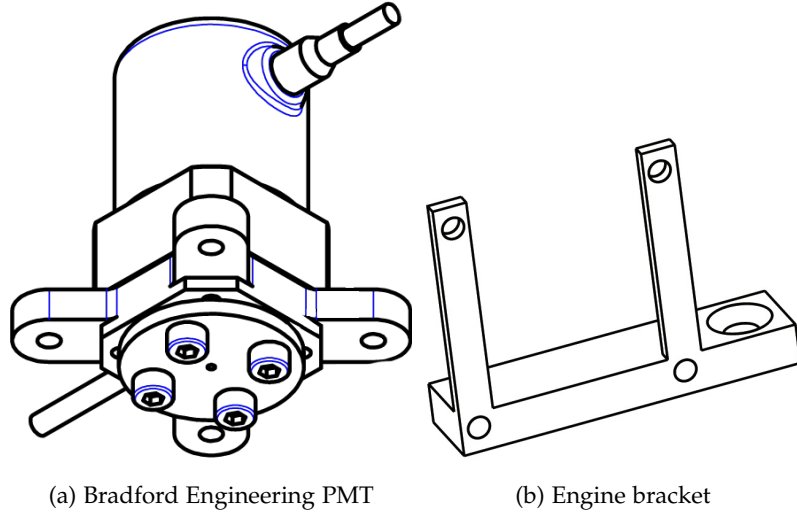


Figure 17: The Bradford Engineering PMT will be used to validate the thrust stand with hardware in the loop. The bracket is custom for this engine and is used to mount the engine to the pendulum.

4.2.4 Sensor target and calibration mass

Capacitive displacement sensing requires a conductive target that is of at least the same diameter as the sensor head. The thrust stand requires the use of two sensor heads to cover the entire range of $1\ \mu\text{N}$ to $5000\ \mu\text{N}$, the biggest of which is the capaNCDDT CS10. At a diameter of 60 mm [53] the CS10 sets the minimum size for the sensor target. To avoid unwanted electric field effects at the edges, the target is sized at $70 \times 70\ \text{mm}$. The target is mounted on the pendulum arm via a hole that runs through the entire length of the target. Using four bolts (two on each side) it can be fastened to the pendulum.

Two slots are created in the sides to lower the total target mass and to allow the insertion of calibration masses. The calibration masses can

$M_{\text{design}}\ (\text{kg})$	$M_{\text{actual}}\ (\text{kg})$	$t_{\text{design}}\ (\text{mm})$	$t_{\text{actual}}\ (\text{mm})$
1.2	1.1100 ¹	38.3	38.35
0.3	0.280 ¹	9.6	9.70
0.2	0.1867535	6.4	6.48
0.1	0.0950066	3.2	3.30
0.05	0.0487486	3.3	3.39

Table 10: Counter mass dimensions after production. All counter masses are manufactured from circular rods and have a concentric hole of 8 mm. The masses have been measured using a Mettler Toledo AG245 scale. ¹: Measured using a Mettler Toledo PB8001 because the mass exceeds the limits of the AG245.

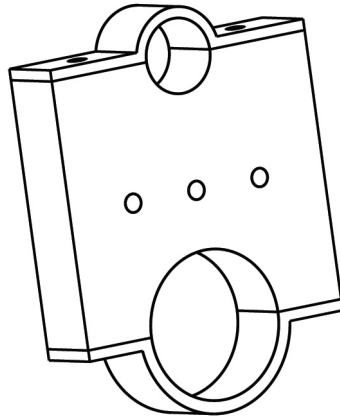


Figure 18: Drawing of the sensor bracket. The bracket is designed to fit the Micro-Epsilon CS1 and CS10 capaNCDT sensor heads.

be inserted to alter the mass moment of inertia of the pendulum. As explained in [Section 4.1.7](#), the change in natural frequency caused by the change in mass moment of inertia can be used to derive the mass moment of inertia of the setup itself. The calibration masses have a symmetric design, such that placement orientation is not important. A hole is drilled in its center to allow any air that is trapped when placing the masses in the slots to evacuate. The ends of the calibration masses were rounded after deliberations with the workshop. Due to the used production techniques, rectangular slots are difficult and expensive to manufacture. Rounded ends are much simpler to produce and therefore also cheaper.

In the back of the target, four threaded holes 20×20 mm apart are available. These holes can be used to mount any target required for the calibration actuator.

The sensor target is depicted in [Figure 19](#). The corresponding engineering drawings can be found in [Appendix I](#). After production the dimensions and mass of the calibration masses and the sensor target have been measured. The target is 70.10 mm high, is 70.04 mm wide and has a thickness of 12.04 mm. Including the mounting bolts the mass adds up to 123.7125 g (compared to the 100 g assumed in the preliminary model of [Section 4.1.4](#)). Without the bolts the mass is equal to 117.7575 g. The mass of the calibration masses was measured to be 15.1766 g and 15.1604 g, respectively.

4.3 TB-2m AND TB-5m COMPARED

The TB-2m has evolved into the TB-5m thrust stand with extended range, higher achievable accuracy and more versatility. Concerning the mechanical design of the thrust stand (see [Figure 20](#)), the TB-5m is designed for tuneability and higher versatility. By splitting

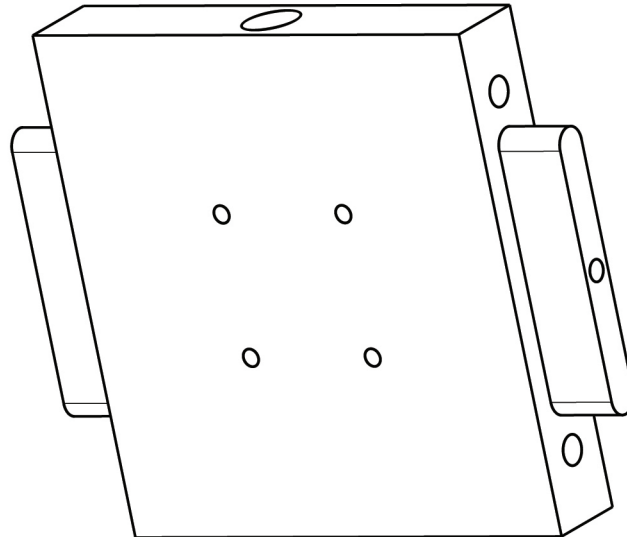


Figure 19: Drawing of the sensor target. The target is mounted on the pendulum arm using four bolts that fall into notches in the arm. Two removable calibration masses can be put into the target for determination of the mass moment of inertia of the pendulum.

the required thrust range into three parts, higher accuracies can be achieved. To do so the torsion spring is either connected or disconnected and instead of a single counter mass of 1.0803 kg a counter mass of 1.2 kg to 1.85 kg is picked. As summarized in [Table 11](#), this causes the thrust range to be extended down to 1 μN and up to 5000 μN . Additionally, the TB-5m features a big sensor target that is required for its sensor system. This target doubles as calibration mass holder. The calibration masses allow well-defined changes in mass moment of inertia that aid in the determination of the mass moment of inertia of the pendulum. Also, the LASER based sensor system of the TB-2m has been replaced by a capacitive distance measurement system. The latter has the advantage of being vacuum compatible, allowing measurement at medium vacuum conditions.

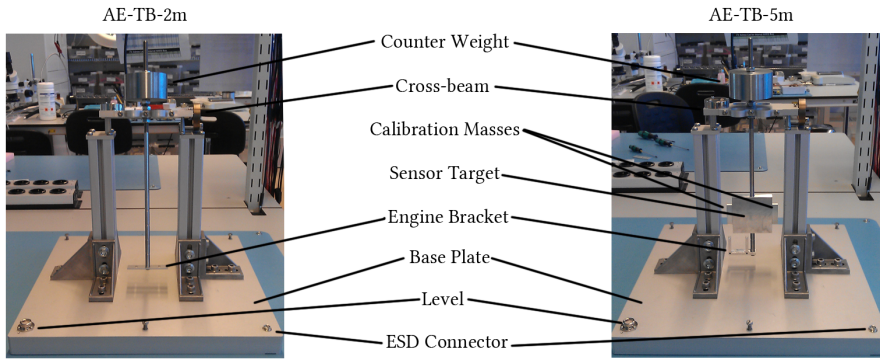


Figure 20: Comparison of the TB-2m and the TB-5m.

PARAMETER	TB-2m	TB-5m
Thrust range [accuracy], (μN)	10 – 2000 [≤ 2]	1 – 45 [0.1], 10 – 420 [1.0], 200 – 5000 [10]
Spring constant, (N m rad^{-1})	0.3	0.64
Counter mass, (kg)	1.0803	1.2 – 1.85 in steps of 0.05

Table 11: Comparison between TB-2m and TB-5m.

CALIBRATION ACTUATOR

The MOP has shown that electromagnetic and electrostatic actuators make the best candidates out of the considered systems. They can be used for in situ calibration of both steady thrust and impulse bits. In this chapter, the design options are branched into different topologies and the individual options are assessed. The final actuator topology is selected in Section 5.2 and its sizing and design are detailed in Section 5.3.

5.1 DESIGN OPTIONS

In the MOP, several options have been considered ranging from impact pendula to electromagnetic and electrostatic techniques. In Table 12, the considered techniques are compared. From these options the electromagnetic and electrostatic techniques are considered the best candidates, because they can be used to calibrate both steady state thrust and impulse bits and do not require physical contact with the pendulum. The electromagnetic and electrostatic design options have been branched into specific topologies that are currently used in test and measurement setups as found in literature. In Figure 21, the considered design options are listed in a Design Option Tree (DOT).

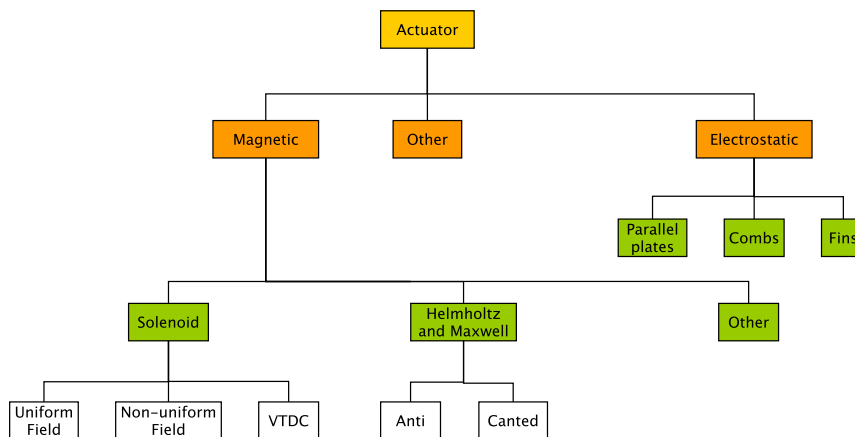


Figure 21: DOT for the calibration actuator selection. The MOP has shown that electromagnetic and electrostatic actuators are most suitable for the in situ calibration of steady thrust and impulse bits.

METHOD	THRUST RANGE	IMPULSE BIT RANGE	NOTES
Impact Pendulum	N/A	Scalable with mass of pendulum.	Requires a sensor to measure the movement of the pendulum before and after impact. Practical implementation for vacuum is cumbersome for it requires a friction free method of resetting the pendulum.
Piezo-electric Hammer	Impact N/A	10 – 750 mNs	Tip materials influence the transferred impulse.
Dropping ball	N/A	Scalable by ball mass and dropping height	Requires a high speed camera to monitor the motion of the ball. Method requires that no slip occurs between the pendulum and the balls.
Weight Pulley Calibration	Scalable	N/A	Moot whether microNewton range is practically feasible.
Gas Dynamic	0.01 – 0.1 μ N	Scalable with thrust time	GD method is calibrated using Direct Monte Carlo Simulation. Only available in vacuum due to the required molecular flow (0.1 – 0.001 mbar).
Electro-static Plates)	(Parallel > 1 nN	Unknown	Inverse quadratic dependency on engagement distance.
Electro-static Combs	35 nN – 1 μ N	Unknown	Inverse quadratic dependency can be reduced to inverse linear.
Electro-static Fins	10 μ N – 1 mN	0.01 – 20 mNs	3D fringing effects are present but their influence can be limited by proper design.
EM	0.1 μ N – 10 mN	Unknown	Problems were encountered before for the TB-50m, but can possibly be mitigated by careful design.

Table 12: Comparison of known calibration techniques for both steady state and impulse bit calibrations [7].

5.1.1 Solenoid

A solenoid - in engineering terms - is an electromagnet composed of a coil that typically has a metallic rod in its core to enhance the magnetic field. The electromagnet can be used to attract or repel another (electro)magnet or ferromagnetic target. This method was used to create a calibration actuator by Wong et al. [85] and Janssens [39] among others. A target is mounted on the pendulum arm and the solenoid is mounted closeby. This has the advantage that no additional wiring is required on the pendulum, reducing the parasitic forces on the thrust stand. The electromagnetic force created by a solenoid with a metallic core is given by [39]:

$$F = \frac{\mu^2 N^2 i^2 \pi r^2}{2\mu_0 L^2} \quad (34)$$

where F is the force, μ the magnetic permeability of the core material, N the number of windings, i the electric current, r the radius of the core, μ_0 the magnetic permeability of vacuum and L the combination of the length of the core and the distance between the magnet and the target. As can be concluded from this relation, the force is in this case quadratically dependent on the electric current and quadratically inversely proportional to the distance between the target and the solenoid. Because the reaction force of the thrust stand under loading is related to the rotation of the pendulum, and thus the distance between solenoid and target, the dependency on target distance requires additional displacement measurements to ensure a steady calibration force. This can for example be achieved using a displacement measurement and control loop that controls the electric current in the solenoid to correct for changes in engagement distance.

For thrust stands using direct force measurement, such as the TB-50m by Janssens [39], the movement of the stand is (almost) zero. In such case, no additional distance measurement is required.

5.1.2 Solenoid placed in a uniform magnetic field

A variant of the standard solenoid setup as described above is used by Tang et al. [80]. The solenoid is placed on the thrust stand and suspended in a uniform magnetic field. In the case of Tang et al. [80] this field is created using a specific arrangement of permanent magnets, but this could also be achieved using specific arrangements of larger solenoids such as Helmholtz and Maxwell setups (Appendix A). When a solenoid is placed in a homogeneous field, the electromagnetic force generated by an electric current is given as

$$F = BN\pi r i \quad (35)$$

Because the magnet is suspended in a uniform magnetic field, the dependency on distance is removed and the dependency on electric current is reduced to a linear relation. This is advantageous for reasons explained above. However, the design of the uniform magnetic

field using permanent magnets is complicated and the creation of such fields using electromagnets (such as Helmholtz setups) requires accurate winding and placement of the required solenoids.

5.1.3 Varying Turn-Density Coil

In an ideal solenoid with constant turn-density a uniform magnetic field is generated along the axis of the solenoid. The flux density is proportional to the electric current I and the turn-density of the wire n . The strength of the uniform magnetic field inside the coil is given by Ampere's law:

$$B = \mu_0 n i \quad (36)$$

A Varying Turn-Density Coil (VTDC) was proposed by Friedman et al. [24], who uses a varying turn-density along the length of the coil to create a constant magnetic field gradient. Partial differentiation shows that based on Ampere's law, the magnetic field gradient is linearly dependent on the variation in turn-density:

$$\frac{\partial B}{\partial x} = \mu_0 i \frac{dn}{dx} \quad (37)$$

Using Biot-Savarts law and classical electromagnetic theory [9], it can be derived that the force experienced by a magnetic dipole with magnetic moment μ_1 in a nonuniform field is equal to

$$\mathbf{F} = \mu_0 \mu_1 i \frac{dn}{dz} \hat{\mathbf{x}} \quad (38)$$

This is true, given that the magnetic dipole is suspended in the radial center of the VTDC and that the magnetic moment is parallel to the field direction. Using a constant change in turn-density along the length of the coil results in an electromagnetic force that is linear with the coil current, independent of the location along the axis of the coil. This is advantageous for calibration purposes as the calibration force is not dependent on the engagement distance between the pendulum and the actuator. This leads to a more robust calibration method, because it becomes less sensitive to alignment. The VTDC produced by Friedman et al. [24] is composed of discrete connected bundles of turns as depicted in Figure 22. This design was tested using different sizes of magnets and at different locations along the axis of the coil. The electromagnetic force was found linear with magnet length and thus magnetic moment. A slight increase in force was found when the dipole was moved into the areas of higher turn density. It is expected this is caused by grouping the turns. A continuous change of turn-density is expected to give a better result.

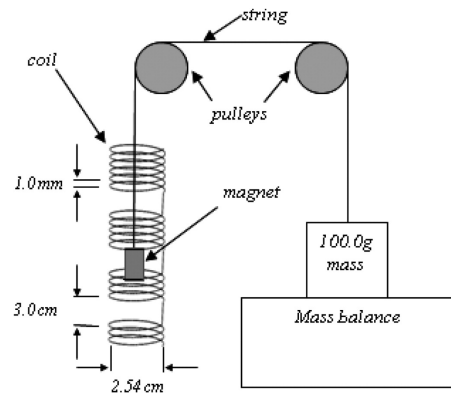


Figure 22: Original design of a Varying Turn Density Coil by Friedman et al. [24]. The VTDC was created from a 1 mm diameter copper wire, wound helically around plastic tubing. The turns were separated into discrete bundles, each bundle with one more turn than the previous. The bundles were separated by and spaced evenly 3 cm apart.

5.1.4 Anti-Helmholtz

By reversing the electric current in one of the two coils that together compose the Helmholtz coil, an anti-Helmholtz coil is created. The magnetic field within the Helmholtz coil is no longer uniform, but rather an area of (high) field gradient is created. As explained in Section 5.1.3, such fields can be used to create a magnetic force on a magnetic dipole that is (nearly) independent of the on-axis location of the dipole in the coil. The positioning of the coils, however, is critical in this setup. Misalignment quickly causes non-constant magnetic gradients. More details on (Anti-)Helmholtz setups can be found in Appendix A.

5.1.5 Canted Helmholtz

Canting the individual coils of the Helmholtz coil creates a constant magnetic field gradient, as proposed by Cape and Young [16]. The field has a constant gradient in the vertical direction. The geometry is depicted in Figure 23. It has been shown that a canting angle of $\theta = 29^\circ$ results in a field gradient of $5.65 \pm 0.05\%$ in the vertical direction. A variation in electric current changes the minimum strength of the field, but only slightly influences the gradient. The effect on the gradient is considered negligible. It can therefore be concluded that for this topology the field gradient can only be controlled by changing the canting angle. In practice this will result in additional mechanisms that complicate the design.

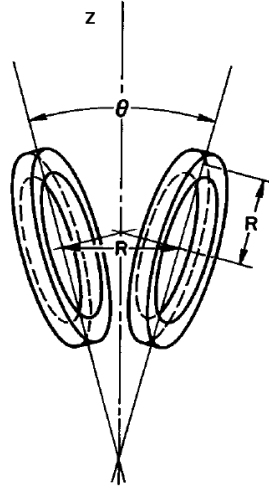


Figure 23: Geometry of a canted Helmholtz coil [16]. The magnetic force is along the z-axis as indicated in the figure.

5.1.6 Parallel plates

The electrostatic force created by an electric field between two parallel plates can be used to create a calibration force. This electrostatic force is quantified using [87]:

$$F = \frac{1}{2} \epsilon_0 \left(\frac{V_{\text{act}}}{L} \right)^2 A \quad (39)$$

where ϵ_0 is the permittivity of vacuum, V_{act} is the electric potential between the plates, L represents the separation of the plates and A is the frontal area of the electrodes. This equation does not account for fringing effects that occur on the edges. The inverse quadratic dependency of the force on separation distance is disadvantageous for reasons described before. As the calibration force is controlled via the potential between the plates, a control loop would be required. This technique has been demonstrated for calibration purposes in the $10 \mu\text{N}$ to $50 \mu\text{N}$ range using parallel disks of 12 mm diameter, 1.56 mm separation distance and potentials of 80 V to 200 V.

5.1.7 Electrostatic combs

To increase the calibration force the electrostatic force between combs can be used. The calibration force can be approximated [87] using

$$F \approx \epsilon_0 V_{\text{act}}^2 \left\{ \frac{d}{g} + K \left[\sin \left(\frac{\pi c}{2(c+g)} \right) \right] / K \left[\cos \left(\frac{\pi c}{2(c+g)} \right) \right] \right\} \quad (40)$$

where d, g and c are geometrical properties as defined by Figure 24. K is the complete elliptic integral of the first kind as given by

$$K(\eta) = \int_0^{\pi/2} \frac{d\theta}{\sqrt{1 - \eta^2 \sin^2 \theta}} \quad (41)$$

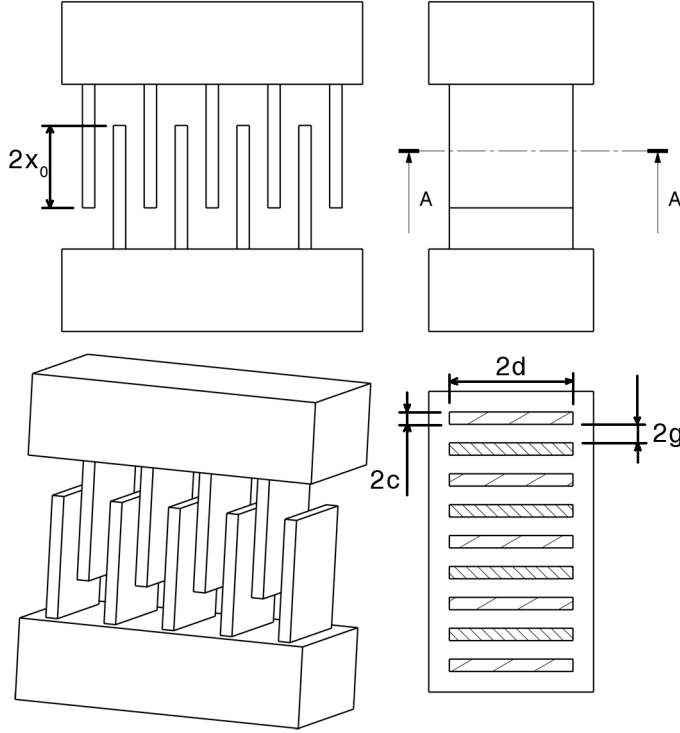


Figure 24: Geometry of electrostatic fin setup based on sketches of Yan et al. [87]. Top left: front view. Top right: side view. Bottom left: isometric view. Bottom right: section view of fins.

The use of Electrostatic Combs (ESC) has been demonstrated for the $1 \mu\text{N}$ to $35 \mu\text{N}$ range by Selden and Ketsdever [74].

5.1.8 Electrostatic fins

Yan et al. [87] updated the ESC design by changing from combs to fins to increase the calibration force to the 0.01 mN to 1 mN range. The force created by an array of electrostatic fins can be calculated using

$$F_{\text{ESF}} \approx 2N_{\text{fins}}\epsilon_0 V_{\text{act}}^2 \left[2.2464 - \frac{c+g}{\pi x_0} \right] \quad (42)$$

where x_0 is the engagement distance and N_{fins} the total number of fins. For the limit case where $x_0 \ll c + g$, the inverse dependency on engagement distance disappears. This was confirmed by finite element modelling. This behavior is desirable for a calibration device

when a changing engagement distance is expected. Experimental results have shown that a $1/V$ dependency is evident in the results, which does not follow from theory. A theoretical-empirical relation that describes the Electrostatic Fins (ESF) attractive force is

$$F_{\text{ESF}} \approx 2N\epsilon_0 V_{\text{act}}^2 \left[2.5 - \frac{106}{V_{\text{act}}} \frac{c+g}{\pi x_0} \right] \quad (43)$$

This discrepancy between (42) and (43) indicates that the attractive force is not yet completely understood and more modelling is required. Yan et al. [87] have shown that ESF is an appropriate calibration method for the 0.029 mN to 0.794 mN with a resolution of 0.01 mN or better.

5.2 DESIGN OPTION TRADE-OFF

From the actuator options presented in Section 5.1, the VTDC is selected for the detailed design. The trade-off is based on three criteria: range, linearity and complexity. All three are weighed equally in this trade-off. For the range criterium the demonstrated forces are considered, as well as the possibilities to adapt the designs to meet the requirements. For the linearity, the applied force as a function of engagement distance is considered. The last criterium, complexity, concerns the design complexity of the actuator. This includes sensitivity of the design to manufacturing inaccuracies and to alignment, the required hardware, knowledge or experience and the overall time and cost associated with the design. Each option is graded with respect to the three given criteria using the following scheme:

- ++ Has been demonstrated for use in the required range; applied force is independent of engagement distance; insensitive to manufacturing inaccuracies, to alignment and does not require specific knowledge or equipment.
- + Can be scaled to meet required range; mild dependency on engagement distance or nonlinearity can be accepted or mitigated; sensitivities to manufacturing inaccuracies or alignment can be mitigated and only required minimum specific knowledge and equipment.
- 0 Insufficient information to judge in this stage of the design.
- Requires additional design effort to meet required range; dependency on engagement distance that can be mitigated with additional design effort; requires additional knowledge, special tooling or manufacturing techniques.
- Cannot be changed to meet requirements within the given resources; very sensitive to engagement distance; requires expert knowledge or special equipment.

The plusses and minuses are added up to determine the total score of each option. The results are summarized in Table 13. In the following sections the rationales for the scores are given.

METHOD	RANGE	LINEARITY	COMPLEXITY	$\Sigma+$	$\Sigma-$	Σ
Solenoid	+	--	++	3	2	+1
Solenoid, uniform field	+	++	--	3	2	+1
VTDC	+	++	-	3	1	+2
Anti-Helmholtz	+	--	--	1	4	-3
Parallel plates	--	-	+	1	3	-2
Electrostatic combs	--	-	-	0	4	-4
Electrostatic fins	--	-	-	0	4	-4

Table 13: Trade-off table for calibration actuator.

5.2.1 Solenoid

The basic solenoid with a proper target (see Section 5.1.1) has been used in multiple thrust stands and has been demonstrated for the required thrust ranges. However, as shown by Janssens [39], the close windings make their application limited in vacuum conditions due to the risk of excessive heating. Combined, this results in a + score for the 'range' criterion. For linearity, however, a -- score is given. This option is very non-linear with engagement distance and requires additional sensors for mitigation. A basic solenoid actuator will have to be calibrated for engagement distance and electric current. The engagement distance has to be measured to an accuracy equal to or better than that for the displacement measurement in the thrust stand. This requires an additional displacement sensor or the sensor of the thrust stand to be removed and placed in a calibration rig. Both options lead to increased complexity and additional cost. The setup is, however, simple to construct and not very sensitive to manufacturing inaccuracies. Also, it does not require expert knowledge or special tooling. This yields a ++ score for 'complexity'.

5.2.2 Solenoid placed in a uniform magnetic field

A solenoid suspended in a uniform magnetic field (see Section 5.1.2) has been demonstrated to be independent of engagement distance.

This is a very favorable characteristic, leading to a ++ score for 'linearity'. The required force range has not been demonstrated yet, but the design can be scaled by changing the strength of the external field, the number of turns on the coil and the electric current through the coil. This results in a + score for 'range'. However, the required uniform external magnetic field is difficult to create. Either a special arrangement of permanent magnets or specific arrangement of coils (e.g. Helmholtz or Maxwell) is required. The setup used by Tang et al. [80] is bulky and heavy. Alternative setups using electromagnets also tend to be bulky. To keep the mass of the pendulum to a minimum, the solenoid has to be placed on the thrust stand. The electric wires that provide electric current to the solenoid will introduce additional parasitic forces that have to be mitigated. For these reasons, a -- score is given for 'complexity'.

5.2.3 *Varying Turn-Density Coil*

The VTDC concept (see Section 5.1.3) has been demonstrated to create a constant magnetic field gradient within the coil, resulting in a force that is independent of engagement distance. The presented design can be changed to optimize the magnetic field to improve the actuator. The created force can be scaled and modulated using the electric current. These reasons yield a + score for the 'range' and a ++ score for linearity. The design methods need to be improved to include three-dimensional effects and edge effects. The variable-turn density renders the VTDC more difficult to manufacture compared to a normal solenoid, but it is expected this can be overcome with production techniques such as 3D printing. Therefore, a - is given for 'complexity'.

5.2.4 *Anti-Helmholtz*

A magnetic field gradient can be used to apply a force onto a magnetic dipole. The anti-Helmholtz setup (see Section 5.1.4) can be used to create large gradients and the applied force can be scaled. As shown in Appendix A, the gradient is not constant along the center line of the coil. This introduces a dependency on engagement distance. The location of the dipole within the coil arrangement is therefore important. The coils also have to be of equal dimensions and number of turns and be separated by one radius. These points combined result in a -- score for 'complexity' and 'linearity' and a + score for 'range'.

5.2.5 *Canted Helmholtz*

The canted Helmholtz setup (Section 5.1.5) can be used to create a constant field gradient independent of engagement distance. This allows for the delivered force to be independent of engagement distance as well. The field gradient is nearly independent of applied electric current. The gradient can only be changed by changing the canting angle between the two Helmholtz coils. For a device that is used for in situ calibration under vacuum conditions, this results in a need for moving components. As for all Helmholtz based setups, the two coils need to have an equal amount of turns, equal dimensions and need to be located exactly one radius apart. Therefore, the complexity of the design goes up and a — score is assigned. For linearity and range both a + score is given, for the reasons mentioned above.

5.2.6 *Parallel plates*

Parallel plates are conceptually very simple actuators (see Section 5.1.6). They are composed of two plates with an electric potential between them. This results in a '+' score for 'complexity'. Their applicability, however, has only been demonstrated for small ranges in the μN -regime. In addition to this, the applied force is quadratically dependent on engagement distance. This requires additional hardware to measure the distance between the target and the actuator. For these reasons, a — score is given for 'range' and 'linearity'.

5.2.7 *Electrostatic combs and fins*

The electrostatic combs (Section 5.1.7) and electrostatic fins (Section 5.1.8) both have not been demonstrated for the required force range. The designs can be scaled, using multiple combs or fins or by increasing the electric potential between the target and actuator. However, higher potentials cannot be used as arcing between the combs and fins needs to be avoided. Increasing the number of fins and combs is possible, but quickly results in bulky and heavy combs. Therefore these options are considered not sufficiently scalable for the required purposes and a — score is awarded for 'range'. Both systems are also nonlinear with engagement distance, which limits their use to small movements. The nonlinearity can partially be mitigated by proper design of the combs and fin dimensions. For this reason a – score is assigned to 'linearity'. The geometry of the combs and fins is relatively simple and it is expected that these can be easily manufactured. This combined with the required knowledge and equipment for the use of high electric potentials results in a – score for 'complexity'.

5.2.8 Trade-off conclusion

From the results presented in Table 13, it is concluded that the VTDC is the best candidate actuator, because it can be scaled to meet the required force range and can have a large region where the applied force is independent of engagement distance. The design of the VTDC actuator is worked out in detail in the following sections. It is interesting to note that the trade-off method is sensitive for subjectivity, but the author's lack of experience in the design of electrostatic or electromagnetic actuators and the lack of direct technical comparisons in literature make it hard to provide a less sensitive trade-off method.

5.3 DESIGN OF A VARIABLE-TURN DENSITY COIL BASED ACTUATOR

The concept of a VTDC actuator is already summarized in Section 5.1.3. A VTDC has a magnetic field and geometry that are considerably more complex compared to an ideal solenoid. In contrast to a classical ideal solenoid, the VTDC does not have axial symmetric geometry. In locations of low turn-density (areas with very low axial symmetry) three-dimensional effects dominate the magnetic field. The design parameters that define the VTDC need to be tuned for the required performance. This class of coils is not commercially available and each coil needs to be designed. Therefore, the analysis of Friedman et al. [24] requires extension to account for the three-dimensional effects in the design of a VTDC calibration actuator. In this section, the calculation method is outlined and the results of the simulation are presented and subsequently used for the sizing of the actuator.

5.3.1 Mathematical model of Variable Turn-Density Coil based actuator

As described earlier, the actuator is composed of a VTDC coil and a (small) permanent magnet suspended in the coil along its center line. By shaping the magnetic field appropriately, a force that is independent of engagement distance can be applied to the magnet. The permanent magnets are modeled as magnetic dipoles, which is an appropriate approximation when the magnets are small compared to the radius of the coil [18, 55].

A right-handed reference frame is used in which the x-axis is aligned with the center line of the coil and the yz-plane intersects the beginning of the coil. Using Biot-Savart's law and classical electromagnetic theory [9], it can be derived that the force experienced by a magnetic dipole with magnetic moment m in a nonuniform field is equal to

$$\mathbf{F} = \nabla (\vec{\mu}_1 \cdot \mathbf{B}) \quad (44)$$

with \mathbf{F} the force vector, $\vec{\mu}_1$ the magnetic moment vector and \mathbf{B} the magnetic field. When it is assumed that the magnetic moment μ_1 is constant, it can be taken outside the gradient. This is justified for small magnetic fields, because smaller magnets approach the ideal dipole. When the additional assumption is made that the magnetic moment is aligned with the magnetic field, the given expression simplifies to

$$\mathbf{F} = \nabla (\mu_1 B) = \mu_1 \nabla B \quad (45)$$

Assuming that the dipole is suspended in the radial center of the VTDC, the radial component of the force can be neglected. This results in

$$\mathbf{F} = \mu_1 \frac{\partial B}{\partial x} \hat{\mathbf{x}} \quad (46)$$

Following the derivation of Friedman et al. [24], this can be rewritten to include the current in the coil and the turn-density variation as prior given by (38):

$$\mathbf{F} = \mu_0 \mu_1 i \frac{dn}{dx} \hat{\mathbf{x}}$$

This, however, does not account for the effect of the asymmetry of the field in locations of low turn-density. The magnetic field of the VTDC is evaluated (numerically) using the Biot-Savart law [26], which describes the magnetic field around an infinitesimally small wire element:

$$d\mathbf{B}(\mathbf{r}) = \frac{\mu_0 i}{4\pi} \frac{d\mathbf{L} \times (\mathbf{r} - \mathbf{r}_L)}{|\mathbf{r} - \mathbf{r}_L|^3} \quad (47)$$

In this, $d\mathbf{B}$ is the infinitesimally small contribution to the magnetic field vector, $d\mathbf{L}$ is the infinitesimally small wire element and i is the electric current. The VTDC can be parameterized and described by a curve C given by vector \mathbf{r}_L . Integration of (47) over curve C yields an expression of the net magnetic field strength at \mathbf{r} :

$$\mathbf{B}(\mathbf{r}) = \frac{\mu_0 i}{4\pi} \oint_C \frac{d\mathbf{L} \times (\mathbf{r} - \mathbf{r}_L)}{|\mathbf{r} - \mathbf{r}_L|^3} \quad (48)$$

For specific cases, this integral can be evaluated analytically and a closed form solution is easily found that describes the entire field. Due to the lack of rotational symmetry in the VTDC, finding a closed form, analytical solution is considerably more complicated. Because the entire field within the coil is required, no simplifying assumptions can be made and a numerical solution is justified.

The coil geometry is given by curve C , described by the vector \mathbf{r} . Friedman et al. [24] define the VTDC as a cylindrical coil with a constant varying turn-density. With the total number of turns given by N , the

turn-density can be given as $n = \frac{dN}{dx}$. The constant varying turn-density is given by $\frac{dn}{dx} = c_0$. By repeated integration of the latter identity, the total amount of turns in a coil of length x can then be expressed as

$$N = \frac{c_0}{2}x^2 + n_0x + N_0 \quad (49)$$

with n_0 being the initial turn density at $x = 0$, $n_0 = \left. \frac{dn}{dx} \right|_{x=0}$ and N_0 the initial number of turns at $x = 0$. It is assumed that $x = 0$ corresponds with the head of the coil, yielding that $N_0 = 0$. Solving this equation for x as a function of N results in the two solutions given by

$$x_{1,2} = -\frac{n_0}{c_0} \pm \frac{1}{c_0} \sqrt{n_0^2 + 2c_0N} \quad (50)$$

of which only the positive solution yields realistic results. Using (50), the x coordinate of a VTDC can be parameterized as a function of the number of turns. Similarly, the two other coordinates, y and z , can be given using

$$y = R \cos(2\pi N) \quad (51)$$

$$z = R \sin(2\pi N) \quad (52)$$

with R the radius of the coil in m. The curve parameterization is now given by $\mathbf{r} = (x, y, z)^T$. The corresponding infinitesimally small wire element is tangent to the curve and can be expressed as

$$d\mathbf{L} = \begin{pmatrix} \frac{dx}{dN} \\ \frac{dy}{dN} \\ \frac{dz}{dN} \end{pmatrix} = \begin{pmatrix} (n_0^2 + 2c_0N)^{-1/2} \\ -2\pi R \sin(2\pi N) \\ 2\pi R \cos(2\pi N) \end{pmatrix} \quad (53)$$

Using the equations above, a coil can be defined using the coil radius R , the initial turn-density n_0 , the turn-density variation c_0 and the total number of turns. The latter parameter does not provide insight in the dimensions of the coil and on how these can be constrained. Therefore, the required number of turns is calculated from the total coil length first. This figure can be derived easily from (49) as a function of total coil length L_t as

$$N_t = \frac{c_0}{2}L_t^2 + n_0L_t \quad (54)$$

5.3.2 Magnetic moment of permanent magnet

The magnetic dipole of the permanent magnet needs to be known in advance to select the sizing parameters of the VTDC - radius R , length L , initial turn-density n_0 and constant turn-density variation

c_0 . Small neodymium raw-earth magnets have been obtained in various sizes and corresponding strengths (see [Appendix K](#)). The magnetic moment of these small magnets is not provided by the manufacturer and cannot easily be calculated. A magnetic piston ([Appendix C](#)) was used to estimate this parameter. The estimate of the magnetic moment of the S-06-06-N magnets is $\mu_1 = 0.19 \pm 0.014 \text{ A m}^2$. Similarly, the resulting estimate of the magnetic moment of the S-04-04-N magnets is $\mu_1 = 0.057 \pm 0.0071 \text{ A m}^2$. Two smaller types of magnets were obtained as well, but these proved to be too small to determine the magnetic moment experimentally using a magnetic piston at a reasonable accuracy. For these magnets, the S-02-02-N and S-1.5-0.5-N respectively, the magnetic moment was estimated based on the results for the bigger magnets. For each magnet the magnetization class was specified by the manufacturer. The magnetization is defined as the quantity of magnetic moment per unit volume, often given in A m^{-1} :

$$\mathbf{M} = n\vec{\mu}_1 = \frac{\vec{\mu}_1}{V} \quad (55)$$

with M the magnetization, n the number density of magnetic moments in m^{-3} and V the volume in m^3 . The magnetization classes are given by the manufacturer in terms of an approximate maximum energy product of the magnets in MGOe. The S-02-02-N and S-06-06-N magnets are class N48, while the S-1.5-0.5-N and S-04-04-N are class N45. The number refers to the maximum energy product and the N indicates the magnets can be used at a temperature no higher than 80°C . This quantity cannot easily be related to the actual magnetization. However, if the classes of different magnets are similar, their magnetization can be assumed similar as well. This implies that the magnetic moment can be estimated by scaling the magnetic moment found for the S-06-06-N and S-04-04-N by the relative volume of the magnets of which the strength is yet to be measured. Using the pairs of similar classes, the magnetic moment can be estimated. Shorthand notations are used; e.g S-2 refers to S-02-02-N.

$$1 \text{ MGOe} \approx 7957.75 \text{ J m}^{-3}$$

$$\mu_1|_{\text{S-2}} = \mu_1|_{\text{S-6}} \frac{V_{\text{S-2}}}{V_{\text{S-6}}} = 0.19 \frac{\pi \cdot 2^3}{\pi \cdot 6^3} = 0.0070 \text{ A m}^2$$

$$\mu_1|_{\text{S-1.5}} = \mu_1|_{\text{S-4}} \frac{V_{\text{S-1.5}}}{V_{\text{S-4}}} = 0.057 \frac{\pi \cdot 1.5^2 \cdot 0.5}{\pi \cdot 4^3} = 0.0010 \text{ A m}^2$$

The accuracy of these estimations depends on the dimensions of the magnets and the accuracy of the measurements. Rewriting (55) for the magnetic moment of a magnet of unknown strength, but known size and known magnetization, results in

$$\mu_1 = \mu_1|_{\text{ref}} \frac{V}{V_{\text{ref}}} \quad (56)$$

where the subscript 'ref' refers to the reference values of another magnet and V is the volume. The accuracy of this estimation can then be derived using

$$\Delta\mu_1 = \left| \frac{\partial\mu_1}{\partial\mu_1|_{\text{ref}}} \right| \Delta\mu_1|_{\text{ref}} + \left| \frac{\partial\mu_1}{\partial V} \right| \Delta V + \left| \frac{\partial\mu_1}{\partial V_{\text{ref}}} \right| \Delta V_{\text{ref}} \quad (57)$$

The partial derivatives are easily evaluated and (57) can be rewritten to

$$\Delta\mu_1 = \frac{V}{V_{\text{ref}}} \Delta\mu_1|_{\text{ref}} + \frac{\mu_1|_{\text{ref}}}{V_{\text{ref}}} \Delta V + \frac{\mu_1|_{\text{ref}} V}{V_{\text{ref}}^2} \Delta V_{\text{ref}} \quad (58)$$

For the cylindrical magnets the volume is given by $V = \pi r^2 h$, with r the radius and h the height. The uncertainty in volume is then found to be

$$\Delta V = \left| \frac{\partial V}{\partial \pi} \right| \Delta \pi + \left| \frac{\partial V}{\partial r} \right| \Delta r + \left| \frac{\partial V}{\partial h} \right| \Delta h \approx 2\pi r h \Delta r + \pi r^2 \Delta h \quad (59)$$

In this equation, the error caused by the uncertainty in the used value of π is neglected. Using (59), one can calculate that the uncertainties of the estimations are $\Delta\mu_1|_{S-2} = 0.0019 \text{ A m}^2$ and $\Delta\mu_1|_{S-1.5} = 0.00036 \text{ A m}^2$. In this calculation, the tolerances on the dimensions are taken to be 0.1 mm in height and 0.05 mm in radius. The values are provided by the manufacturer. An overview of all relevant values for the permanent magnets can be found in Table 14. The magnetic moment of the S-02-02-N magnets was determined experimentally to be $0.0073 \pm 0.0044 \text{ A m}^2$. The estimate of $0.0070 \pm 0.0019 \text{ A m}^2$ is well within the experimental uncertainty and only deviates $\approx 4\%$ from the mean of the experimental value.

MAGNET	CLASS	$\varnothing \times H$ (mm)	MASS (g)	μ_1 (A m^2)
S-1.5-0.5-N	N45	1.5 × 0.5	0.0067	0.0010 ± 0.00036 (est.)
S-02-02-N	N48	2 × 2	0.048	0.0070 ± 0.0019 (est.) and 0.0073 ± 0.0044 (exp.)
S-04-04-N	N45	4 × 4	0.38	0.057 ± 0.0071 (exp.)
S-06-06-N	N48	6 × 6	1.3	0.19 ± 0.014 (exp.)

Table 14: Specification of estimated (est.) and experimentally determined (exp.) magnet magnetization class, dimensions, mass and strength.

5.3.3 Coil optimization

Using the mathematical descriptions above, the magnetic field of a VTDC can be simulated. A computer model was developed to calculate the magnetic field within the coil along the xz -plane. The geometry of the VTDC is calculated using (50) and (51). The magnetic field vectors are then calculated for discrete points on the xz -plane by numerically integrating (48). The resulting component of the magnetic field is sampled and a linear least-squares fit is performed. The quality of this fit is estimated by calculation of the coefficient of determination (also known as R^2). This parameter can be used to judge the linearity of the magnetic field. The linear fit also returns the gradient of the field along the coil length within the sampled space. In addition to these parameters, the total number of turns is calculated using (54) and the separation of turns at the end of the coil is calculated. This latter value determines whether the coil can be manufactured, because it limits the radius of the copper wire to be used. A symbolic relation for the separation of turns is easily derived via the definition of turn-density $n = \frac{dN}{dx} = \int c_0 dx$. Performing the integration results in the following after some manipulation:

$$\frac{dx}{dN} = \frac{1}{c_0x + n_0} \quad (60)$$

The separation of turns at the end of the coil is then easily calculated using (60):

$$\Delta x = \frac{dx}{dN} \Delta N = \frac{1}{c_0L + n_0} \quad (61)$$

5.3.3.1 Model verification

The model was verified using an ideal solenoid: a coil with constant turn-density of infinite length. The field strength of such a coil is homogeneous and has a constant field strength that is given by Ampere's law of (36) (repeated):

$$B = \mu_0 n i$$

where n is the turn-density and i is the electric current. An ideal solenoid with a constant turn-density of 1000 m^{-1} was used. The electric current was chosen at an arbitrary 1 A and the radius at 0.030 m. This yields a constant magnetic field strength $B \approx 0.00126 \text{ T}$. In Figure 25, the magnetic field in the xz -plane of the 10 cm ideal solenoid is depicted. As can be seen, the field is homogeneous at its center and the field lines are parallel and homogeneously distributed as predicted. As can be seen in Figure 26, the calculated field strength closely approximates Ampere's law for the longer coil. For the shorter

coil, edge effects influence the field considerably. This results in Ampere's law being an over-approximation. From this result, it is concluded that the model calculates the magnetic field strength as expected.

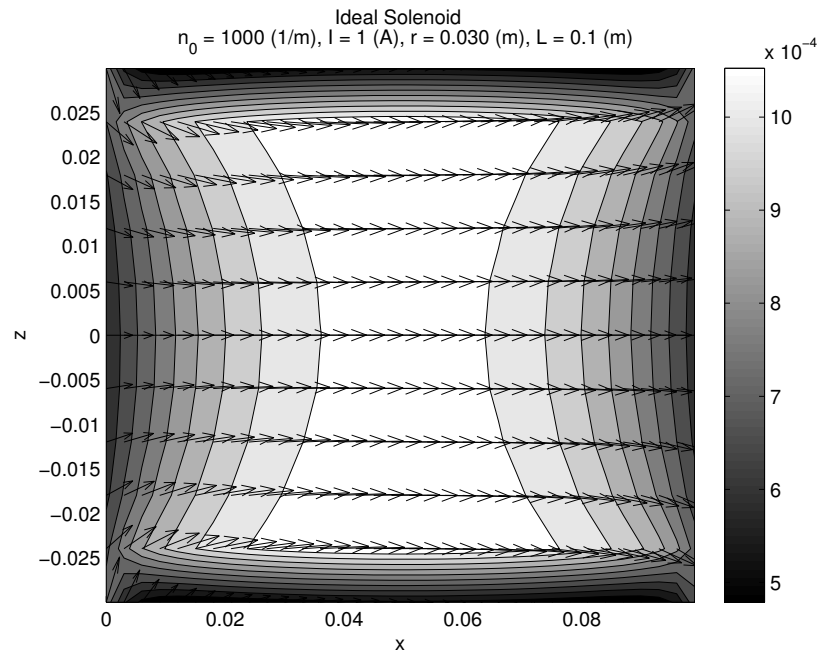


Figure 25: Simulated magnetic field for a 10 cm ideal solenoid. The field is homogeneous and parallel as predicted by theory.

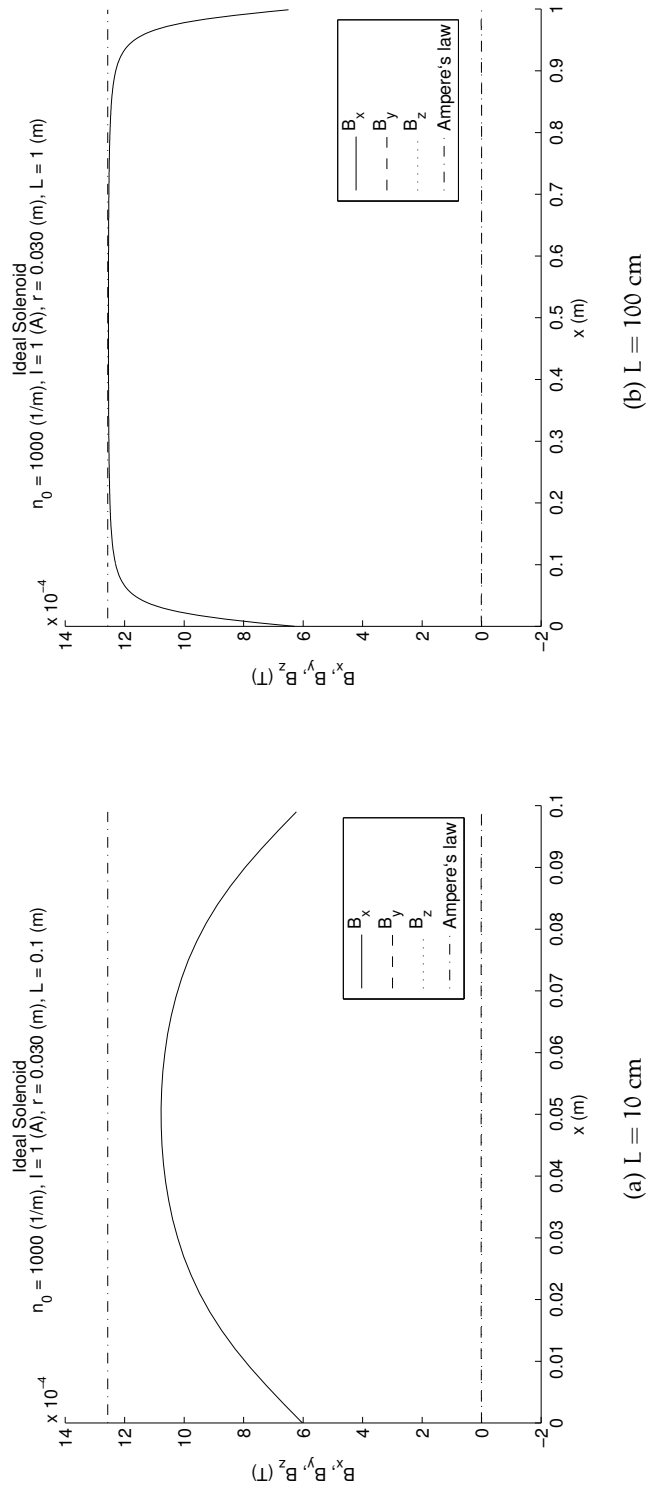


Figure 26: Simulation results for 10 cm and 100 cm ideal solenoids. For longer coils the results closely approximate Ampere's law.

5.3.3.2 Optimization

The optimization was performed using a Monte Carlo search [32]. For the selected design parameters (length L , initial turn-density n_0 and the turn-density variation dn/dx), n_{sample} random samples are generated. For each variable the samples are picked from a uniform distribution for which the limits are given in Table 15.

PARAMETER	VALUE	DESCRIPTION
R	0.030 m	Coil radius
i_c	1.0 A	Electric current
ΔN	1/50 turn	Length for each wire element expressed in turns
n_{sample}	2500 samples	Total number of coils simulated
L	0.030 – 0.10 m	Total length of coil
n_0	100 – 500 m^{-1}	Initial turn-density
$\frac{dn}{dx}$	100 – 5000 m^{-2}	Turn-density variation
Δx_{search}	0.03 m	Length of box to sample for fitting of linear function

Table 15: Simulation parameters for VTDC optimization.

The radius of the coil was fixed to 0.030 m and chosen to be slightly smaller than the sensor target. This allows for a minimum of a 1 cm clearance between the calibration actuator and any engine or engine bracket in the final setup.

The current was fixed to 1 A to allow easy scaling of the magnetic field strength and field gradient in the data analysis. The coil total length was limited to a minimum of 3 cm and a maximum of 10 cm. The lower bound was estimated to be the minimum coil length that would still allow a constant field gradient. The upper bound was chosen to allow sufficient space in the setup wiring, alignment and mounting of the coil. A short coil is preferred for these reasons, whenever possible.

The bounds for the initial turn-density and turn-density variation were based on initial experiments with the VTDC presented by Friedman et al. [24]. Their coil has an overall length of 50 cm, a turn-density variation of 1100 m^{-2} and no initial turn-density. By means of experiments, it was investigated how the parameters influenced the field and how the overall length of the coil could be reduced. This was done by halving or doubling parameters consecutively and studying the magnetic field shape and strength after each change. It was found,

that in reducing the coil length, unwanted field curvature was introduced at the start of the coil. This could be remedied by introducing an initial turn-density in the order of 100 m^{-1} to 500 m^{-1} . Other non-linear behaviour could be delayed by introducing higher turn-density variations. It was therefore chosen to bound the turn-density variation in optimization to 100 m^{-2} to 5000 m^{-2} . In total 2500 coils were evaluated.

5.3.3.3 Results and discussion

Of the 2500 random samples on the search space (that was defined in Section 5.3.3.2) the best combination was selected. The selection was done based on the coefficient of determination, after which the field of the coil was inspected to make sure no unwanted effects were present. The selected VTDC is defined by its parameters: $L = 0.0840 \text{ m}$, $R = 0.03 \text{ m}$, $n_0 = 102.6180 \text{ m}^{-1}$ and $\frac{dn}{dx} = 4745.1 \text{ m}^{-2}$. An impression of the resulting geometry is given in Figure 27.

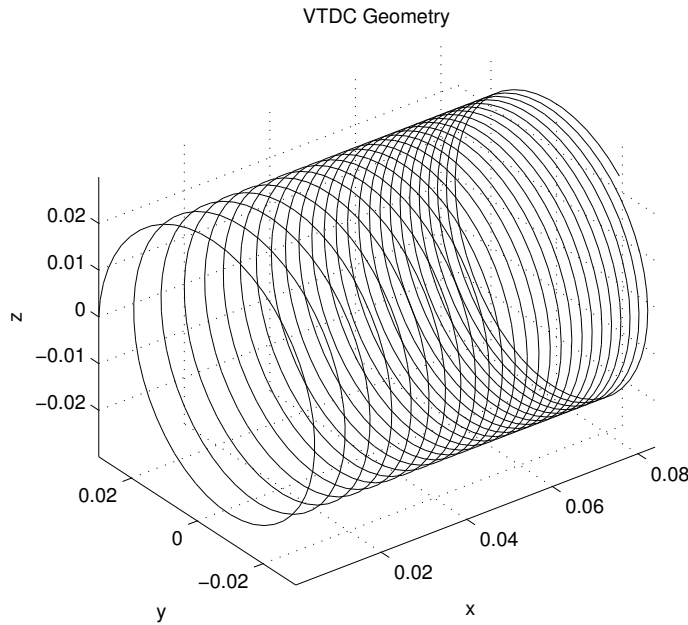


Figure 27: Geometry of the optimized VTDC. Parameters: $L = 0.0840 \text{ m}$, $R = 0.03 \text{ m}$, $n_0 = 102.6180 \text{ m}^{-1}$, $\frac{dn}{dx} = 4745.1 \text{ m}^{-2}$. Electric current: $I = 1 \text{ A}$.

At a current of $i = 1 \text{ A}$ this results in a linear least squares fit of

$$B_x = 0.0048x + 0.00012 \quad (62)$$

with a coefficient of determination $R^2 = 0.997$. The magnetic field gradient at the given electric current is found to be $\left. \frac{dB_x}{dx} \right|_{I=1 \text{ A}} = 0.0048 \text{ T m}^{-1}$. The field strength on the geometric center line of the

coil is depicted in Figure 28. In the figure, also the fit is given including the data points. The length of the fitted interval is 0.030 m.

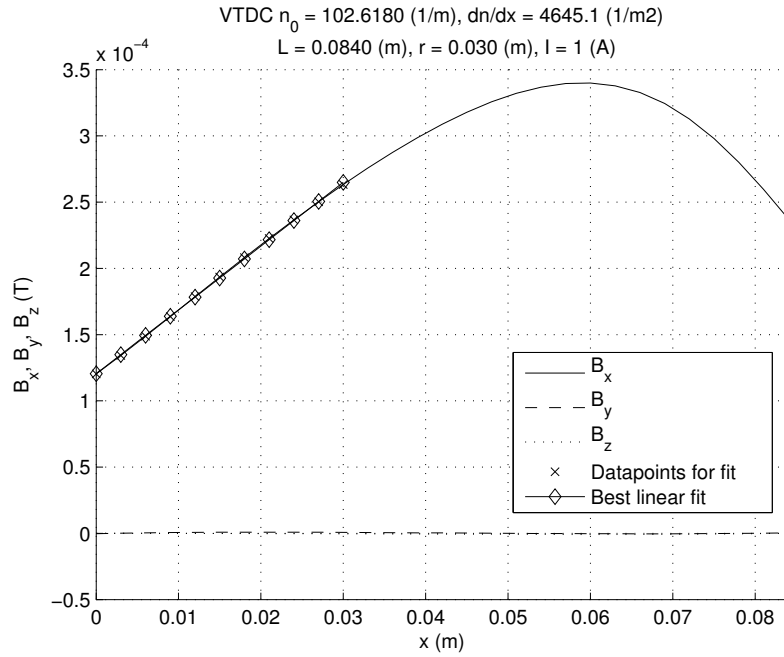


Figure 28: Magnetic field at the geometric center of the optimized VTDC. Parameters: $L = 0.0840$ m, $R = 0.03$ m, $n_0 = 102.6180$ m⁻¹, $\frac{dn}{dx} = 4745.1$ m⁻². Electric current: $I = 1$ A.

The separation of turns is 0.002 m at the end of the coil ($x = 0.0840$ m), leaving sufficient space for winding with copper wire of ≤ 2 mm diameter. A large diameter wire is preferred over thin wires, because they are structurally stronger and provide ample advantages regarding thermal effects in the coil that can limit its operation as is discussed below.

The power dissipated in a resistor, e.g. a copper wire, is directly proportional to the current and the resistance. This is known as Joule heating and is described by

$$P = i^2 R \quad (63)$$

where P is the dissipated power in W, R the electric resistance in Ω and i the electric current in A [77]. The resistance is given by Pouillel's law:

$$R = \rho \frac{l_{\text{wire}}}{A_{\text{wire}}} \quad (64)$$

where ρ is the resistivity ($\approx 1.6 \cdot 10^{-8}$ Ω m at 0°C for copper [77]), l_{wire} the length of the wire in m and A_{wire} the cross-sectional area in m². For a circular cross-section the latter is simply $A_{\text{coil}} = \frac{\pi}{4} d_{\text{coil}}^2$,

with d_{wire} the diameter of the wire in m. For a wire, this translates into

$$P = \frac{4\rho l_{\text{wire}}}{\pi d_{\text{wire}}^2} i^2 \quad (65)$$

As can be concluded from this equation, the power dissipated is inversely quadratically proportional to the wire diameter. In addition to a lower power dissipation, the total thermal capacity also increases quadratically proportional to the wire diameter and its dissipating area increases linearly proportional to the wire diameter. All this together results in a slower heating of the coil and consequently longer operating times with higher wire diameter.

The magnetic field of the chosen VTDC is depicted in Figure 29. As can be seen in the figure, the field lines are nearly parallel close to the center line and the radial components of the field B_y and B_z are small compared to the longitudinal component B_x . This allows for a small misalignment with respect to the center line.

The coil holder and wire are limited by operating temperature. Exceeding these limits may cause permanent damage to either.

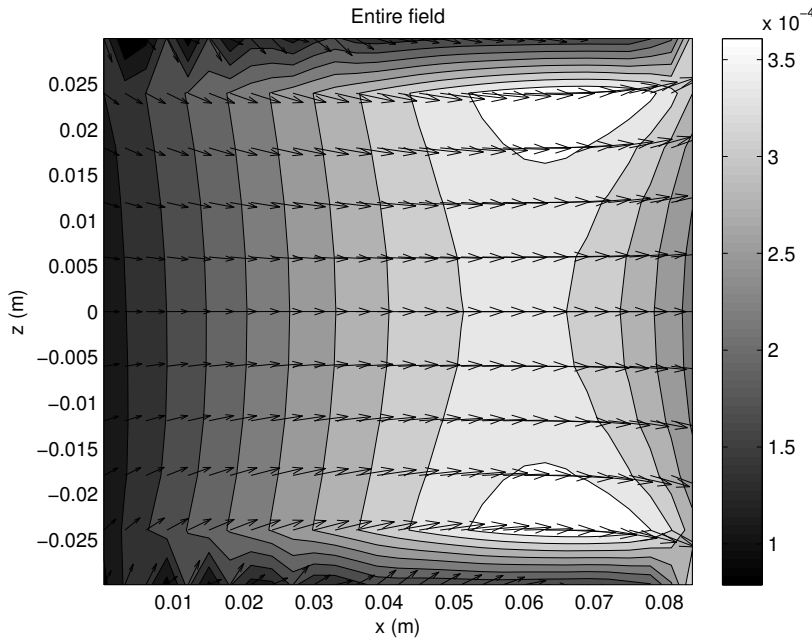


Figure 29: Magnetic field of the optimized VTDC. Parameters: $L = 0.0840$ m, $n_0 = 102.6180$ m⁻¹, $\frac{dn}{dx} = 4745.1$ m⁻². Electric current: $I = 1$ A.

5.3.4 Actuator sizing

The selected VTDC is paired with (a group of) permanent magnets to create a constant force. Using the data of the magnetic moments presented in Table 14, the electric currents required to exert sufficient

force on the permanent magnets can be calculated. The force exerted on a dipole by a magnetic field was derived to be (46)

$$\mathbf{F} = \mu_1 \frac{\partial \mathbf{B}}{\partial \mathbf{x}} \hat{\mathbf{x}}$$

In the optimization, the magnetic field gradient $\frac{\partial \mathbf{B}}{\partial \mathbf{x}}$ was only calculated for an electric current $i_0 = 1$ A. For any other current, the magnetic field gradient is scaled by the ratio of the current i and the simulated current i_0 .

$$F_x(i) = \mu_1 \left. \frac{\partial \mathbf{B}}{\partial \mathbf{x}} \right|_{i_0} \frac{i}{i_0} \quad (66)$$

This equation can be rewritten for $i(F_x)$, such that the required electric current can be calculated.

$$i(F_x) = \frac{F_x i_0}{\mu_1 \left. \frac{\partial \mathbf{B}}{\partial \mathbf{x}} \right|_{i_0}} \quad (67)$$

The calibration actuator has to provide similar or better performance than the thrust stand. The thrust stand performance was presented in Figure 14 of Section 4.1.4. The thrust stand covers three thrust ranges, with three slightly different setups. Therefore, it is justified to have three slightly different calibration setups when required. The calibration setup has to cover the ranges listed in Table 16.

RANGE (μN)	ACCURACY (μN)
1 – 45	0.1
45 – 420	1
200 – 5000	10

Table 16: Required calibration force ranges and accuracies.

The 1 μN to 45 μN range can be covered using one S-1.5-0.5-N magnet, with a magnetic moment of 0.0010 ± 0.00050 A m^2 . The uncertainties in magnetic moment are taken into account in these estimations and the minimum, maximum and typical currents are all listed in Table 17. In case the magnet has a magnetic moment of $\mu_1 = 0.00064$ A m^2 , the required electric current is 14.65 A. As explained earlier, high currents can lead to the unwanted excessive heating of the wire. The current can be limited to 7.324 A, by using two magnets of this type.

For the 45 μN to 420 μN range, a pair of S-02-02-N magnets can be used. The required currents are listed in Table 18. Similar to the 1 μN to 45 μN range, the maximum current can get high when the magnets turn out to be at the weak end of the estimate for magnetic moment. This problem can be remedied by using three instead of two magnets

FORCE (μN)	MIN (A)	TYP (A)	MAX (A)
1	$1.532 \cdot 10^{-1}$	$2.083 \cdot 10^{-1}$	$3.255 \cdot 10^{-1}$
45	$6.893 \cdot 10^0$	$9.375 \cdot 10^0$	$14.65 \cdot 10^0$
$\Delta F = 0.1$	$1.532 \cdot 10^{-2}$	$2.083 \cdot 10^{-2}$	$3.255 \cdot 10^{-2}$

Table 17: Required electric current for calibration force of $1 \mu\text{N}$ to $45 \mu\text{N}$ range at $0.1 \mu\text{N}$ accuracy. Used magnet: S-1.5-0.5-N magnet, with a total magnetic moment of $(0.0010 \pm 0.00036) \text{ A m}^2$.

FORCE (μN)	MIN (A)	TYP (A)	MAX (A)
45	$4.006 \cdot 10^{-1}$	$6.421 \cdot 10^{-1}$	$1.616 \cdot 10^0$
420	$3.739 \cdot 10^0$	$5.993 \cdot 10^0$	$15.08 \cdot 10^0$
$\Delta F = 1.0$	$8.903 \cdot 10^{-3}$	$1.427 \cdot 10^{-2}$	$3.592 \cdot 10^{-2}$

Table 18: Required electric current for calibration force of $45 \mu\text{N}$ to $420 \mu\text{N}$ range at $1.0 \mu\text{N}$ accuracy. Used magnet: two S-02-02-N magnets, with a total magnetic moment of $2 \times (0.0073 \pm 0.0044) \text{ A m}^2$.

of this type. In that case the electric current has to be controlled from 1.078 A to 10.06 A at $2.395 \cdot 10^{-2} \text{ A}$ accuracy.

The last range from $200 \mu\text{N}$ to $5000 \mu\text{N}$ can be covered using a single S-06-06-N magnet. With a magnetic moment of $0.19 \pm 0.014 \text{ A m}^2$ the required currents are calculated and listed in Table 19. This option is preferable over a stack of two or three S-04-04-N magnets that could produce similar results, to keep the required length of the stack to a minimum. A stack of multiple S-04-04-N magnets has a length of 8 mm to 12 mm compared to 6 mm of a single S-06-06-N magnet.

FORCE (μN)	MIN (A)	TYP (A)	MAX (A)
200	$2.042 \cdot 10^{-1}$	$2.193 \cdot 10^{-1}$	$2.367 \cdot 10^{-1}$
5000	$5.106 \cdot 10^0$	$5.482 \cdot 10^0$	$5.919 \cdot 10^0$
$\Delta F = 10$	$1.021 \cdot 10^{-2}$	$1.096 \cdot 10^{-2}$	$1.183 \cdot 10^{-2}$

Table 19: Required electric current for calibration force of $200 \mu\text{N}$ to $5000 \mu\text{N}$ range at $10 \mu\text{N}$ accuracy. Used magnet: one S-06-06-N magnet, with a total magnetic moment of $(0.19 \pm 0.014) \text{ A m}^2$.

5.3.5 Mechanical design

Based on the calculations presented in the previous sections, the parts for the calibration setup are designed. In the following sections the

coil holder, the calibration arm and the magnet holders are discussed consecutively.

5.3.5.1 Coil holder

The coil holder is designed to hold the copper wire that makes up the VTDC. The holder consists of a $\varnothing 60$ mm cylindrical tube with a wall thickness of 3 mm. In the outer wall a $\varnothing 1$ mm semicircular groove has been created that describes the complicated turn geometry. This groove allows the center of the wire to describe the required path and aids in the manufacturing of the coil. The coil holder can be mounted to a surface or Boikon frame using four M5 bolts that fit in the holes on the integrated bracket. The holder is manufactured from SLS PA2200 [22] using 3D-printing techniques. The technique is chosen, since tolerances of 0.1 mm can be obtained at a relatively low price point of less than € 100 [1].

A sketch of the coil holder is depicted in Figure 30. The corresponding engineering drawings can be found in Appendix I. In these latter drawings the description of the turns has been omitted.

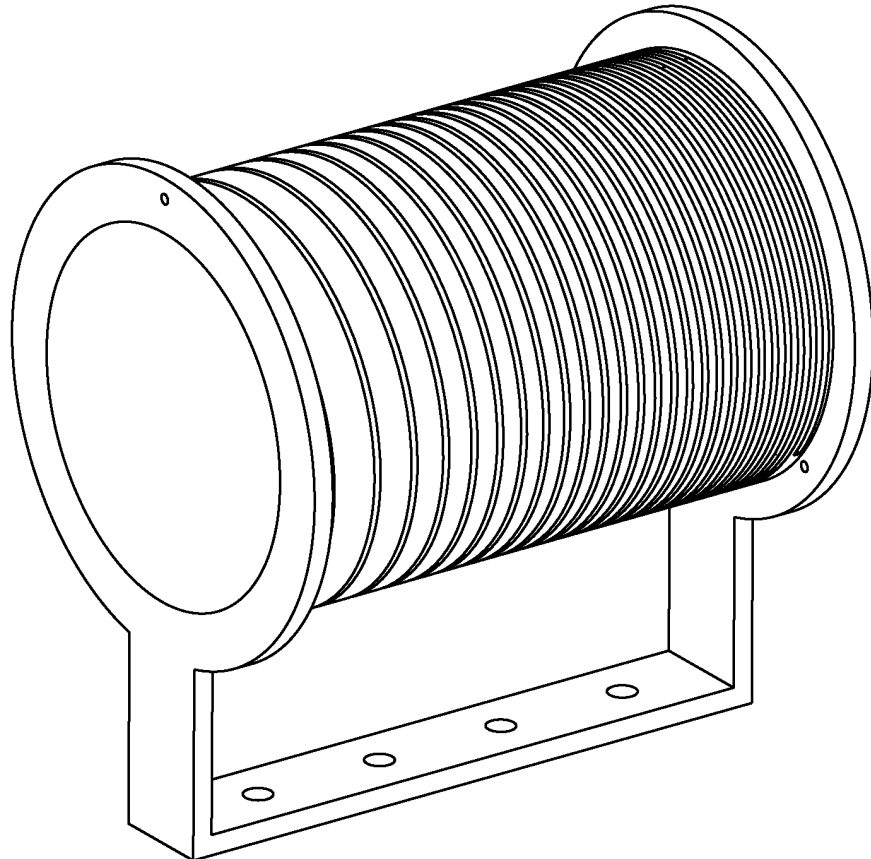


Figure 30: Sketch of the coil holder of the calibration actuator.

5.3.5.2 Calibration arm

The calibration arm separates the coil and permanent magnet from the pendulum. Using four M3 bolts it can be connected to the back-side of the sensor target (Section 4.2.4). A sketch of the structure is depicted in Figure 31. The corresponding engineering drawings can be found in Appendix I. The structure is composed of a 3 mm thick mounting plate, a 150 mm long arm and an end-block of 11 mm long. In the end block a 24 mm deep, 8 mm thick slit is created in which the magnet holders can be placed. The calibration arm is constructed from SLS PA2200 [22] using 3D-printing techniques. As the material does not have any significant magnetic behavior, it serves as an ideal separator between the metallic pendulum and the magnetic field generated by the coil.

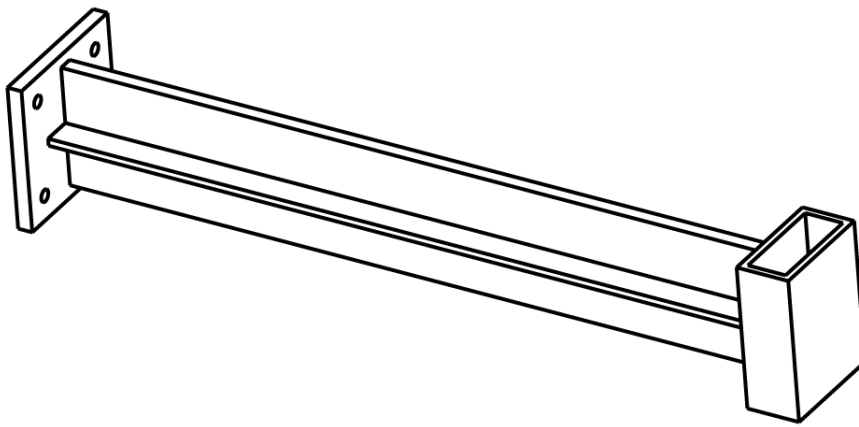


Figure 31: Sketch of the calibration arm of the calibration actuator.

The length of the arm was set to 150 mm to separate the coil sufficiently from the pendulum. The influence of the magnetic field on the pendulum is hard to estimate analytically. The chosen length was considered sufficiently large based on the influence the field would have on a permanent magnet of similar strength as used in calibration. The magnet is now assumed to be placed at the location of the pendulum. From field strength calculations for the VTDC, it was concluded that at 150 mm the magnetic field gradient $\frac{\partial B}{\partial x} \approx 0.0000289 \text{ T m}^{-1}$ is $166\times$ smaller than at the location of actuation, with a field gradient of $\frac{\partial B}{\partial x} = 0.0048 \text{ T m}^{-1}$. Consequently, the force exerted on such a magnet would be $166\times$ smaller than the actuator force. The field lines outside the coil are depicted in Figure 32. The corresponding field strength along the center line of the coil is depicted in Figure 33. The effect of the VTDC has to be verified experimentally. This can be done by comparing the movement with and without a permanent magnet placed in the holder while electric current in the coil generates the magnetic field.

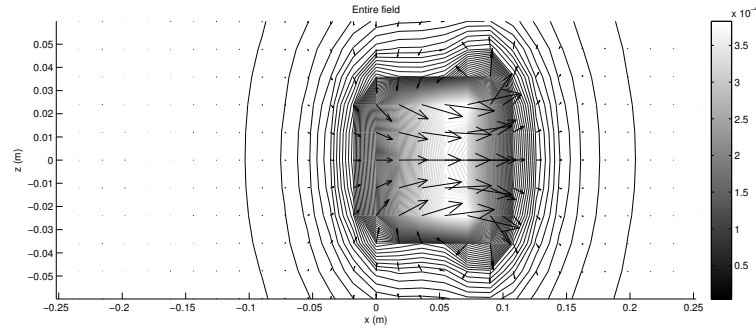


Figure 32: Magnetic field outside of the VTDC.

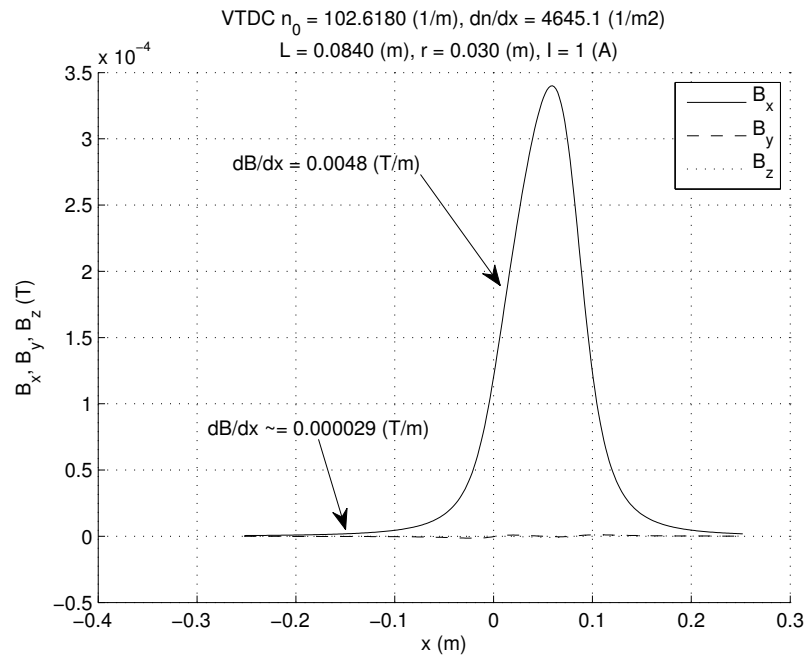


Figure 33: Magnetic field strength outside of the VTDC, along the center line.

The arm has been reduced to a cross-shaped cross-section with a 3 mm thick web of 25 mm high and 1.5 mm thick flanges of 15 mm wide. Using basic mechanics, one can calculate that this results in a cross-sectional area $A = 9.3 \cdot 10^{-5}$ m² and a bending moment of inertia $I = 3.9096 \cdot 10^{-9}$ m⁴. Using the forget-me-nots (specific solutions to the bending beam set of differential equations) as presented in Hartsuijker and Welleman [31], the bending and rotation of the calibration arm can be estimated. For this the arm is modeled as a cantilever arm with a point load at its tip and a constant distributed load over most of its length. The rotation and bending are caused by its end mass and a distributed load caused by the dead weight of the cross-shaped center part. The end mass is estimated by assuming it is a solid cuboid of $23 \times 11 \times 30$ mm. The estimation then yields

$m_{\text{end}} = 0.00706$ kg. The used model is depicted in Figure 34. The total tip deflection can be calculated using

$$\delta_{\text{end}} = \frac{ql_1^4}{8EI} + \frac{ql_1^3}{6EI}l_2 + \frac{m_{\text{end}}g(l_1 + l_2)^3}{3EI} \quad (68)$$

where δ_{end} is the deflection in m, q is the distributed load in N m^{-1} , E is the Young's modulus of the material, I is the bending moment of inertia, l is the length of the beam and g is the local gravitational acceleration in m s^{-2} . The distributed load q is due to the dead weight of the arm:

$$q = \frac{m_{\text{arm}}g}{l} = \frac{\rho A l g}{l} = \rho A g \quad (69)$$

The tip rotation can be calculated in a similar fashion. The rotation is important, because it adds to any alignment error between the permanent magnets and the magnetic field lines of the VTDC.

$$\theta_{\text{end}} = \frac{ql_1^3}{6EI} + \frac{m_{\text{end}}g(l_1 + l_2)^2}{2EI} \quad (70)$$

The density of the material is listed by the manufacturer as 930 kg m^{-3} , the Young's modulus at 1650 MPa [22]. Using this given data, the tip sag is calculated to be $\delta_{\text{end}} = 22 \text{ }\mu\text{m}$ and the tip rotation to be $\theta_{\text{end}} = 2.04 \cdot 10^{-4} \text{ rad}$ or equivalently $\approx 1.2 \cdot 10^{-2}^\circ$. Both are negligibly small compared to the errors made in manual alignment of the thrust stand. For manual alignment accuracies of 0.5 mm and 0.5° , respectively, are expected.

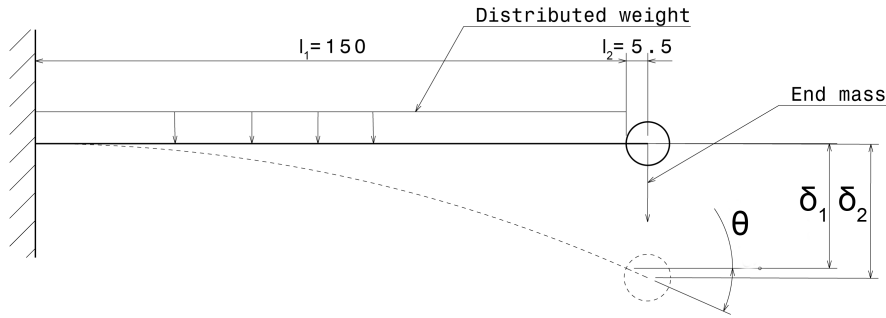


Figure 34: Schematic drawing of simplified bending model for the calibration arm. Given dimensions are in mm.

5.3.5.3 Magnet holders

The magnet holders hold the three different magnets chosen for the calibration setup. The magnets are press-fitted in the holders, which have holes that are trimmed to fit tightly. The holes are tapered at the opening, to allow easy placement of the magnets. The holders are printed 0.5 mm thicker than required. They are sanded down to

fit tightly in the calibration arm, such that no movement of the magnet or holder within the slot of the arm is possible. The holders are slightly taller than 24 mm and have small slots in the top to allow easy placement using pliers.

A sketch of the coil holder is depicted in [Figure 35](#). The corresponding engineering drawings can be found in [Appendix I](#).

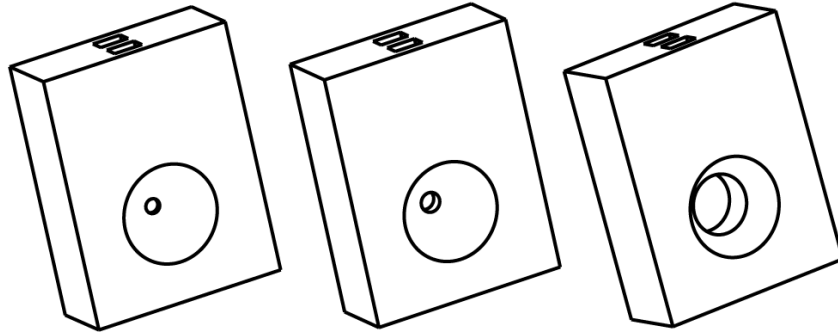


Figure 35: Sketches of the magnet holders of the calibration actuator. Holders will be placed in the slit of the calibration arm.

5.3.5.4 3D printed components

The calibration arm, the magnet holders and the coil holder are created using a 3D-printing technique called laser sintering. In this technique a layer of deposited powder is locally melted using a focussed laser. By melting consecutive layers of powder locally, a three dimensional structure is created. In this instance, the components are made of PA 2200, a polyamid powder based on engineering polymer PA 11, also known under its commercial name Rilsan (produced by the Arkema company) [51]. The material can hold up to 1.8% of its mass of moist from the environment. It is confirmed by the Arkema company that PA 11 is stable at [UHV](#) pressures and does not transfer into a gaseous state [2]. However, [UHV](#) vacuum facilities often use elevated temperatures of ≈ 180 °C for longer periods of time to evaporate all the moisture that is present in the tank. The sintered material, PA 2200, has a melting temperature of 176 °C [22]. The presence of the 3D-printed parts increases the complexity of [UHV](#) operations, but may not be completely ruled out. It should be noted here, that testing at [UHV](#) is not required. The [PMT](#) of Bradford Engineering, for example, was tested at Medium to High Vacuum Conditions at ONERA and ESA ESTEC (see [Section 6.2.13](#)). The pressures corresponding to the used gradations are listed in [Table 20](#). There is no standard available for the precise pressures corresponding to each label, therefore the values used by NPL [64] are used here.

GRADE	PRESSURE (Pa)	PRESSURE (mbar)
Low Vacuum	$1 \cdot 10^5 - 3 \cdot 10^3$	1000 – 30
Medium Vacuum	$3 \cdot 10^3 - 1 \cdot 10^{-1}$	30 – $1 \cdot 10^{-3}$
High Vacuum	$1 \cdot 10^{-1} - 1 \cdot 10^{-4}$	$1 \cdot 10^{-3} - 1 \cdot 10^{-6}$
Very High Vacuum	$1 \cdot 10^{-4} - 1 \cdot 10^{-7}$	$1 \cdot 10^{-6} - 1 \cdot 10^{-9}$
Ultra High Vacuum	$1 \cdot 10^{-7} - 1 \cdot 10^{-10}$	$1 \cdot 10^{-9} - 1 \cdot 10^{-12}$
Extreme-Ultra High Vacuum	$\leq 1 \cdot 10^{-10}$	$\leq 1 \cdot 10^{-12}$

Table 20: Gradation of vacuum level according to NPL [64].

5.4 VERIFICATION AND VALIDATION

Early iterations of TEST-110 (Section 6.2.1) were used to verify and validate the performance of the calibration actuator. For a given engagement distance, the coil performance is linear as expected. These results and the related sensitivities are discussed in Section 7.3.1.

The actuator coil is designed to have a calibration force that is independent of engagement distance within the given boundaries. To verify this, the force produced by the actuator was measured following the methods of TEST-110 at a constant current of $I = 4.027$ A and different engagement distances. The results of this test are plotted in Figure 36. As can be seen in this figure, the calibration force is not constant with engagement distance. Advanced modelling, in which the first order numerical derivative of the magnetic field is used instead of a linear fitting function to estimate the field gradient dB/dx , is represented in the same figure.

Taking an engagement distance of 1.0 cm as a reference, a deviation from the reference of -1.7% and -1.5% is found for a change in engagement distance of 0.5 cm forward or backward, respectively. This is too large, considering a relative accuracy of 0.2% is required at a calibration force of 5000 μN .

From the comparison it can be concluded that the model predicts the same behavior as found by measurements. The original optimization method, that judges the linearity of the field based on the coefficient of determination R^2 , is not accurate enough to capture the found non-linearities. An improved model that uses the second order numerical derivative of the field strength to minimize the non-linearity is used to find a new optimized design. The results hereof are discussed and presented in Section 5.5.

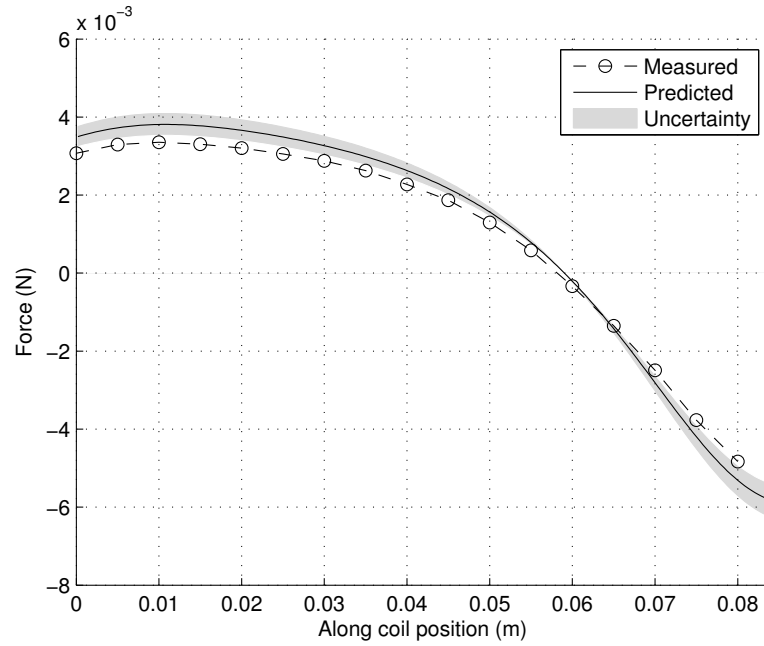


Figure 36: Calibration force as a function of engagement distance using a S-06-06-N magnet. Theoretical predictions are compared to measurements.

5.5 REDESIGN OF THE CALIBRATION COIL

A linear variation of magnetic field strength requires a constant field gradient dB/dx . A constant gradient implies that $d^2B/dx^2 = 0$. The new optimization method calculates the second order derivative within the search box in the magnetic field of the coil. It takes the sum of squares of the second order derivative at the sampled points and finds the configuration in which this is minimized. This way, a near constant gradient is achieved.

In [Figure 38](#) the magnetic field strength, gradient and second derivatives are compared. The new VTDC is most linear at an engagement distance of approximately 4.0 cm. With a total excitation of 0.5 cm forward and backward a respective variation in the gradient of 0.00% and -0.15% is found.

The magnetic field of the new designed coil is depicted in [Figure 37](#). As can be seen the field resembles that of the old coil, in both parallelism of the field lines close to the center line and the characteristics of the field. In [Table 21](#) the parameters of the old and redesigned coil are compared. Although the redesigned coil presents a better linearity, this comes at the cost of coil length and gradient strength. The gradient of 0.0019 T m^{-1} at a current of 1 A is considerably lower than the gradient of 0.0048 T m^{-1} at the same current. This means that the total magnetic moment of the used magnets has to be increased

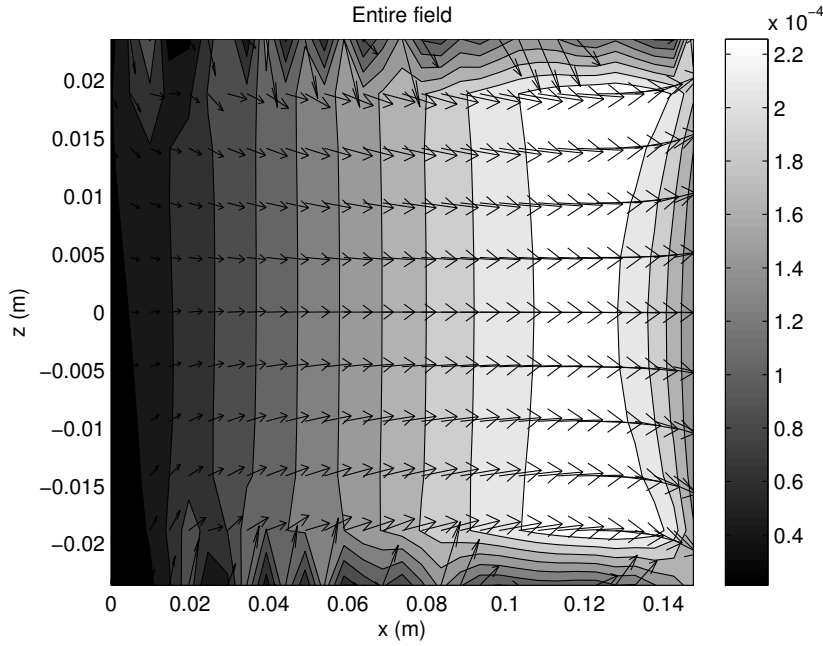


Figure 37: Magnetic field of the redesigned VTDC. Parameters: $L = 0.1476$ m, $n_0 = 20.5521$ m $^{-1}$, $\frac{dn}{dx} = 1689.0$ m $^{-2}$. Electric current: $I = 1$ A.

by adding extra magnets to the stacks or that the supply current has to be increased to provide the same calibration force. Provided that the maximum current should not exceed 10 A, the simplest solution is adding additional magnets. To provide sufficient space, a slot is created at the end of the calibration arm to allow placement of the magnet holder with protruding magnets. The required currents are listed in Table 22, Table 23 and Table 24 for the 1 μ N to 45 μ N, 45 μ N to 420 μ N and 200 μ N to 5000 μ N ranges, respectively. To the first magnet holder (holding S-1.5-0.5-N magnets) either one or two magnets have to be added to cover the range. With a total height of 0.5 mm per magnet, the new stack will not exceed the boundaries of the magnet holder. Similarly, the second magnet holder that holds S-02-02-N magnets has to be expanded with one or two magnets as well. In case two magnets have to be added, the stack of magnets will slightly exceed the boundaries of the magnet holder in which case a slot has to be created in the calibration arm. The last magnet holder, that holds S-06-06-N magnets, also has to be extended by one magnet. With a height of 6 mm per magnet, this stack of two magnets exceeds the boundaries of the magnet holder and a > 6 mm wide slot is required in the calibration arm.

In conclusion, a new actuator is designed to provide better linearity and accuracy. To limit the modifications to other components of the setup, the loss of magnetic gradient is compensated by adding extra magnets to the magnet holders and creating a slot in the calibration

arm to give way to the magnets that would protrude through the wall of the calibration arm in order to fit.

PARAMETER	OLD DESIGN	NEW DESIGN
Radius (m)	0.0300	0.0236
Length (m)	0.0840	0.1476
n_0 (m^{-1})	102.6180	20.5521
$\frac{dn}{dx}$ (m^{-2})	4745.1	1689.0
$\frac{dB}{dx}$ (T m^{-1})	0.0048	0.0019

Table 21: Comparison between original VTDC design and the redesign.

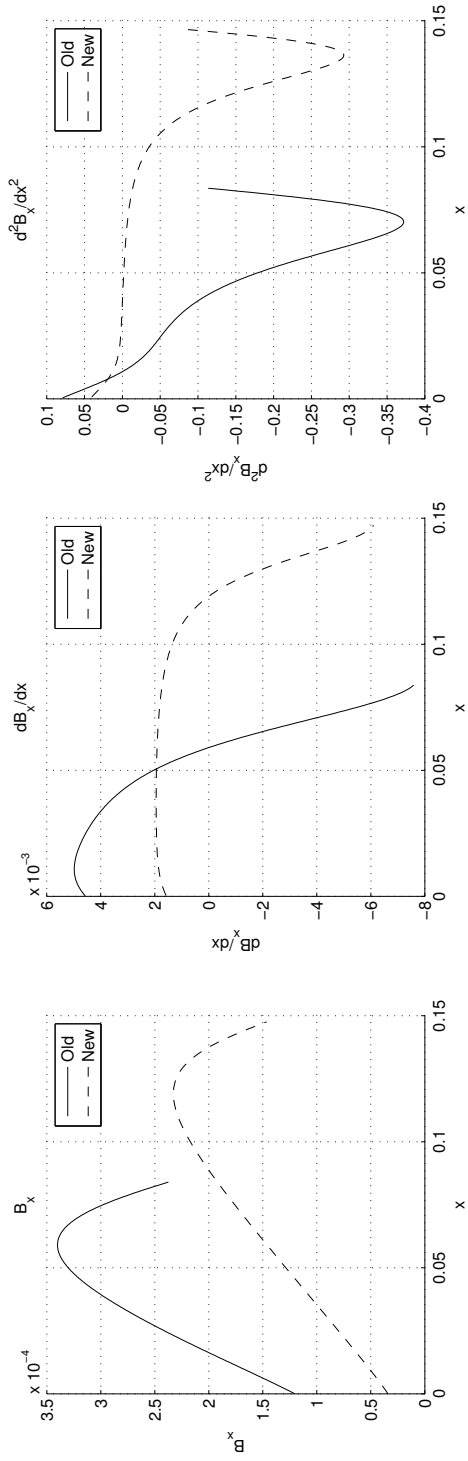


Figure 38: Comparison between old and new actuator coil.

FORCE (μN)	MIN (A)	TYP (A)	MAX (A)
1	$1.290 \cdot 10^{-1}$	$1.754 \cdot 10^{-1}$	$2.740 \cdot 10^{-1}$
45	$5.805 \cdot 10^0$	$7.895 \cdot 10^0$	$12.33 \cdot 10^0$
$\Delta F = 0.1$	$1.290 \cdot 10^{-2}$	$1.754 \cdot 10^{-2}$	$2.740 \cdot 10^{-2}$

Table 22: Required electric current for calibration force of $1 \mu\text{N}$ to $45 \mu\text{N}$ range at $0.1 \mu\text{N}$ accuracy with the redesigned actuator. Used magnet: three S-1.5-0.5-N magnets, with a total magnetic moment of $3 \times (0.0010 \pm 0.00036) \text{ A m}^2$.

FORCE (μN)	MIN (A)	TYP (A)	MAX (A)
45	$6.750 \cdot 10^{-1}$	$1.080 \cdot 10^0$	$2.722 \cdot 10^0$
420	$6.300 \cdot 10^0$	$10.08 \cdot 10^0$	$25.40 \cdot 10^0$
$\Delta F = 1.0$	$1.500 \cdot 10^{-2}$	$2.400 \cdot 10^{-2}$	$6.05 \cdot 10^{-2}$

Table 23: Required electric current for calibration force of $45 \mu\text{N}$ to $420 \mu\text{N}$ range at $1.0 \mu\text{N}$ accuracy with the redesigned actuator. Used magnet: three S-02-02-N magnets, with a total magnetic moment of $3 \times (0.0073 \pm 0.0044) \text{ A m}^2$.

FORCE (μN)	MIN (A)	TYP (A)	MAX (A)
200	$2.580 \cdot 10^{-1}$	$2.770 \cdot 10^{-1}$	$2.990 \cdot 10^{-1}$
5000	$6.450 \cdot 10^0$	$6.925 \cdot 10^0$	$7.476 \cdot 10^0$
$\Delta F = 10$	$1.290 \cdot 10^{-2}$	$1.385 \cdot 10^{-2}$	$1.495 \cdot 10^{-2}$

Table 24: Required electric current for calibration force of $200 \mu\text{N}$ to $5000 \mu\text{N}$ range at $10 \mu\text{N}$ accuracy with the redesigned actuator. Used magnet: two S-06-06-N magnet, with a total magnetic moment of $2 \times (0.19 \pm 0.014) \text{ A m}^2$.

VERIFICATION AND VALIDATION PLAN

The performance of the thrust stand is verified and validated during a two week long test campaign in the clean room of the [SSE](#) department. Herein the definitions of [Section 2.2](#) are used. In this chapter, the test campaign is described in full and it includes a description of the available facilities, used hardware and test procedures.

The objectives of this test campaign are limited to:

- the verification and validation of the thrust stand performance in terms of accuracy, resolution and range in steady thrust and impulse bit measurements;
- the characterization of the Bradford Engineering [PMT](#) in terms of thrust and specific impulse;
- and the identification of potential problems, optimizations and improvements that can be made to the [DARTS](#) facility and the TB-5m thrust stand.

6.1 TEST CONDITIONS AND EQUIPMENT

In this section, the test conditions and the used equipment are described. The required tests are performed in the clean room of the chair of [SSE](#) of Delft University of Technology. This clean room is operated by faculty staff and students and is located on the 8th floor of the Aerospace Engineering faculty. The facility provides a 10.000 class [\[35\]](#) / ISO 7 [\[38\]](#) equivalent clean room at the conditions that are listed in [Table 25](#).

*Building 62, room
8.01
Kluyverweg 1, 2629
HS Delft, The
Netherlands*

ENVIRONMENTAL	NOMINAL VALUE
Cleanliness	ISO 7 / 10.000 class
Temperature (average)	21.8°C
Pressure	Ambient
Relative Humidity	90.4%

Table 25: Environmental conditions in the clean room of chair of [SSE](#). Measurements from LASAIR II particle counter.

The test setup is placed on a heavy, damped table that attenuates any environmentally induced vibrations. Although the facility is located on the 8th floor of the building, this is expected to reduce the vibration

levels considerably compared to the levels measured by Janssens [39] and Perez-Grande [68]. The facility does not provide seismic isolation, and especially low-frequency oscillations, such as the swinging of the building, are not damped.

6.1.1 *System overview*

A system-level overview is depicted in Figure 39. On the highest level, the system can be split into seven main system blocks: i) the thrust stand, ii) the feed system to provide the engine with propellant (in this case N₂ gas), iii) the power system to provide the engine and sensor with power and control signals, iv) the sensors and DAQ, v) the calibration actuator, vi) the engine and vii) the environment.

The parts have been labeled with the following shorthand notations for brevity:

PR Pressure Regulator

SOV Shut-off Valve

FIL Filter

CV Check Valve

MV Manual Valve

MFC Mass Flow Controller

PMT Bradford Engineering Proportional Micro-Thruster (repeated)

PC Personal Computer / Lab Computer

DAQ National Instruments PXI 6229 Data-Acquisition System

TC Thermocouple

PSU Power Supply Unit

SCB-68 National Instruments Shielded I/O Connector Block for DAQ

CS1(0) Micro-Epsilon capaNC DT CS1 / CS10 sensor head

PXM209 Omega Engineering PXM209 – 006A10V

PX139 Omega Engineering PX139 – 030A4V

6.1.2 *Equipment used*

In this section, the individual hardware components are discussed. The engine is discussed separately in Section 6.1.3, because it is not part of the thrust measurement system.

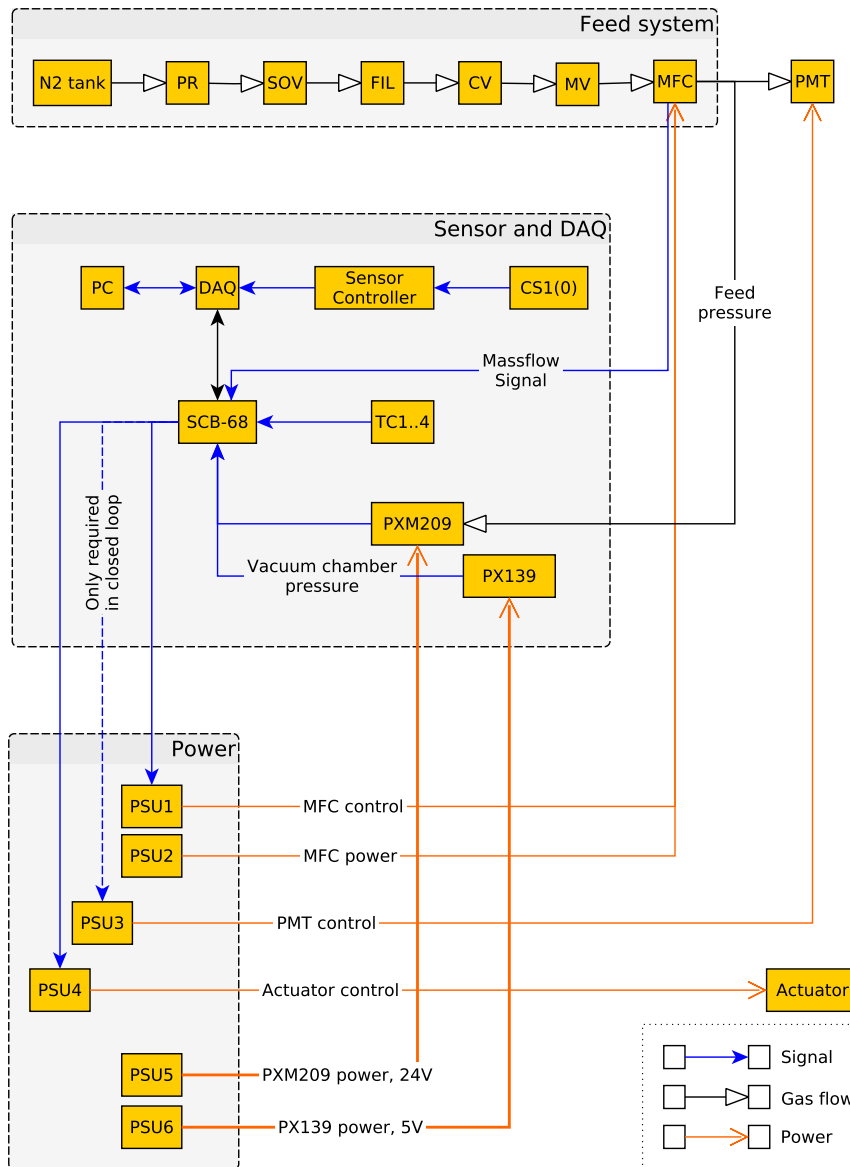


Figure 39: System overview of the complete measurement chain.

6.1.2.1 Feed system

The feed system consists of a chain of components that transfer the gas to the engine and modulate the pressure and mass flow. For these experiments N₂ gas of purity 5.0 is used as propellant. Using a manual pressure regulator the pressure is reduced to a maximum of 10 bar.

A Brooks Instrument 5850S Mass Flow Controller (MFC) is used in override mode as a sensor. In this mode, the orifice is completely opened ($\geq 100\%$) and does not limit the flow rate. As the MFC still measures and outputs a signal that is proportional to the mass flow rate, it is used as a mass flow sensor. The MFC is a Thermal Mass

The purity number represents the percentual fraction of named gas in the mixture. The first digit represents the number of nines in the percentage value and the decimal digit refers to the first number that differs from a nine. Purity 5.0 thus represents a purity of 99.9990%.

Flow controller and uses a differential temperature measurement and a heater that is located between the two temperature sensors [13]. When there is no flow, the heater heats the gas equally in both directions and no temperature difference is measured. A mass flow, however, will cause the heat to reach one temperature transducer sooner, resulting in a temperature difference that is proportional to mass flow. The Brooks 5850S has a full scale output of 144 mL_n/min. This n subscript refers to normal conditions, which are defined as a temperature of T_s = 273.15 K and a pressure of P_s = 1013.25 hPa. From the current output of the transducer of 4 mA to 20 mA that corresponds to a standard volume flow of 0 mL_n/min to 144 mL_n/min, the standard volume flow is calculated. The standard volume flow is converted into actual mass flow using

$$\dot{m} = \frac{P_s}{T_s} \dot{V} \frac{M}{R_u} \quad (71)$$

where \dot{m} is the mass flow in kg s⁻¹, \dot{V} is the standard volume flow in m³ s⁻¹, M is the molar mass in kg mol⁻¹ and R_u is the universal gas constant in J mol⁻¹ K⁻¹.

Up to the MFC the gas is fed through high pressure copper tubing with a 12.7 mm inner diameter. From the MFC, the flow is fed to the vacuum chamber through 6 mm inner diameter, reinforced low pressure hoses. The feed system is shown in Figure 40.

LABEL	DESCRIPTION	REMARKS
N2 tank	N ₂	Purity 5.0
PR	Kayser Pressure Regulator	Max. inlet pressure of 300 bar, max. outlet pressure of 10 bar.
SOV	Gachot V ₃ Shut-off Valve	—
FIL	Tecon G-series Type 01 Filter	Mounted vertically with filter pointing down.
CV	Tecon G-series Type 03 Check valve	Requires a minimum pressure difference of 0.7 bar.
MV	Unknown brand and type	—
MFC	Brooks 5850S Model BC1KA1BA0BA1B1	1 mL _n /min to 144 mL _n /min

Table 26: Used hardware components in the feed system.

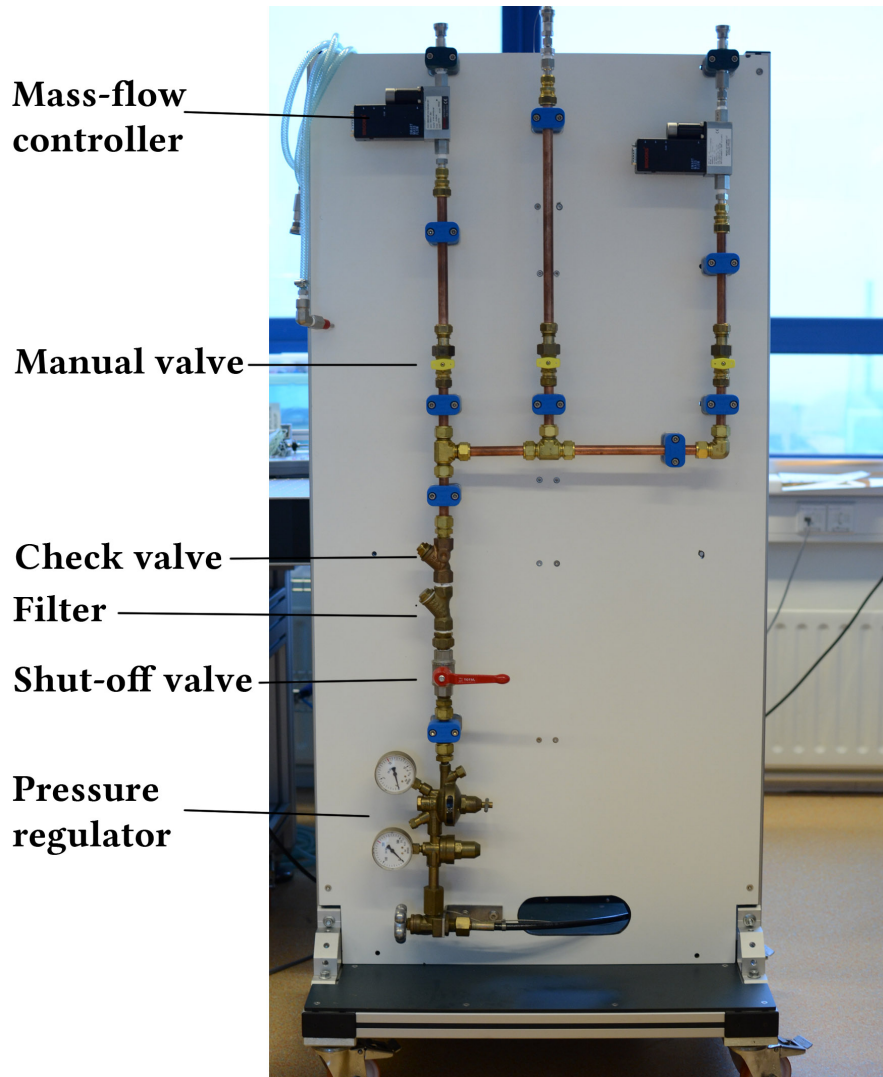


Figure 40: Photograph of the used feed system. Shown are the components up to the engine. Not shown are the vacuum transition and the low pressure tubing.

6.1.2.2 Power system

The power system is composed of six Delta-Elektronika power supplies that are used to power and control individual components. Two of the available power supplies can be controlled via analog programming. These two are connected to the DAQ via the SCB-68 insulated terminal. In case the PMT is used in closed loop actuation, a third power supply with analog programming is required. This is, however, not possible in the current setup as such power supply is not available.

LABEL	MODEL	RANGE	CV/CC	REMARKS
PSU1	ES030 – 5	≤ 30 V, ≤ 5 A	CV	To control the MFC via analog programming.
PSU2	ES030 – 10	≤ 30 V, ≤ 10 A	CV	To power the MFC at 24 V.
PSU3	ES030 – 10	≤ 30 V, ≤ 10 A	CC	To control the PMT manually.
PSU4	ES030 – 10	≤ 30 V, ≤ 10 A	CC	To control the actuator via analog programming.
PSU5	ES030 – 10	≤ 30 V, ≤ 10 A	CV	To power the PXM209.
PSU6	ES030 – 5	≤ 30 V, ≤ 10 A	CV	To power the PXM139.

Table 27: Used hardware components in the feed system. CV and CC refer to Controlled Voltage and Controlled Current, respectively.

6.1.2.3 Sensors and Data Acquisition

During the measurements in total seven sensors are used: i) four K-type thermocouples to monitor the temperature gradient on the pendulum arm (two locations), the temperature of the coil holder and the temperature of sensor holder; ii) two pressure transducers to measure the feed pressure and vacuum chamber pressure and iii) the capacitive displacement sensor.

Two thermocouples are clamped to the pendulum arm using hose clamps. One is mounted under the sensor target, close to the engine bracket, while the other one is mounted close to the bottom side of the cross-beam. When the separation distance is known, the effect of thermal gradients can be determined. The temperature of the sensor head is determined by measuring the temperature of the sensor holder. It is herein assumed that both are in thermal equilibrium and attain the same temperature. Lastly, the temperature of the coil holder is measured. Changing temperatures of the coil holder will cause it to shrink or expand, changing the coil geometry. Measuring how the temperatures vary over time helps identifying sources of thrust signal drift and determine the overall accuracy of the measurements.

The feed pressure is measured at the vacuum transition of the feed system using an Omega Engineering PXM209 pressure transducer. With a total range of 0 bar to 6 bar it covers the range of required feed pressures of 1 bar to 2 bar. The pressure in the vacuum chamber is measured using the Omega Engineering PX139 sensor. It measures absolute pressures from 0 bar to 2 bar. The vacuum pressure can also

be monitored using a gauge on the vacuum chamber, but this is no longer accurate below 200 mbar absolute pressure.

A new vacuum transition is manufactured for the thermocouples and the PX139 pressure transducer, as no dedicated transition exists. Photos of the new vacuum transition are given in [Figure 41](#). The vacuum transition is made of a flange that fits on an already available vacuum transition that is available for experiments. The flange has three holes: one $M10 \times 0.75$ hole in the center for the vacuum transition of the sensor cable and two $1/4$ " holes for two hoses. The hoses have a $1/8$ " inner diameter and are used to guide either four thermocouples or allow the use of the PX139 absolute pressure transducer as visible in the photos.



Figure 41: Photos of the vacuum transition flange.

6.1.2.4 Calibration Actuator and Precision Scale

The calibration actuator is a VTDC based actuator and is described in [Section 5.3](#). The actuator is calibrated by measuring the force exerted on a permanent magnet that rests on a Mettler Toledo AG245 precision scale. The calibration procedure is detailed in [Section 6.2.1](#).

6.1.2.5 Vacuum chamber and pump

The thrust stand, the engine, the sensor head, the thermocouples and the actuator are placed in a medium vacuum of ≈ 6 mbar of the Heraeus Vacutherm vacuum oven. The vacuum is created by a Vacuubrand MD-1 diaphragm pump with an ultimate absolute vacuum capacity of 1.5 mbar. The pressure is depicted as a function of time in [Figure 42](#). After 60 minutes the pressure has dropped to approximately 6 mbar. Once the pump is switched off, the tank will slowly fill again due to leaks at a rate of approximately $0.06 \text{ mbar min}^{-1}$ as depicted in [Figure 43](#).

In this characterization, the pressure in the vacuum tank is measured using the Omega Engineering PXM209-006A10V pressure transducer. At the moment of measurement, the calibration is overdue and no calibration data are available. A sensitivity of 600 mbar V^{-1} is assumed

in accordance with the typical values listed in the datasheet [65]. At ambient pressure, a pressure is read out that is higher than the ambient pressure measured by the Koninklijk Nederlands Meteorologisch Instituut / Royal Netherlands Meteorological Institute (KNMI) by approximately 23 mbar at the time of measurement. The data are corrected for this offset. Note that not the ambient pressure of the clean room is used, but that measured outside the building. This is admissible, because the clean room is only at an overpressure of approximately 15 Pa \approx 0.15 mbar [83].

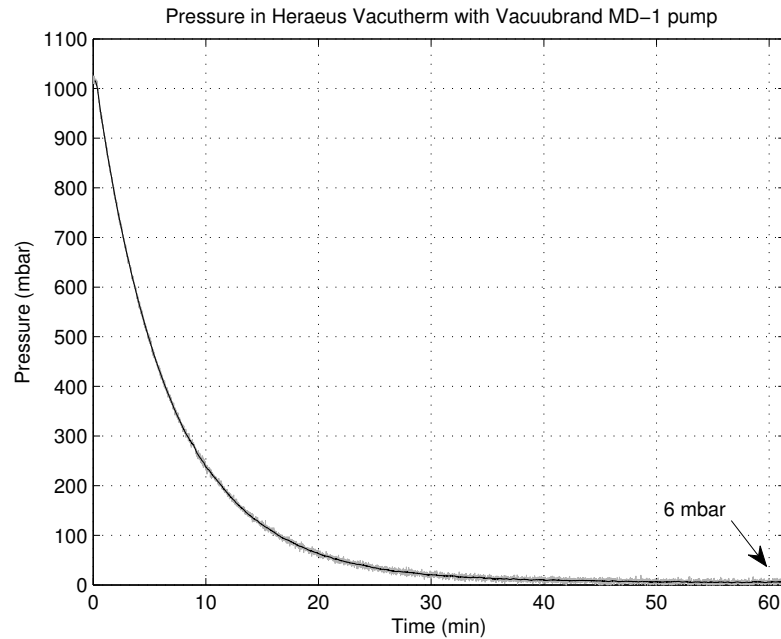


Figure 42: Vacuum pumping pressure characteristic. Measurement data offset to correct for atmospheric pressure of 1017 mbar.

6.1.2.6 Overview of relevant hardware specifications

An overview of the relevant hardware specifications is given in [Table 28](#).

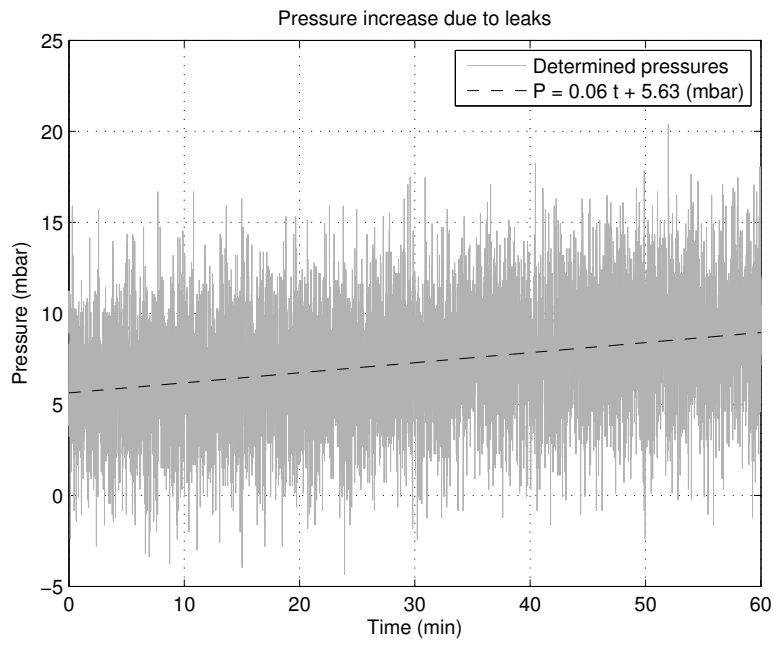


Figure 43: Vacuum pressure leak characteristic. Measurement data offset to correct for atmospheric pressure of 1017 mbar.

PRODUCT	RANGE	ACCURACY	WARM-UP	LAST CALIB.	REMARKS
Brooks Instrument 5850S BC1KA1BA0BA1B1	0 mL _n /min to 144 mL _n /min	0.7% of rate +0.2% of F.S.	45 min	27 Sept, 2007	Recalibration costs 175 €
Kayser Pressure regulator	0bar to 10bar	-	-	-	Manual
Delta-Elektronika ES030 – 5	≤ 30 V, ≤ 5 A	CV: 0.6 mV rms, 10 mV point to point; CC: 0.5 mA rms, 2 mA point to point	60 min	Unknown	One programmable PSU is available.
Delta-Elektronika ES030 – 10	≤ 30 V, ≤ 10 A	CV: 5 mV rms, 15 mV point to point; CC: 6 mA rms, 15 mA point to point	60 min	Unknown	One programmable PSU is available.
K-type thermocouples	–75 °C to 260 °C	Depends on SCB-68 and PXI6229 DAQ.	-	17-11-2004	Calibration of PXI6229 costs 174 € - 350 € [61].
Omega Engineering PX139-030A4V	0 PSIA to 30 PSIA 0 barA to 2 barA	≈ 0.5% of F.S.	30 min ¹	Unknown	Absolute pressures. Based on imperial units. Calibration costs 100 € excl. shipping.
Omega Engineering PXM209-006A10V	0bar to 6 bar	1.5% of F.S.	30 min ¹	Unknown	Absolute pressures. Based on metric units. Calibration costs 100 € excl. shipping.
Micro Epsilon capaNCDT system	0 mm to 1 mm (CS1), 0 mm to 10 mm (CS1)	Section 4.1.2	10 min	Unknown	-
Mettler Toledo AG245	TBD	TBD	30 min	27-05-2009	Not accurate enough for calibration in the 1 µN to 10 µN range.
FLUKE 175	0.01 mA to 10.00 A	1.0% + 3 counts	–	Never ²	Recalibration costs 66.10 € + 25 € Shipping and handling fee
SensorTechnics 144SC0811BARO	800 mbar to 1100 mbar	±0.05% F.S.	Unknown	Unknown	Calibration costs 16 € per point, excl. VAT and shipping.

Table 28: Overview of relevant hardware components. ¹: Estimate provided by Omega Engineering. ²: Provided by FLUKE.

6.1.3 Tested hardware

In this campaign, the TB-5m thrust stand is verified and validated. Towards this goal, the Bradford Engineering PMT is installed in the setup and used for hardware-in-the-loop validation. The engine uses proportional mass flow regulation with a remote nozzle to create thrust [45]. The throat diameter is $\approx 110 \mu\text{m}$ [46]. The proportional valve inside uses a voice-coil inspired design. A solenoid and spring are used to open and close the valve. The valve circuit is controlled by either current or voltage control and has a resistance of $\approx 90 \Omega$ without a preferential direction. It is advised to limit the electric current to 140 mA and to limit the inlet pressure to 7 bar [46].

The temperature of the engine can vary up to 10 K between cold and hot states [45]. Also the magnetic field of the engine can interact with the environment or the setup. This has to be checked and corrected for, e.g. by installing magnetic shielding around the engine. Lastly, one should take into account the shift in the CoG when the engine is actuated. This will influence the pendulum equilibrium position.

For validation purposes, the results of tests conducted at the thrust measurement facilities of ONERA [45, 44] and ESA ESTEC [88] are made available under limited distribution. The results of this test campaign are compared to the results obtained in these prior tests. At ESTEC a 100 μm and a 200 μm throat were tested with mass flows up to $1.5 \text{ mg s}^{-1} \text{ N}_2$. This resulted in a thrust of approximately 1100 μN . At ONERA tests were conducted using the 200 μm throat with mass flows between approximately 0.01 mg s^{-1} to 0.20 mg s^{-1} which resulted in thrust levels between 4 μN to 110 μN . In both cases the inlet pressure was approximately 1 barA.

6.2 TEST SEQUENCE AND DESCRIPTION

In this section, the performed tests are listed and discussed. Every test is labeled with an identifier as listed below. This allows for quick referencing of test procedures that need to be repeated. In the following sections all test procedures are discussed. The procedures are written as an operation manual with future users in mind. This means that some parts are repeated several times. General readers are advised to read the introductions of each test and to skip the enumeration of steps. If any additional equipment or software is required, this is noted explicitly. In all other cases, the equipment discussed in Section 6.1 is used without further explanation. Unless noted otherwise, the LabVIEW Virtual Instrument (VI) and the corresponding data-processing scripts of each test can be found in their respective folders of 'DISC/Experiments/TEST-XXX/YYY', where YYY refers to the identifying number. The tests are labeled and structured as follows.

- TEST-100 Actuator calibration
 - TEST-110 Force-current calibration
 - TEST-120 Impulse calibration
- TEST-200 Feed-system leak tests
- TEST-300 Characterization
 - TEST-310 of environmentally induced noise
 - TEST-320 of feed system positioning
 - TEST-330 of pendulum properties
 - TEST-331 Natural frequency and damping ratio
 - TEST-332 Dynamic attenuation
- TEST-400 Hardware-in-the-loop validation
 - TEST-410 Pendulum characterization
 - TEST-411 Sensitivity
 - TEST-412 Drift
 - TEST-420 Characterization of the effect of the magnetic field of the [PMT](#)
 - TEST-421 Pendulum is fixed
 - TEST-422 Pendulum is free to move
 - TEST-430 Characterization of the effect of the [CoG](#) shift in [PMT](#)
 - TEST-440 Characterization of the effect of changing vacuum pressure
 - TEST-450 Steady-state thrust validation
 - TEST-460 Impulse bit validation
 - TEST-461 Thrust stand calibration for impulse bits
 - TEST-462 Impulse bit measurements

6.2.1 TEST-110: Force-current calibration

As described in [Section 5.3.4](#), the actuator consists of a [VTDC](#) and three sets of small magnets, each set with a specific magnetic dipole that is tuned for a specific thrust range. The actuator force is calibrated as a function of applied electric current and the chosen magnet set. The force is traceable to a national standard by calibrating it against a Mettler Toledo AG245 precision scale. The scale itself is calibrated using calibrated masses that can eventually be traced back to a national standard.

6.2.1.1 Required equipment

The required hardware is listed in [Table 29](#). A custom stand is used to mount the [VTDC](#) in a vertical position above the scale. The stand is displayed on the left in [Figure 44](#).

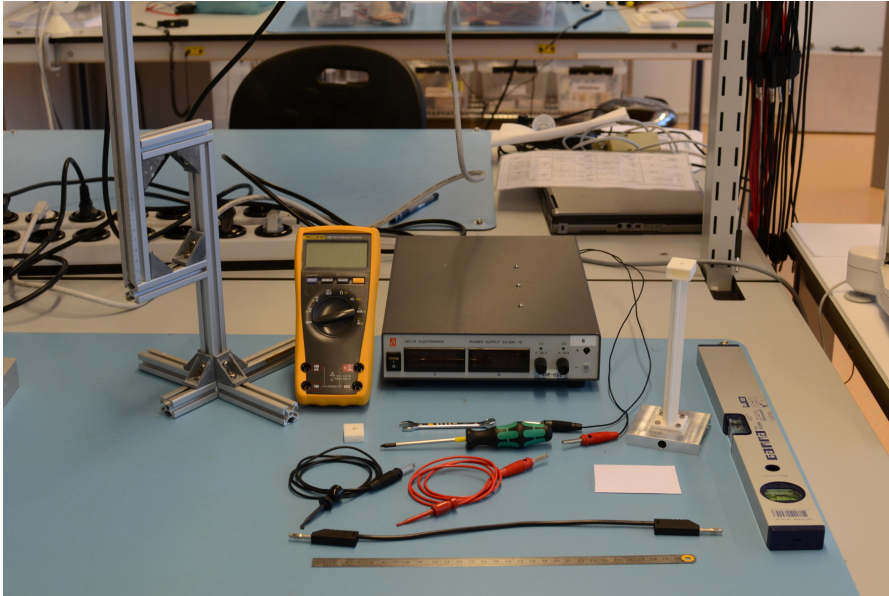


Figure 44: Required hardware for TEST-110. [VTDC](#) is not shown. From left to right, top to bottom: actuator stand, multimeter, PSU, magnet holder, combination wrench and screwdriver, calibration arm mounted on the sensor target, spirit level, black and red crocodile clamped wire, piece of folded paper, quick release wire and ruler.

6.2.1.2 Procedure

1. Gather the required equipment, listed in [Table 29](#).
2. Prepare the scale
 - a) Remove the draft shield of the Mettler Toledo AG245 following the steps described in the maintenance manual of the scale Mettler-Toledo [52, p. 64-66].
 - b) Level the scale. Level is checked using the spirit level on the right aft of the scale.
 - c) Plug the power cable into the power socket and switch on the scale. Allow it to self-calibrate and to warm up. Warm-up time is **30 minutes**.
3. Prepare the [PSU](#)
 - a) Place the Delta-Elektronika ES030 – 10 next to the scale and connect it to the power socket.
 - b) Check on the back of the [PSU](#) that the switches for I and V are both switched to M(annual).

PRODUCT	NO.	REMARKS
High precision scale	1	Mettler Toledo AG245 with draft shields removed.
Actuator VTDC	1	—
Actuator stand	1	Custom stand to hold the VTDC in a vertical position above the scale.
Magnets in holders	3	Three sets are available.
Actuator arm mounted on the sensor target	1	The sensor target allows for easy stabilization of the actuator arm on the scale.
Multimeter	1	In series with the coil, DC current mode.
Delta-Elektronika ES030 — 10	1	Set to CC mode.
Electric wire with male banana connector, black	1	Used to connect the multimeter to the PSU.
Spirit level	1	—
Ruler	1	Accuracy of ≤ 0.5 mm.
Sturdy piece of paper	1	For easy reading of the ruler.
Torx TX10 screwdriver	1	To fasten the sensor target back the to pendulum.

Table 29: TEST-110 required equipment.

- c) Switch on the PSU and turn the potentiometer that controls the voltage clockwise until it can be turned no further. Make sure the potentiometer that controls the current is completely turned anti-clockwise until it can be turned no further. The light 'CC' should turn green.
 - d) Allow the PSU to warm up. Warm-up time is **60 minutes**.
4. Slide the required magnet holder in the calibration arm, until it can no longer move (Figure 46a). Note the orientation of the magnet in the holder. Reversing this orientation in later tests results in a sign reversal of the force vector.
 5. Place the arm on the weighing pan of the scale. Only for the $1 \mu\text{N}$ to $45 \mu\text{N}$ range, the calibration arm is removed from the sensor target. In all other cases the sensor target remains attached.
 6. Mount the VTDC on the custom stand.

- a) Mount the VTDC vertically on the custom stand. The side with the highest turn-density has to point upward.
 - b) Align the bottom side of the bracket with the 1 cm mark on the stand.
 - c) Tighten the two mounting bolts loosely.
 - d) Check if the engagement distance is correct (Figure 46b).
 - i. Place the ruler on the cross that is visible on top of the calibration arm.
 - ii. Lay a piece of paper over the opening of the VTDC and align it with the ruler.
 - iii. Read off the ruler.
 - iv. Remove the ruler.
 - e) Re-adjust the engagement distance as necessary and fasten the bolts.
7. Move the stand such that the alignment cross (visible on top of the calibration arm) is at the center line of the coil. This is done visually (Figure 46c).
 8. Place a spirit level on top of the coil to check if it is vertical (Figure 46d). Adjust the stand alignment accordingly by using pieces of paper under the legs of the stand.
 9. Connect the wires (diagram in Figure 45)
 - a) Connect the red wire to the '+' of the PSU and connect it to the flying lead of the bottom side of the VTDC.
 - b) Connect the black wire to the flying lead of the top side of the VTDC. Plug it into the '+' port of the multimeter.
 - c) Connect a second black wire to the '-' port on the multimeter and connect it to the '-' port on the PSU.
 - d) Make sure that the flying leads are perpendicular to the axis of the coil (Figure 46e). This minimizes the influence from the magnetic field around the flying leads on the field inside the coil.
 10. Tare the scale once the warm-up time has passed. Allow the scale to self-calibrate and stabilize.
 11. Switch on the multimeter and set it to DC current measuring mode. On the FLUKE 175 one switches between AC and DC mode by pressing the blue button in the top right corner.
 12. Take calibration measurements.
 - a) Use the potentiometer that controls the current to set the required level. Make sure the light 'CC' remains green.

- b) Read off the set current from the multimeter.
 - c) The reading on the scale changes due to the changed current. Allow the reading to stabilize.
 - d) Once the reading has stabilized, write down the mass reading and the current.
 - e) Repeat the last four steps until the desired maximum current is reached. It is advised to keep the current ≤ 10 A to avoid excessive heating of the coil wire or coil holder.
13. After calibration with one magnet set, dial the current back to zero. Replace the magnet holder and repeat the steps for alignment of the coil. As long as the devices are not unplugged from their power supplies or switched off completely, the warm-up times can be ignored. The devices can be considered to be in thermal equilibrium in that case. The accuracy of the power supply is guaranteed up to eight hours of operation after it has warmed up.
 14. When calibration has completely finished, switch off the PSU. Disconnect all wires and remove the coil from its stand. It can now be installed in the thrust stand setup and other tests can be performed.

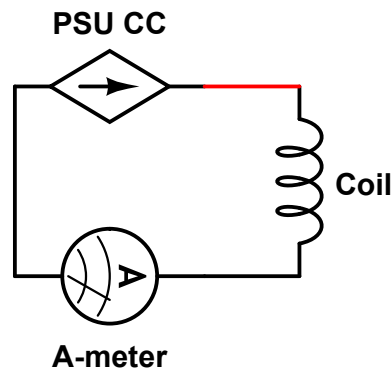


Figure 45: Electrical circuit diagram for TEST-110. Color of used wires has been indicated in diagram. Power supply is set in current control (CC) mode.

6.2.1.3 Data-processing

The measurement data need to be processed before the results can be used. In this section, the required data-processing is outlined.

1. Tabulate the obtained data in two columns: electric current and measured mass.
2. Convert the current reading to the correct units of A where necessary. Convert the mass readings to the correct units of kg.

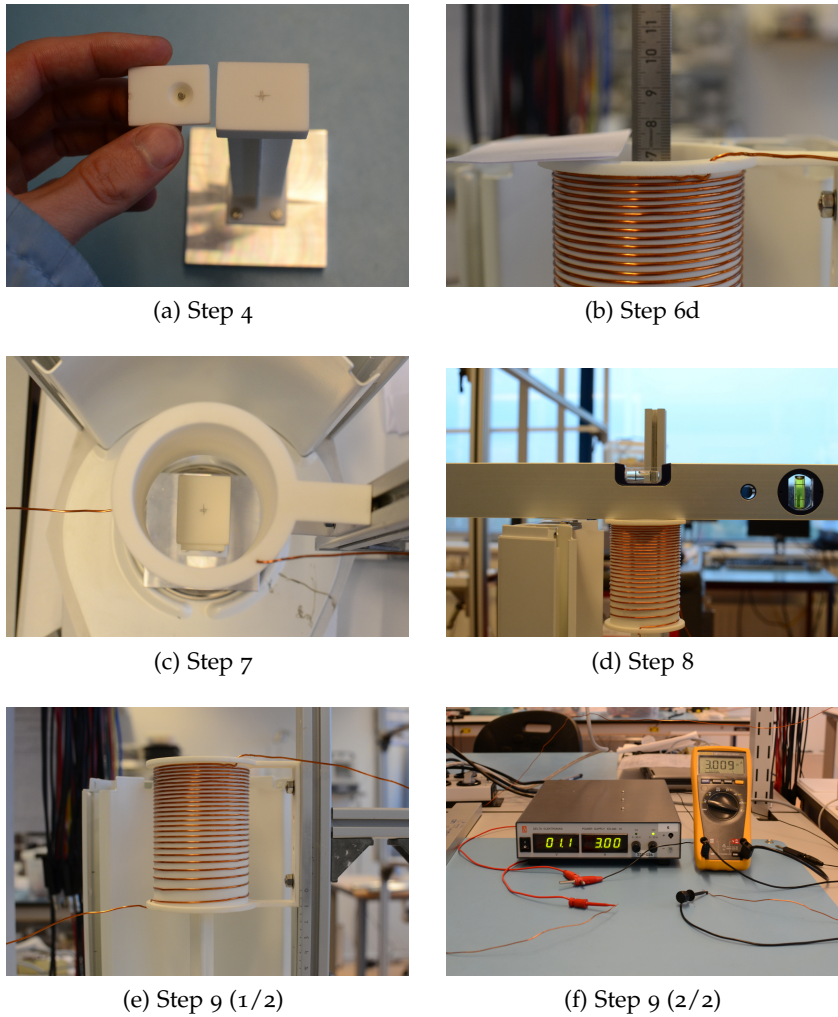


Figure 46: Photos of TEST-110 procedure.

3. Calculate the force that has been exerted on the calibration arm in N by multiplying the measured mass by the gravitational acceleration, $g = 9.80665 \text{ m s}^{-2}$.
4. Use a linear least squares procedure to fit a linear function of the form $F = ai$ to the data. Use the current as independent variable and the calculated force as dependent variable.
5. Calculate the Coefficient of Determination or R^2 to quantify the quality of the fit ([Section E.6](#)).
6. Calculate the standard deviation of the residuals of the measurement data with respect to the fit.
7. Check for the following rules-of-thumb:
 - a) The coefficient of determination is ≥ 0.9990 . This confirms the fit is indeed linear.

- b) The triplex of the standard deviation of the residuals is smaller than the allowed accuracy of the calibration force.
8. If the conditions are met, the coil is calibrated and the applied force F can be calculated as a function of electric current i using the found linear function $F = ai$ with the force in N, the current i in A and the sensitivity a in N A^{-1} .

6.2.2 TEST-120: Impulse calibration

Impulse bits are generated using the calibration coil. By sending a current pulse through the coil, a pulsed force will be exerted on the suspended dipole of the actuator. The magnitude of the force is known as a function of current through calibration as explained in [Section 6.2.1](#).

6.2.2.1 Calibration method

A pulse is generated using a Delta-Elektronica ES030 – 10 PSU that is controlled via the DAQ. The coil can be modeled as an inductor with internal resistance [77] as depicted in [Figure 47](#). When a current is applied, the inductor opposes the current by creating a potential over itself. The current through the system can be given in the Laplace domain as a function of the voltage over the resistor R in Ω and the inductance L in H as

$$i(s) = \frac{U_{\text{meter}}(s)}{R + L_c s} \quad (72)$$

In the time domain this transforms back into

$$i(t) = \frac{1}{L} \int_0^t U(\tau) \exp\left(-\frac{R}{L}(t-\tau)\right) d\tau \quad (73)$$

The inductance of the VTDC is not easily calculated, but is estimated by comparison with a solenoid of equal dimensions and turns. The inductance for a normal, air-filled solenoid is estimated using [77]:

$$L_c = \frac{\mu_0 A_{\text{coil}} N^2}{L_{\text{coil}}} = \frac{\mu_0 \pi D_{\text{coil}}^2 N^2}{4 L_{\text{coil}}} \quad (74)$$

where L_c is the inductance in H, μ_0 the vacuum permeability in $\text{Vs A}^{-1} \text{m}^{-1}$, A_{coil} the cross-sectional area in m^2 , N the number of turns, L_{coil} the solenoid length in m and D the solenoid diameter in m. With a length of 8.4 cm, a diameter of 6.0 cm and 25.36 turns, the inductance is

$$L_c = \frac{4\pi \cdot 10^{-7} \cdot \pi \cdot 0.060^2 \cdot 25.36^2}{4 \cdot 0.084} = 2.72 \cdot 10^{-5} \text{ H} = 27.2 \text{ } \mu\text{H}$$

The resistance of the coil has been measured to be $(0.3 \pm 0.1) \Omega$ using a FLUKE 175 multimeter. The response of such a system to a voltage

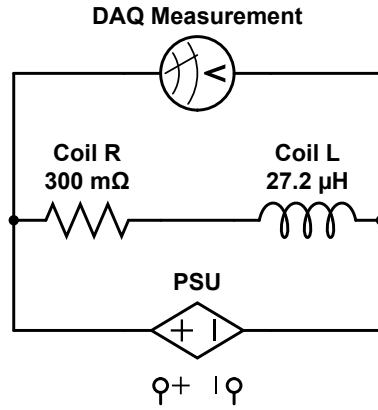


Figure 47: Resistor-Inductor (RL circuit) representation of the actuator coil.

step of 10 ms and 3.5 ms is depicted in [Figure 48](#). As can be seen in the figure, the circuit responds rapidly and only needs approximately 0.5 ms to reach a stable state. When the voltage is measured over the coil, the current through the coil can be approximated by

$$i(t) \approx \frac{U(t)}{R} \quad (75)$$

A more accurate approximation of the current can be obtained by applying the transfer function (72) to the obtained data. The transfer function can be applied to the discrete measurement points via MATLAB's `tf()` and `lsim()` functions, for example. The applied force is calculated from calibration of force as a function of electric current (TEST-110). The delivered impulse is found by integration of the force over time.

$$I_{\text{bit}} = \int_{\text{pulse}} \frac{\partial F}{\partial i} i(t) dt \quad (76)$$

The uncertainty of the calculated impulse bit is calculated based on the current calculated using (75). The effect of the inductance is small and neglected in this uncertainty estimation because the uncertainties introduced by the black box function that is used to apply the transfer function of (72) to the data are unknown. The force applied by the actuator is found via

$$F = \frac{\partial F}{\partial i} i \approx S \frac{U}{R} \quad (77)$$

For every instant in time, the uncertainty in the applied force can then be derived based on this equation:

$$\Delta F = \left| \frac{\partial F}{\partial S} \right| \Delta S + \left| \frac{\partial F}{\partial U} \right| \Delta U + \left| \frac{\partial F}{\partial R} \right| \Delta R \quad (78)$$

After working out the partial derivatives this is rewritten as

$$\Delta F = \frac{U}{R} \Delta S + |S| \left(\frac{\Delta U}{R} + \frac{U \Delta R}{R^2} \right) \quad (79)$$

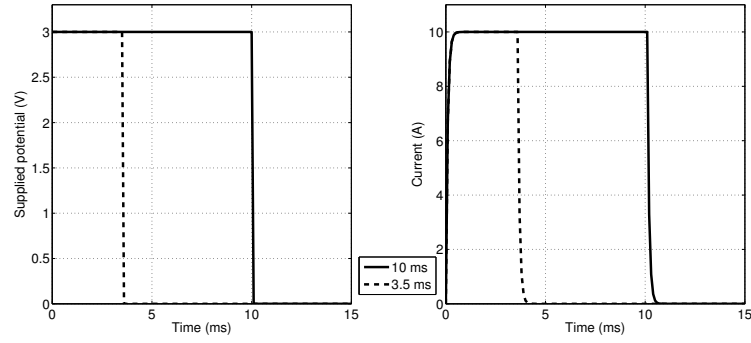


Figure 48: Coil response to a step input. The coil is represented as a resistor and inductor in series (RL circuit) of 0.3Ω and $27.2 \mu\text{H}$, respectively. The modeled voltage input is presented on the left and modeled current in the coil on the right. The PSU voltage is modeled as an ideal step function.

The uncertainty in the total delivered impulse is found through numerical integration of the uncertainty of force as a function of time:

$$\Delta I_{\text{bit}} = \int_{\text{pulse}} \Delta F(t) dt \quad (80)$$

When the coil is installed in the setup and a current pulse is generated, the magnet will exert a force on the suspended dipole, causing it to move. The motion of the dipole causes a local change in magnetic flux that induces an electromotive force over the coil, opposing the current that causes the flux change. The induced electromotive force is given by Faraday's law [26]:

$$\oint \mathbf{E} \cdot d\mathbf{L} = -\frac{d\Phi}{dt} \quad (81)$$

where \mathbf{E} is the induced electric field around the coil, $d\mathbf{L}$ is a infinitesimally small wire element and Φ is the flux density. However, the complex magnetic field around the dipole and the varying turn-density of the coil make this effect hard to model. The effect is therefore studied by comparison of measured voltages over the coil with a pulsed current in- and outside the setup.

6.2.2.2 Required equipment

This test is split into two series. In the first series, only the VTDC, the DAQ, the CB-68LP terminal block and corresponding cable and the Delta-Elektronika ES300-10 are used. In this series, the electrical response of the coil is measured independent of the magnet. For the second series, also the considered magnet, the thrust stand pendulum

with the engine mounted, the sensor target and calibration arm are needed. In the second series, the thrust stand is set up as it would be for thrust measurements with the used engine. The magnet is placed in the calibration arm and suspended in the required location of the VTDC. The response of the entire electrical actuator is now measured.

The CP-68LP terminal block is used to connect the VTDC and the PSU to the input and output pins of the DAQ. It is wired as depicted in the circuit diagram of Figure 49. As can be seen in the figure, two inputs are measured. The voltage over the coil is measured, but also the voltage delivered by the DAQ on its output pins.

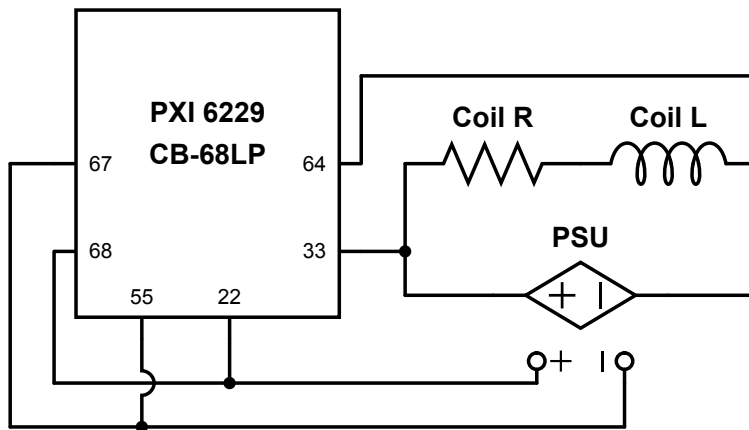


Figure 49: Circuit diagram for TEST-120. Pin numbering: (22, AO0); (55, AOGND); (68, AI0); (67, AIGND); (33, AI1); (64, AIGND).

Because the used power supply has the minus probe of the output and the minus pin of the control signal internally connected, two ground loops exist. Ground loops can introduce interference by picking up electromagnetic radiation as an antenna and by modulating the signal. Tests have shown that the effect in this case is an increased gain between control voltage and output voltage. The effective gain increases from the expected 6 V V^{-1} to a gain of 11 V V^{-1} .

When the ground loops are approximated as resonant loop antennas, the resonant frequency can be calculated. Antenna theory [4] states, that a resonant loop antenna resonates at a wavelength equal or close to its perimeter. The corresponding resonant frequency is calculated using

$$f = \frac{c}{\lambda} = \frac{c}{\pi D_{\text{ant}}} \quad (82)$$

where f is the frequency in Hz, c the speed of light in m s^{-1} , λ the wavelength in m and D_{ant} the diameter of the loop in m. For a loop with a diameter of a few centimeters to a few meters this results in a resonant frequency of MHz to GHz. As the pulsed signals have a period in the order of kHz, the interference is considered negligible.

PRODUCT	NO.	REMARKS
Actuator VTDC	1	—
Magnets in holders	3	Three sets are available.
Thrust stand	1	Assumed to be assembled for the chosen engine or dummy mass. No feed system connected.
Engine or dummy mass	1	Engine bracket assumed included.
Delta-Elektronika ES030 – 10	1	Set to VC mode.
Electric wires with crocodile clamps	2	One black, one red. Used to connect the coil to the PSU.
Spirit level	1	—
Ruler	1	Accuracy of ≤ 0.5 mm.
Sturdy piece of paper	1	For easy reading of the ruler.
(Combination) wrench, M8	1	To fasten the bolts that fix the VTDC to the frame.
Torx TX10 screwdriver	1	To fasten the sensor target back the to pendulum.
National Instruments PXI-6229 DAQ	1	Installed in PXI system in clean room.
National Instruments CL-68LP unshielded terminal block	1	Wired as depicted in Figure 49.
National Instruments data cable	1	Used to connect the CL-68LP to the DAQ.

Table 30: TEST-120 required equipment.

6.2.2.3 Procedure

Series I: Electric response of coil

1. Perform TEST-110. The resulting sensitivity $\frac{\partial F}{\partial i}$ is required to calculate the impulse from the current in the coil as a function of time.
2. Prepare the setup.
 - a) Mount the VTDC on the actuator mount in horizontal position.

- b) Connect the coil to the PSU using crocodile clamps. Make sure the side with the lowest turn density is connected to the positive output of the PSU.
 - c) Plug the D-sub connector (labeled VC) that is connected to the terminal block in the D-sub female connector on the back of the PSU. Make sure the switches on the back of the PSU are set to: V → P(rogramming), I → M(annual).
 - d) Connect the terminal block to the PCI / PXI 6229 DAQ port 0.
 - e) Switch on the DAQ. Once this has booted, switch on the PC and PSU. Log on to the computer when required and allow the components to warm up. The warm-up time is **60 minutes**.
3. Run LabView program TEST120.vi
- a) Open LabView on the lab PC and load program 'TEST120.vi'.
 - b) Start the VI. Use the opened dialog to indicate where the measurement file is saved.
 - c) Check if all hardware is connected correctly.
 - d) If the warm-up time has expired, run the program. Pulses of 10 ms length and increasing magnitude are now generated at 20 ms interval. Each pulse train takes 400 ms and is complemented with a 600 ms break after which the pattern is repeated until the VI is stopped. The program automatically saves the measurements in a measurement file. The output voltage of the DAQ that is used to control the PSU as well as the voltage over the coil are measured. The signal is sampled and generated at a rate of 10 kHz.

The required Labview and Matlab programs are located in /experiments/TESTS-XXX/120/.

Series II: Electric response of coil and moving magnet

1. Change the setup to include the pendulum and engine.
 - a) Assemble the thrust stand and mount the engine as dummy mass. Follow the procedures of Section 6.3. The feed system and power systems are not required within the scope of this test.
 - b) Slide the magnet holder that was also used for actuator calibration (TEST-110) in the calibration arm.
 - c) Align the cross (visible on top of the calibration arm) at the center line of the coil. This is done visually (Figure 46c).
 - d) Check if the engagement distance is correct (Figure 46b).
 - i. Place the ruler on the cross that is visible on top of the calibration arm.

- ii. Lay a piece of paper over the opening of the VTDC and align it with the ruler.
 - iii. Read off the ruler.
 - iv. Remove the ruler.
 - e) Re-adjust the engagement distance as necessary by moving the actuator stand or by moving the actuator coil on the stand and fasten the bolts accordingly.
 - f) Place a spirit level on top of the coil to check if it is horizontal (Figure 46d). Adjust the stand alignment accordingly by using pieces of paper under the legs of the actuator stand.
2. Adjust the settings of the VI and change the location where the measurement file is saved.
 3. If the DAQ or PSU have been switched off in the meantime, switch them on and allow them to reach thermal equilibrium again. The warm-up time is **60 minutes**. If the warm-up time has expired, run the VI. Pulses of increasing magnitude are now generated at the set interval. The program automatically saves the measurements in a measurement file and performs initial data-processing. Both raw and pre-processed data are stored.
 4. Once the test has ended, switch off the PSU and disconnect the terminal block from the DAQ.
 5. Disconnect all components and clear the workspace.

6.2.2.4 Data-processing

The current through the coil is calculated from the measured voltage over the coil, using the transfer function (72). The current is multiplied by the actuator sensitivity S_F in N A^{-1} , obtained in TEST-110, to calculate the applied force. Using numerical integration, the integral of the applied force is evaluated numerically using Simpson's rule to arrive at the impulse bit.

1. Load the measurement data into Matlab program 'TEST120.m' and change the variable 'file' to point the program to the desired measurement file.
2. Run the program. The measurement file is read and the measured voltages and timestamps are loaded. The electric current is calculated by applying (72) to the measured voltages or using the approximation of (75). The impulse bits are calculated using numerical integration of (76) and Simpson's rule: $I_{\text{bit}} \approx \sum_{i=1}^n \frac{\partial F}{\partial i} i(t) \Delta t$. The uncertainty of the calculated impulse bit is determined using (79) and (80).
3. Print/Save the results.

6.2.3 TEST-200: Feed system leak test

Assembly of the feed system does not guarantee a leak-tight setup. A leak test has to be performed to localize any leaks and quantify the leak rates. The leak tests are performed following the methods of Zandbergen [90]. Parts of the system are pressurized and different methods are employed to trace leaks. The feed system is compartmentalized by means of various shut-off valves. The total system is tested for leaks by means of a long duration pressure measurement. A pressure drop indicates a leak in the feed system. The separate compartments are tested for leaks by means of a bubble test and audible indications of gas leaks.

6.2.3.1 Required equipment

The required hardware is listed in Table 31. The PSU, DAQ and pressure transducer are connected as represented schematically in Figure 50.

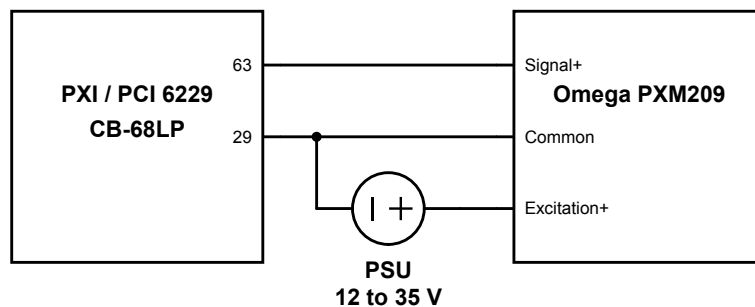


Figure 50: Circuit diagram for TEST-200. Pin numbering: (63, AI11); (29, AI GND). The wires connected to the transducer are color labeled: excitation+ (red), signal+ (white) and common (yellow).

6.2.3.2 Procedure

1. Connect the feed system as explained in Section 6.3.4. Leave all shut-off valves in their closed position.
2. If no audible hiss is present, perform a bubble test on the pressurized part.
 - a) Apply the soapy solution on the fittings and transitions.
 - b) Wait for 10 minutes.
 - i. If no bubbles have appeared, clean the soaped spots with a dry, clean cloth. Close and depressurize the feed system according to the steps of Section 6.3.4.3.
 - ii. In case bubbles have appeared, close the feed system according to the steps of Section 6.3.4.3 and evacuate the remaining gas. Repair the leak accordingly.

PRODUCT	NO.	REMARKS
Cylinder of propellant	1	For the PMT , 10 L cylinder 5.0 purity N ₂ .
Gas distribution system	1	Pre-installed system in the clean room.
Low pressure hoses (outside)	1	Available with gas distribution system, for transfer from distribution to vacuum chamber.
Low pressure hoses (inside)	1	For connection from vacuum feed through to engine.
Soapy solution	1	Griffon Gaslek Zoeker (Spray-on solution).
Thruster and/or end shut-off valve.	1	Used to shut off the end of the feed system.
Omega PXM209	1	Connected to the vacuum transition. Used to measure the feed pressure changes.
PXI 6229 and CB-68LP	1	Data acquisition system that is connected to the PXM209.
Delta Elektronika ES030 – 1	1	Analog PSU , used to power the PXM209.
Heraeus Vacuotherm	1	Vacuum chamber.
Vacuubrand MD-1	1	Vacuum pump.

Table 31: TEST-200 required equipment.

3. If the main feed system is leak tight, connect the flexible low pressure hoses from the main feed system to the vacuum transition.
4. Connect the low pressure hoses on the inside of the vacuum chamber to the vacuum transition. Apply vinyl tape to the thread.
5. Connect the engine to the low pressure hose. Use vinyl tape to seal the connection.
6. Connect the Omega PXM209 sensor to [DAQ](#) by wiring it to the terminal board. The pins are connected according to [Figure 50](#).
7. Depressurize the vacuum chamber by starting the vacuum pump. Wait **60 minutes** for the chamber to reach an operating pressure of ≤ 10 mbar.

8. Pressurize the feed system. Open the shut-off valves one by one.
9. Start VI 'TEST200.vi' and monitor the pressure in the feed system over time. If no pressure drop occurs, the feed system is leak tight. If the pressure drops, the leak is likely located near the vacuum transition, or the last part of the feed line. Perform a bubble test when possible. Note: The PMT may not externally be exposed to fluids.
10. Stop the VI and save the measurement file.
11. Close the feed system according to the steps of Section 6.3.4.3.
12. Repressurize the vacuum chamber.

6.2.3.3 Data-processing

1. Open Matlab program TEST200.m and change variable 'filen' to point to the location of the measurement file.
2. Run the program. It converts the measured voltages to pressures by multiplying it by the sensor sensitivity of 600 mbar V^{-1} . A running average function is used to smooth the data. For every smoothed data point 20 measurements before, the data point itself and 20 measurements after the considered moment are used.
3. Confirm no pressure drop is apparent. If a pressure drop is visible in the considered time frame, trace and fix the leak accordingly.

6.2.4 TEST-310: Characterization of environmentally induced noise

Janssens [39] and Perez-Grande [68] have characterized the environmentally induced vibrations by using a set of three Colibrys SF1500-A accelerometers. These accelerometers are no longer available due to damages and malfunction. No replacements are readily available for loan or rental. The environmentally induced vibrations can thus not be assessed in terms of accelerations and be plugged into the analytical model. This renders it impossible to measure the environmental vibrations independently from the other noise sources. The environmentally induced noise is therefore measured integral with the other noise sources. This noise is an important parameter as shown in Chapter 4. The noise influences the thrust reading to a great extent and minimization of it is required to improve the quality of the measurements.

The environmentally induced noise is determined by measuring the free movement of the pendulum. Via multiplication of the measured displacements of the sensor target with the thrust stand sensitivity in

N m^{-1} , the noise can be determined in terms of measured thrust. The thrust stand sensitivity is determined according to the procedures of TEST-411, which are outlined in [Section 6.2.8](#).

To determine whether a preferential orientation of the thrust stand in the vacuum chamber exists, the thrust stand is placed into the vacuum chamber in two well-defined perpendicular orientations. Either orientation is preferential when the noise levels are measurably lower than in the other orientation. A preferential orientation may exist, because environmentally induced vibrations can be of greater amplitude in one direction.

The feed system may vary from thruster to thruster. To exclude the damping effect of the used feed system on the pendulum, the tests are repeated with the feed system connected and disconnected. No gas or power is supplied to the engine when the feed system is connected.

6.2.4.1 *Thrust stand orientations*

The two orientations in which the noise of the thrust stand signal is measured are depicted in [Figure 51](#). In the first orientation the pendulum plane of moment is aligned with the short side of the building while in the second orientation it is aligned with the long side of the building. As the stiffness of the building differs in both orientations, the noise amplitudes and frequencies found in the measured thrust signal are expected to differ. In the second orientation the found frequencies are expected to be higher and of lower magnitude.

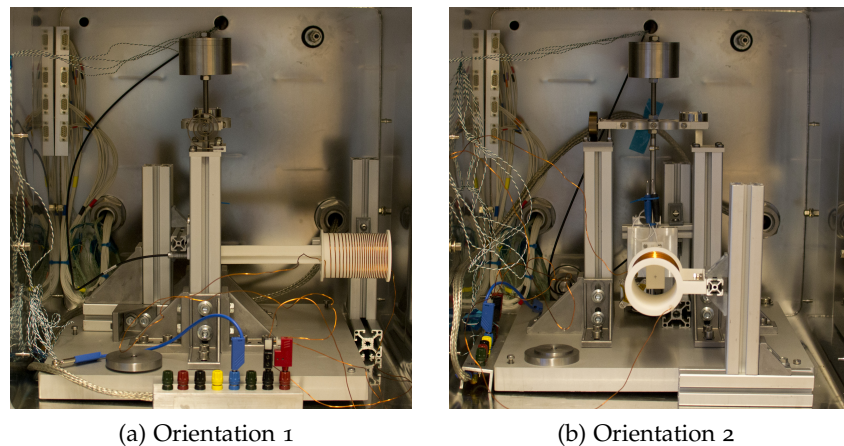


Figure 51: Photos of the setup placed in two orientations used for the noise measurements of TEST-310.

6.2.4.2 *Required equipment*

The thrust stand is set up in the vacuum chamber according to the steps described in [Section 6.3](#). No additional equipment is required.

The used sensor is chosen in accordance to the thrust range that the setup is calibrated for.

6.2.4.3 Procedure

1. Perform TEST-411 (Section 6.2.8).
2. Set up the thrust stand in the vacuum chamber in orientation 1, according to the steps in described in Section 6.3.
3. Switch on the PXI 6229 DAQ followed by the lab PC (order is essential). Switch on the PSUs and allow them to reach thermal equilibrium. Warm-up time is **60 minutes**.
4. Close the vacuum chamber and start the pump.
5. Start LabView and open VI 'vacuumPressureReadOut.vi' or wait for at least 60 min for the vacuum chamber to reach its minimum pressure.
6. Monitor the vacuum chamber pressure. Once the vacuum pressure has reached a maximum pressure of 6 mbar, switch off the pump. Allow the remaining atmosphere in the vacuum chamber to settle. A period of **5 minutes** is advised.
7. Open VI 'TEST310.vi' and change its settings. The test duration and measurement file location are required. Set the sampling rate to 250 Hz.
8. When the settling time has expired, run the VI. The VI automatically saves the measurement file once the test has ended.
9. Open the shut-off valve on the front side of the vacuum chamber to allow the chamber to fill with air.
10. Open the vacuum chamber and change the setup orientation.
11. Repeat steps 4 to 8 for the next orientation. Take into account the warm-up time of the electrical components, if they have been switched off completely in the meantime.

6.2.4.4 Data-processing

The data are processed using Matlab program 'TEST310.m'.

1. Start Matlab and open program 'TEST310.m'.
2. Change the settings of the program.
 - a) Change variable 'filen' to direct to the right measurement file.
 - b) Change variable 'S' to set the setup sensitivity in VN^{-1} . This parameter is obtained from TEST-411.

3. Start the program. It automatically subtracts the signal average voltage from the measurement. The resulting signal is converted into force readings by division by the sensitivity S . A Fast-Fourier Transform (FFT) is performed on the data to analyse the frequency spectrum. The transform is single-sided and corrected for the Nyquist criterion. The spectrum analysis is only used to identify peak frequencies at which the stand is excited. Also the standard deviations of the measured forces are calculated. This allows to set boundaries on the experienced noise levels.
4. The program automatically creates graphs that correspond to the generated output.

6.2.5 TEST-320: Characterization of feed system positioning

Sutherland et al. [79] have shown that feed systems that are not connected in a systematic way can introduce unwanted thermal drift, creep and hysteresis in the thrust measurements as well as add non-uniform stiffness and damping to the thrust stand. To understand the influence of the feed system on the quality of the measurements, the feed system positioning is investigated and its effects are quantified. Based on the results of TEST-320, the feed system positioning can be standardized for measurements with the TB-5m.

As proposed for similar pendulum thrust stands [73, 86], the feed system and power system lines will be connected from the top. This way thermal expansion of the wires only introduces forces normal to the thrust vector and does (ideally) not influence the thrust reading. Photos of the actual setup are given with the results in Figure 73 in Section 7.3.5.

6.2.5.1 Required equipment

The thrust stand is set up in the vacuum chamber according to the steps described in Section 6.3. No additional equipment is required.

6.2.5.2 Procedure

1. Perform TEST-411 (Section 6.2.8).
2. Set up the thrust stand in the vacuum chamber in orientation 1, according to the steps in described in Section 6.3.
3. Switch on the PXI 6229 DAQ followed by the lab PC (order is essential). Switch on the PSUs and allow them to reach thermal equilibrium. Warm-up time is **60 minutes**.
4. Close the vacuum chamber and start the pump.

5. Start LabView and open VI 'vacuumPressureReadOut.vi' or wait for at least 60 min for the vacuum chamber to reach its minimum pressure.
6. Monitor the vacuum chamber pressure. Once the vacuum pressure has reached its minimum operating pressure, switch off the pump. Allow the remaining atmosphere in the vacuum chamber to settle. A period of **5 minutes** is advised.
7. Open VI 'TEST320.vi' and change its settings. The test duration and measurement file location are required. Set the sampling rate to 100 Hz.
8. When the settling time has expired, run the VI. Fill the gas lines of the feed system by pressurizing the system at 1 bar. Apply a current of 90 mA to the PMT. This prevents gas from flowing, but allows the feed lines to relax at operating pressure and the power lines to warm up. The VI automatically saves the measurement file once the test has ended.
9. Open the shut-off valve on the front side of the vacuum chamber to allow the chamber to fill with air.
10. Open the vacuum chamber and change the setup orientation.
11. Repeat steps 4 to 8 for the next feed system orientation. Take into account the warm-up time of the electrical components, if they have been switched off completely in the meantime.

6.2.5.3 Data-processing

To identify drift that is caused by the feed and/or power system, the signal is analyzed.

1. Start Matlab and open program 'TEST320.m'.
2. Change the settings of the program.
 - a) Change variable 'filen' to direct to the right measurement file.
 - b) Change variable 'S' to set the setup sensitivity in VN^{-1} . This parameter is obtained from TEST-411.
3. Start the program. It automatically subtracts the signal initial zero voltage (based on the average of the first 10 s of signal) from the measurement. The resulting signal is converted into force readings by division by the sensitivity S. The zero is determined also for the last 10 s of signal. A difference between the initial zero and last zero is indicative of drift.
4. The program automatically creates graphs that correspond to the generated output. The operator can identify the drift from the signal.

6.2.6 TEST-331: Natural frequency and damping ratio

The thrust stand performance is not only characterized by its sensitivity and accuracy. Its operation is also limited by its dynamic behavior, especially for the measurement of transient processes and pulsed thrust. The measurement envelope is determined using a series of dynamic tests that result in the damped natural frequency, the damping ratio (TEST-331) and the frequency response of the pendulum (TEST-332). From the frequency response, the signal attenuation can be calculated. As the pendulum is forced into vibration by repetitive thrusting, the response will be attenuated at higher frequencies. This has to be either calibrated or corrected for in data-processing. The techniques used are also described by Inman [36].

The TB-5m thrust stand is based on the TB-2m design by Perez-Grande [68]. The friction in the pendulum support is minimized using razor edge and conic supports. As the contact areas are not infinitely small, friction and mechanical damping are introduced. The pendulum motion is further damped by aerodynamic damping, but this effect drops off with lower ambient pressures. Assuming a low resulting damping ratio, a large amount of cycles pass before for any oscillation damps out. Based on the assumption that sufficient cycles are available, the damping coefficient can be calculated from the logarithmic decrement. Typical friction damped oscillators show an exponential decay in oscillation magnitude. A measure for this decay is given by the logarithmic decrement δ . It is typically calculated from measurements of the amplitude difference between the first peak and the peak n_{cyc} cycles later. In this expression, the signal is represented generically by $x(t)$ and T is the oscillation period.

$$\delta = \frac{1}{n_{cyc}} \ln \frac{x(t)}{x(t + n_{cyc} \cdot T)} \quad (83)$$

The damping ratio is then calculated from the logarithmic decrement using

$$\zeta = \frac{\delta}{\sqrt{4\pi^2 + \delta^2}} \quad (84)$$

Here it is assumed that the oscillator is in free vibration and that the damping is proportional to the oscillation velocity. Aerodynamic damping, however, is proportional to the square of the oscillation velocity. This higher order is approximated by a linear dependency on velocity for low rotational rates. The drag experienced by a section of the pendulum at a distance r from the pivot is proportional to

$$D_{aero}(r) = \frac{1}{2} \rho c(r) \omega^2 r^2 \quad (85)$$

where ρ is the air density in kg m^{-3} , c the product of drag coefficient and surface area in m^2 and ω the rotational rate in rad s^{-1} . For a rotational rate $\omega \ll 1$, the drag can be linearized to

$$D_{\text{aero}}(\tau) = \frac{\partial D}{\partial \omega} \omega = \rho c(\tau) \omega r^2 \quad (86)$$

When the oscillation is caused by an impulse input, the oscillator oscillates at its damped natural frequency. The damped natural frequency is extracted from the measured response via the Fourier transform of the data. In the frequency domain the damped natural frequency is apparent as a strong peak which is easily identified from the spectral analysis.

6.2.6.1 Required equipment

The thrust stand is set up in the vacuum chamber according to the steps described in [Section 6.3](#). No additional equipment is required.

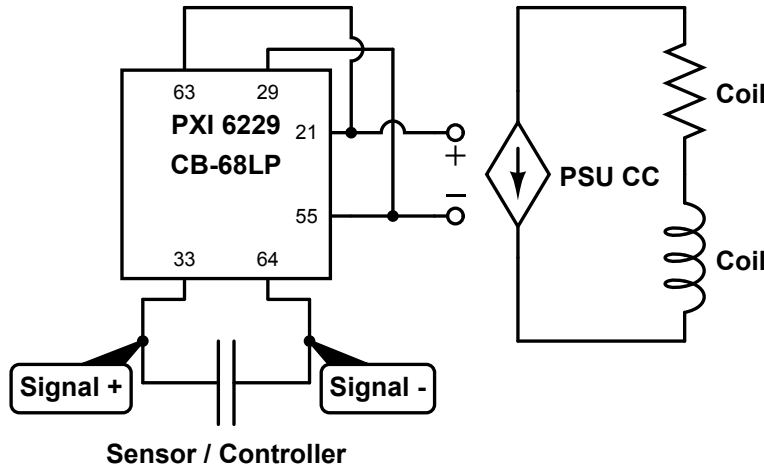


Figure 52: Circuit diagram for TEST-331, TEST-332 and TEST-411. Pin numbering: (63, AI11); (29, AI GND); (21, AO1); (55, AO GND); (33, AI1); (64, AI GND)

6.2.6.2 Procedure

1. Set up the stand following the procedures of [Section 6.3](#).
2. Allow all electronic components to warm up. The warm-up time is **60 minutes**.
3. Start LabView and open VI 'vacuumPressureReadOut.vi' or wait for at least 60 min for the vacuum chamber to reach its minimum pressure.
4. Check if all components are connected correctly. Close the vacuum chamber and switch on the pump.

5. Start the [VI](#) and monitor the vacuum chamber pressure. Once the pressure has dropped to its minimum operating pressure, switch off the pump and allow the remaining atmosphere in the vacuum chamber to settle. A period of **5 minutes** is advised.
6. Once the settling time has expired, load [VI TEST-331](#). Change the settings according to the results of TEST-120 and set the filepath where the measurement file is saved.
7. Start the [VI](#). The program generates a pulse in the coil of 10 ms duration. The resulting motion of the thrust stand is measured. The program automatically stops measuring and saves the measurement data after 60 s.
8. Open the shut-off valve on the front side of the vacuum chamber to allow the chamber to fill with air.
9. Switch off the power supplies and disconnect the electric components from the [DAQ](#). Open the vacuum chamber, disconnect all components and clear the workspace.

6.2.6.3 *Data-processing*

The data are analyzed using Matlab program 'TEST330.m'. The damped natural frequency and damping ratio are determined from the first measurement sequence obtained through [VI](#) 'TEST330.vi'.

1. Open Matlab program and change the settings. Make sure variable 'filen' contains the path to the measurement file.
2. Start the program. It performs a [FFT](#) on the data and selects the highest peak. The frequency at which the largest amplitude occurs is selected and taken as the damped natural frequency. The data in the time domain are analyzed to find the damping ratio. The peaks of the oscillations are identified and [\(83\)](#) and [\(84\)](#) are used to calculate the damping ratio. The program also outputs the spectrum from the [FFT](#) and the signal including the found peaks.

6.2.7 *TEST-332: Dynamic attenuation*

When the thrust stand is forced into vibration via a pulsed actuation force (either created by the calibration actuator or the thruster), the resulting oscillation amplitude is attenuated dependent on the pulse frequency. This attenuation behavior is characterized using a vibration that is forced using the calibration actuator. The attenuation factor χ is calculated as a ratio of the response δ at steady input force and oscillated input force.

$$\chi(\omega) = \frac{\delta(\omega, F_{\max}) - \delta(\omega, F_{\min})}{\delta(0, F_{\max}) - \delta(0, F_{\min})} \quad (87)$$

This measurement is repeated for input frequencies ω in the range of 0.1 Hz to 100 Hz.

6.2.7.1 *Required equipment*

The thrust stand is set up in the vacuum chamber according to the steps described in [Section 6.3](#). No additional equipment is required.

6.2.7.2 *Procedure*

1. Set up the stand following the procedures of [Section 6.3](#).
2. Allow all electronic components to warm up. The warm-up time is **60 minutes**.
3. Start LabView and open VI 'vacuumPressureReadOut.vi' or wait for at least 60 min for the vacuum chamber to reach its minimum pressure.
4. Check if all components are connected correctly. Close the vacuum chamber and switch on the pump.
5. Start the VI and monitor the vacuum chamber pressure. Once the pressure has dropped to its minimum operating pressure, switch off the pump and allow the remaining atmosphere in the vacuum chamber to settle. A period of **5 minutes** is advised.
6. Load VI 'TEST332.vi' and change the settings. Set the filepath where the measurement file is saved and set the range of frequencies to be sampled.
7. Start the VI. The program now drives the actuator at a series of set frequencies and measures the resulting response. Once the program has finished, it automatically saves the measurements to the selected measurement file.
8. Open the shut-off valve on the front side of the vacuum chamber to allow the chamber to fill with air.
9. Switch off the power supplies and disconnect the electric components from the DAQ. Open the vacuum chamber, disconnect all components and clear the workspace.

6.2.7.3 *Data-processing*

The data are analyzed using Matlab program 'TEST332.vi'. The damped natural frequency and damping ratio are determined from the first measurement sequence obtained through VI 'TEST330.vi'.

1. Open Matlab program 'TEST332.m' and change the settings. Make sure variable 'filem' contains the path to the measurement file.

2. Start the program. It calculates ratio (87). All given frequencies are analyzed and the results are plotted in a graph.

6.2.8 TEST-411: Pendulum characterization - Sensitivity

The sensitivity of the thrust stand is determined using the calibration actuator. The actuator exerts a known force at a known distance l_{t1} from the pivot. This causes the pendulum to rotate and consequently a changing displacement measurement from the sensor at a distance l_{t2} from the pivot. The measured displacement is tabulated as a function of applied force. It is assumed that the thrust force is applied perpendicular to the thrust stand at a distance l_e from the pivot. By scaling the applied force with the ratio $\frac{l_{t1}}{l_e}$, the force that needs to be applied by the engine to cause the same displacement can be calculated. The sensitivity S_f is then given as

$$S_f = \Delta x \left(F_{\text{actuator}} \frac{l_{t1}}{l_e} \right)^{-1} \quad (88)$$

where Δx is the measured displacement in m. However, in the measurement the displacement is stored as a voltage instead of a distance. Therefore the sensitivity has the unit of $V N^{-1}$.

6.2.8.1 Required equipment

The thrust stand is set up in the vacuum chamber according to the steps described in [Section 6.3](#). No additional equipment is required.

6.2.8.2 Procedure

1. Perform TEST-110.
2. Set up the thrust stand following the procedures of [Section 6.3](#). Connect the PSU using the D-sub cable labeled with the blue marker. Make sure the PSU is set to Controlled Current programming mode by setting the switches accordingly on the back of the PSU.
3. Measure the distance from pivot to the center of the calibration arm. This is measured along pendulum arm, perpendicular to the calibration arm. Similarly, measure the distance from the pivot to the center of the exhaust of the engine.
4. Allow all electronic components to warm up. The warm-up time is **60 minutes**.
5. Check if all components are connected correctly. Close the vacuum chamber and switch on the pump.

6. Start LabView and open VI 'vacuumPressureReadOut.vi' or wait for at least 60 min for the vacuum chamber to reach its minimum pressure.
7. Start the VI and monitor the vacuum chamber pressure. Once the pressure has dropped to the minimal operating pressure, switch off the pump and allow the remaining atmosphere in the vacuum chamber to settle. A period of **5 minutes** is advised.
8. Once the settling time has expired, load VI 'TEST411.vi'. Change the settings according to the results of TEST-110 and set the filepath where the measurement file is saved.
9. Check if all electric systems are connected correctly. In case all components are connected correctly, run program TEST-411. The actuator now slowly increases the calibration force by increasing the current and takes a displacement measurement at a rate of 100 Hz. Once the maximum force has been reached, the calibration force is slowly reduced to zero again. The program starts with a 10 s measurement at a current of 0 A and ends similarly. These measurement allow the determination of the zeros and to calculate any measurement drift by comparing the zero reading at the beginning and at the end of the sequence. The current is increased linearly from 0 A to 10 A in 60 s and decreased back to 0 A in a similar fashion. The VI automatically saves the measurement data in comma separated file for further processing.
10. Once the automated calibration has finished, close the VI.
11. Open the shut-off valve on the front side of the vacuum chamber to allow the chamber to fill with air.
12. Switch off the power supplies and disconnect the electric components from the DAQ. Open the vacuum chamber, disconnect all components and clear the workspace.

6.2.8.3 Data-processing

The sensitivity of the stand is determined using the calibration actuator. The actuator, however, is not in the same location as the thruster. Using the following data-processing program, the data are scaled to match the thrust produced by a thruster.

1. Load Matlab program 'TEST411_3files.m' and change the settings. Change the variable 'filen' to direct to the location of the measurement files. Also insert the distance from pivot to calibration arm center l_t and the distance from pivot to center of the exhaust l_e .

2. Run the program. It loads the measurement file and converts the applied forces to equivalent engine thrust by multiplying it by the ratio $\frac{l_t}{l_e}$. The data now represent measured sensor output voltage as a function of applied thrust force. The sensitivity is determined by fitting a function of the form $U = SF$ to the data. This results in a sensitivity S in VN^{-1} .

6.2.9 TEST-412: Pendulum characterization - Drift

Thermo-mechanical effects cause drift in the measurements. During the natural day the temperature in the clean room varies slowly. During a test, the temperature of the setup can vary more quickly, due to heating of electronic components and the thrusting engine. The former can be (partially) avoided by allowing components to reach thermal equilibrium before commencing the measurements, but both effects will lead to thermal expansions and contractions of components. Additionally, flexible parts - such as PTFE hoses - may show a considerable relaxation effect after they have been installed. The caused deformations are the cause for measurement drift that needs to be characterized. During these measurements two characteristics are important: the magnitude of the drift and its trend. Data that exhibit either a linear drift or highly repeatable drift can be corrected in post-processing.

The tests are conducted with the full system assembled and an engine mounted. The feed system is connected, but no gas is flowing. All electronic components are connected to their required power supplies and powered to allow components and electric feed wires to heat. Measurements are done during the entire natural day and the movement of the thrust stand pendulum is measured, as well as the ambient vacuum chamber temperature, the temperature at two locations on the pendulum, the calibration actuator and the sensor mount (Section 6.2.9.1). The temperature changes in these locations are then related to the drift in measurement signal.

6.2.9.1 Temperature measurements

The temperature measurements are performed using K-type thermocouples. This type of thermocouple is known for its good linearity and relatively low price compared to other types [3]. A thermocouple does not measure absolute temperatures, but uses the Seebeck effect to measure a temperature difference between its ends. To determine absolute temperatures, the temperature should be known at one of the two ends of the thermocouple. In the National Instruments SCB-68 the absolute temperature of the terminal is measured using a calibrated thermistor. The thermistor on the available SCB-68, however, is no longer functional and a new cold junction is created using

ice water which is at a constant $0\text{ }^{\circ}\text{C}$. The thermocouples that are used to determine the temperature changes of components in the setup are connected to the SCB-68. In normal operations, the thermistor on the terminal is switched on by the right jumper settings on the terminal board that route it to CH0. instead, an additional thermocouple is connected to the terminal at one end, while the other end is suspended in ice water. The setup is schematically depicted in Figure 53. The potentials generated by thermocouples 1 and 2 are $U_1 = S_k (T_1 - T_{daq})$ and $U_2 = S_k (T_2 - T_{daq})$, respectively. The potential generated by the cold junction thermocouple generates a potential $U_{ref} = S_k (T_{ref} - T_{daq})$. With $T_{ref} = 0^{\circ}\text{C}$, the latter relationship is used to find the temperature of the shielded terminal block. Using the two former relations, the absolute temperatures of the measurement points are then found. Herein it is assumed that the temperature of the shielded terminal block is homogeneous. The thermocouples are fastened using narrow hose clamps as close as possible to the interface of the engine bracket and the pendulum arm and the interface between cross beam and the pendulum arm.

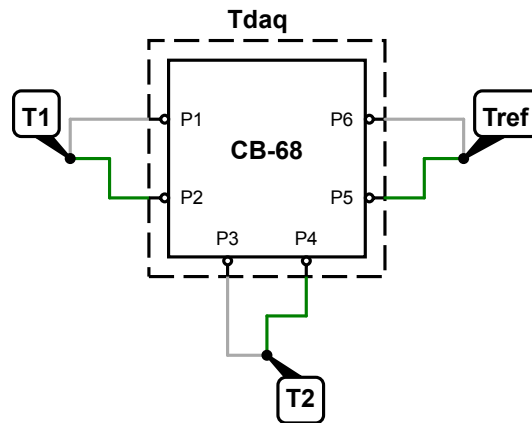


Figure 53: Sketch of setup for cold junction compensation.

6.2.9.2 Required equipment

The thrust stand is set up in the vacuum chamber according to the steps described in Section 6.3. The temperature is measured using four K-type thermocouples that are prepared and glued into a vacuum transition disc (Figure 41). Two thermocouples are fixed to the pendulum arm using small hose clamps. Two pieces of tape are used to stick the remaining thermocouples to the calibration actuator and to the sensor holder.

6.2.9.3 Procedure

1. Perform TEST-411 (Section 6.2.8).

2. Set up the thrust stand following the procedures of [Section 6.3](#). Take care that also the four thermocouples are installed and the vacuum transition is installed and locked.
3. Allow all electronic components to warm up. The warm-up time is **60 minutes**.
4. Check if all components are connected correctly. Close the vacuum chamber and switch on the pump.
5. Start LabView and open [VI](#) 'vacuumPressureReadOut.vi' or wait for at least 60 min for the vacuum chamber to reach its minimum pressure.
6. Start the [VI](#) and monitor the vacuum chamber pressure. Once the pressure has dropped to the minimal operating pressure, switch off the pump and allow the remaining atmosphere in the vacuum chamber to settle. A period of **5 minutes** is advised.
7. Once the settling time has expired, load [VI](#) 'TEST412.vi'. Change the settings according to the results of TEST-411 and set the filepath where the measurement file is saved.
8. Check if all electric systems are connected correctly. In case all components are connected correctly, run program 'TEST412.vi'. The program now determines the temperatures, the vacuum pressure and the displacement sensor signal for the requested amount of time.
9. Once the measurement period has expired, the [VI](#) automatically saves the measurement data. Close the [VI](#) manually.
10. If necessary, open the shut-off valve on the front side of the vacuum chamber to allow the chamber to fill with air. As soon as ambient pressure has been reached, the chamber door can be opened safely.

6.2.9.4 *Data-processing*

The data are processed by reading the measurement file and converting the signals into physical quantities of interest. The thermocouple signals are converted from V to temperatures, the sensor signal is converted to forces. The program generates graphs of the history of each converted signal and calculates the correlation between each of the temperature signals and the thrust reading.

6.2.10 *TEST-420: Characterization of the effect of the magnetic field of the Proportional Microthruster*

The [PMT](#) consists of a proportional valve that uses a voice-coil type actuator to open or close the orifice. This actuator creates a magnetic

field that can potentially influence the reading of the stand by electromagnetic interference. To study the effect, two measurements are performed. In the first measurement (TEST-421), the engine is installed on the thrust stand, but the pendulum is immobilized. This allows for determining the effect of the electromagnetic field on surrounding equipment. The **PMT** is therefore controlled by varying the electric current in the full 0 mA to 140 mA range. In the second measurement (TEST-422), the pendulum is free to move and the current is varied from 0 mA to 90 mA. This series allows for determining the effect on the displacement reading due to electromagnetic forces. The current range is lower in the second measurement, to avoid crosstalk with the **CoG** shift effects that are measured in TEST-430. From flow-rate data of the **PMT** at inlet pressures of 1.0 bar and 1.5 bar with Xenon gas [46], it can be concluded that the valve is closed up to currents of ≈ 90 mA. Above this current, the two effects can no longer be separated.

6.2.10.1 Required equipment

The thrust stand is set up in the vacuum chamber according to the steps described in [Section 6.3](#). No additional equipment is required. For the first series, the pendulum is immobilized. For the second series, the **PMT** is also mounted on the pendulum arm.

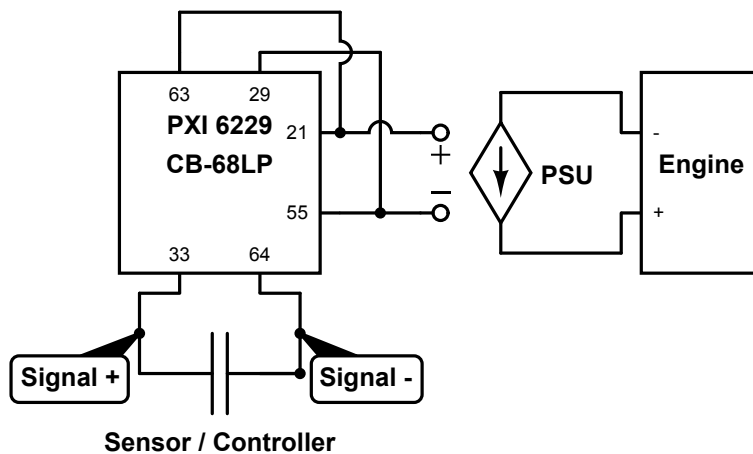


Figure 54: Circuit diagram for TEST-420 and TEST-430. Pin numbering: (63, AO11); (29, AI GND); (21, AO1); (55, AO GND); (33, AI1); (64, AI GND)

6.2.10.2 Procedure

Repeat the procedure below for both series. Set up the **VI** accordingly.

1. Perform TEST-411 ([Section 6.2.8](#)).
2. Set up the thrust stand following the procedures of [Section 6.3](#). Connect the **PSU** using the D-sub cable labeled with the blue

marker. Make sure the PSU is set to Controlled Current programming mode by setting the switches accordingly on the back of the PSU.

3. Close the vacuum chamber and switch on the pump.
4. Start LabView and open VI 'vacuumPressureReadOut.vi' or wait for at least 60 min for the vacuum chamber to reach its minimum pressure.
5. Start the VI and monitor the vacuum chamber pressure. Once the pressure has dropped to the minimal operating pressure, switch off the pump and allow the remaining atmosphere in the vacuum chamber to settle. A period of **5 minutes** is advised.
6. Open VI 'TEST420.vi'.
7. Set up the VI choosing a location to save the measurement data. Also select the series by toggling the button labeled 'Long Range?'. For the first series the long range of 140 mA is used, for the second series the short range of 90 mA is used.
8. Check if all electric systems are connected correctly. In case all components are connected correctly, run program TEST-420. The program now uses the PSU to run current through the PMT. By slowly increasing the current, the electromagnet creates a stronger magnetic field. Once the maximum current has been reached, the current is reduced back to zero. The current is changed linearly at a rate of 20 mA min^{-1} . Measurements are taken at a rate of 100 Hz.
9. Once the VI has finished, it automatically saves the measurement file in the desired location.
10. If necessary, open the shut-off valve on the front side of the vacuum chamber to allow the chamber to fill with air. As soon as ambient pressure has been reached, the chamber door can be opened safely.

6.2.10.3 Data-processing

Using the results of the sensitivity determination of TEST-411, the results are easily converted into force readings.

1. Open Matlab program 'TEST420.m' and set up the variables. Change variable 'fileN' to direct to the desired measurement file. Plug the results of TEST-411 into variable S. Make sure the units are in VN^{-1} .
2. Run the program. It reads the measurement file and converts the read voltages into force readings by division of the measured voltage by the sensitivity S.

3. Depending on the results, a polynomial is fit to the signal to estimate the magnitude of the caused signal change.

6.2.11 TEST-430: Characterization of the effect of the center of gravity shift in the Proportional Microthruster

The **PMT** is a cold gas thruster that is composed of a big proportional valve and a nozzle. When the valve is actuated, the **CoG** of the thruster shifts. To characterize the effects of the **CoG** shift on the output of the thrust stand, the engine is connected and the valve is actuated without any gas flowing. Knowing the effect of the **CoG** shift allows for accuracy budgeting and correction in post-processing of the measurement data. The test is performed using the full setup as described in [Section 6.3](#). The feed system, however, is closed and no thrust is produced. The effect is measured as a function of valve actuation current.

When the valve opens, a mass of ≈ 5 g travels towards the solenoid inside the **PMT** over a distance of maximum ≈ 1 mm [46]. This causes a moment on the pendulum that is opposing the moment created by the thrust vector. To estimate the equivalent thrust force required to create a moment as big as that caused by a shift in **CoG** of the **PMT**, the following equivalency is used.

$$-\Delta M = l_e \Delta T \quad (89)$$

$$\begin{aligned} \Delta M &= mg \Delta x_m \cos \theta \\ &= 5 \cdot 10^{-3} \text{ [kg]} \cdot 9.80665 \text{ [m s}^{-2}\text{]} \cdot 1 \cdot 10^{-3} \text{ [m]} \cdot 1 \\ &\approx 4.9 \cdot 10^{-5} \text{ [Nm]} \quad (90) \end{aligned}$$

where m is the traveled mass, g the local gravitational acceleration, Δx_m the distance over which the mass travels and θ the angle at which the thrust stand is oriented. As this angle remains very small, it is assumed that $\cos \theta \approx 1$. From this the equivalent force is calculated when the engine arm length l_e is known. Assuming this is 230 mm the equivalent thrust is $\Delta T = -2.1 \cdot 10^{-4}$ N at maximum opening of the valve. The equivalent force is plotted in [Figure 55](#) as a function of mass displacement. The depicted numbers are dependent on the engine arm length and the actual values of the mass and traveled distance. The quoted numbers are exactly not known and may be different.

6.2.11.1 Required equipment

The thrust stand is set up in the vacuum chamber according to the steps described in [Section 6.3](#). No additional equipment is required.

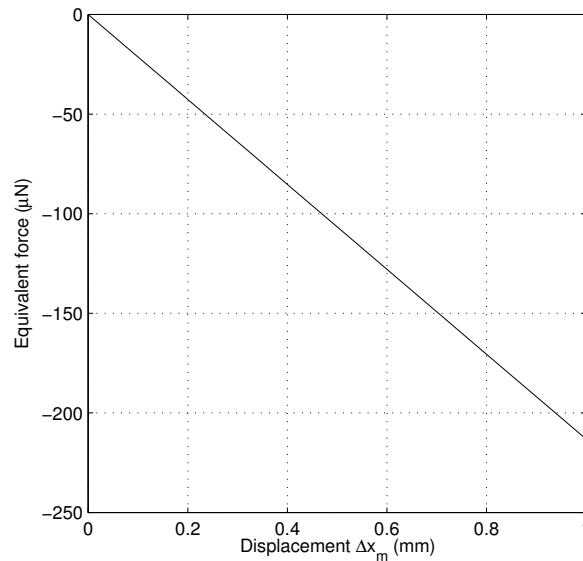


Figure 55: Expected change in measured thrust due to center of gravity shift. Graph is valid for an engine arm length $l_e = 230$ mm.

6.2.11.2 Procedure

1. Perform TEST-411 (Section 6.2.8).
2. Set up the thrust stand following the procedures of Section 6.3. Connect the PSU using the D-sub cable labeled with the blue marker. Make sure the PSU is set to Controlled Current programming mode by setting the switches accordingly on the back of the PSU.
3. Allow all electronic components to warm up. The warm-up time is **60 minutes**.
4. Check if all components are connected correctly. Close the vacuum chamber and switch on the pump.
5. Start LabView and open VI 'vacuumPressureReadOut.vi' or wait for at least 60 min for the vacuum chamber to reach its minimum pressure.
6. Start the VI and monitor the vacuum chamber pressure. Once the pressure has dropped to the minimal operating pressure, switch off the pump and allow the remaining atmosphere in the vacuum chamber to settle. A period of **5 minutes** is advised.
7. Once the settling time has expired, load VI TEST-430. Change the settings according to the results of TEST-411 and set the filepath where the measurement file is saved.

8. Check if all electric systems are connected correctly. In case all components are connected correctly, run program TEST-430. The program now uses the PSU to run current through the PMT. By slowly increasing the current, the electromagnet creates a stronger magnetic field and the valve opens. Once the maximum current has been reached, the current is reduced back to zero. The current is changed linearly at a rate of 20 mA min^{-1} . Measurements are taken at a rate of 10 Hz.
9. Once the VI has finished, it automatically saves the measurement file in the desired location.
10. If necessary, open the shut-off valve on the front side of the vacuum chamber to allow the chamber to fill with air. As soon as ambient pressure has been reached, the chamber door can be opened safely.

6.2.11.3 Data-processing

The data-processing is equal to that of TEST-420.

6.2.12 TEST-440: Characterization of the effect of changing vacuum pressure

While the engine thrusts, the chamber slowly fills with gas. This gas can either be pumped out by the vacuum pump at the cost of increased environmentally induced noise, or accepted if the effect on the thrust reading is negligible or can be corrected for. The latter scenario is studied, by measuring the effect of increased vacuum pressure on the thrust stand.

Using the ideal gas law, the pressure in the vacuum chamber can be estimated as a function of time and mass flow rate:

$$P(t) = \frac{(m_0 + \dot{m}t) RT_{\text{gas}}}{V_{\text{chamber}}} \quad (91)$$

where T_{gas} is chamber temperature in K, R the specific gas constant in $\text{JK}^{-1} \text{kg}^{-1}$, V_{chamber} the chamber volume in m^3 , m_0 the gas mass contained in the chamber at $t = 0 \text{ s}$ and \dot{m} the mass flow rate in kg s^{-1} . It is assumed that the gas has a specific gas constant of $R = 287.058 \text{ JK}^{-1} \text{ kg}^{-1}$, reminiscent of dry air. This assumption is justified by the use of N_2 gas and the high concentration of N_2 ($\approx 80\%$) in the air. The temperature is assumed to be constant at $293.15 \text{ K} = 20^\circ\text{C}$. Finally, it is assumed that the gas is at rest and instantaneously mixed. For a mass flow rate of 2.5 mg s^{-1} (maximum expected mass flow for PMT [45]), the results are given in Figure 56. Typical engine tests are not expected to last longer than 20 minutes of continuous thrusting. From the figure it can be concluded, that when a test duration in the

order of 10 – 20 minutes is sufficient, an increase from 10 mbar to 30 mbar is to be expected.

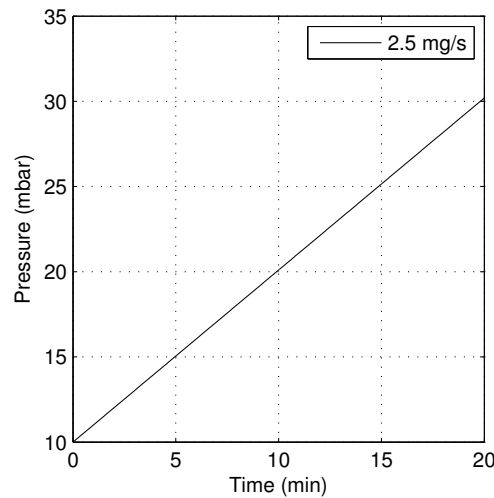


Figure 56: Expected vacuum chamber pressure increase caused by continuous engine thrusting.

6.2.12.1 Required equipment

The thrust stand is set up in the vacuum chamber according to the steps described in [Section 6.3](#). No additional equipment is required.

6.2.12.2 Procedure

1. Perform TEST-411 ([Section 6.2.8](#)).
2. Set up the thrust stand following the procedures of [Section 6.3](#).
3. Allow all electronic components to warm up. The warm-up time is **60 minutes**.
4. Check if all components are connected correctly. Close the vacuum chamber and switch on the pump.
5. Start LabView and open VI 'vacuumPressureReadOut.vi' or wait for at least 60 min for the vacuum chamber to reach its minimum pressure.
6. Start the VI and monitor the vacuum chamber pressure. Once the pressure has dropped to the minimal operating pressure, switch off the pump and allow the remaining atmosphere in the vacuum chamber to settle. A period of **5 minutes** is advised.
7. Once the settling time has expired, load VI 'TEST440.vi'. Change the settings according to the results of TEST-411 and set the filepath where the measurement file is saved.

8. Check if all electric systems are connected correctly. In case all components are connected correctly, run program 'TEST440.vi'. The program now uses the PSU to run current through the PMT. By slowly increasing the current to the desired level, the valve opens further and the flow rate increases. Once the valve has reached the desired position, the current is kept at the same level. Once the pendulum has stabilized, the mass flow rate, chamber pressure and thrust reading are recorded. At the end of the measurement, the mass flow is slowly reduced to allow the pendulum to reach its zero thrust position without oscillations.
9. Once the VI has finished, it automatically saves the measurement file in the desired location.
10. If necessary, open the shut-off valve on the front side of the vacuum chamber to allow the chamber to fill with air. As soon as ambient pressure has been reached, the chamber door can be opened safely.

6.2.12.3 Data-processing

Using the results of the sensitivity determination of TEST-411, the results are easily converted into force readings.

1. Open Matlab program 'TEST440.m' and set up the variables. Change variable 'filen' to direct to the desired measurement file. Plug the results of TEST-411 into variable S. Make sure the units are in V N^{-1} .
2. Run the program. It reads the measurement file and converts the read voltages into force readings by division of the measured voltage by the sensitivity S. The voltages produced by the pressure transducer are converted into pressure readings via the transducer sensitivity.
3. The zero is determined based on the average of the first 10 s of signal after the valve has completely opened.
4. The second zero is determined based on the average of the last 10 s of signal before the valve closes again.
5. The signal history is plotted, to give an indication of the linearity of the effect. Based on the history, the sensitivity of reading as a function of vacuum pressure is derived.

6.2.13 TEST-450: Steady state thrust measurements

All previous tests are prerequisites for the hardware-in-the-loop validation of the thrust stand. They guarantee that the measurement

accuracy is known and the system is characterized. In these tests the calibration actuator is used to generate a force or impulse on the pendulum. In TEST-450 the actuator is only used for calibration purposes. The Bradford Engineering **PMT** is actuated and is used to control the mass flow. The orifice of the Brooks **MFC** is fully opened to effectively transform the **MFC** into a mass flow transducer. The **PMT** has been tested at ONERA and ESA ESTEC. For hardware-in-the-loop validation of the thrust stand performance, the test conditions at both facilities are matched as close as possible.

*The brooks **MFC** is a volume flow controller. The mass flow is obtained through calibration with a specific gas at a known temperature and inlet pressure.*

CONDITION	ONERA	ESTEC	DUT
Vacuum pressure	$10 \cdot 10^{-3}$ mbar	$10 \cdot 10^{-4}$ - $10 \cdot 10^{-3}$ mbar	6 mbar
Mass flow	$2.5 \cdot 10^{-4}$ mg s^{-1} - $2.5 \cdot 10^{-1}$ mg s^{-1}	≤ 2.5 mg s^{-1}	$\approx 5 \cdot 10^{-2}$ mg s^{-1} - 2.5 mg s^{-1}
Engine actuation	Closed loop	Closed loop	Open loop
Nozzle throat diameter	200 μm	100 μm and 200 μm	110 μm

Table 32: Environmental conditions and test conditions at ONERA [45], ESA ESTEC [88] and **DUT** compared.

The difference in vacuum pressure between the ONERA and **DUT** vacuum chambers is cause for an offset in measured thrust. According to ideal rocket motor theory, the thrust is composed of impulse and pressure components as described by

$$T = mU_e + (p_e - p_a) A_e \quad (92)$$

where m is the mass flow in kg s^{-1} , U_e the exhaust velocity in m s^{-1} , p_e the exhaust pressure in Pa, p_a the ambient pressure in Pa and A_e the exhaust area in m^2 . The sensitivity of the thrust force with ambient pressure is found via the partial derivative

$$\frac{\partial T}{\partial p_a} = -A_e \quad (93)$$

The change in thrust due to a change in ambient pressure is then easily found as

$$\Delta T = \frac{\partial T}{\partial p_a} \Delta p_a \quad (94)$$

For the **PMT** the exhaust area equals

$$A_e = \frac{\pi}{4} D_e^2 = \frac{\pi}{4} \cdot 1.28 \cdot 10^{-3} = 1.29 \cdot 10^{-6} \text{ m}^2 \quad (95)$$

With a pressure difference of ≈ 600 Pa, this equates to a force difference of -0.000774 N = -0.774 mN. For an inlet pressure of 1 bar and a mass flow of 2.5 mg s $^{-1}$, the PMT is designed to generate a thrust of 1.5 mN. Including the thrust correction due to the ambient pressure difference, this leaves a 0.726 mN range left for measurements. For validation purposes the caused offset needs to be corrected in data-processing.

The thrust force of the engine is calculated as a function of mass flow and ambient pressure using ideal rocket motor theory [91]. From the geometry of the nozzle, the expansion ratio is estimated to be $A_e/A_t = (D_e/D_t)^2 = (1.28 \cdot 10^{-3}/110 \cdot 10^{-6})^2 \approx 135$. The expansion ratio is related to the pressure ratio of exhaust pressure and the (combustion) chamber pressure via

$$\frac{A_e}{A_t} = \Gamma \left(\frac{2\gamma}{\gamma-1} \left(\frac{p_e}{p_c} \right)^{\frac{2}{\gamma}} \left(1 - \left(\frac{p_e}{p_c} \right)^{\frac{\gamma-1}{\gamma}} \right) \right)^{-1/2} \quad (96)$$

For N₂ the ratio of specific heat $\gamma = 1.4$, and the Vanderkerckhove function is evaluated to $\Gamma = 0.6847$:

$$\Gamma = \sqrt{\gamma} \left(\frac{2}{\gamma+1} \right)^{\frac{\gamma+1}{2(\gamma-1)}} \quad (97)$$

Using a graphical solution method, the pressure ratio is determined to be $p_e/p_c = 1/6111$. The results are plotted in Figure 57.

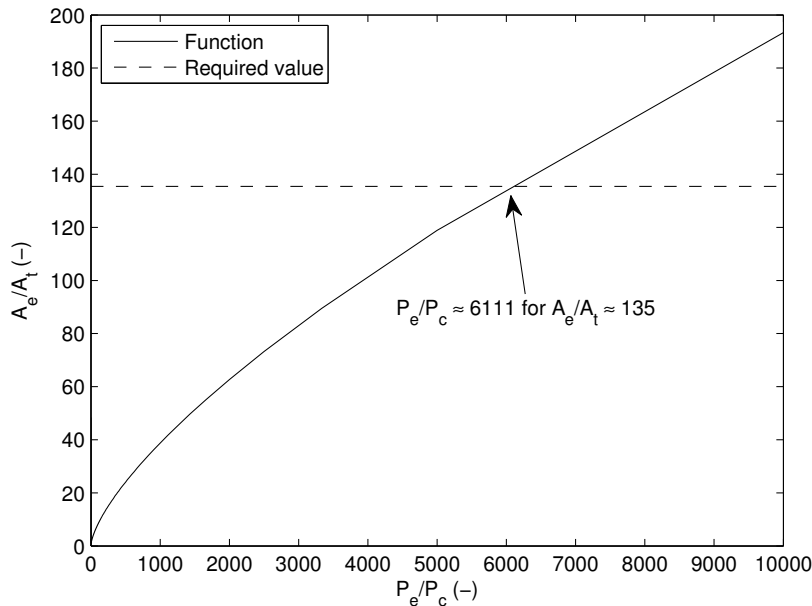


Figure 57: Estimated pressure ratio of the PMT using an geometric expansion ratio $A_e/A_t = 135$.

From the assumed pressure ratio, the exhaust pressure is calculated by simple multiplication with the pressure ratio, $p_e = p_c \frac{p_e}{p_c}$. From an

assumed value of the gas temperature in the (combustion) chamber, T_c , the exhaust velocity is calculated:

$$u_e = \sqrt{2 \frac{\gamma}{\gamma+1} \frac{R_a}{M} T_c \left(1 - \left(\frac{p_e}{p_c} \right)^{\frac{\gamma-1}{\gamma}} \right)} \quad (98)$$

The chamber pressure is calculated from the required mass flow, nozzle geometry, gas temperature and the (thermo)chemical properties of the gas:

$$p_c = \frac{m \sqrt{RT_c}}{\Gamma A_t} \quad (99)$$

Plugging all calculated parameters into (92) yields the thrust. These relations, however, are only valid when the throat is choked, or in other words, when the flow reaches sonic conditions in the throat of the nozzle. It is also assumed here that there are no shockwaves inside the nozzle or expansion waves at the end.

Using the model presented above, N_2 as propellant ($M = 28.0134 \text{ g mol}^{-1}$), a gas temperature $T_c = 293.15 \text{ K}$ and a mass flow of 0 mg s^{-1} to 2.5 mg s^{-1} , the thrust has been calculated for ambient pressures of $1 \cdot 10^{-3} \text{ mbar}$, 3 mbar and 6 mbar , respectively. The results are presented in Figure 58. As shown, the model predicts zero thrust at positive mass flow, which is physically not possible. This is caused by the assumed choked nozzle and the absence of shock waves and expansion waves. When the throat is not choked, the flow shows subsonic expansion and a small amount of thrust is generated. This is neither modeled nor shown in the graph.

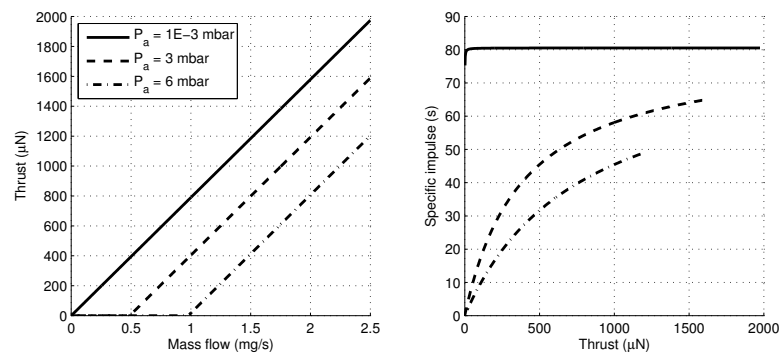


Figure 58: Simulated thrust and specific impulse for the PMT assuming choked flow, a gas temperature of 293.15 K in the (combustion) chamber and three different ambient pressures. Results are calculated using ideal rocket motor theory.

The modeled thrust is compared to the thrust determined at ESA ESTEC in 2006. Although the nozzle geometry is slightly different than modeled ($200 \mu\text{m}$ nozzle versus a $110 \mu\text{m}$ nozzle in the model),

the found thrust-mass flow relation resembles the modeled relation. The ambient pressure that is used in the model is equal to the value quoted by Bradford Engineering at $p_a = 1 \cdot 10^{-3}$ mbar [88, 46]. The results from ESA ESTEC also show that there is a small difference between the tested nozzles of 100 μm and 200 μm throats, but for this comparison the difference is neglected. From the comparison of the experimental results and the model, it is concluded that the PMT behaves like an ideal rocket motor at the quoted conditions.

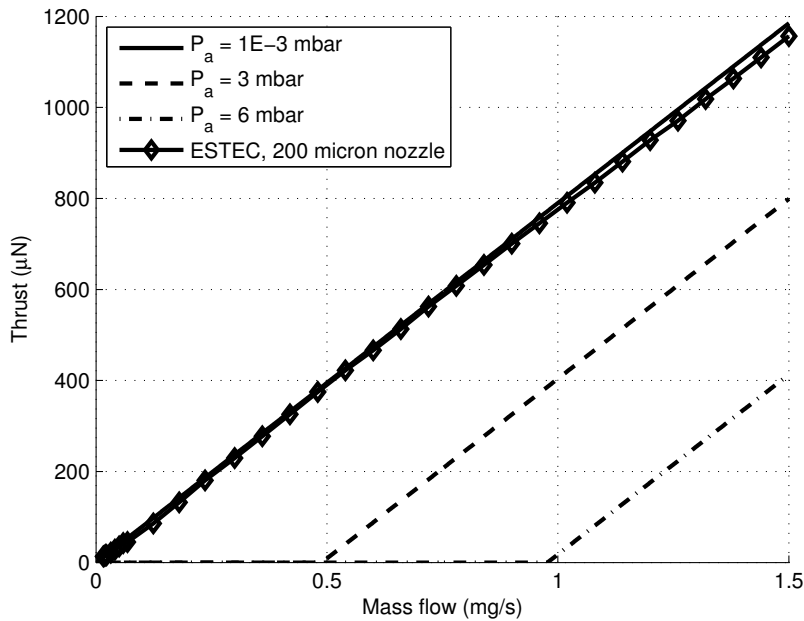


Figure 59: Modeled thrust compared to results obtained at ESA ESTEC (data courtesy of Bradford Engineering [88, 46]). Simulated thrust for the PMT assuming choked flow, a gas temperature of 293.15 K in the (combustion) chamber and three different ambient pressures. Results are calculated using ideal rocket motor theory for a nozzle with a 110 μm throat.

6.2.13.1 Required equipment

The thrust stand is set up in the vacuum chamber according to the steps described in Section 6.3. No additional equipment is required.

6.2.13.2 Procedure

1. Calibrate the setup by performing TEST-411.
2. Set up the thrust stand following the procedures of Section 6.3. Connect the PSU using the D-sub cable labeled with the blue marker. Make sure the PSU is set to Controlled Current programming mode by setting the switches accordingly on the back of the PSU.

3. Connect the [MFC](#) to its power supply and the [DAQ](#). Make sure that the pin labeled 'override' is connected to the [PSU](#) plus as well. This makes sure that the orifice of the [MFC](#) is fully opened. Once connected, switch on the [PSU](#) and set it to 24 V. With the orifice completely opened, a current of approximately 285 mA is drawn from the [PSU](#).
4. Allow all electronic components to warm up. The warm-up time is **60 minutes**.
5. Check if all components are connected correctly. Close the vacuum chamber and switch on the pump.
6. Start LabView and open [VI](#) 'vacuumPressureReadOut.vi' or wait for at least 60 min for the vacuum chamber to reach its minimum pressure.
7. Start the [VI](#) and monitor the vacuum chamber pressure. Once the pressure has dropped to the minimal operating pressure, switch off the pump and allow the remaining atmosphere in the vacuum chamber to settle. A period of **5 minutes** is advised.
8. Pressurize the system according to the steps of [Section 6.3.4](#). Open the consecutive valves slowly and allow the feed system to fill.
9. Start [VI](#) 'feedPressureReadOut.vi' and monitor the pressure on the feed line. Tune the pressure regulator such that the required feed pressure is reached.
10. Close the [VI](#). Once the settling time has expired, load [VI](#) 'TEST450.vi'. Change the settings according to the results of TEST-411 and set the filepath where the measurement file is saved.
11. Check if all electric systems are connected correctly. In case all components are connected correctly, run program TEST-450. The program takes a zero reading of 10 s and then varies the supply current of the [PMT](#) in 13 steps from 80 mA to 140 mA, each step lasting for 30 s. Once the maximum current has been reached, the current is reduced back to zero gradually in 10 s. Another zero reading is made for another 10 s after which the program stops. Measurements are taken at a rate of 100 Hz. During each measurement, the output voltages of the capacitive sensor, the feed pressure transducer and the [MFC](#) are registered.
12. Once the [VI](#) has finished, it automatically saves the measurement file in the desired location.
13. If necessary, open the shut-off valve on the front side of the vacuum chamber to allow the chamber to fill with air. As soon

as ambient pressure has been reached, the chamber door can be opened safely.

6.2.13.3 Data-processing

1. The data are loaded into the memory and the time stepsize is determined.
2. The displacement sensor output is converted from V to a thrust reading in N by division by the sensitivity S_s in $V N^{-1}$.
3. The pressure transducer output is converted from V to a pressure reading in mbar by multiplication by its noted sensitivity in $mbar V^{-1}$.
4. The mass flow is calculated following the procedure of [Section 6.1.2.1](#).

6.2.14 TEST-461: Thrust stand calibration for impulse bits

The motion of a pendulum with frictional damping is given by the generic equation of motion [36]:

$$I\ddot{\theta}(t) + C\dot{\theta}(t) + K\theta(t) = f(t) \quad (100)$$

where I is the mass moment of inertia, C the damping coefficient and K the effective spring constant. The rotation of the pendulum is indicated by rotation angle θ and the forcing function is given by $f(t)$. A perfect impulse is described using a Dirac delta function scaled by its magnitude I_{bit} in N s and the distance between center of rotation and the point of force application l_t in m. The equation of motion is generalized using the damping ratio ζ . The damping ratio is defined as the ratio of the damping coefficient and the critical damping coefficient. The critical damping coefficient is given by $C_{cr} = 2I\omega_n$, where ω_n is the eigenfrequency of the system as given by $\omega_n^2 = \frac{K}{I}$. Using these identities, the equation of motion is rewritten as

$$\ddot{\theta}(t) + 2\zeta\omega_n\dot{\theta}(t) + \omega_n^2\theta(t) = \frac{I_{bit}l_t}{I}\delta(t) \quad (101)$$

In the Laplace domain this transfers to

$$(s^2 + 2\zeta\omega_n s + \omega_n^2)\Theta(s) - (s - 2\zeta\omega_n)\theta(0) - \dot{\theta}(0) = \frac{I_{bit}l_t}{I} \quad (102)$$

Assuming zero initial conditions, this equation is solved for $\Theta(s)$ and transformed back into the time domain:

$$\theta(t) = -\frac{I_{bit}l_t}{I} \frac{1}{2\sqrt{(\zeta^2 - 1)\omega_n^2}} \left(\exp\left(t \left[-\sqrt{(\zeta^2 - 1)\omega_n^2} \right] - \zeta\omega_n\right) - \exp\left(t \left[\sqrt{(\zeta^2 - 1)\omega_n^2} \right] - \zeta\omega_n\right) \right) \quad (103)$$

For an underdamped system with $\zeta \leq 1$ and the damped eigenfrequency defined as $\omega_d = \sqrt{1 - \zeta^2} \omega_n$, this is rewritten as

$$\theta(t) = \frac{I_{\text{bit}} l_t}{I} \frac{1}{\sqrt{(\zeta^2 - 1) \omega_n^2}} \exp(-\zeta \omega_n t) \sin(\omega_d t) \quad (104)$$

As can be concluded from (104), the magnitude of the oscillation of the pendulum is linearly dependent on the magnitude of the impulse bit. Therefore, the mass moment of inertia is not required, and the thrust stand can be calibrated directly for impulse bits.

The calibration actuator is used to apply impulse bits of known magnitude to the pendulum arm. For every impulse bit, the maximum amplitude of the oscillation is recorded. Once the engine fires, the maximum amplitude of the resulting oscillation is measured, scaled to correct for the ratio between thruster arm and calibration arm, and interpolated between the calibrated data points. From this, the actual impulse bit is measured.

6.2.14.1 Required equipment

The thrust stand is set up in the vacuum chamber according to the steps described in Section 6.3. No additional equipment is required.

6.2.14.2 Procedure

1. Set up the thrust stand in its optimized configuration for the used thruster. The thruster and feed system need to be mounted and pressurized.
2. Perform TEST-120 (Section 6.2.2) to determine the required pulse lengths and required currents that are needed to generate a specific impulse bit.
3. Perform TEST-411 (Section 6.2.8) to determine the thrust stand sensitivity.
4. Perform TEST-331 (Section 6.2.6) to determine the damping coefficient of the thrust stand. From the damping coefficient the time required for the induced pendulum oscillations to damp out is determined.
5. In case the thruster shall be fired at a frequency higher than the eigenfrequency of the pendulum, TEST-332 needs to be performed. This test yields the correction factors that are required for force calculation.
6. Allow all electronic components to warm up. The warm-up time is **60 minutes**.

7. Check if all components are connected correctly. All prerequisite tests are performed at vacuum conditions. If the vacuum has been disturbed, close the vacuum chamber and switch on the pump.
8. Start LabView and open VI 'vacuumPressureReadOut.vi' or wait for at least 60 min for the vacuum chamber to reach its minimum pressure.
9. Start the VI and monitor the vacuum chamber pressure. Once the pressure has dropped to the minimal operating pressure, switch off the pump and allow the remaining atmosphere in the vacuum chamber to settle. A period of **5 minutes** is advised.
10. Pressurize the system according to the steps of [Section 6.3.4](#). Open the consecutive valves slowly and allow the feed system to fill.
11. Start VI 'feedPressureReadOut.vi' and monitor the pressure on the feed line. Tune the pressure regulator such that the required feed pressure is reached.
12. Close the VI. Once the settling time has expired, load VI 'TEST461.vi'. Change the settings according to the results of TEST-120, TEST-331 (and TEST-332) and set the filepath where the measurement file is saved.
13. Start the VI. A pulse of the required magnitude is generated, and the voltage over the calibration coil and the output signal of the displacement sensor are measured. The measurement duration is dependent on the damping ratio of the thrust stand and its eigenfrequency. This is repeated for all required pulses.
14. Once the VI has finished, it automatically saves the measurement file in the desired location.
15. If necessary, open the shut-off valve on the front side of the vacuum chamber to allow the chamber to fill with air. As soon as ambient pressure has been reached, the chamber door can be opened safely.

6.2.14.3 *Data-processing*

The data-processing for TEST-461 is performed using Matlab program 'TEST461.m'. Below a description of the algorithm is given.

1. The data are loaded into the memory and preprocessed for further usage.
2. Per pulse, the generated impulse bit is calculated from the voltage over the coil and its resistance ([Section 6.2.2](#)).

3. Using a peak-searching algorithm, the maximum value of the sensor signal, U_{\max} , is determined.
4. A linear function of the form $U_{\max}(I_{\text{bit}}) = \frac{\partial U_{\max}}{\partial I_{\text{bit}}} I_{\text{bit}}$ is fitted to the data.
5. The Standard Error of Estimation (SEE), coefficient of determination R^2 and standard error of the slope are calculated following the procedures of [Appendix E](#).

6.2.15 TEST-462: Impulse bit measurements

From the calibration of TEST-461, a calibration line of the form $U_{\max}(I_{\text{bit}}) = \frac{\partial U_{\max}}{\partial I_{\text{bit}}} I_{\text{bit}}$ is obtained. By measuring the maximum amplitude of the sensor signal, the magnitude of the generated impulse bit is calculated. The VI for this test requires adaptation for each specific thruster, as the control signals typically differ.

6.2.15.1 Required equipment

The thrust stand is set up in the vacuum chamber according to the steps described in [Section 6.3](#). No additional equipment is required.

6.2.15.2 Procedure

1. Perform the calibration of TEST-461 ([Section 6.2.14](#)).
2. Allow all electronic components to warm up. The warm-up time is **60 minutes**.
3. Check if all components are connected correctly. All prerequisite tests and calibrations are performed at vacuum conditions. If the vacuum has been disturbed, close the vacuum chamber and switch on the pump.
4. Start LabView and open VI 'vacuumPressureReadOut.vi' or wait for at least 60 min for the vacuum chamber to reach its minimum pressure.
5. Start the VI and monitor the vacuum chamber pressure. Once the pressure has dropped to the minimal operating pressure, switch off the pump and allow the remaining atmosphere in the vacuum chamber to settle. A period of **5 minutes** is advised.
6. Pressurize the system according to the steps of [Section 6.3.4](#). Open the consecutive valves slowly and allow the feed system to fill.
7. Start VI 'feedPressureReadOut.vi' and monitor the pressure on the feed line. Tune the pressure regulator such that the required feed pressure is reached.

8. Close the VI. Once the settling time has expired, load VI 'TEST462.vi'. Change the pulse duration and pulse amplitude of the control signal (engine dependent) and set the filepath where the measurement file is saved.
9. Start the VI. A pulse of the required magnitude and duration is generated. The measurement duration is dependent on the damping ratio of the thrust stand and its eigenfrequency. This is repeated for all required pulses.
10. Once the VI has finished, it automatically saves the measurement file in the desired location.
11. If necessary, open the shut-off valve on the front side of the vacuum chamber to allow the chamber to fill with air. As soon as ambient pressure has been reached, the chamber door can be opened safely.

6.2.15.3 Data-processing

The data-processing of TEST-462 requires the calibration curve of TEST-461 and the measurement file.

1. The data are loaded into the memory and preprocessed for further usage.
2. Using a peak-searching algorithm, the maximum value of the sensor signal, U_{\max} , is determined.
3. This maximum value is plugged into the calibration curve, $U_{\max}(I_{\text{bit}}) = \frac{\partial U_{\max}}{\partial I_{\text{bit}}} I_{\text{bit}}$, from which the I_{bit} is calculated.
4. The uncertainty of the estimate is obtained from the standard error of the slope:

$$I_{\text{bit}}|_{\max} = U_{\max} / \left(\frac{\partial U_{\max}}{\partial I_{\text{bit}}} - \hat{c} \Delta \frac{\partial U_{\max}}{\partial I_{\text{bit}}} \right)$$

$$I_{\text{bit}}|_{\min} = U_{\max} / \left(\frac{\partial U_{\max}}{\partial I_{\text{bit}}} + \hat{c} \Delta \frac{\partial U_{\max}}{\partial I_{\text{bit}}} \right)$$

where \hat{c} determines the size of the confidence interval, e.g. $\hat{c} = 2.326$ for a double sided 95% confidence interval and $n \rightarrow \infty$ [20].

6.3 FULL SETUP ASSEMBLY AND INTEGRATION

For most tests the entire system setup is required. In this section, the required equipment and generic assembly and integration procedure is described. Whenever necessary, steps of this procedure are skipped and/or replaced.

6.3.1 Required equipment

The equipment used in the full set up of the thrust stand is listed in [Figure 60](#). An overview of the components is given in [Figure 60](#).

PRODUCT	NO.	REMARKS
Thrust stand base plate with rests mounted	1	For assembly instructions, see the report of Perez-Grande [68].
Spring	1	—
Calibration masses	5	See Section 4.2.1 .
M8 nuts	4	Used to fasten calibration masses to the pendulum and the pendulum to the cross-beam.
M8 spacers	4	Used in combinations with the M8 nuts.
8 mm hose clamps	2	Used to fasten thermocouples to the pendulum arm.
Sensor target	1	Bolts are pre-mounted and only need to be fastened.
Calibration arm	1	3D-printed component.
M3 bolts	4	Used to mount the calibration arm to the sensor target.
Engine bracket	1	Custom for each thruster.
M5 bolt	1	Used to mount the bracket to the pendulum arm.
M5 spacer	1	Used in combination with the M5 bolt.
Cross-beam	1	—
Pendulum arm	1	—
Calibration coil	1	With banana plugs mounted to the flying leads.
Calibration coil holder	1	Construction of Boikon profiles.
Magnet holders	3	See Section 5.3.4 .
Sensors	2	capaNCDT CS1 and CS10
Sensor controller	1	capaNCDT 6530
Sensor bracket	1	—
Sensor holder	1	Construction of Boikon profiles.
Sensor cables	2	From the controller to the vacuum transition and from the vacuum transition to the sensor.

Continued on next page

Table 33 – Continued from previous page

PRODUCT	NO.	REMARKS
Thruster	1	In this case the PMT .
Power lines	2	For plus and minus side of circuit.
Feed line	1	To supply the thruster with propellant.
Cable ties	≥ 5	Cable ties are used to fasten feed and power lines to the pendulum and surrounding structures.
Capiler	1	–
Ruler	1	Range of ≥ 30 cm
Several drivers	1	Torx, philips and flat head.
Vacuum transition	1	Provided by Micro-Epsilon.
Vacuum transition flange	1	Custom made to also provide a transition for the thermocouples.

Table 33: Required equipment and hardware for full system assembly.

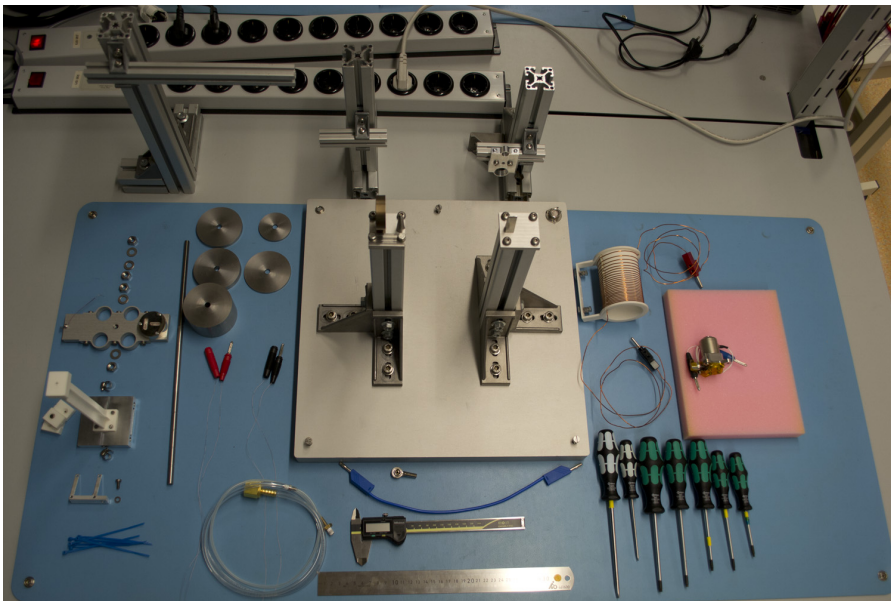


Figure 60: Required hardware for thrust stand assembly.

6.3.2 Selection of arm lengths and counter masses

For each thruster and required thrust range, the thrust stand needs to be optimized to provide the required performance. The optimization is done using a grid search algorithm that is implemented in Matlab

program 'optimizationStand.m' that is available on the accompanying disc in folder './Scripts/Measurement Plans/optimizationStand.m'. Below an explanation of the algorithm is given.

1. User definition of parameters:
 - a) requirements for the required range and the required accuracy;
 - b) parameters for the sample (engine mass M_e and thrust vector offset Δl_e);
 - c) whether a spring is connected to the thrust stand;
 - d) what sensor head is used (CS1 or CS10);
 - e) and the target setting (typically 'low' when the engine bracket / engine size allows so).
2. Calculation of counter mass properties:
 - a) Combinations of the counter masses are made to get total masses of approximately 1.10 kg to 1.75 kg in steps of 0.05 kg.
 - b) The total height of the stack and the center of gravity with respect of the top of the stack is calculated. The nuts and spacers used to mount the counter mass to the pendulum arm are included.
3. For every combination of counter masses, the performance of the thrust stand is calculated.
 - a) Iterate over all possible value for the engine arm length l_e in steps of 1 mm and determine all other arm lengths.
 - i. $l_1 = l_a - l_2$
 - ii. $l_c = l_1 - x_{cm}$
 - iii. $l_t = l_2 - \Delta l_t$, $\Delta l_t = 0.050$ m for setting 'low' or $\Delta l_t = 0.075$ m for setting 'high'.
 - iv. $l_e = l_2 - \Delta l_e$
 - v. $l_{br} = l_2 - \Delta l_{br}$
 - b) Calculate performance
 - i. Calculate the location of the CoG along the pendulum.
 - ii. Calculate the range using (16) (repeated):

$$T_R = (K + W_t l_{cg}) \frac{R}{2l_t l_E}$$

- iii. Calculate the accuracy using (15) (repeated):

$$\delta T = (K + W_t l_{cg}) \frac{\delta x}{l_t l_E} + \left| \left(\ddot{x} + \ddot{y} \frac{\delta x}{l_t} \right) M_t \frac{l_{cg}}{l_E} \right|$$

4. Iterate over all solutions and find the solution that meets the requirements. When a solution is found that provides a better accuracy at a range that is larger or equal to the required range, that solution is selected as the current best solution.
5. After iteration an error is shown when no solution is found that meets the requirements. The user then needs to change the definition of the search space by either connecting or disconnecting the spring and choosing a different sensor. If a solution is found, the best solution is shown and the engine arm length is given including the combination of counter masses that are required.

6.3.3 Placement and alignment of components

1. The program gives the length of the bottom half of the pendulum, l_2 , as output. Take the pendulum rod and measure from the bottom of the bare rod the distance $l_2 - 1.3$ cm. This is the length of the arm minus the distance from the bottom of the cross beam to the pivot and the thickness of the bolt and spacer. Screw on the bolt and spacer such that the top side hits the given mark ([Figure 61a](#)).
2. Screw on the cross beam, followed by another spacer and a nut. Check the distance to the bottom of the arm. This should be $l_2 - 0.5$ cm. Fasten the nuts tightly. Make sure the grounding wire is placed between the spacer and the top nut when fastening ([Figure 61b](#)).
3. If the spring needs to be mounted, place the required pin in the hole on the side of the cross beam. Use the two screws to fasten the pin lightly. Make sure that the grounding wire is wound around the top screw.
4. Place the arm horizontally on a flat surface and support the arm using a block.
5. Slide the sensor target in position and mount it to the arm using the pre-installed bolts ([Figure 61c](#)). These bolts require Torx 9 to be fastened. Make sure the bolts align with the slots in the pendulum. Also, keep in mind that there are two possible locations on the rod where the target can be fastened: a high and a low position. The position is chosen in accordance with the required engine clearance and bracket height. When fastened, move the block under the target.
6. Place the calibration magnet in the calibration arm. Make sure the correct magnet orientation is used in accordance with actuator calibration of TEST-110.

7. Mount the engine in its bracket. For the [PMT](#) spacing nuts are required to provide sufficient clearance from the pendulum arm.
8. Mount the bracket on the pendulum using the fastening screw. Fasten tightly so that the bracket can no longer rotate ([Figure 61d](#)).
9. Lift the pendulum and support it at both the target and the cross beam. The target is top heavy and has a tendency to rotate. Rotation of the rod causes the nuts that keep the cross beam in place to loosen.
10. Fit the pendulum on the pivots. Slide the pin on the spring when required.
11. Make sure that the engine feed system has sufficient clearance within the structure of the thrust stand.
12. Pick the required counter masses and measure the total thickness of the stack t_c . Place a bolt and nut on the top arm at a distance of $t_c + 0.8$ cm ([Figure 61e](#)) from the top. This is the height of the stack plus the thickness of a nut and bolt.
13. Place the counter masses on the top arm, starting with the heaviest and finishing with the lightest. A spacer and nut are placed on top to fasten the counter masses.
14. Align the pendulum arm vertically and fasten the pin tightly.
15. Place the thrust stand in the vacuum chamber and level it using the three leveling screws.
16. Place the sensor
 - a) Take the sensor head from its container and mount it in the sensor bracket. The sensor bracket can be pre-mounted on its holder ([Figure 61f](#)).
 - b) Place the sensor holder on the base plate of the thrust stand, such that the sensor is at approximately half its range from the target ([Figure 61g](#)).
 - c) Align it vertically such that the center of the sensor and the center of the target are aligned.
 - d) Align the sensor such that the target and the sensor plane are parallel.
 - e) Connect the cable from the sensor to the vacuum transition and from the transition to the controller. The controller analog outputs are connected to pins AI1 and AI8 on the [DAQ](#).

- f) Open National Instruments Measurement & Automation Explorer (MAX) and read out the signal in differential, continuous sampling mode. This is done via the menu on the left of the screen: *Devices and Interfaces* → *NI-DAQmx Devices* → *NI-PCI6229* → *Test panels* (in bar on top of the right screen).
 - g) Adjust the distance between the sensor and the target such that the sensor output voltage is close to 5 V. Proper adjustment is hard to do manually. Future setups require a linear stage with a micrometer for sensor alignment.
 - h) Stop the data acquisition and close MAX.
17. Mount the actuator coil
- a) Mount the coil on the coil holder and fasten the bolts lightly (Figure 61h).
 - b) Place the coil holder against the base plate, such that it is stable and cannot move.
 - c) Align the coil vertically, such that the cross on the back of the calibration arm aligns with the center line of the coil.
 - d) Adjust the coils horizontal position, such that the engagement distance is correct.
18. Place the dummy holder and mount the feed system to the pendulum. Use the dummy arm to guide and hold any wires.
19. Connect a grounding wire to the ESD contact on the base plate. The wire is then connected to one of the female banana plug connectors that is present in the vacuum chamber. Outside the vacuum chamber another set of female banana plugs is available. Using the appropriate equipment, the corresponding plug is connected to a grounding point. This has to be the same extension cord as the sensor controller is connected.

6.3.4 *Connecting the gas feed system*

The gas feed system is connected to the thruster via a system of pipes and tubes and several other components. In the description below the safety and operation guidelines are outlined. More information is available in the Facility Handbook 2 [76] that is available in the clean room and/or in the documentation available in the student room adjacent to the clean room facility. Always take into account the safety precautions. It is advised that new operators review the manual below carefully and review the instruction videos available [63].

6.3.4.1 *Ordering a new gas bottle*

If the current gas bottle is (almost) empty or no gas bottle is available, a new bottle has to be ordered. Instructions are given by Migliaccio [54] in the Facility Handbook 2 [76].

1. Contact the Gas Team of Delft University of Technology. This team is responsible for the ordering, transport and installation of gas bottles on the university. The team is contacted via phone on +31 (0) 15 27 86940.
2. Specify the required purity (e.g. 5.0) and the required volume (e.g. 10 L).
3. Specify the BAAN code L10-L13882 (check with secretary if this code is still current).
4. The gas team contacts the ordering party. Provide the contact person with the location of delivery.
5. If a cylinder is empty, the gas team also retrieves the bottle.

6.3.4.2 *Installation and connection of the gas bottle*

The new bottle is installed in the set up according to the following steps:

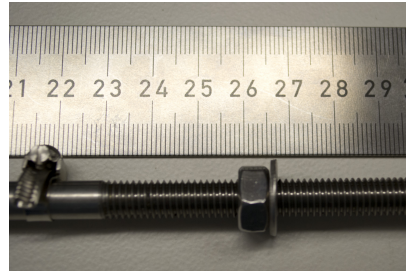
1. Install the cylinder on the feed system cart.
2. Fasten the cylinder using the available belts such that it is secure.
3. Clean the orifices with a dry, clean cloth to remove any debris that may be left.
4. Inspect the pressure regulator for damages and debris. A damaged pressure regulator may never be used.
5. Clean the pressure regulator orifices with a dry, clean cloth to remove any debris that may be left.
6. Connect the cylinder connection of the pressure regulator to the cylinder and fasten it with the appropriate size spanner or wrench. Do not use teflon tape or pipe dope to seal the connection.
7. Open the release adjusting spring (T-shaped knob) until it can rotate freely.
8. Close the shut-off valve on the pressure regulator and the consumption equipment.

9. Open the cylinder valve **slowly**. The high pressure gauge shows the cylinder pressure. Opening the valve too quickly results in rapid pressure and temperature increases.
10. Adjust the desired outlet pressure at the adjusting screw. The low pressure gauge shows the set pressure.
11. Open the shut-off valves of both the regulator and the consuming equipment slightly.
12. Correct the pressure setting in case of a pressure decrease.

6.3.4.3 *End of operation*

At the end of the operation, the feed system is shut down in the following sequence.

1. Close the cylinder valve and allow all remaining gas to evacuate through the consuming system.
2. Release the adjusting screw until it can rotate freely.
3. Close the shut-off valves at the pressure regulator up to the consuming equipment.
4. Make sure all pressurized parts of the feed system are depressurized.



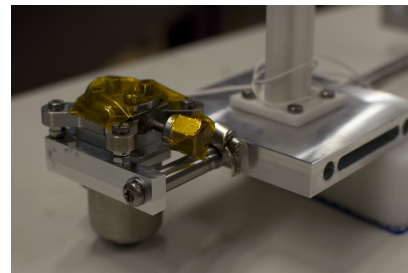
(a) Step 1



(b) Step 2



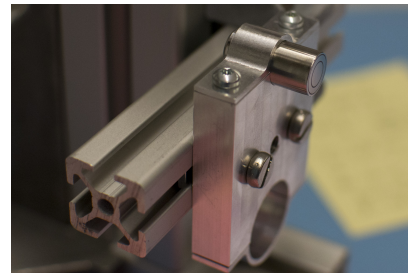
(c) Step 5



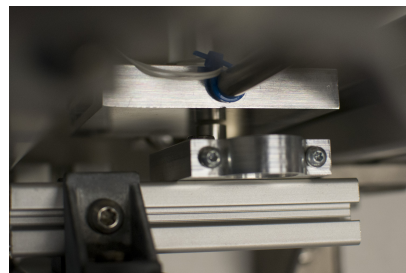
(d) Step 8



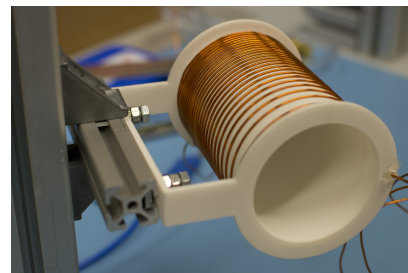
(e) Step 12



(f) Step 16a



(g) Step 16b



(h) Step 17a

Figure 61: Photos of the thrust stand assembly procedure.

EXPERIMENTAL RESULTS

The tests required for verification and validation as described in [Chapter 6](#) have been (partially) conducted. The results of these tests are discussed here. During the two week measurement period problems were encountered with the setup. As these problems influenced the way in which the tests were performed and influenced the achievable accuracies, these problems are discussed first. The obtained data are presented and discussed afterwards.

7.1 ENCOUNTERED HARDWARE PROBLEMS

During the measurement period, problems were encountered on multiple parts of the setup that were not foreseen or encountered before. These problems cover pressure transducers, thermocouples, the feed system and the [DAQ](#). In the presentation of the test results, it is mentioned when a test was influenced by a technical problem.

7.1.1 *Broken coil*

Fatigue caused the copper wire of the [VTDC](#) to break at a corner. The remaining copper wire was removed from the coil holder and reapplied. Hot glue was applied over the length of the coil to keep the wire in place and two dots of glue were applied at the corners to provide additional stiffness and prevent bending over the sharp edges of the coil holder.

7.1.2 *Pressure transducers*

The Omega Engineering PX139 was used to measure the pressure in the vacuum chamber. The transducer was tested by using it as a pressure gauge for ambient pressure. The ambient pressure was taken from data available from the [KNMI](#). It was found that at its nominal excitation voltage, the transducer gives a faulty reading of 800 mbar when ≈ 1013 mbar is expected. As the transducer is sensitive to its excitation voltage, the voltage was increased from 5 V to 5.6 V to get a proper reading. However, as only one reference pressure is available, it cannot be clarified whether the found difference is a pure offset, a pure scaling or a completely faulty reading. The pressure transducer could therefore not be used reliably to measure the vacuum pressure during measurements. It is advised that the transducer is shipped back to the manufacturer for re-calibration.

The vacuum pressure was determined based on timing. Before the measurement campaign, the approximate vacuum pressure was determined as a function of time. The results are plotted in [Figure 42](#). A pumping time of 1 hour was used as a reference time in which the minimum attainable pressure was realised.

Given sufficient time, the sensor could have been calibrated against the Omega Engineering PXM209 that was used to measure this pressure characteristic. More urgent problems with the [DAQ](#) have reprioritized the transducer problem. It should also be noted here, that this is a temporary solution as also the PXM209 is outside calibration.

7.1.3 *Thermocouples*

With the typical data acquisition setup available in the [DARTS](#) facility, thermocouples are connected to the SCB-68 terminal in differential mode. As a thermocouple can only be used to determine temperature differences between the terminal and the measuring tip, the absolute temperature at the terminal is required as well to be able to determine the temperature at the measuring location. The SCB-68 has a thermistor installed that can be used to determine the temperature of the terminal itself. In all acquisition modes available on the terminal, the thermistor returned a 0 V output. This indicates that either the thermistor or one of the connections is broken. As suggested in the test plans of [Chapter 6](#), an absolute temperature reference can be made using an ice bath and one additional thermocouple. Unfortunately, problems with the [DAQ](#) prohibited thermocouple measurements using the SCB-68 or SB-68LP.

7.1.4 *Data-acquisition system*

The used data-acquisition system showed multiple issues that severely influenced the acquisition capability. These problems are discussed in this section. All tried solution methods are included.

7.1.4.1 *Occasional clipping*

The capaNCDDT sensor system has an analog output voltage of 0 V to 10 V. It was noted during the initial tests and setup calibrations, that the signal is occasionally clipped at 7.3 V. To identify the cause of this issue, the entire measurement setup was disconnected. A Delta-Elektronika [PSU](#) was connected to the inputs of the [DAQ](#) and a DC signal was generated at arbitrary voltages between 0 V to 10 V. The problem reproduced multiple times on all tested channels. When measured in reversed polarity (connecting the negative terminal of the [PSU](#) to the positive terminal of the [DAQ](#) channel and vice versa),

the problem occurred occasionally. National Instruments is not familiar with the problem and the issue is addressed under reference #1361586.

The problem was addressed by using a 1 : 1 voltage divider constructed using two 10 k Ω resistors. The resistors are chosen at this level to limit the drawn current to 1 mA. The voltage divider effectively reduced the [FSO](#) of the [capaNCDT](#) from a range of 0 V to 10 V to a range of 0 V to 5 V. This also increased the uncertainty of the measurements.

7.1.4.2 *Ghosting / crosstalk*

It was noted that when the sensor was connected and registered an oscillating signal (caused by the oscillating pendulum), this oscillation was also apparent on all the other channels. This can be caused by two mechanisms: ghosting or crosstalk. To eliminate the problem, the guidelines of National Instruments [59] were followed.

Ghosting has the effect of copying the oscillation onto another channel and simultaneously lowering the (mean) voltage on that channel [60]. This was tested by connecting a [PSU](#) that provided a DC signal in the 0 V to 5 V range to an empty channel, while the [capaNCDT](#) system was connected to the [DAQ](#) as well. After confirmation that these effects were indeed apparent, the proposed solution methods were tried.

1. Ghosting can be caused by an output impedance of the sensor of ≥ 1 k Ω . The [capaNCDT](#) system has an output impedance of ≈ 100 Ω , but the voltage divider introduces an output impedance of 10 k Ω . As the voltage divider is required due to the clipping issue, a unity gain buffer is installed. The buffer is constructed using an operational amplifier [81] that has a very low (ideally 0 Ω) output impedance. Lowering the output impedance did not remedy the problem.
2. To test if the problem was caused in the [DAQ](#) or in the circuitry between the sensor and the [DAQ](#), the sensor was replaced by a signal generator. A 1 Hz sine wave with an amplitude of ≈ 2 V and an offset of ≈ 2 V was generated. The problem was still apparent, eliminating the sensor as the cause.
3. Improper grounding of the signal can also cause ghosting. Both the sensor and the PC that holds the PCI 6229 [DAQ](#) card were grounded on the same socket. It was also confirmed that the negative terminal of the sensor cable was indeed the same as the ground of the sensor controller.

4. The PCI 6229 does not have the ability to measure multiple channels simultaneously. instead it uses a multiplexer that quickly alternates between all channels. Ghosting can occur when the previous channel that was scanned did not have sufficient time to unload its potential to ground. The remaining potential is then dumped via the current channel, resulting in ghosting. This problem can be eliminated by shorting the intermediate channel with ground, such that all remaining potential can be dumped to ground instead of the next channel. This was tried, even with multiple intermediate channels. This was not succesful. Also introducing dummy channels in the measurement software did not remedy the problem. Dummy channels are guaranteed to be multiplexed by the [DAQ](#) to ensure dumping of remaining energy.
5. The effects of faulty terminals were eliminated by replacing the used SB-68LP by two other copies and by the SCB-68. The shielded terminal SCB-68 was also used to make sure that the problem was not caused by electromagnetic interference between cables.

Multiple discussions on the measurement setup with dr. ir. Chris Verhoeven and Nuno Baltazar dos Santos did not unveil any other causes or potential remedies. It is therefore concluded that the problem cannot be fixed by the tried means and that the [DAQ](#) should be shipped back to National Instruments for inspection.

*A support call is
open under reference
#1361586.*

The apparent effect has as a consequence that no other sensors can be connected to the [DAQ](#) apart from the displacement sensor. As a temporary solution a USB powered [DAQ](#) system, the National Instruments USB-6008, was used to acquire data from the PXM209 (used to measure the feed pressure) and the Brooks 5850S [MFC](#).

7.2 SETUP AS CALCULATED BY PROGRAM

The optimization program is used to tune the setup such that it provides the best resolution at a range equal to or larger than the set requirements. Because the [PMT](#) can produce up to 1.2 mN of thrust at the achievable mass flows, the range should be ≥ 1.2 mN. In the design stage it was already estimated that the performance of the thrust stand in this range exceeds ≤ 10 μ N. This is used as a threshold to pre-select solutions in the optimization. In [Table 34](#), the parameters used and the optimized parameters are listed.

PARAMETER	VALUE	NOTES
M_e	0.2148 kg	-
$\Delta l_e = l_2 - l_e$	0.0131 m	From PMT CAD drawings.
K	0.64	Spring connected.
l_a	0.37 m	-
M_a	0.1556 kg	-
l_b	0.001 m	Estimated based on geometry.
M_b	0.225 kg	-
$\Delta l_{ta} = l_2 - l_{ta}$	0.075 m	Preset
M_{ta}	0.1521 kg	Including calibration arm and magnet holder with S-06-06-N magnet.
$\Delta l_{br} = l_2 - l_{br}$	0.001832 m	Determined from CAD drawings.
Δx	$1.15 \cdot 10^{-6}$ m	CS1 accuracy
R	$1 \cdot 10^{-3}$ m	CS1 range
l_2	0.250 m	Optimized
M_c	1.6768 kg	Optimized, 1.2 + 0.3 + 0.2 + 0.1 kg masses.
ΔT	3.1 μ N	Achievable accuracy over full range.
R_T	1.338 mN	Achievable thrust range.

Table 34: Optimized setup parameters for measurements with [PMT](#).

7.3 RESULTS

In this section, the results of the performed tests and changes to the test setup required for the specific tests are discussed. A list of all used data files is given in [Appendix J](#).

7.3.1 TEST-110: Force-current calibration

The calibration coil was calibrated following the procedures of TEST-110 ([Section 6.2.1](#)). For each set of magnets, the calibration was repeated four times. The calibration curves are determined based on the data points of the four sets combined, assuming a function $F = S_{\text{actuator}}i$. The measured masses are converted into force by multiplication of the read-off weight by 9.80665 m s^{-2} . The [SEE](#) and standard error of the estimator are calculated using the techniques described in [Appendix E](#).

The results for the high end force range are depicted in [Figure 62](#). Based on the measurements, a sensitivity of $833 \mu\text{N A}^{-1}$ is found with a [SEE](#) of $6 \mu\text{N}$ and a standard error of the estimator $s = 0.32 \mu\text{N A}^{-1}$. The parameters of the estimation are listed in [Table 35](#).

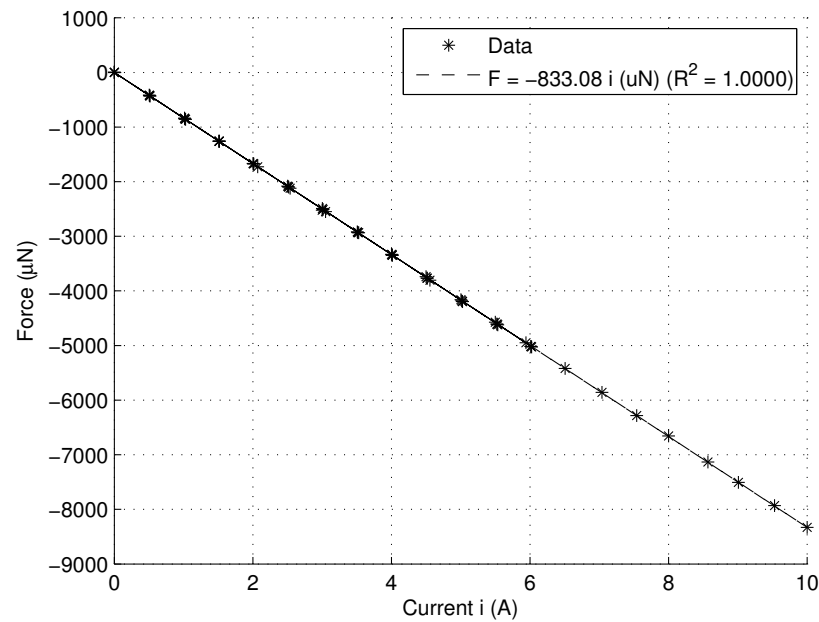


Figure 62: Calibration curve for actuator using S-06-06-N magnet. Fit of form $F = ai$. Based on four datasets.

For the middle force range, a sensitivity is found of $60.5 \mu\text{N A}^{-1}$ with a [SEE](#) of $4.1 \mu\text{N}$ and a standard error of the estimator $s = 0.13 \mu\text{N A}^{-1}$.

The calibration curve is depicted in Figure 63. The corresponding parameters are listed in Table 35. It was noticed that the scale occasionally shows 'sticky' behavior. Even though the current through the coil was changed, the scale would stay at its previous reading for more than 10 s before it suddenly changed. This was not caused by the actuator, as the monitored current did indeed change immediately when it was set. No cause was found for this behavior and it was not noticed in other occasions.

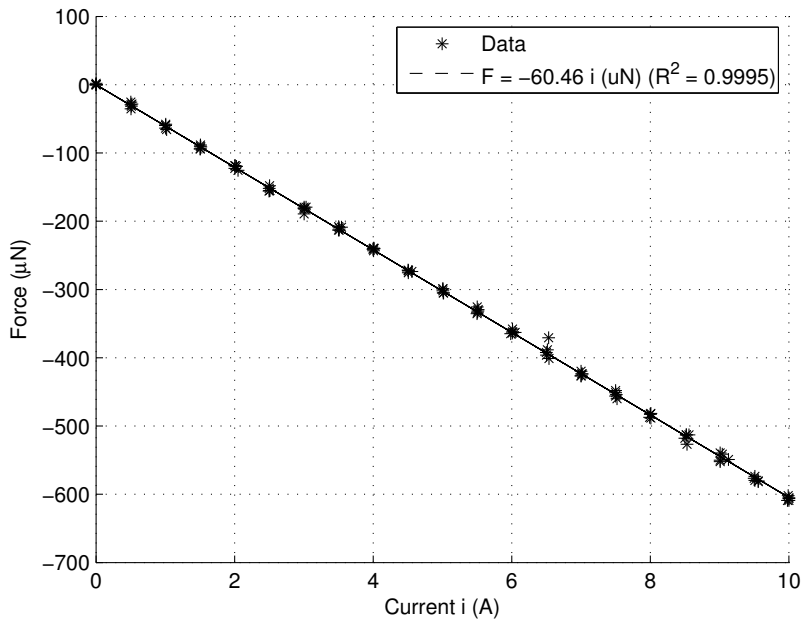


Figure 63: Calibration curve for actuator using two S-02-02-N magnet. Fit of form $F = ai$. Based on four datasets.

Similarly, the results for the low end force range are depicted in Figure 64. A considerably larger relative spread is apparent from the data. For the linear fit, a sensitivity of $5.93 \mu\text{N A}^{-1}$ is found with a SEE of $5.52 \mu\text{N}$ and a standard error of the estimator of $0.24 \mu\text{N A}^{-1}$. The parameters of the fit are listed in Table 35. During the calibration it was noted that the used scale required long settling times, especially when the actuator was used at lower currents.

Comparing the found sensitivities to the predicted sensitivities, the following is observed. In Section 5.3.4, in which $\frac{\partial B}{\partial x} = 0.0048 \text{ T m}^{-1}$ is assumed, a sensitivity of $S_a = (9.120 \cdot 10^{-4} \pm 0.672 \cdot 10^{-4}) \text{ NA}^{-1}$ is predicted for using a single S-06-06-N magnet. The measured value of $8.33 \cdot 10^{-4} \text{ NA}^{-1}$ is not within this interval. For two S-02-02-N magnets a sensitivity of $S_a = (7.008 \cdot 10^{-5} \pm 4.224 \cdot 10^{-5}) \text{ NA}^{-1}$ is predicted. The found value of $6.046 \cdot 10^{-5} \text{ NA}^{-1}$ is within this interval on the lower end. For two S-1.5-0.5-N magnets a sensitivity $S_a = (9.600 \cdot 10^{-6} \pm 3.456 \cdot 10^{-6}) \text{ NA}^{-1}$ is predicted, while a value

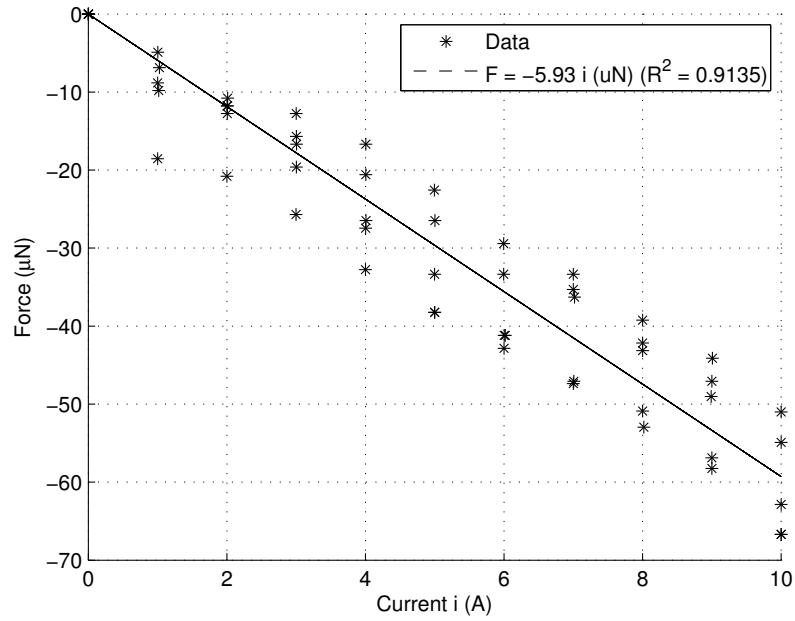


Figure 64: Calibration curve for an actuator that uses two S-1.5-0.5-N magnets. Fit of form $F = ai$. Based on four data sets.

PARAMETER	HIGH	MID	LOW
Sensitivity ($\mu\text{N A}^{-1}$)	-833.08	-60.46	-5.93
s_β ($\mu\text{N A}^{-1}$)	0.32	0.13	0.24
$\mu_{\text{residuals}}$ (μN)	0.01	-0.20	0.58
$\sigma_{\text{residuals}}$ (μN)	6.19	4.12	5.49
SEE (μN)	6.19	4.13	5.52

Table 35: Calibration parameters for the actuator using one S-06-06-N magnet (High), two S-02-02-N magnets (Mid) or two S-1.5-0.5-N magnets (Low).

of $S_a = 5.93 \cdot 10^{-6} \text{N m}^{-1}$ is found. This value is also outside the predicted interval. From this is concluded that the gradient of the magnetic field, $\frac{\partial B}{\partial x}$, is likely smaller than 0.0048 T m^{-1} . The actual value cannot be determined based on this measurement, and additional research is required. Using magnetometers the strength of the magnitude of the magnetic field vector can be measured from which the gradient can be derived. The deviation is explained by geometrical differences between the model and the actual coil. Although great care has been taken to guarantee the turn-geometry resembles the modeled geometry as close as possible, manufacturing inaccuracies introduce variations from the modeled design.

Looking at the found standard deviation of the residuals of the fits, it is concluded that the predicted accuracy is not guaranteed from the current measurements. The 3σ values exceed the calculated achievable accuracies presented in [Section 5.3.4](#) based on PSU performances. These larger spreads can be traced back to several sources. First, there is the accuracy of the scale. At a repeatability of 0.1 mg and a linearity of 0.2 mg a total uncertainty of $\sqrt{0.2^2 + 0.1^2} \approx 0.22$ mg or equivalently 2.2 μN uncertainty is introduced. However, this would be the uncertainty when the scale is calibrated and when the draft shield is mounted. The calibration of the scale has expired and, as can be read in [Section 6.2.1](#), the draft shield has been removed. Therefore, this uncertainty is expected to be larger. Second, there is also operator error that needs to be considered. Read-off errors may be introduced or the setup may be influenced by for example breathing or letting ones arm rest on the table, which results in a slight tilt of the scale, in turn resulting in a faulty reading.

7.3.2 TEST-120: Impulse calibration

The first series of TEST-120 was performed to proof the actuator is capable of generating small impulse bits. The second series, in which the thrust stand is also set up, was skipped due to time constraints. For TEST-120, 20 pulses of 20 ms were generated with a duty cycle of 50% as shown in [Figure 65](#). Each control pulse caused a block pulse of current through the actuator coil of increasing magnitude. As can be seen in [Figure 66](#), the behavior of the current resembles the modeled behavior ([Section 6.2.2](#)) very well.

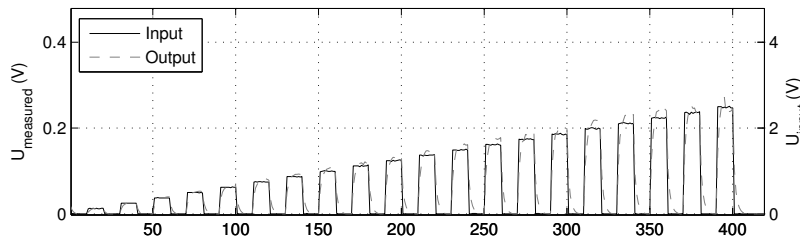


Figure 65: Generated and measured pulses for impulse bit calibration.

As described in [Section 6.2.2](#), two methods are available to convert the measured voltage over the coil into the coil current that is required to calculate the delivered impulse. Both methods have been used and the results are compared in [Figure 67](#). Given the time scale of the pulses and the responses, the difference between both methods is negligible. When the inductance of the VTDC is considerably larger than that of an ideal solenoid of similar dimensions and turns, a larger difference is expected.

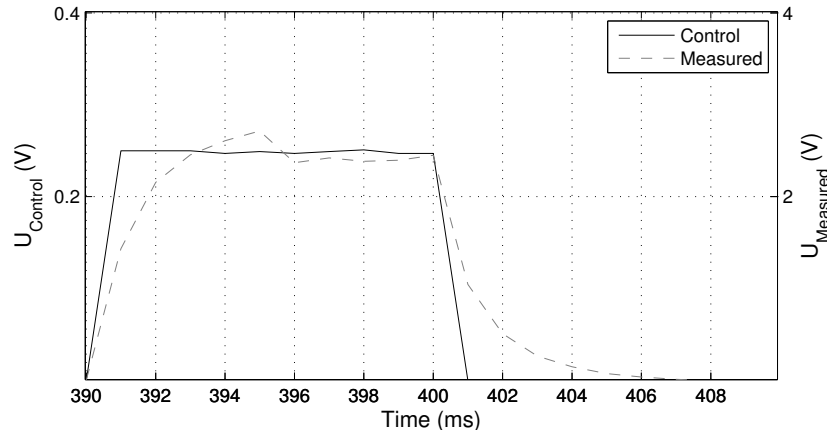


Figure 66: Generated and measured pulses for impulse bit calibration. Graph is zoomed into the last section of the data to show the effects more clearly.

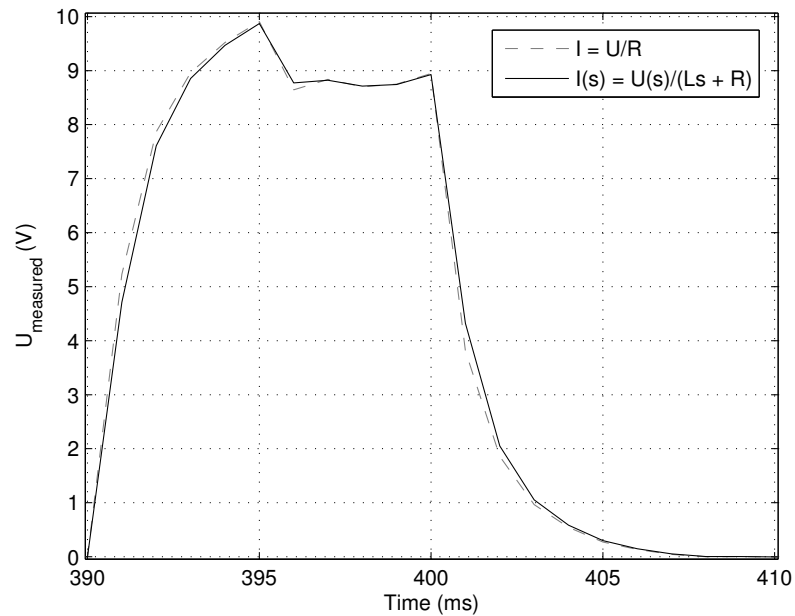


Figure 67: Comparison between methods to obtain current from transient voltage.

Based on the calculated current in the coil, the impulse bit and the corresponding uncertainty is calculated using [Equation 76](#) and [\(80\)](#), respectively. From actuator calibrations the following sensitivities (99% confidence) are used: $\frac{dF}{di} = (833.08 \pm 0.82) \text{ N A}^{-1}$ using an S-06-06-N magnet, $\frac{dF}{di} = (60.46 \pm 0.33) \text{ N A}^{-1}$ using two S-02-02-N magnets, $\frac{dF}{di} = (5.93 \pm 0.62) \text{ N A}^{-1}$ using two S-0.5-1.5-N magnets. The coil has a resistance of $(0.274 \pm 0.001) \Omega$ and an uncertainty in measured voltage $\Delta U = 366 \mu\text{V}$. The calculated impulse bits are presented in

Table 36. From the table it is concluded that the actuator is capable of delivering an impulse bit of 1 μNs at a pulse length of 10 s in agreement with requirement RANGE-2. To reach impulse bits of 1 mNs the impulse length has to increase to 200 ms as shown in [Section 7.3.15](#). The accuracies of the delivered impulses are in agreement with requirement ACCUR-2.

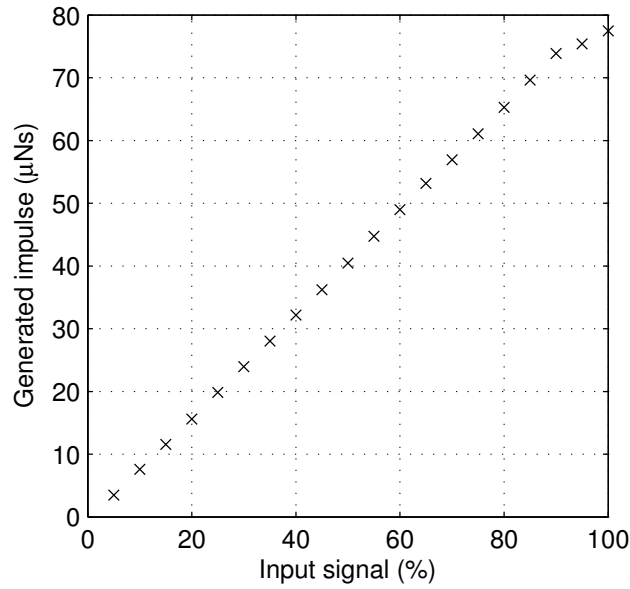


Figure 68: Generated impulse bits as a function of given control signal. Signal is normalized for a specific coil such that a 100% signal corresponds to an estimated 10 A pulse.

S-06-06-N magnet			Two S-02-02-N magnets			Two S-0.5-1.5-N magnets		
I_{BIT} ($\mu\text{N s}$)	ΔI_{BIT} ($\mu\text{N s}$)	ΔI_{BIT} (%)	I_{BIT} ($\mu\text{N s}$)	ΔI_{BIT} ($\mu\text{N s}$)	ΔI_{BIT} (%)	I_{BIT} ($\mu\text{N s}$)	ΔI_{BIT} ($\mu\text{N s}$)	ΔI_{BIT} (%)
3.48E+00	3.73E-02	1.07	2.53E-01	3.86E-03	1.53	2.48E-02	2.83E-03	11.40
7.60E+00	5.64E-02	0.74	5.52E-01	6.61E-03	1.20	5.41E-02	5.99E-03	11.07
1.16E+01	7.47E-02	0.65	8.38E-01	9.24E-03	1.10	8.22E-02	9.02E-03	10.97
1.56E+01	9.47E-02	0.61	1.13E+00	1.20E-02	1.06	1.11E-01	1.21E-02	10.93
1.98E+01	1.13E-01	0.57	1.44E+00	1.48E-02	1.03	1.41E-01	1.54E-02	10.90
2.40E+01	1.32E-01	0.55	1.74E+00	1.75E-02	1.01	1.71E-01	1.86E-02	10.88
2.80E+01	1.51E-01	0.54	2.03E+00	2.02E-02	0.99	2.00E-01	2.17E-02	10.87
3.22E+01	1.70E-01	0.53	2.33E+00	2.30E-02	0.98	2.29E-01	2.49E-02	10.86
3.62E+01	1.89E-01	0.52	2.63E+00	2.57E-02	0.98	2.58E-01	2.80E-02	10.85
4.05E+01	2.09E-01	0.52	2.94E+00	2.85E-02	0.97	2.88E-01	3.12E-02	10.84
4.47E+01	2.29E-01	0.51	3.25E+00	3.14E-02	0.97	3.19E-01	3.45E-02	10.84
4.90E+01	2.48E-01	0.51	3.55E+00	3.42E-02	0.96	3.49E-01	3.78E-02	10.83
5.31E+01	2.68E-01	0.50	3.86E+00	3.70E-02	0.96	3.78E-01	4.10E-02	10.83
5.69E+01	2.86E-01	0.50	4.13E+00	3.96E-02	0.96	4.05E-01	4.39E-02	10.83
6.11E+01	3.04E-01	0.50	4.43E+00	4.23E-02	0.95	4.35E-01	4.71E-02	10.83
6.53E+01	3.24E-01	0.50	4.74E+00	4.51E-02	0.95	4.65E-01	5.03E-02	10.82
6.96E+01	3.44E-01	0.49	5.05E+00	4.80E-02	0.95	4.96E-01	5.36E-02	10.82
7.39E+01	3.65E-01	0.49	5.36E+00	5.09E-02	0.95	5.26E-01	5.69E-02	10.82
7.54E+01	3.71E-01	0.49	5.47E+00	5.18E-02	0.95	5.37E-01	5.81E-02	10.82
7.75E+01	3.81E-01	0.49	5.62E+00	5.32E-02	0.95	5.52E-01	5.97E-02	10.82

Table 36: Estimated deliverable impulse bits with a pulse length of 10 s. From actuator calibrations the following sensitivities (99% confidence) are used: $\frac{dF}{dt} = (833.08 \pm 0.82) \text{ N A}^{-1}$ using a S-06-06-N magnet, $\frac{dF}{dt} = (60.46 \pm 0.33) \text{ N A}^{-1}$ using two S-02-02-N magnets, $\frac{dF}{dt} = (5.93 \pm 0.62) \text{ N A}^{-1}$ using two S-0.5-1.5-N magnets. The coil has a resistance of $(0.274 \pm 0.001) \Omega$. The uncertainty in measured voltage is 366 μV .

7.3.3 TEST-200: Feed system leak test

The system was tested for leaks following the procedures of TEST-200 (Section 6.2.3). Below the found leaks and the corresponding fixes are discussed shortly.

1. Relief valve and filter.
The leaks were solved by retightening the fittings of the components and reversing the rubber seals.
2. Vacuum transition of the gas feed.
The connection of the gas feed system inside the vacuum chamber was leaky. The NPT connection was made leak tight using three windings of vinyl tape on the tapered thread according to SwageLok instructions [34].
3. Feed system transition from large to small diameter hose.
The feed system includes a transition from a large diameter hose to a small diameter hose that feeds to the engine. This transition was found to be leaky. This was remedied by using two turns of vinyl tape on the threads of transition. The fixed transition is depicted in Figure 69a.
4. Connection to the engine.
The transition from the feed system to the engine was found to be leaky by audible hissing. The was remedied by applying two layers of vinyl tape to the transition. Once tightened wrench tight, the leak was no longer audible. As the PMT may not be exposed to fluids externally, this leak was not checked using a bubble test. Photos of the feed system connection are shown in Figure 69b and Figure 69c.

Once the leaks were fixed, no feed pressure drop was noticed over a period of 30 min.

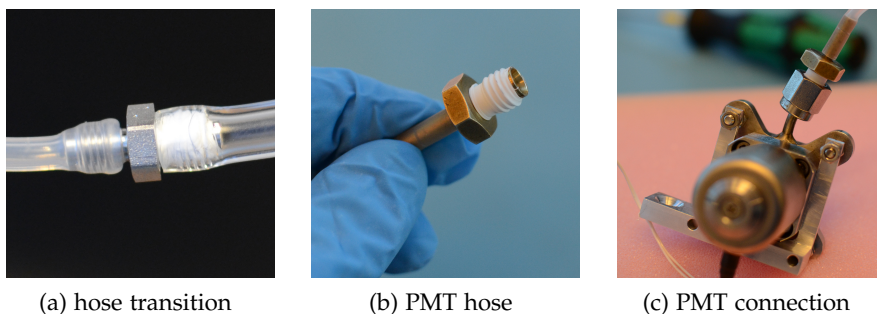


Figure 69: Photos of the leak fixes.

7.3.4 TEST-310: Characterization of environmentally induced noise

Following the plan of [Section 6.2.4](#) TEST-310 has been conducted. The test gives insight in the environmentally induced noise and the effects on the thrust stand output.

It should be noted that the noise content of the signal is largely composed of an oscillation of the pendulum at its (damped) natural frequency. At time scales in the order of seconds, this oscillation is clear as also depicted in [Figure 70](#). This oscillation does seemingly not damp out and is always present. On top of this oscillation, random noise components are present that are caused by random vibrations induced via the environment and the measurement chain. The random components result in an absolute deviation of approximately $60 \mu\text{N}$ in the current setup. The amplitude of the resonance is variable due to a beat that is present in the signal.

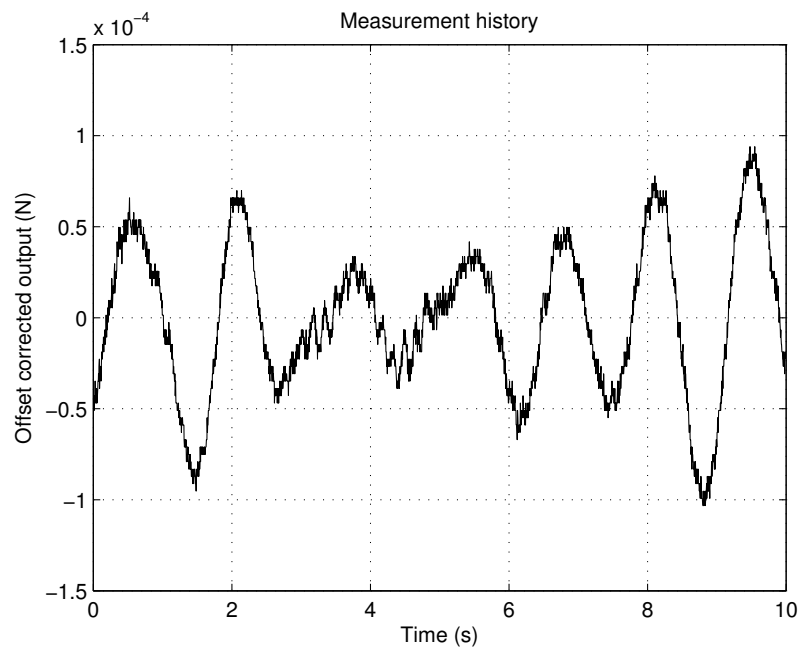


Figure 70: Ten second sample of noise measurement in the first orientation. Measurements taken on 14 November 2013 from 09:53 to 10:53 in the morning. Calibrated sensitivity $S_s = 248.395 \pm 0.976 \text{ V N}^{-1}$.

In accordance with the measurement plan, the noise content has been measured in two directions. The results for both orientations are presented in [Figure 71](#) and [Figure 72](#), respectively. For both series the time signal of the measured thrust is given which is normalized for an averaged offset. Also, the single sided Fourier transform is given in both figures. This transform is used to determine what harmonics are present in the signal at what frequencies. This aids in the determination of noise sources. In [Table 37](#), the peaks that are identified

are listed with their frequencies and corresponding magnitudes. Frequencies that are common to both series are highlighted. The most energy is present in the strongest and broadest peak which is around the pendulum natural frequency at approximately 0.6 Hz.

ORIENTATION 1		ORIENTATION 2	
f (Hz)	F (N)	f (Hz)	F (N)
0,60	$6,5 \cdot 10^{-5}$	0,61	$3,0 \cdot 10^{-4}$
0,83	$1,5 \cdot 10^{-5}$		
1,12	$3,2 \cdot 10^{-6}$		
		2,67	$2,5 \cdot 10^{-7}$
3,16	$2,6 \cdot 10^{-7}$	3,17	$2,3 \cdot 10^{-7}$
4,20	$9,4 \cdot 10^{-8}$		
		5,02	$3,8 \cdot 10^{-7}$
6,31	$2,5 \cdot 10^{-7}$	6,33	$2,9 \cdot 10^{-7}$
6,85	$1,9 \cdot 10^{-7}$		
		10,47	$1,1 \cdot 10^{-7}$
		12,03	$1,6 \cdot 10^{-7}$
13,81	$7,5 \cdot 10^{-8}$	13,88	$1,4 \cdot 10^{-7}$
20	$4,0 \cdot 10^{-8}$		
22,41	$1,3 \cdot 10^{-7}$		
23,48	$1,8 \cdot 10^{-7}$		
26,17	$1,5 \cdot 10^{-7}$	26,04	$2,3 \cdot 10^{-7}$
49,97	$3,9 \cdot 10^{-7}$	49,99	$4,5 \cdot 10^{-7}$
		85 – 95	$4,0 \cdot 10^{-8}$
95 – 100	$4,00 \cdot 10^{-8}$		

Table 37: The noise components of the thrust signal as measured in TEST-310 for both orientations. Common frequencies are highlighted.

It is apparent from the data, that the noise content in the first orientation ($\sigma = 1.5 \cdot 10^{-4}$ N) is lower compared to the second orientation ($\sigma = 5.5 \cdot 10^{-4}$ N). This is counter intuitive because the stiffness of both the optical table and the building are lower in this orientation compared to the second orientation.

It is expected that some of the peaks that appear in the spectral density are caused by the natural movement of the building. This is confirmed by a first order estimate via the analysis shown below. The building is approximated by a slender, thin walled tube with a plan-form of 40×10 m² (h \times w). At 13 storeys tall, the building is estimated

to be 45.5 m high (3.5 m/storey). The natural frequency of a cantilever beam is found from classical beam theory

$$\omega_n = \alpha_n^2 \sqrt{\frac{EI}{mL^4}} \quad (105)$$

where $\alpha_n = \{1.875; 4.694; 7.885\}$ for the first, second and third eigenmode, respectively, E the Young's modulus in Pa, I the moment of inertia about the axis of vibration in m^4 , m the total mass in kg which is assumed to be homogeneously distributed along the beam and L the length of the beam in m. For concrete a Young's modulus of $13 \cdot 10^9$ Pa is assumed, as well as a density of 2400 kg m^{-3} . It is assumed that between two storeys is a concrete floor of 30 cm thick. The walls have the same thickness as the floors. From this, the total volume of the structure is estimated at

$$\begin{aligned} V &= V_{\text{floors}} + V_{\text{walls}} \\ &= n_{\text{floors}} t ((h - 2t)(w - 2t)) + L(hw - (h - 2t)(w - 2t)) \\ &= 13 \cdot 0.3 ((40 - 2 \cdot 0.3)(10 - 2 \cdot 0.3)) \\ &\quad + 45.5(40 \cdot 10 - (40 - 2 \cdot 0.3)(10 - 2 \cdot 0.3)) \approx 2793 \text{ m}^3 \end{aligned}$$

With an average density of 2400 kg m^{-3} this equates to a total mass of the structure of 6703258 kg. The total mass is assumed to be 20% higher than this, due to furniture, equipment etc. The total mass of the building is 8043909 kg. For this approximation, it is assumed that only the walls provide bending stiffness. The corresponding moment of inertia in lateral direction of the building (in plane of motion in orientation 1) is calculated to be

$$\begin{aligned} I_1 &= 2 \left(\frac{1}{12} wt^3 + \frac{1}{12} ht^3 + htw^2 \right) \\ &= 2 \left(\frac{1}{12} \cdot 10 \cdot 0.3^3 + \frac{1}{12} \cdot 40 \cdot 0.3^3 + 40 \cdot 0.3 \cdot 10^2 \right) \approx 2400 \text{ m}^4 \end{aligned}$$

In the second orientation, the moment of inertia is

$$\begin{aligned} I_2 &= 2 \left(\frac{1}{12} ht^3 + \frac{1}{12} wt^3 + wth^2 \right) \\ &= 2 \left(\frac{1}{12} \cdot 40 \cdot 0.3^3 + \frac{1}{12} \cdot 10 \cdot 0.3^3 + 10 \cdot 0.3 \cdot 40^2 \right) \approx 9600 \text{ m}^4 \end{aligned}$$

Plugging the found figures into (105) yields the resonance frequencies presented in Table 38. It should be noted that the first resonance frequencies are (very) close to the found damped natural frequency of the pendulum of 0.6055 Hz (Section 7.3.8). As beat is caused by a superposition of waves of similar frequencies, the building resonance may give rise to the found beat in the signal of the thrust stand.

ORIENT.	MODE	ω (rad s ⁻¹)	ω (Hz)
1	1	3.42	0.544
1	2	21.4	3.41
1	3	60.5	9.62
2	1	6.84	1.08
2	2	42.8	6.82
2	3	121	18.2

Table 38: First order estimated resonance frequencies of the high rise building of Aerospace Engineering (building 62), Delft University of Technology.

Peaks are found in the spectral densities of both sets. The sets have peaks at ≈ 0.6 Hz and at 50 Hz in common, the former being the damped natural frequency of the pendulum and the latter caused by electromagnetic interference of the power system. It is interesting to note that a broad peak exists around 95 Hz to 100 Hz in the first orientation and a similar peak around 85 Hz to 95 Hz in the second orientation. The causes for these peaks are yet unknown. In case both peaks are caused by a common source, the shift in measured frequency can be explained through different damping coefficients. As is known from classical vibration theory, the damped natural frequency is linked to the natural frequency via $\omega_d = \omega_n \sqrt{1 - \zeta^2}$. If the damping coefficient changes dependent on the orientation of the thrust stand, the frequency is modulated. A possible damping source that has different damping coefficients depending on the orientation is the optical table on which the vacuum chamber rests. In the first orientation, the pendulum moves in the short direction of the table - the direction in which the table has its smaller mass moment of inertia and thus the smaller inertial damping. A smaller damping coefficient results in a higher frequency. Similarly, in the second orientation the thrust stand moves in the long direction of the table - the direction in which the table has the larger mass moment of inertia.

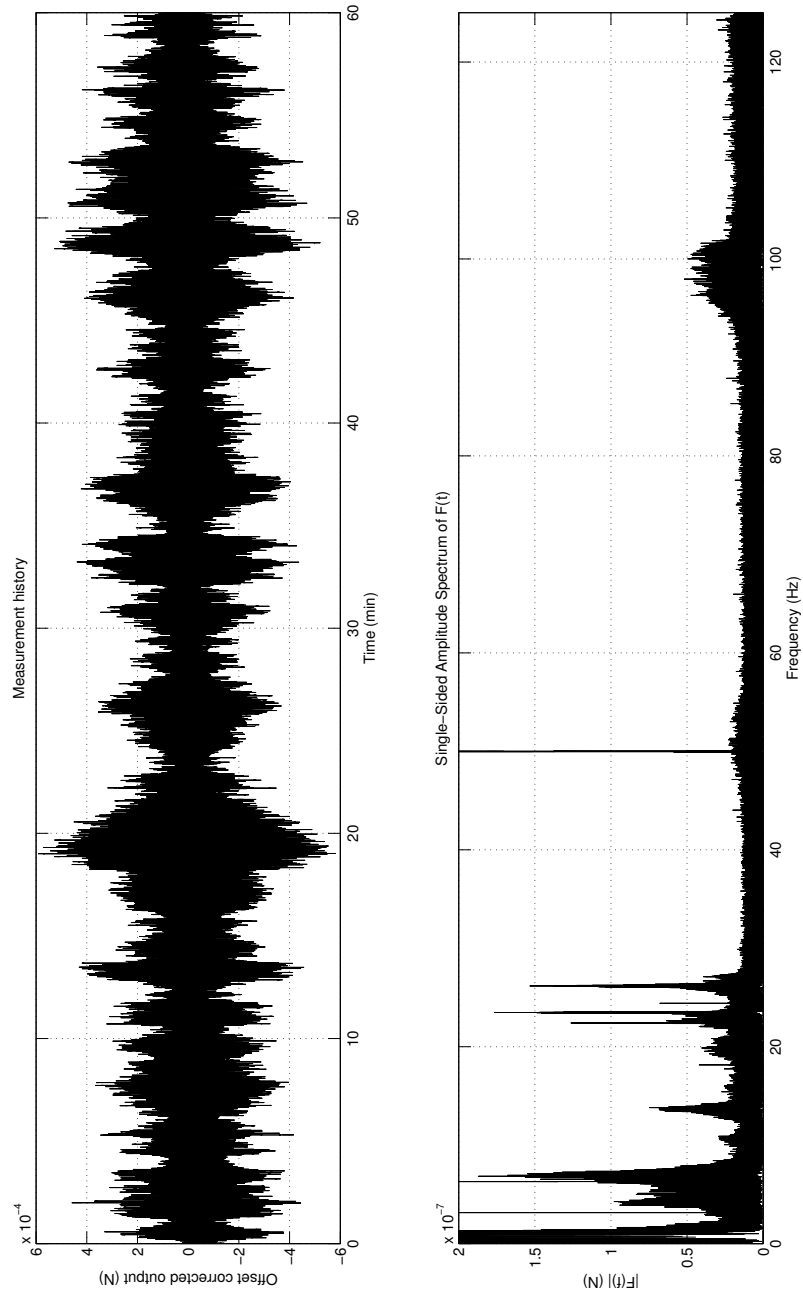


Figure 71: Noise measurement in the first orientation. Measurements taken on 14 November 2013 from 09:53 to 10:53 in the morning. Calibrated sensitivity $S_s = 248.395 \pm 0.976 \text{ V N}^{-1}$.

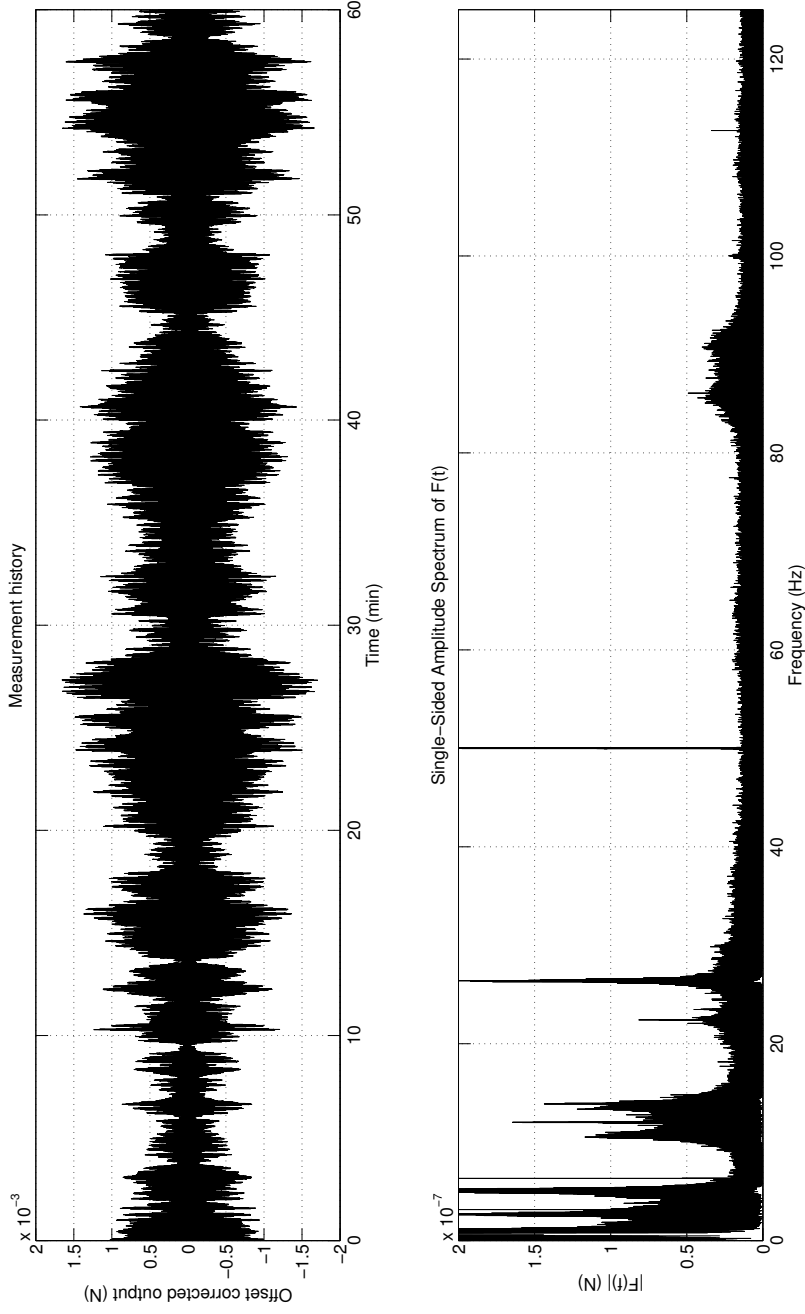


Figure 72: Noise measurement in the second orientation. Measurements taken on 14 November 2013 from 12:35 to 13:35 in the afternoon. Calibrated sensitivity $S_s = 264.840 \pm 1.413 \text{ V N}^{-1}$.

From the total noise amplitude it is concluded that orientation 1 is the preferential direction for thrust measurements, as the total noise content is lower. The random noise present on both natural oscillations, however, does not seem to differ by inspection. Therefore, when the natural oscillation is removed, new noise measurements have to show if a preferential direction still exists.

7.3.5 TEST-320: Characterization of feed system positioning

This test was not performed. Due to the problems with the data acquisition hardware, other tests were prioritized. The drift caused by the feed system are apparent in the total drift that is measured in TEST-412 (Section 7.3.9). The stiffness that is added to the system by the feed system is found in the thrust sensitivity of the thrust stand as measured in TEST-411 (Section 7.3.8).

Photos of how the feed system was connected to the pendulum are displayed in Figure 73. The feed and power lines are brought close to the pendulum via a 'waterfall' manner. This allows the line to be aligned with the pendulum as much as possible, such that thermal expansions take place along the pendulum instead of in the plane of motion. The power lines are made of 0.15 mm thick enamelled copper wire. This aids in minimizing the added spring constant by having as little stiffness as possible.

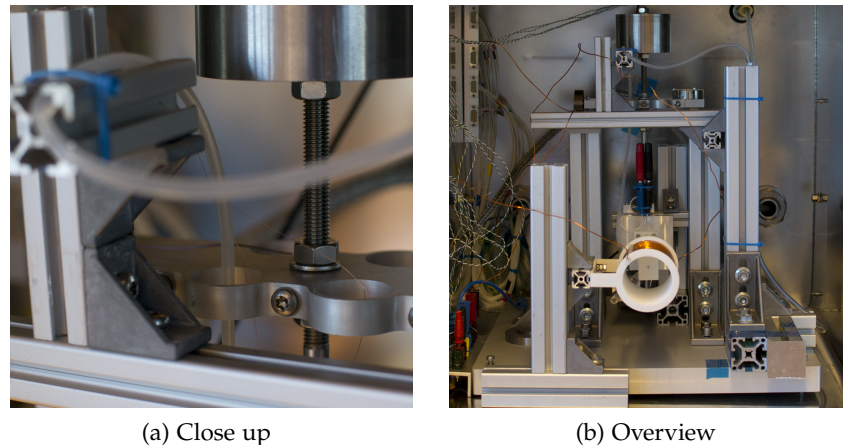


Figure 73: Photos of the used feed system positioning. The feed and power lines are brought close to the pendulum via a 'waterfall' manner, in which the line is aligned as much as possible with the pendulum.

7.3.6 TEST-331: Natural frequency and damping

Following the procedures of Section 6.2.6 the natural damped frequency and the damping ratio are determined. In this section, the

problems experienced in determining the damping ratio and the corresponding results are discussed.

Due to the environmentally induced vibrations, the pendulum is in constant oscillation. As apparent from the signal presented in [Figure 76](#), the oscillation contains a beat. The beat introduces a varying amplitude that disturbs the expected (and required) exponential decay as described in [Section 6.2.6](#). This is problematic in the estimation of the damping ratio. This problem was avoided by repeating the measurement 10 times for 300 s each. For each set the damping ratio was determined based on a windowed signal of a given window length that varies from 10 s to 300 s in steps of 10 s. Using different window lengths allows to identify the effect of the always present natural oscillation and the beat.

In [Figure 74](#) and [Figure 75](#), the estimates for damping ratio ζ and the natural damped eigenfrequency are presented. Each estimate is composed of the average of the 10 measurements and the selected window length. As can be deduced from the graphs, the estimates for both damping ratio and the damped natural frequency are almost constant up to a window length of 100 s. From [Figure 75](#) the effect of beat is clearly identified. Although the beat is present in all measured signals, it becomes apparent enough to shift the determined damped natural frequency at a window length ≥ 100 s.

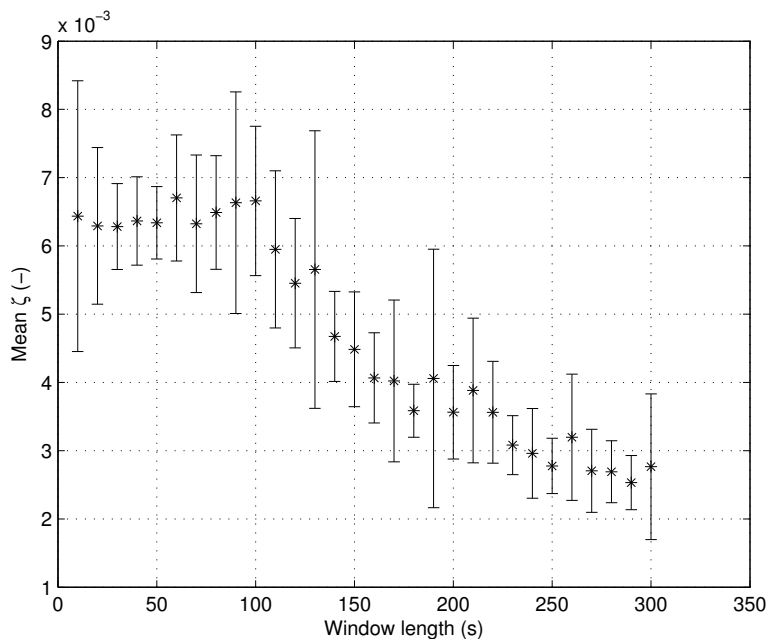


Figure 74: Average damping ratio as a function of window length. Each data point is the average of ten data sets. The error bars indicate a 1σ error bound.

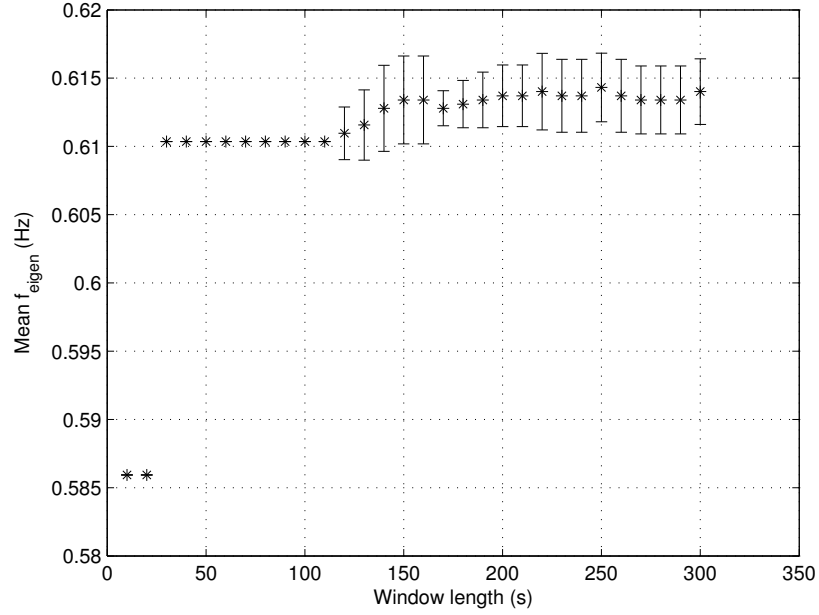


Figure 75: Average damped natural frequency ratio as a function of window length. Each data point is the average of ten data sets. The error bars indicate a 1σ error bound.

The damping ratio ζ is calculated from the logarithmic decrement via (84). In the calculation of the logarithmic decrement δ , an exponential decay is assumed and only two peaks of the oscillation are used in the estimator of (83), which is repeated below. The always present oscillation causes the peaks to reach a minimum level and never damp out completely. Because of this, a longer window length results in an erroneous underestimate of the actual ζ .

$$\delta = \frac{1}{n_{\text{cyc}}} \ln \frac{x(t)}{x(t + n_{\text{cyc}} \cdot T)}$$

From the processed data, estimates for the damped natural frequency and the damping ratio are obtained from the averages for these parameters for window lengths from 10 s to 100 s: $\zeta = 0.00645 \pm 0.00109$ (s.d.) and $\omega_d = 0.6055 \pm 0.0098$ (s.d.) Hz. From this the natural frequency is estimated. The (undamped) natural frequency and the damping ratio are related through

$$\omega_n = \frac{\omega_d}{\sqrt{1 - \zeta^2}} \quad (106)$$

This yields an estimate for the natural frequency of 0.6055 ± 0.0095 Hz or equivalently 10.37 ± 0.18 rad s⁻¹.

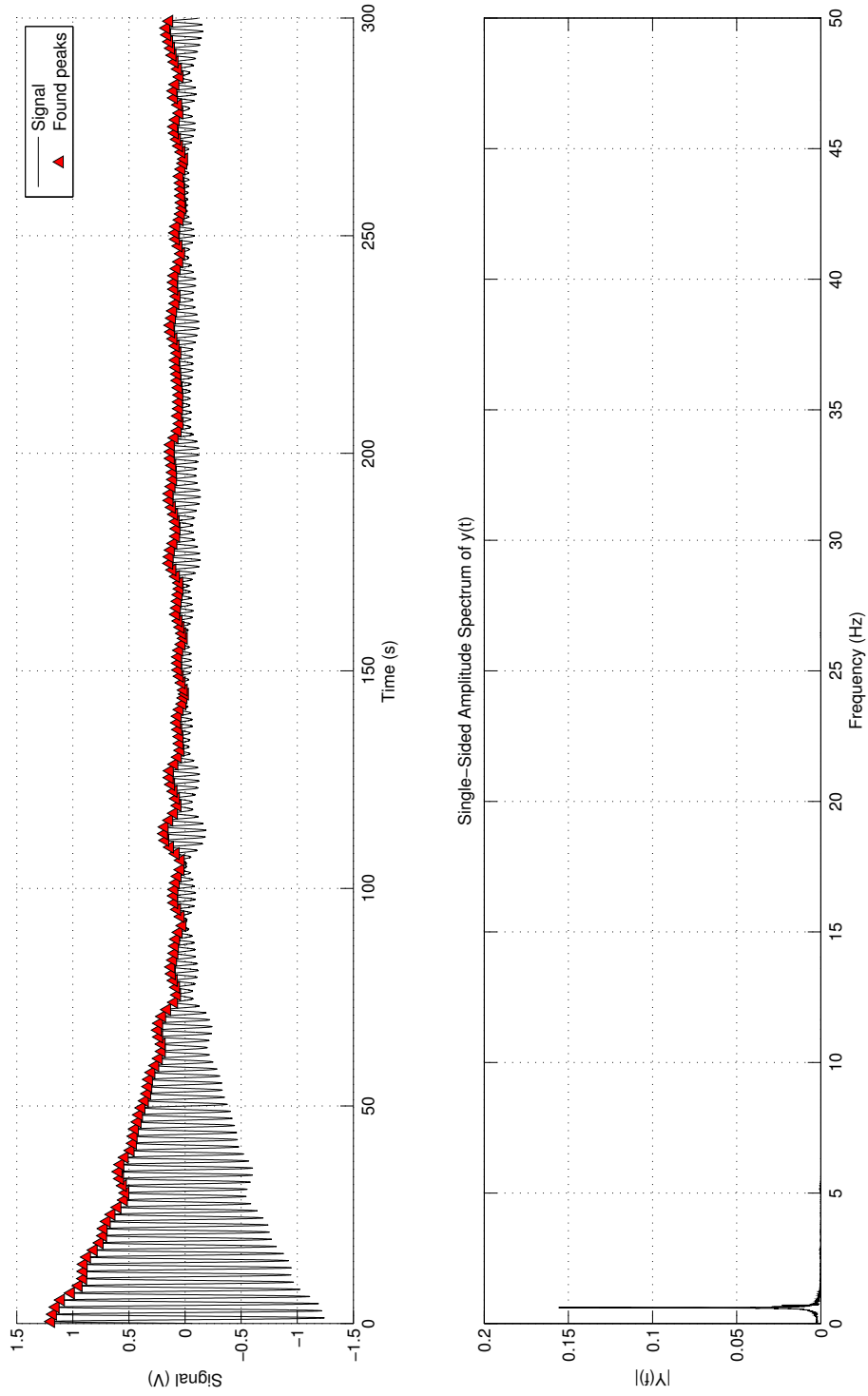


Figure 76: Sample output for TEST-331 generated from dataset of 21 November 2013, data file 'TEST311 - 20131121 - 310s_10.dat'. Signal after impulse input with found peaks marked (top) and the corresponding FFT (down).

7.3.7 TEST-332: Dynamic attenuation

This test was not performed. The natural oscillation that is present makes obtaining proper data for this test difficult. Other tests were given priority due to time constraints.

7.3.8 TEST-411: Pendulum characterization - Sensitivity

Before performing other tests, TEST-411 is typically conducted to determine the thrust stand sensitivity. For this, the calibration actuator is used to exert a known force in a known location (and therefore a known torque) on the pendulum, causing it to rotate. The force is applied in the form of an upward ramp followed by a downward ramp. The signal is translated into a reading of voltage as a function of actuator input current. Through calibration of the actuator, this is in turn translated into a reading of voltage as a function of the applied force. This is depicted in Figure 77. It is noted that the found sensitivity varies between the upward and downward ramp and also between repetitions of the experiment (see Table 39). The variation seems random and is expected to disappear with averaging. TEST-411 is repeated three times to obtain an estimate for the sensitivity. Following the statistics of Appendix E, the sensitivities per ramp are considered independent, identically distributed samples. The final estimate for the sensitivity is then $\mu \pm \frac{S_6}{\sqrt{6}}$ as listed in Table 39.

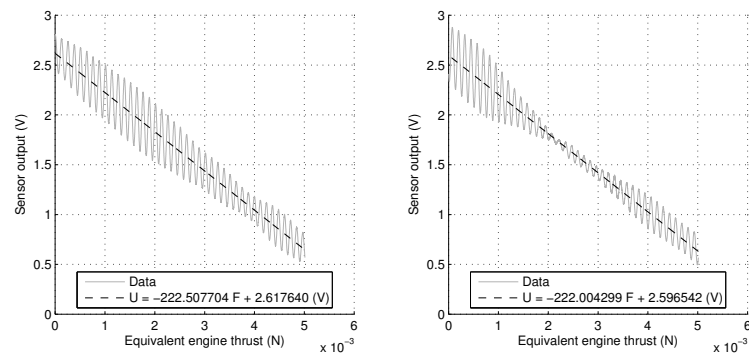


Figure 77: Sample output for TEST-411 generated from dataset of 19 November 2013, data file series 'TEST411-20131119-Orientation1-Vacuum-PMT-Pressurized-Line.dat'.

As listed in Section 7.2, the thrust stand was set up for a total range of 1.388 mN. However, a calibrated force of ≈ 5.0 mN is required to cover the full scale of the CS1 sensor. This is partially explained by operator error. From photographic material it was found that not all four required counter weights were installed on the thrust stand. The counter weight with a mass of ≈ 0.3 kg was not installed. With all

RAMP	SENSITIVITY V N^{-1}
1, upward	-222.508
1, downward	-222.107
2, upward	-223.163
2, downward	-222.004
3, upward	-221.262
3, downward	-222.945
μ	-222.332
S_n	0.693

Table 39: Found thrust stand sensitivities and spread. Generated from dataset of 19 November 2013, data file series 'TEST411-20131119-Orientation1-Vacuum-PMT-Pressurized-Line.dat'.

other parameters as required, the performance is recalculated. In this case an accuracy of $7.8 \mu\text{N}$ is predicted with a range of 3.338 mN . An additional increase in spring stiffness to $0.80 \text{ N m rad}^{-1}$, e.g. caused by non uni-axial loading of the spring, can increase the range to $\approx 5 \text{ mN}$.

7.3.9 TEST-412: Pendulum characterization - Drift

The drift measurements have been adapted compared to the plan of TEST-412 (Section 6.2.9). Because no thermocouples could be used in the measurements, the obtained drift data are mere qualitative and cannot be directly correlated to potential drift sources such as thermal gradients or relaxation. A long-term drift trend of 10 hours was obtained from the data of TEST-310. The drift has also been studied on shorter time scales (minutes) by comparing the zero levels before and after a thrust measurement sequence of TEST-450.

7.3.9.1 Long-term drift

The long-term drift is apparent in the 10 hour noise measurement of TEST-310. The results are plotted in Figure 78. As can be seen the drift is neither linear nor uni-directional. The trend resembles the variation of room temperature as measured by Janssens [39, p. 77]. This resemblance is indicative of a possible correlation between the ambient temperature and the thrust stand signal. To confirm this correlation and to determine the temperature sensitivity of the stand, it is advised that future measurement include temperature measurements on the thrust stand and of the ambient temperature to characterize the effect.

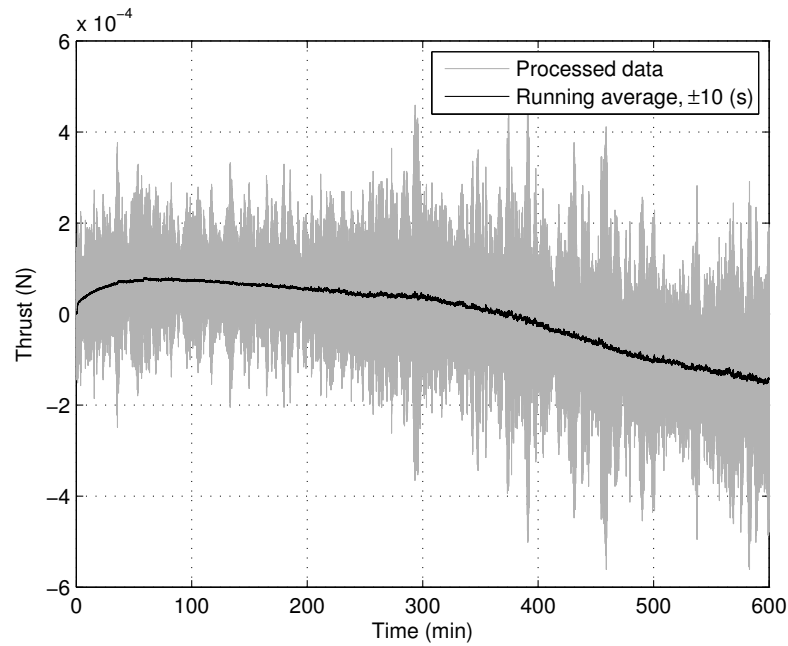


Figure 78: Results of a long-term drift measurement. Data were taken from a long-term noise measurement TEST-310 that was performed in the night of 13 November 2013 from 21:00 to 08:00 the next morning. Dataset: 'TEST310-20131113-0900PM-0800AM-Sideways-Ambient-Chamber-closed.dat'. A running average is included to show the trend more clearly. The running average is created from the measurement points on an interval of ± 10 s around the datapoint.

7.3.9.2 Short-term drift

The short term drift is studied by considering the difference in zero before and after measurements of TEST-450. This drift represents the drift found in actual applications, but is limited to measurements with the *PMT*. As discussed in [Section 6.1.3](#), the temperature of the *PMT* can vary up to 10 K between cold and hot states. This temperature variation can introduce drift that is non-linear or not reproducible. On 20 November 2013 two sequences of TEST-450 were performed. The sensitivity of the thrust stand was determined before each sequence, but not between individual tests. The first sequence consists of 5 measurements of each 470 s in total, while the second sequence consists of 10 measurements of each 100 s. The uncorrected thrust, mass flow and pressure signals of one of these measurements is depicted in [Figure 79](#).

At first sight no drift is apparent, but scrutiny reveals a consistent drift in all three signals (thrust, mass flow and feed pressure). As these parameters are linked physically in producing thrust, the correlation of the respective drifts is studied. For each set the values of mass flow, feed pressure and thrust are plotted in [Figure 80](#). As can

be seen from the figure, the drift in mass flow and thrust are not correlated. The correlation coefficients r are included in the figure. Comparing the two sets, a similar spread in thrust drift is found at a different level of mass flow drift. Also, the drift in mass flow is negative, while the drift in thrust is positive. This sign reversal cannot be explained by rocket motor theory as they should have the same sign when correlated. Similarly, the thrust drift and the pressure drift are not correlated. Based on a comparison between the two sequences, the behavior is not repeatable. Lastly, the correlation between mass flow drift and feed pressure drift is inconclusive based on the data. A large variation in feed pressure does not seem to result in a large variation of mass flow drift (sequence 1). The two sequences cannot be compared directly, because sequence 1 is composed of less samples than sequence 2. More data are required to confirm the existence of a possible correlation.

The pressure transducer is set up such that it measures the pressure perpendicular to the flow and therefore measures the static pressure. Bernoulli states that along a flow line the total pressure is constant, and that it is given by the sum of static pressure P_s and dynamic pressure P_d :

$$P_t = P_s + P_d = P_s + \frac{1}{2}\rho V^2 \quad (107)$$

where ρ is the fluid density and V the flow velocity. With $m = \rho AV$, where A is the cross-sectional area of the flow tube, this is rewritten to

$$P_s = P_t - \frac{1}{2} \frac{m^2}{\rho A^2} \quad (108)$$

Following this relation, the measured pressure and mass flow are negatively correlated as is also apparent in [Figure 79](#).

From the data the trend of the drift cannot be deduced, even though the signs of the drift are consistent. The thrust drift is consistently positive. It is hypothesized that this is caused by an engine induced temperature gradient over the pendulum. The thrust is derived from the sensor output voltage by division by the stand sensitivity:

$$T = \frac{U_{\text{measured}}}{S_s} \left[\frac{V}{V N^{-1}} \right] \quad (109)$$

The stand sensitivity is the ratio of the signal of the sensor and the force generated by the calibration actuator required to cause this signal. Because the calibration actuator and the thruster do not act along the same line, the sensitivity is corrected by the fraction l_t/l_e . When the engine heats up, a temperature gradient is created over the pendulum. The temperature gradient causes the pendulum to expand. Because the temperature increase is not uniform and higher at the

end of the engine, l_e changes faster than l_t , resulting in a drop in ratio l_t/l_e . The actual sensitivity of the thrust stand hereby drops as well, resulting in an increased thrust reading. This hypothesis can be tested when temperature measurements are made on the indicated locations on the setup.

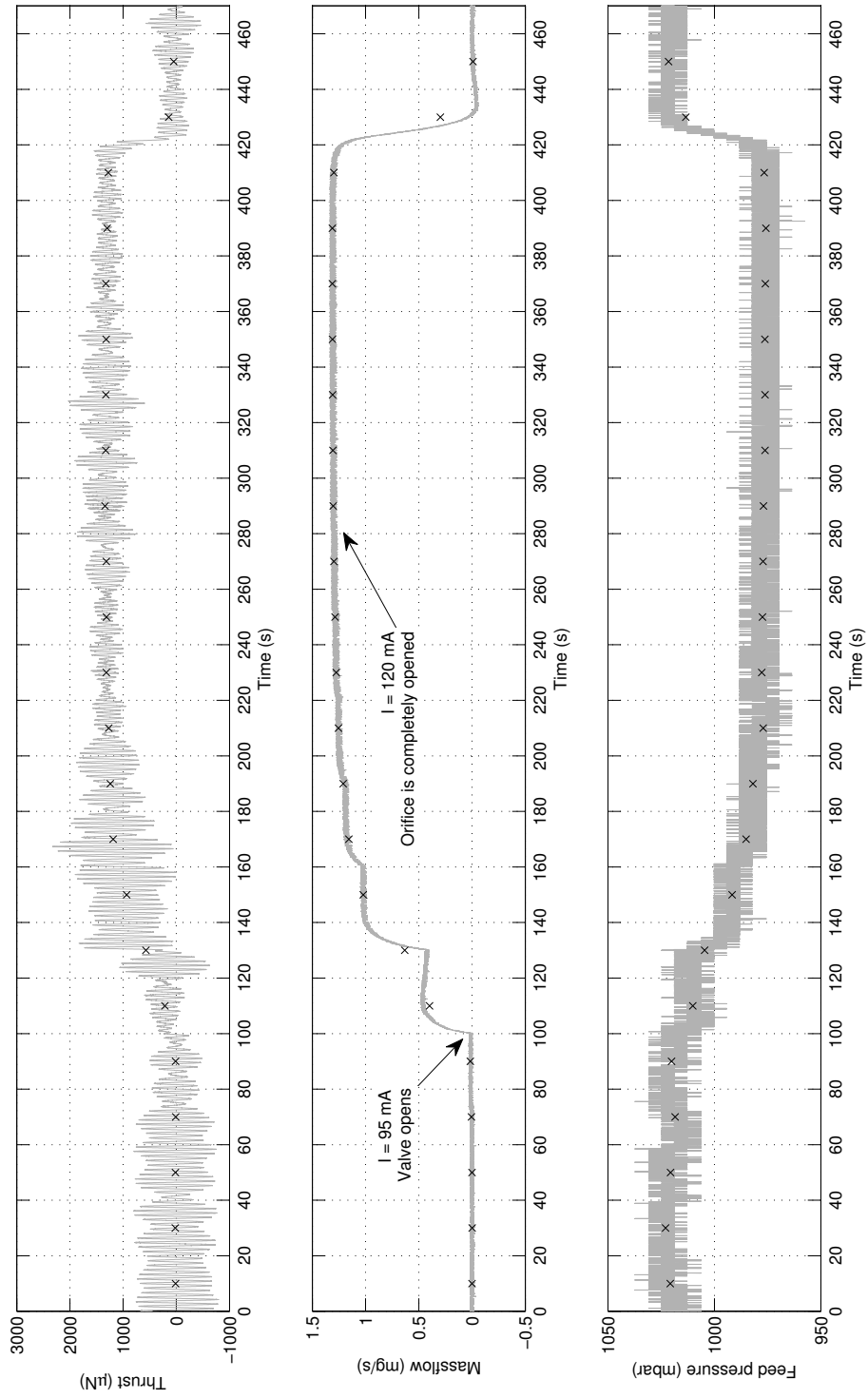


Figure 79: Uncorrected measurements of thrust, mass flow and feed pressure. Data taken from the second sequence of TEST-450 that was on 20 November 2013. Data set: 'TEST450-20131120-Seq1_5.dat'

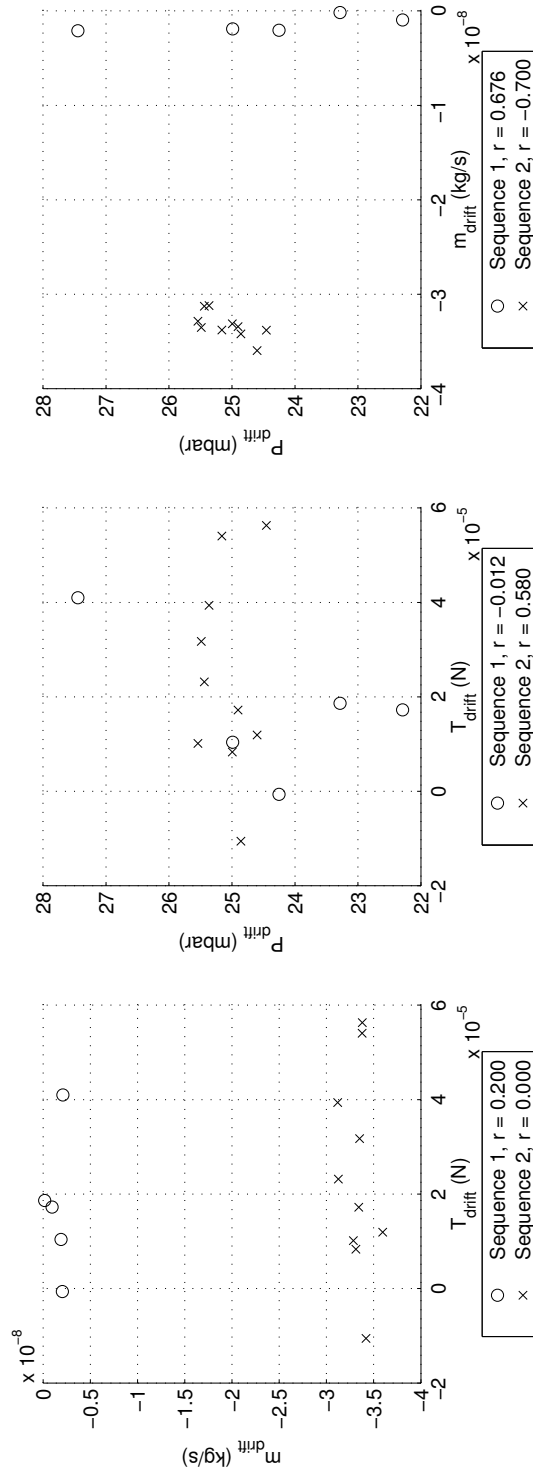


Figure 80: Correlation between drift in thrust, mass flow and feed pressure. Data taken from TEST-450 iterations that were performed on 20 November 2013.

7.3.10 TEST-420: Characterization of the effect of the magnetic field of the Proportional Microthruster

The PMT uses a voicecoil as actuator to open and close the valve. The coil generates a magnetic field and can generate an attractive force when ferromagnetic materials are in the proximity. To quantify the effect TEST-420 is performed according to the guidelines of Section 6.2.10. In this section, the results of this test sequence are discussed.

When the engine is supplied with a current of 0 mA to 90 mA at a rate of 20 mA/min, the valve remains shut and no CoG shift occurs in the engine. Any measured effect is solely due to the generated magnetic field. The applied current and the running average of the signal are presented in Figure 81. The thrust stand output clearly changes proportional to the applied current. At 90 mA a reading of approximately 45 μN is found. The fact that the reading is positive means that the engine is attracted in the direction of the sensor head. This may be caused by the sensor head itself (which is of unknown materials) or by ferromagnetic components in the sensor frame. The source is currently unknown and is subject of further investigations.

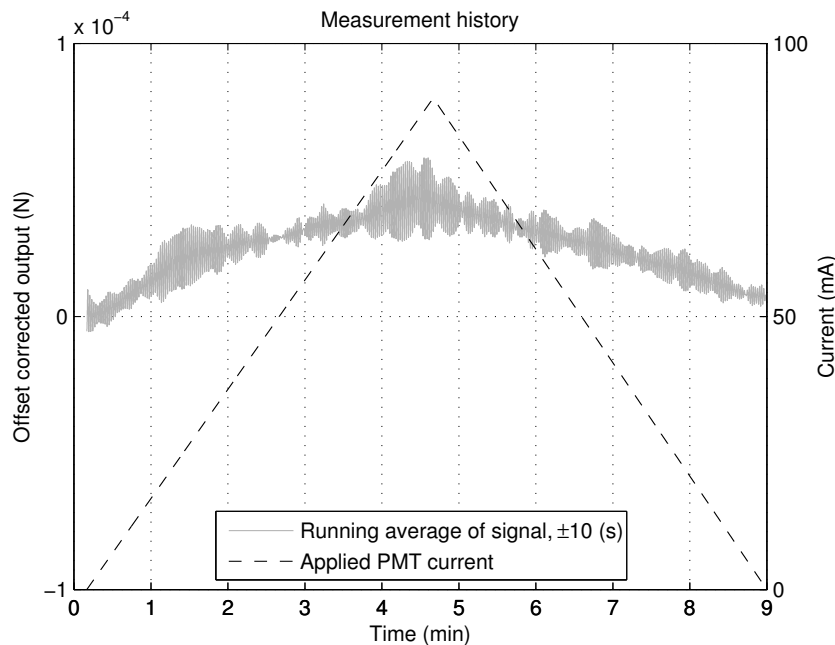


Figure 81: Effects of magnetic field generated by the valve of the PMT. Data set: 'TEST420-20131121-Short-Range-Mag-Field.dat'.

From Figure 81 it is apparent that the change is not perfectly linear with current and is also not consistent between the upward and downward ramp, indicative of some form of hysteresis. This may be caused by initial heating of the engine that results in CoG shifts due

to thermal expansion. A linear approximation of the effect in the data of 20 November results in $T = 0.000470i + 0.000005$ N with current in A for the upward ramp and $T = 0.000366i + 0.000008$ N for the downward ramp. These fits are depicted in Figure 82 and are superimposed on the calculated thrust measurements. However, for the data of 19 November, that show the same trend but different magnitudes, a linear approximation results in $F = 0.000470i - 0.000010$ N for the upward ramp and $F = 0.000194i + 0.000006$ N for the downward ramp. All four fits are only valid for the 0 mA to 90 mA range. As the functions approximate the mean and not the resulting oscillation itself, the SEE cannot be used as a proper indicator of the quality of the fit. The averages of the residuals are for all four much smaller than the signal at $\leq 1 \cdot 10^{-19}$ N. It should be noted that the fits of each pair do not meet at 90 mA, but represent the best linear fits for their respective slope. As the effect is not fully understood and the linear fits only represent a first approximation, no other fitting function that joins the two slopes at the peak is enforced.

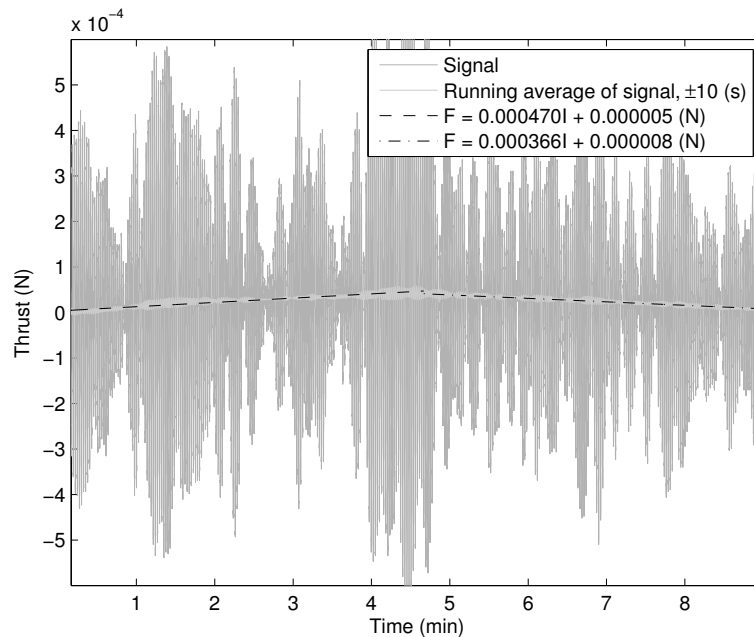


Figure 82: Effects of magnetic field generated by the valve of the PMT. Data set: 'TEST420-20131121-Short-Range-Mag-Field.dat'.

Although the effect is reproducible, the magnitude is clearly not. It is hypothesized this is caused by a different placement of the sensor assembly with respect to the engine. Because of manual realignment that is performed between tests, the sensor assembly may be at a slight angle with respect to the target or at a different distance. Both can result in a different magnetic force. For future measurements it

is advised that this test is performed before the actual thrust measurements are performed as part of the calibration. Alternatively, the engine is wrapped in magnetic shielding to eliminate the problem.

7.3.11 TEST-430: Characterization of the effect of the center of gravity shift in the Proportional Microthruster

Once the supply current exceeds ≈ 90 mA, the valve starts to open. The moving pin causes the CoG of the PMT to move backwards, resulting in a small moment on the pendulum. This moment causes the pendulum to rotate to a new equilibrium position. This effect is characterized using TEST-430 which is performed following the procedures of Section 6.2.11. The results of this test are discussed in this section and compared to the results of TEST-420 that describes the effect of the magnetic field of the PMT (Section 7.3.10).

The engine is supplied with a current of 0 mA to 140 mA at a rate of 20 mA/min. From TEST-420 it is known that the magnetic field of the PMT results in a positive thrust reading. From Figure 83, however, a reversal of the effect is apparent in the 90 mA to 140 mA range. This reversal is explained by a larger effect of the CoG shift in the engine compared to the effect of the magnetic field.

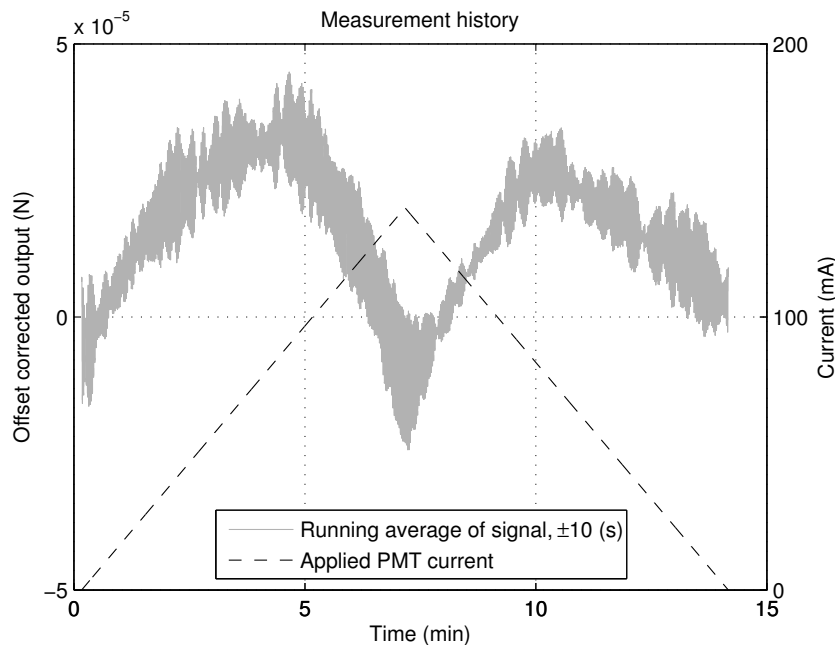


Figure 83: Combined effects of magnetic field and center of gravity shift caused by the valve of the PMT. Data set: 'TEST420-20131121-Long-Range-Grav-Field.dat'.

Similar to the results of TEST-420, the data indicate that the net effect of the magnetic attraction and the CoG shift are not perfectly linear.

In TEST-450, the engine is used with supply currents of 80 mA to 140 mA. For that reason, linear fits are applied to the data in this range for both the upward and downward ramp. For the data of 21 November, a fit for the upward ramp of $T = -0.000717i + 0.000098 N$ is found. Similarly, for the downward ramp the fit is found to be $T = -0.000518i + 0.000065 N$. For the data of 19 November, correspondingly fits of $T = -0.000839i + 0.000106 N$ and $T = -0.000293i + 0.000039 N$. The difference between the data sets of the two dates is already explained in [Section 7.3.10](#).

In [Section 6.2.11](#), a maximum drift in the thrust reading due to the opening of the valve of $-2.1 \cdot 10^{-4} N$ is predicted. Using the results for the upward ramps of the magnetic field and shift in CoG for the data set of 21 November, the following is concluded. Extrapolating the effect of the magnetic field, a shift of $\Delta T = 0.000470 \cdot 0.140 + 0.000005 = 7.08 \cdot 10^{-5} N$ is expected. The combined effects of magnetic field and CoG shift, have resulted in a shift of $\Delta T = -0.000717 \cdot 0.140 + 0.000098 = -2.38 \cdot 10^{-6} N$. This means that the CoG shift results in a shift in thrust reading of $-2.38 \cdot 10^{-6} - 7.08 \cdot 10^{-5} = -7.32 \cdot 10^{-5} N$. Compared to the predicted effect, this is lower by a factor of 2.87. It is hypothesized that this is caused by a combinations of factors. First, the magnetic attraction typically varies to the fourth power with distance and is therefore very nonlinear. The linear approximation that is extrapolated here, is likely to give an underestimate of the real contribution. Second, the given mass of the valve and the distance over which it travels are estimated values that were provided by Bradford Engineering and cannot be checked without a better insight in the inner workings of the PMT. Lastly, it is not guaranteed that the maximum travel is reached at a current of 140 mA as is assumed here. If the required current is bigger, the difference in measured thrust reading and predicted thrust reading drops.

7.3.12 TEST-440: Characterization of the effect of changing vacuum pressure

This test was not performed. The output of the Omega PX139 pressure transducer that was used to measure the vacuum pressure was out of calibration and possibly broken. At ambient pressure, the sensor output was equivalent to ≈ 800 mbar, 200 mbar lower than expected. Therefore the effect of changing vacuum pressure could not be characterized. As predicted, the vacuum pressure increases when the engine is thrusting and the vacuum pump is switched off. This effect is apparent on the pressure gauge on the front of the vacuum chamber. With the vacuum pump on, this effect is not noticed. The influence that this pressure increase has on the thrust measurement is unknown. Also, the actual pressure increase is unknown due to the limited readability of the gauge.

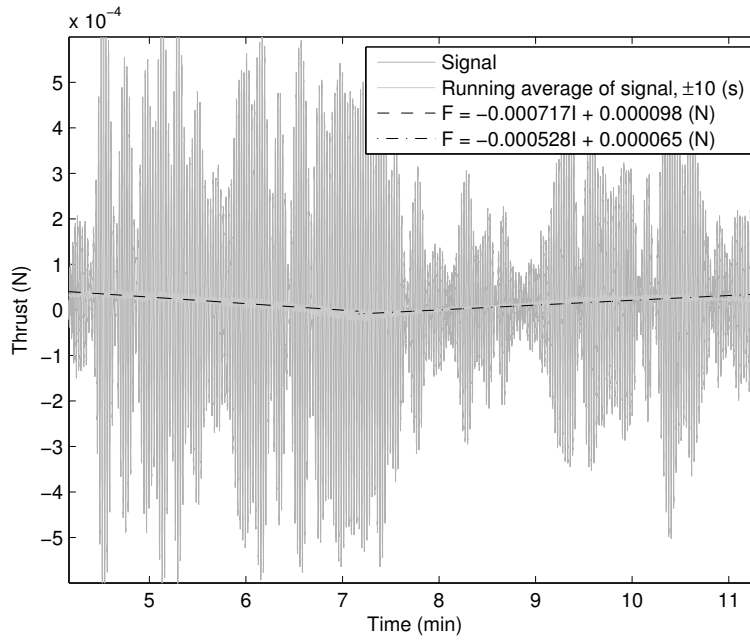


Figure 84: Linear fit through data for **PMT** valve induced force readings. The fits represent the effect from 80 mA to 140 mA. Data set: 'TEST420-20131121-Short-Range-Mag-Field.dat'.

7.3.13 TEST-450: Steady state thrust measurements

This test was performed according to the plans of [Section 6.2.13](#). The valve was actuated in 13 steps of 5 mA from 80 mA to 140 mA. During the measurements it was noted that the Brooks **MFC** required ≈ 20 s to settle. Therefore each setting was kept for 30 s. In data processing the last 5 s of each interval were used to estimate the value of each parameter.

7.3.13.1 Required corrections and thrust calculations

The thrust is calculated from the thrust stand signal. The signal is converted from its voltage output to a force reading by division by the calibrated sensitivity:

$$F_{\text{balance}} = \frac{u_{\text{sensor}}}{S_s} \quad (110)$$

The force reading is then corrected for various systematic errors. First, the signal is corrected for its non-zero reading at zero thrust. The first 10 s of the signal are averaged and subtracted from the reading. As shown in [Section 7.3.9](#), a zero drift is present over the duration of a measurement. It is assumed this drift is linear on the time scales of the tests and is proportional to the time of measurement subtracted from the signal. It should be noted that this is an assumption and it requires more characterization. Similarly, a signal offset is introduced

by the magnetic field of the engine and the shift of CoG that is caused by the opening and closing of the valve. These effects are subtracted from the signal as a function of supply current to the engine. If characterized, the signal can also be corrected for other error sources such as known thruster misalignment angle α or changes induced by a changing vacuum pressure.

$$F_{\text{thrust}} = \cos^{-1}(\alpha) (F_{\text{balance}} - F_{\text{zero offset}} - F_{\text{zero drift}} - F_{\text{engine induced}} - F_{\text{corrections}}) \quad (111)$$

In [Figure 85](#) the input current for the PMT is shown including the resulting uncorrected balance reading F_{balance} , the mass flow and the feed pressure. The current is varied between 80 mA to 140 mA in steps of 5 mA. Each step is held for 30 s to allow the pressure and mass flow to stabilize. The last 5 s of data per step is averaged and used for the actual measurement. As can be seen in the figure, the mass flow slowly stabilizes. It is clear that linear steps in supply current do not result in a linear increase in mass flow or thrust. At a supply current of 120 mA the valve is fully opened and the mass flow does no longer increase.

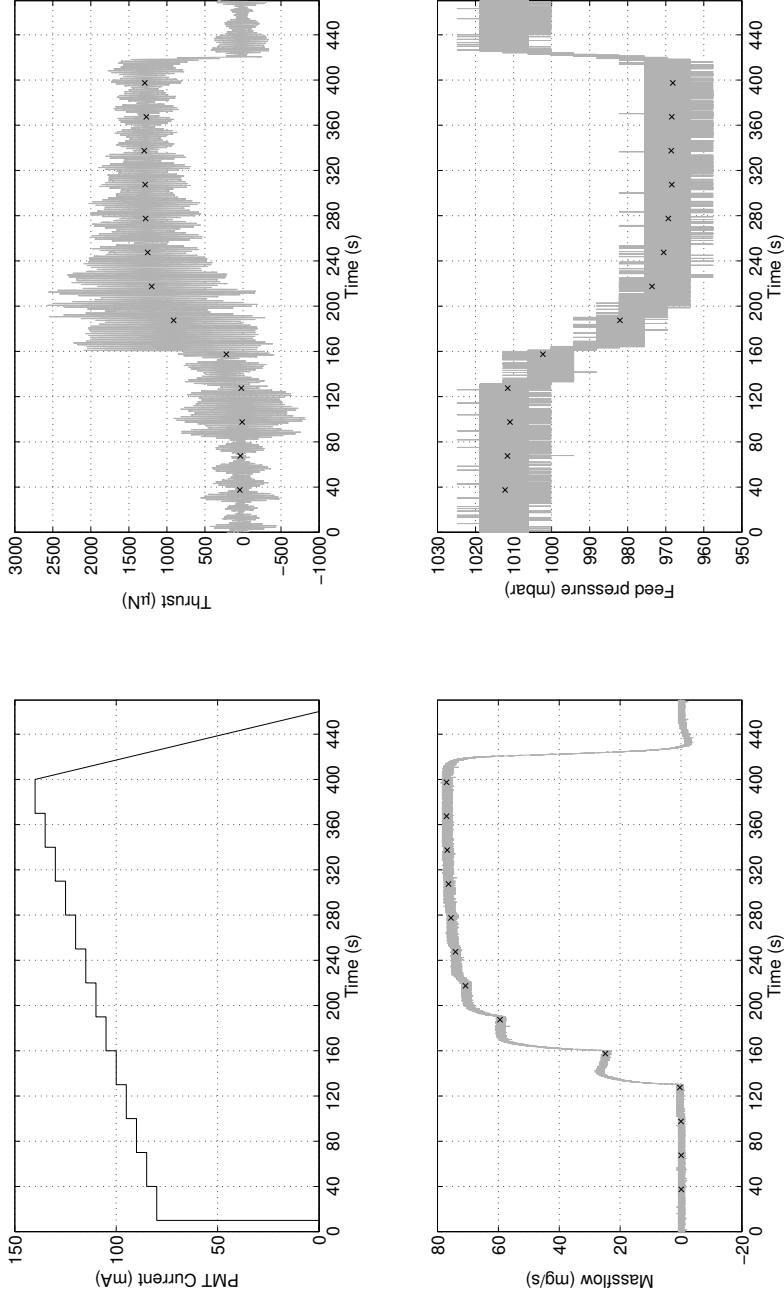


Figure 85: Typical results for TEST-450. Shown are the input current of the thruster valve, the corresponding values for the uncorrected thrust force $F_{battance}$, the mass flow m and the pressure P . Actual data set: "TEST450-20131120-Seq1_5.dat"

7.3.13.2 *Hysteresis*

From data provided by Bradford Engineering [46] it is known that the PMT valve shows hysteresis in mass flow as a function of controller signal. This behavior is replicated with the PMT mounted in the thrust stand. The current supplied to the valve is controlled with a triangular function from 80 mA to 140 mA in 6 minutes and back in the same fashion. The results are reproducible and are shown in Figure 86. While the data of Bradford Engineering were generated for only the valve mechanism without a nozzle attached, the behavior is also apparent with a nozzle present. It is traced back to a soft seal that shuts the orifice when the valve is closed to avoid leaks. This seal relaxes when the valve is opened and changes the internal geometry of the thruster slightly. A change in geometry before the throat of the nozzle can introduce a larger pressure drop at the valve, resulting in a lower exhaust pressure and thus a lower thrust. This, however, requires the relaxation of the seal to be slow and require more time than the test period to fully relax. A second mechanism that can cause this hysteresis is static friction in the valve mechanism. Possibly the closing pin or the spring it is connected to experiences friction from its container. The largest difference between opening and closing the valve of $\approx 136 \mu\text{N}$ is found at $\approx 0.8 \text{ mg s}^{-1}$ mass flow.

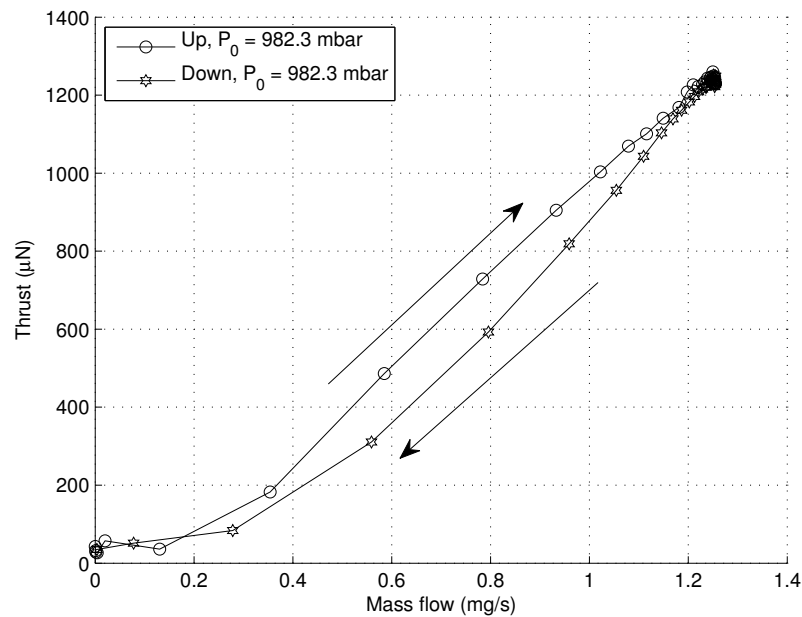


Figure 86: Example of hysteresis in the thrust measurements caused by hysteresis in the PMT. Data set: 'TEST450-20131120-Seq3_2.dat'

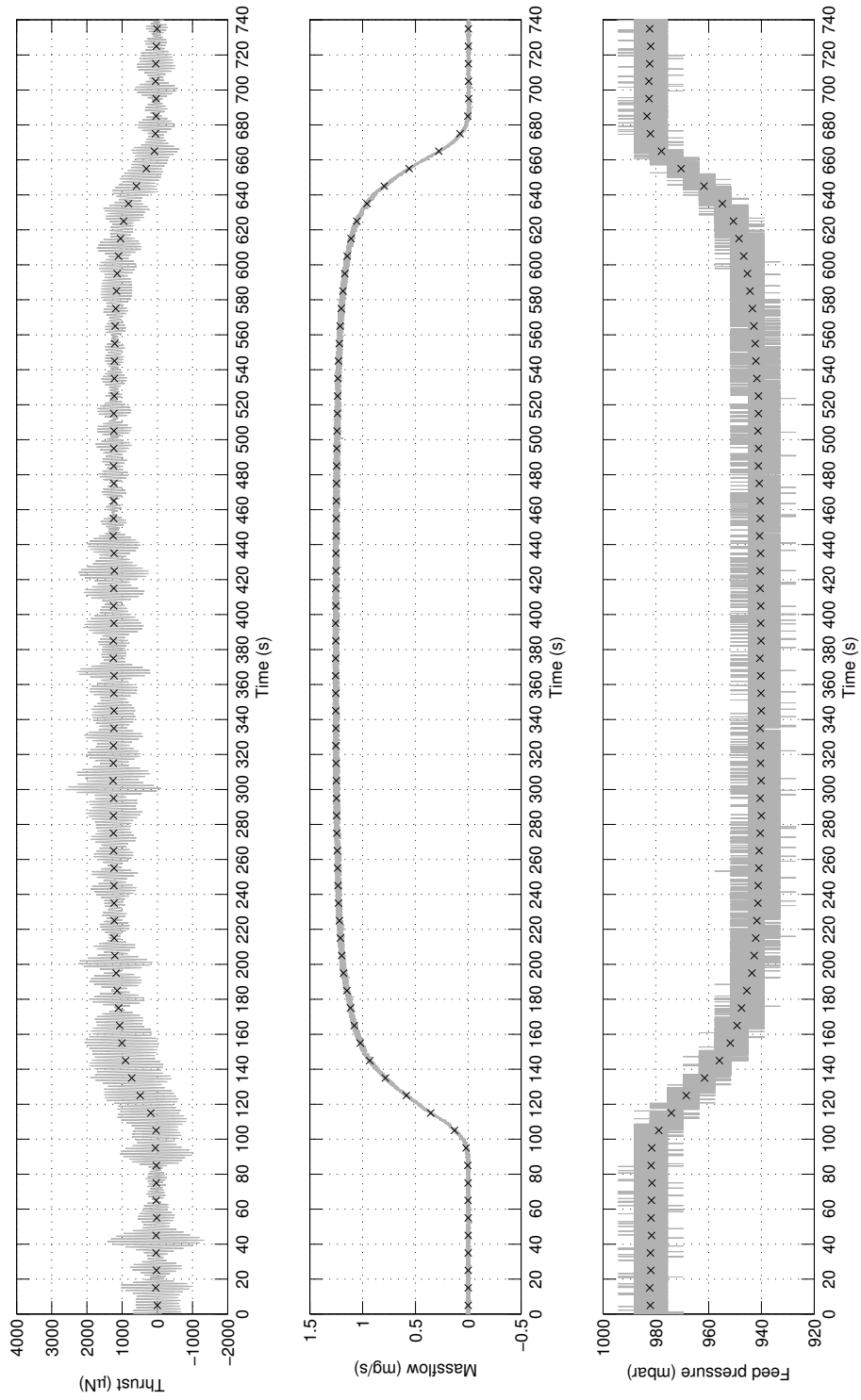


Figure 87: Uncorrected measurements of thrust, mass flow and feed pressure for hysteresis test. Data set: 'TEST450-20131120-Seq3_2.dat'

7.3.13.3 Comparison with results obtained from model

The computational model of Section 6.2.13 predicts that at non vacuum ambient conditions higher mass flows are required to obtain a given thrust level compared to vacuum. In Figure 88, the results of the model are compared to the determined thrust values. As can be seen in the figure, the measured results show similar behavior. The thrust line is indeed shifted to the right, as also predicted by the model. However, the slope of the found thrust-mass flow relation is higher than that of the model. In Section 6.2.13, the model is compared to the data obtained at ESA ESTEC. In that comparison the higher slope in the experimental results is not found.

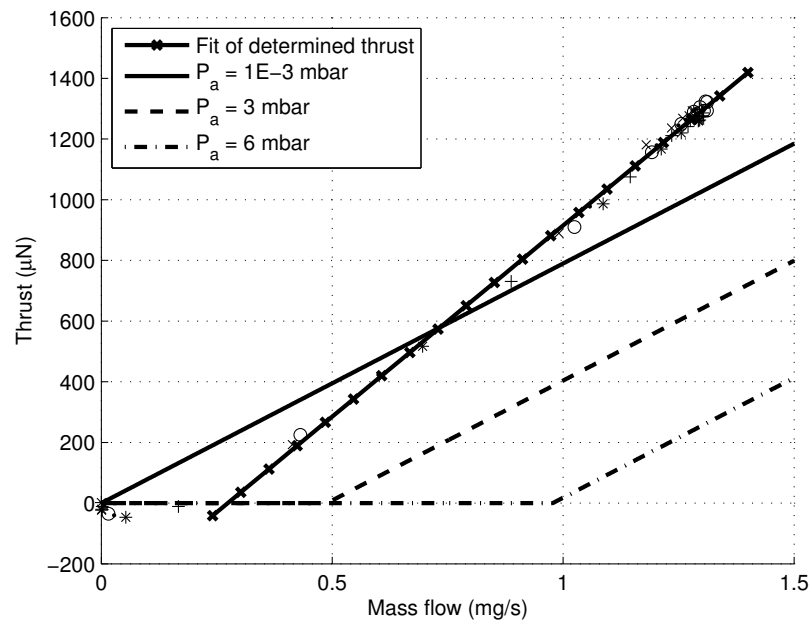


Figure 88: Thrust measurements of 20 November, 2013 compared to results obtained from the computational model. Data sets: 'TEST450-20131120-Seq1.dat' to '...-Seq1_5.dat'.

7.3.13.4 Comparison with results obtained at ESA ESTEC

In Figure 89, the obtained thrust measurements for the PMT are compared to data obtained in 2006. The data are corrected for zero offset and drift. A correction is applied for the effect of the magnetic field of the PMT and the shift of the CoG inside the thruster. The correction data are, however, obtained on 21 November, 2013, one day after the measurement of the thrust. As can be seen at the point $m = 0 \text{ mg s}^{-1}$, the correction is too large as negative thrust levels are found. It is assumed there is no thruster misalignment.

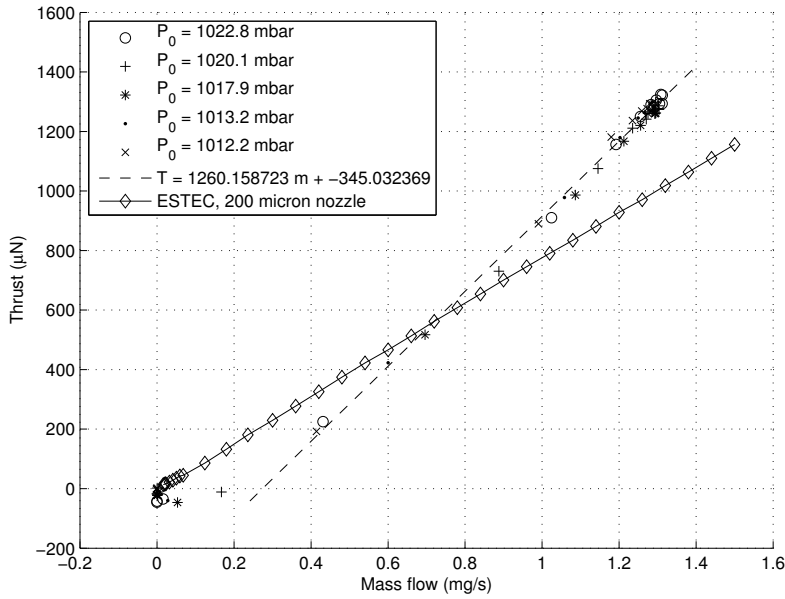


Figure 89: Thrust measurements of 20 November, 2013 compared to results obtained at ESA ESTEC (data courtesy of Bradford Engineering [88, 46]). Data sets: 'TEST450-20131120-Seq1.dat' to '....-Seq1_5.dat'.

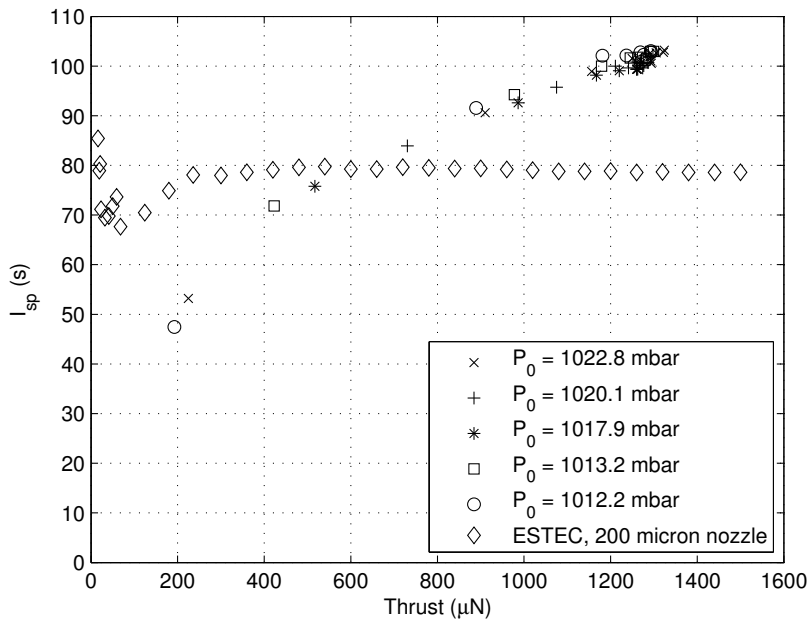


Figure 90: Specific impulse determined on 20 November, 2013 compared to results obtained at ESA ESTEC (data courtesy of Bradford Engineering [88, 46]). Data sets: 'TEST450-20131120-Seq1.dat' to '....-Seq1_5.dat'.

Assuming there is no uncertainty in the measured thrust, the mass flow introduces an uncertainty in the found specific impulse. As explained in [Section 7.3.13.5](#), the error in mass flow is dependent on the reading and the full scale of the mass flow transducer. The corresponding error in specific impulse is then estimated as

$$\Delta I_{sp}^- = \frac{T}{(m - \Delta m) g_0} - \frac{T}{m g_0} = \frac{\Delta m}{(m - \Delta m)} I_{sp} \quad (112)$$

for an overestimated mass flow or

$$\Delta I_{sp}^+ = \frac{T}{m g_0} - \frac{T}{(m + \Delta m) g_0} = \frac{\Delta m}{(m + \Delta m)} I_{sp} \quad (113)$$

for an underestimated mass flow. Applying this error estimate to the found data results in an almost constant error of $\approx \pm 1.2$ s.

A clear difference exists between the measurements and the data obtained at ESA ESTEC. At similar mass flows a considerably higher thrust is measured. Potential causes for this are discussed in [Section 7.3.13.5](#).

7.3.13.5 Possible explanations for differences in thrust

As noted, a difference exists between the modeled performance, the performance measured at ESA ESTEC and the performance measured using the AE-TB-5m. In this section, several possible mechanisms are suggested and supported by analysis.

The first option is an overestimate of the real thrust that is caused by a too low sensitivity for the thrust stand. The procedures and data-processing scripts were checked for errors and none were found. This does, however, not necessarily mean there are no errors. Inspection of the thrust stand shows that the cross beam has an additional degree of freedom and can also slide over its razor edge support. Such sliding is caused by the lateral moment that is caused by the calibration force and the engine thrust with respect to the spike support. It is unknown if the induced moments are sufficiently large to cause any sliding that can be traced back in the measurements.

The second option is an actual higher thrust. The thrust is a function of mass flow, exhaust velocity and pressure difference as per [Equation 92](#) (repeated here for the readers convenience):

$$F = m U_e + (p_e - p_a) A_e$$

The slope of the thrust as a function of mass flow is given by the exhaust velocity of the thruster, which scales with chamber temperature and expansion ratio p_c/p_e . As the gas expands from room temperature, the gas temperature in the chamber is going to be lower than that. As this agrees with the model, a higher gas temperature that is

required to give a higher exhaust velocity is not expected. At room temperature, with an expansion ratio of $p_c/p_e = 6111$ (as per the model of [Section 6.2.13](#)), the exhaust velocity $U_e = 780.40 \text{ m s}^{-1}$. In the limit case of ideal expansion, the exhaust velocity is given by [\[91\]](#):

$$U_L = \sqrt{2 \frac{\gamma}{\gamma - 1} \frac{R_A}{M} T_c} \quad (114)$$

which, given the parameters also used in the simulation, results in a maximum exhaust velocity of $U_L = 780.42 \text{ m s}^{-1}$. The slight increase of 0.02 m s^{-1} is negligible and does not explain the increased thrust found in the measurements.

The third and last option is an underestimate of the mass flow. However, as explained in [Section 6.1.2.1](#) is the mass flow independent of the actual temperature and pressure and only depends on the standard conditions. Any errors in mass flow estimates, therefore, are caused by the transducer itself. As no recent calibration data of the sensor are available, this cannot be confirmed. The manufacturer quotes an uncertainty in volume flow of 0.7% of the reading and 0.2% of the full scale [\[12\]](#). From [\(71\)](#) is derived that this translated directly into an the error in mass flow.

$$\frac{\delta \dot{m}}{\dot{m}} = \frac{\frac{P_s M}{T_s R_u} \delta \dot{V}}{\frac{P_s M}{T_s R_u} \dot{V}} = \frac{\delta \dot{V}}{\dot{V}} \quad (115)$$

At a full scale reading of $144 \text{ mL}_n/\text{min}$ or 3.0 mg s^{-1} this translates in an uncertainty of 0.006 mg s^{-1} to 0.027 mg s^{-1} in the mass flow readings.

7.3.14 TEST-461: Thrust stand calibration for impulse bits

This test was not performed. For the [PMT](#) no data are available on the impulse bits it can generate. Therefore, no direct validation is possible. instead, $1 \mu\text{Ns}$ and 1 mNs impulse bits are generated using the calibration actuator to determine if these can be measured using the thrust stand. The results of this test are discussed in [Section 7.3.15](#).

7.3.15 TEST-462: Impulse bit measurements

To show that impulse bits in the $1 \mu\text{Ns} - 1 \text{ mNs}$ range can be measured using the thrust stand, TEST-462 is performed. However, instead of using the engine to generate a pulse as according to the measurement plan, the actuator is used to generate a known impulse. The required pulse lengths and current magnitudes are depicted in

Figure 91. To correct for the difference in arm length between the actuator and thruster, the required current is calculated using

$$i = \frac{I_{\text{bit}} l_e}{S_{\text{actuator}} \Delta t l_t} \quad (116)$$

where i is the current in A, I_{bit} the required impulse in μNs , l_e and l_t the arm lengths for the engine and actuator, respectively, S_{actuator} the sensitivity of the actuator in NA^{-1} and Δt the chosen step duration in s.

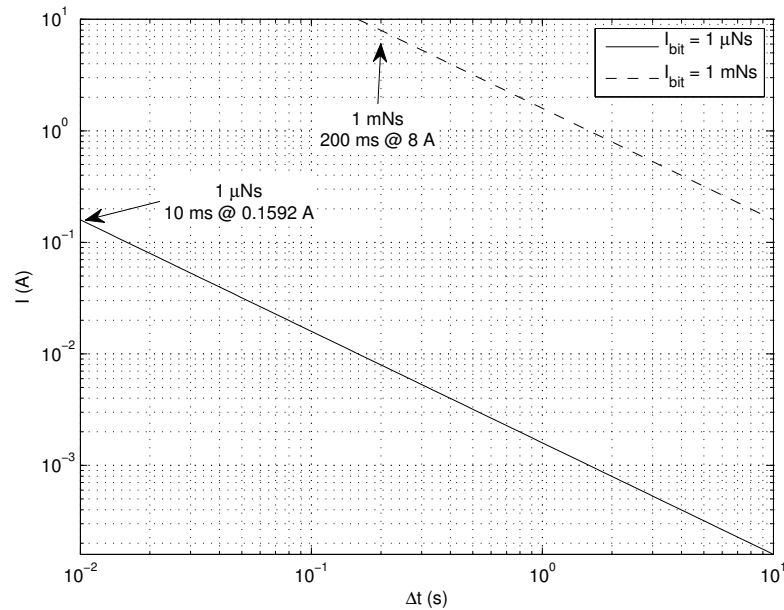


Figure 91: Required coil current and pulse length for given impulse bit. Using an S-06-06-N magnet and an assumed resulting actuator sensitivity $S_a = 0.000835 \text{ NA}^{-1}$. Actuator arm $l_t = 173 \text{ mm}$ and engine arm $l_e = 230 \text{ mm}$.

Based on the estimation, the shortest time steps are chosen that allow generation of the required impulse. The shorter the duration, the better the pulse resembles a Dirac function or an ideal pulse. This results in a peak of 0.159 A of 10 ms duration to generate $\approx 1 \mu\text{Ns}$ and a 8.000 A pulse of 200 ms duration for the 1 mNs.

The thrust stand signal was monitored and after a 10 s period, the pulse was generated. In Figure 92 the results of a 1 mNs pulse are obvious. The test was repeated five times for this impulse magnitude and the effect of an impulsive input on the pendulum is clearly visible in all five sets. However, the magnitudes of the responses vary due to the natural oscillation. Dependent on moment of pulsing, the natural oscillation offsets the magnitude of the resulting wave.

For a 1 μNs impulse, a typical result is depicted in Figure 93. The test was repeated 10 times for this impulse magnitude and in none of the sets the effect is noticeable.

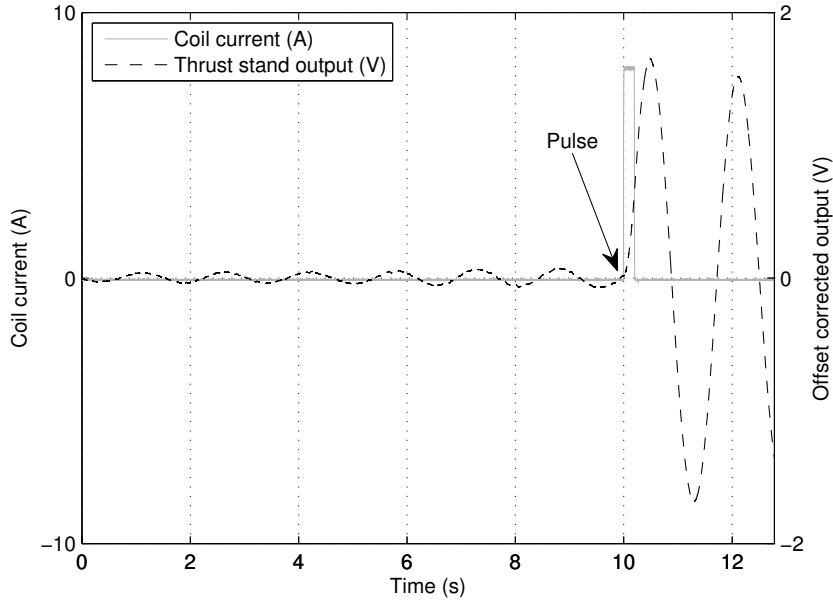


Figure 92: Response for a 1 mNs impulse. Data set: 'TEST460-20131122-1mNs-6mm-magnet_1.dat'. Pulse width of 200 ms using a single S-06-06-N magnet in the holder.

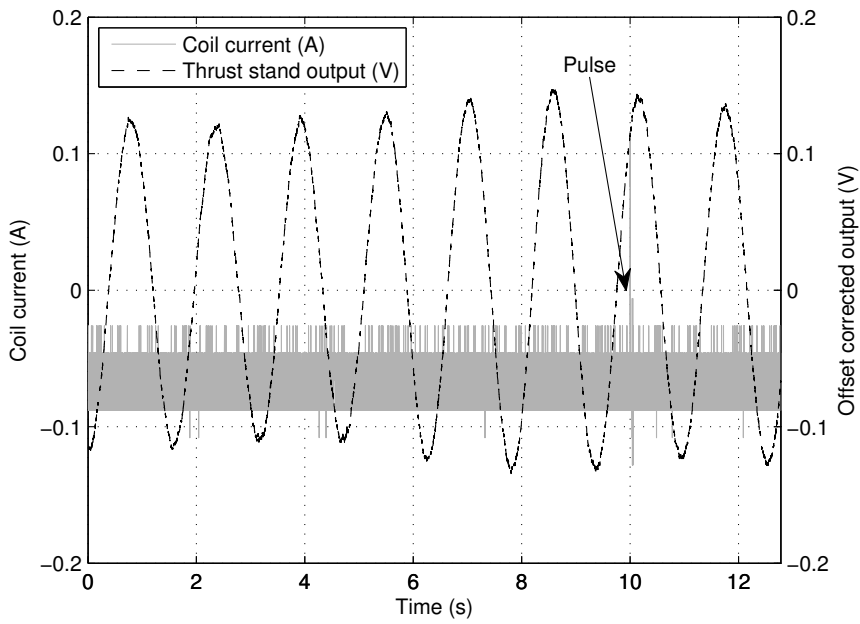


Figure 93: Response for a 1 μ Ns impulse. Data set: 'TEST460-20131122-1 μ Ns-6mm-magnet_9.dat'. Pulse width of 10 ms using a single S-06-06-N magnet in the holder.

7.3.16 Requirement validation

Based on the experimental results the requirements of [Section 3.2](#) are compared to the achieved performance. Insufficient data are available to validate the thrust stand performance on requirements ACCUR-1 and ACCUR-2. Additional measurements are required for this. As discussed in [Section 7.3.15](#), the smallest impulses cannot be measured. Additional tests are required to confirm the smallest impulse bit that can be detected.

IDENTIFIER	THRESHOLD	GOAL	NOTES
RANGE-1	Yes	N/A	Unexpected additional stiffness was found.
RANGE-2	No	N/A	Natural oscillation makes it impossible to detect smallest impulse bits.
ACCUR-1	TBD	TBD	Additional testing required.
ACCUR-2	TBD	TBD	Additional testing required.
DIMEN-1	Yes	N/A	—
OPERA-1	Yes	N/A	Chapter 6
OPERA-2	Yes	N/A	—
VACUU-1	Yes	Partially	Elevated temperatures required to reach UHV exceed melting temperature of polyamide parts and maximum operating temperature of magnets.
SAMPL-1	Yes	N/A	—
RESRC-1	Yes	N/A	Additional funding is provided.
RESRC-2	No	N/A	8 months since kick-off meeting.
CALIB-1	Yes	N/A	—
CALIB-2	Yes	N/A	—

Table 40: Validation of requirements.

DESIGN CHANGES REQUIRED TO MEET DELFFI REQUIREMENTS

During the period of the thesis, the requirements on the DelFFi propulsion system have changed. Changing requirements on the propulsion system can automatically induce requirement changes in the test facilities. In this chapter, the new DelFFi requirements are discussed and the changes to the thrust stand design that are required are discussed.

8.1 NEW REQUIREMENTS

The requirements that influence the thrust stand design directly are listed below. They are cited from the requirements document 'Propulsion System Requirements for the DelFFi Satellites (DelFFi/PROP/REQ/3.0)' [17].

PROP-PERF-200

"The thrust provided by the propulsion system shall be 9.5 mN as a maximum."

PROP-PERF-205

"The thrust provided by the propulsion system shall be at least 0.5 mN."

PROP-PERF-210

"The thrust vector shall have a maximum misalignment of TBD degrees with respect to the nominal geometrical axis of the nozzle."

PROP-SYST-100

"The total wet mass of the propulsion system at launch shall be not higher than 459 g."

PROP-SYST-200

"The total size of the propulsion system shall be within 90 mm × 90 mm × 80 mm."

8.2 REQUIRED DESIGN CHANGES

In the sections below, per given DelFFi requirement a preliminary review is given for the imposed design changes.

8.2.1 *Extension of the range*

Requirements PROP-PERF-200 and PROP-SYST-100 require an extension of the range of the thrust stand in measurable thrust and sample mass, respectively. The current design parameters are chosen with a maximum total sample mass of 300 g in mind (SAMPL-1), which includes the mass of a custom mounting bracket as well. PROP-SYST-100 imposes a maximum total wet mass of the entire propulsion system of 459 g. For testing of just the thruster without the feed system, SAMPL-1 is expected to be sufficient as the mass of the propellant and the feed system are typically considerably higher than that of the thruster. Full-scale testing of the propulsion subsystem including the feed system on the thrust stand is not advised. Shifts in the CoG of the system have already shown to have a major impact on the thrust reading and the required corrections of the measured thrust. Inclusion of the feed system will only render thrust measurements and characterization of the thruster more complicated and less reliable. In case full-system tests are required, the thrust stand needs to be re-designed to allow sample masses ≥ 459 gram. The allowed mass has to be greater than this, to also allow inclusion of a custom bracket. It is advised to set the sample mass to 600 g in this case.

Using the tool of [Section 6.3.2](#), the currently available components are used in the search for updates of the setup. It is found that the lower range cannot be covered at an accuracy required to fulfill ACCUR-1. For the lowest range, of 1 μN to 430 μN an accuracy of ≤ 1 μN can be achieved using a capaNCDT CS005 sensor head. This sensor, however, has a total range of 0.05 mm, making it very hard if not impossible to align the sensor and target manually. Additional equipment and micrometer adjustments are required. The 120 μN to 500 μN is covered using a CS05 sensor head with a total range of 0.5 mm. Here an accuracy of ≤ 6 μN or equivalently an accuracy of $\leq 5\%$ is achieved. The same sensor head is used to provide an accuracy of $\leq 1.2\%$ between 500 μN to 600 μN and an accuracy of $\leq 1\%$ in the 600 μN to 2800 μN range. Using the CS1 sensor head the 2800 μN to 9500 μN range is covered at an accuracy of ≤ 28 μN or equivalently and accuracy of $\leq 1\%$. In none of these setups the spring is connected. The requirements of ACCUR-1 and the PROP-PERF-200 / PROP-PERF-205 are depicted in [Figure 94](#).

To provide sufficient calibration range, the calibration actuator also needs to be upgraded. This is done by adding either one or two additional S-06-06-N magnets to the stack of the already existing magnet holder. For the current VTDC, that has an estimated $\text{dB/dX} = 0.0048 \text{ T m}^{-1}$, one magnet is added to the stack to give a total magnetic moment of $2 \times (0.19 \pm 0.014) \text{ A m}^2$. With this, a nominal current of 1.535 A to 5.208 A is required to provide a calibration force of 2800 μN to 9500 μN with a nominal accuracy of 11 μN . For the

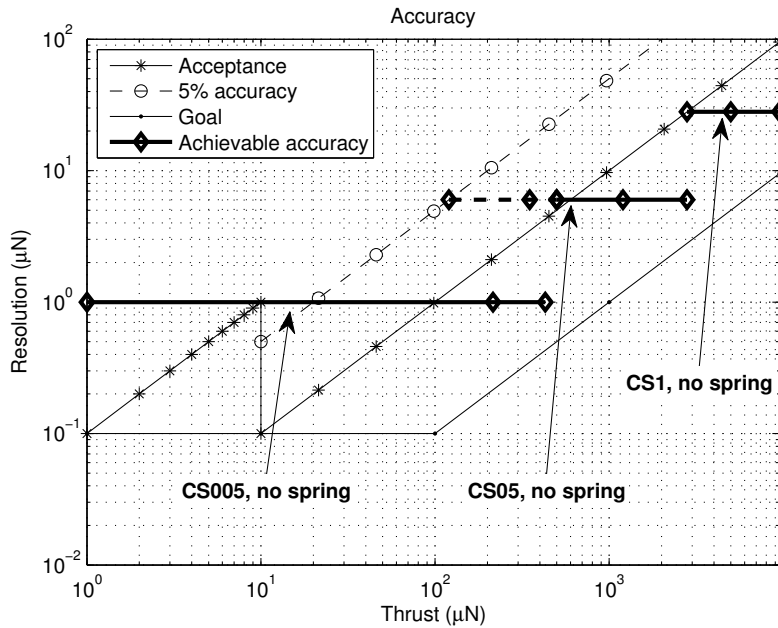


Figure 94: Achievable accuracies in preliminary design for an updated TB-5m design. The thrust range is split into four regions: 1 µN to 430 µN, 120 µN to 500 µN, 600 µN to 2800 µN and 2800 µN to 9500 µN. Assumed thruster mass of 600 g.

redesigned VTDC, that has an estimated $dB/dx = 0.0019 \text{ T m}^{-1}$, a second extra magnet is added to provide a total magnetic moment of $3 \times (0.19 \pm 0.014) \text{ A m}^2$. This consequently results in the need for a current of 2.585 A to 8.772 A to cover the same force range at an accuracy of 6 µN. The required currents with their respective margins are given in Table 41 and Table 42.

FORCE (µN)	MIN (A)	TYP (A)	MAX (A)
2800	$1.430 \cdot 10^0$	$1.535 \cdot 10^0$	$1.657 \cdot 10^0$
9500	$4.851 \cdot 10^0$	$5.208 \cdot 10^0$	$5.623 \cdot 10^0$

Table 41: Required electric current for calibration force of 2800 µN to 9500 µN range using the current coil ($dB/dx = 0.0048 \text{ T m}^{-1}$). Used magnet: two S-06-06-N magnets, with a total magnetic moment of $2 \times (0.19 \pm 0.014) \text{ A m}^2$.

8.2.2 Sample size

The sample size is currently limited to a width of $\leq 11 \text{ cm}$. This is not limiting the tests of the DelFFi propulsion system. However, a maximum height of 8 cm (PROP-SYST-200) can become problematic. This may require lengthening of the pendulum supports, depending

FORCE (μN)	MIN (A)	TYP (A)	MAX (A)
2800	$2.567 \cdot 10^0$	$2.585 \cdot 10^0$	$2.605 \cdot 10^0$
9500	$8.708 \cdot 10^0$	$8.772 \cdot 10^0$	$8.837 \cdot 10^0$

Table 42: Required electric current for calibration force of 2800 μN to 9500 μN range using the new coil ($\text{dB}/\text{dx} = 0.0019 \text{ T m}^{-1}$). Used magnet: three S-06-06-N magnets, with a total magnetic moment of $3 \times (0.19 \pm 0.014) \text{ A m}^2$.

on the thruster and subsystem shape. However, lengthening the supports can cause the thrust stand to no longer fit in the vacuum chamber. It is therefore advised that the required arm lengths are calculated based on the expected thrust range and engine mass and that sufficient clearance is ensured in the subsystem design.

8.2.3 *Alignment issues*

The thrust stand is not capable of determining the direction of the thrust vector and is sensitive to thruster misalignment. Without a complete redesign, the thrust vector cannot be determined directly. Alternative techniques, such as mounting the engine in different well-known orientations and comparing the consecutively generated thrusts to derive the orientation of the thrust vector, need to be employed to meet the measurement capability to validate the performance in accordance with requirement PROP-PERF-210. It is therefore advised that the thruster or subsystem contains an alignment cube that allows alignment of the engine on the thrust stand in a well-known orientation.

CONCLUSIONS AND RECOMMENDATIONS

The conclusions made based on the performed work and gathered insights are presented in this chapter. In [Section 9.1](#) the conclusions are presented and the main research question is answered. In [Section 9.2](#) recommendations are made for future research and for the further development of the [DARTS](#) facility. To conclude some recommendations are given for future students working on the thrust stand and the facility.

9.1 CONCLUSIONS

A thrust stand has been designed, manufactured and tested to provide a thrust measurement capability in the $1\ \mu\text{N}$ to $5000\ \mu\text{N}$ range and the impulse bit measurement capability in the $1\ \mu\text{Ns}$ – $1\ \text{mNs}$ range.

The research question is repeated here from the Introduction ([Chapter 1](#)) for the readers convenience.

How can the DARTS facility be upgraded to measure thrust levels in the $1\ \mu\text{N}$ to $5\ \text{mN}$ range and impulse bits in the $1\ \mu\text{Ns}$ to $1\ \text{mNs}$ range?

The mechanical design is based on the AE-TB-2m, which was designed in 2010 by Perez-Grande [68]. Modeling has shown that by changing the sensor system, the AE-TB-2m could be changed in such a way to extend its range and improve its accuracy and resolution. The laser triangulation sensor is replaced by a capacitive distance measurement and the counter mass has been split into five separate masses that increase the dynamic range by tuning the setup for a specific thruster. A calibration actuator was designed to allow in-situ calibration of both thrust and impulse bits. The design is based on a Variable-Turn Density Coil and is designed to have high linearity. The total range of the thrust stand is divided over three setups: $1\ \mu\text{N}$ to $45\ \mu\text{N}$, $45\ \mu\text{N}$ to $420\ \mu\text{N}$ and $200\ \mu\text{N}$ to $5000\ \mu\text{N}$ with accuracies of $0.1\ \mu\text{N}$, $1\ \mu\text{N}$ and $10\ \mu\text{N}$, respectively. These ranges are covered using two sensors: the Micro-Epsilon capaNCDDT CS1 and the capaNCDDT CS10 which are both connected to a capaNCDDT 6530 controller.

Using hardware-in-the-loop validation the performance of the thrust stand is confirmed to be on par with the requirements for the larger part of the range. Validation of the accuracy requirements require further analysis and testing as insufficient data are currently available.

To provide a measurement capability that is in line with the propulsion system requirements of the DelFFi project (version 3.0), the thrust measurement system (thrust stand, calibration system and data acquisition) needs to be updated. To be able to fulfill the extended range and accuracy requirements at a larger range of engine masses (up to 600 g including mounting bracket instead of up to 300 g), two additional sensors need to be acquired: the capaNCDT CS005 and capaNCDT CS05. Furthermore, additional magnets have to be added to the stacks that are now used in the magnet holders. An increased magnetic moment allows an increase in calibration force.

9.2 RECOMMENDATIONS

From the performed research and development within the scope of this thesis, recommendations are made for further research and updates on the [DARTS](#) facility.

9.2.1 *Future research and development*

The current research has shown that the thrust stand can be improved in specific areas. In this section, the research and development required for these improvements is discussed here.

9.2.1.1 *Damping*

The current damping has shown to be insufficient to suppress the noise from the environment to such an extent that the current natural oscillation that is found in the signal is removed. In order to reduce this oscillation, a damper needs to be installed. The development of a damper can be aimed at two road maps: passive and active damping. A passive damping mechanism should reduce the influence of any unwanted oscillations without influencing the limit sensitivity of the thrust stand. A possible solution can be found in the use of Foucault dampers [15]. This type of dampers uses a piece of metal with high magnetic permeability, typically copper, that is attached to the pendulum. When the pendulum oscillates, the metallic target moves through a magnetic field inducing eddy currents in the target. The eddy currents result in an opposing magnetic field with a restoring force that damps the oscillation. The advantage of these Foucault dampers is that the damping is proportional to the velocity at which the target moves through the field, effectively damping the oscillation, while maintaining the limit sensitivity (in steady state, no damping force is applied). On the downside, additional mass has to be added to the pendulum to provide a target.

Active damping mechanisms can be employed in a null-type thrust stand, in which an actuator is used to actively counter any motion

of the pendulum. Although these systems increase the accuracy of the stand around the equilibrium point and can increase the dynamic range, this is at the cost of increased complexity of the system. Any oscillation that is present in the mechanical system is transferred into the feedback loop.

9.2.1.2 *Symmetric design*

The current setup is asymmetric and uses a spring on only one side. The asymmetry potentially allows unwanted motion of the thrust stand. It is advised to revise the design such that a second spring is installed on the vacant side.

9.2.1.3 *Alignment cubes*

An engine is currently mounted to the stand using a single bolt that fastens it to the pendulum arm. This allows rotational freedom around the axis of the arm, introducing an uncertainty in the alignment of the engine, and thus the thrust vector. It is therefore advised to include alignment cubes on the thrusters or on their respective brackets and introduce an absolute reference on the thrust stand to which they can be aligned.

9.2.1.4 *Translational stages for sensor assembly*

The sensor is currently aligned manually with respect to the target. As one can imagine, aligning a sensor with a total range of 1 mm such that the equilibrium position is at half of the full scale, is challenging and inaccurate. To be able to utilize the full range offered by the sensor, the sensor assembly needs to be accurately placed with respect to the target. This can be achieved by mounting the sensor assembly on a translational stage that is fixed to the thrust stand base plate. Translational stages are typically used in optical assemblies and are controlled using a micrometer that allows placement accurate up to a few micrometers.

9.2.1.5 *Manufacture and verification of the new actuator*

In this thesis, it has been shown that the current calibration actuator has a nonlinearity. This nonlinearity was traced back to an error in the optimization and the model has since been adapted. A new coil design is available, that is ready for manufacturing. For increased linearity of the calibration and an increased accuracy, it is advised that the new design is manufactured and verified.

9.2.1.6 *Spring calibration*

Unexplained stiffness is present in the setup, possibly induced by the mounted spring. It is advised that the spring is tested separately in a

traceable fashion that is more accurate than the currently employed techniques. Accuracy can be gained in the measurement of the rotation. As explained in [Appendix B](#), the relative error introduced by the low absolute accuracy at small rotation angles results in a large uncertainty in spring constant at small angles. Smaller uncertainties in the found spring constant can indicate if the spring is indeed truly linear as concluded in [Appendix B](#) or if there is currently uncharacterized non-linear behavior present.

9.2.2 *Delft Aerospace Rocket Thrust Stand facility*

The [DARTS](#) facility requires upgrades to allow more accurate thrust measurements. The following recommendations are aimed at upgrades related directly to the facility and the available hardware.

9.2.2.1 *Micro scale*

Currently the Mettler Toledo AG245 scale is used for the calibration of the actuator. As discussed in [Section 7.3.1](#), the scale is unstable at low loads and can show sticky behavior. It is therefore recommended that the scale is replaced by a more accurate and more sensitive model. A readability of $\leq 1 \cdot 10^{-2}$ mg is required to provide sufficient accuracy for calibration in the lowest force range of the actuator. Additionally, it is advised that the setup for TEST-110 is placed in the vacuum chamber, which is kept at ambient pressure. Being isolated from air flows in the clean room reduces the induced uncertainties in the actuator calibration.

9.2.2.2 *Recalibration of all transducers*

As listed in [Table 28](#), the calibration of most transducers is overdue. Some sensors, such as the Omega PX139 for example, can no longer be operated because of large offsets or sensitivities. Calibrated sensors are required for traceable and accurate measurements.

9.2.2.3 *High or Ultra High Vacuum facility*

The Heraeus Vacuotherm vacuum oven is limited to an operational pressure of approximately 1 mbar. For thrust measurements of micropropulsion systems, better vacuums are required or wanted to minimize the effect of the ambient pressure on the low thrust that is produced by the engine ([Section 6.2.13](#)). It is recommended that the procurement of an (Ultra) High Vacuum facility is investigated. For students there are also possibilities of performing measurements in the vacuum facilities of ESA [EPL](#), that provide an [UHV](#) environment. The costs associated with procuring such facility or using a commercial facility should be investigated.

9.2.2.4 *Relocation of facility*

The facility is currently located on the eighth floor of an office building. Both the motion of the building and the presence of people in the vicinity disturb the readings by introducing vibrations. It is recommended that the facility is moved to ground floor and is ideally placed on an isolated base. This base is not connected to the rest of the building such that vibrations that are transferred via the base cannot disturb the readings. This recommendation

9.2.3 *Advise for future students*

For future students working on the thrust stand or using it as part of their verification and validation process the following advise is given. The advise is aimed at streamlining tests and usage of the thrust stand.

9.2.3.1 *Planning*

In experiments the operator is dependent on the environment and the hardware. Both influence the tests to a large extend and problems will almost certainly be encountered. One week should be scheduled to be able to overcome problems and to be able to tune the setup to work properly. Also, have data processing programs ready before commencing measurements. The ability to check the outcome of an experiment before starting another one, allows prioritization of measurements and finding unexpected behavior whenever present. Problems with the setup that are not apparent at first glance of the raw data, may become apparent after processing.

9.2.3.2 *Electronic design*

The typical aerospace engineering student does not have a strong background in electronic design, nor does he or she have practical experience with electrical components. It is therefore advised to have an experienced electrical engineer double check any electronics that is designed before usage. This overcomes unwanted damages to the components or third party components.

9.2.3.3 *Documentation*

As shown in [Section 7.3.8](#), photos were examined to show that an operator error had occurred from which a noticed unexpected effect was explained. It is advised to keep both a journal and a photographic log of all activities. This makes it possible to later trace back problems that are encountered and were not noticed during the experimentation.

BIBLIOGRAPHY

- [1] 3DWorknet. Private conversation, 2013. URL www.3dworknet.com.
- [2] Arkema. Private conversation, 2013.
- [3] M.C.M. Bakker. *Measurement Technique and Sensors for Materials and Structures, AE4-736 Reader*. TU Delft, Delft, 2008.
- [4] Constatine A. Balanis. *Antenna Theory: Analysis and Design*. 3 edition, 2005. ISBN 0-471-66782-X.
- [5] E.J. Beiting. Impulse Thrust Stand for MEMS Propulsion Systems. In *35th AIAA/ASME/SAE/ASEE Joint Propulsion Conference and Exhibit*, Los Angeles, CA, USA, 1999.
- [6] FAR Belien, CDH Bertels, A van Ettinger, DW Florijn, JLJ Herpers, CO Janssen, MM van Lith, R Mangon, and SB Nedkov. *E-Moth: Mission to the Moon*. Bsc. thesis / design synthesis exercise, Delft University of Technology, 2011.
- [7] R.J.F. Bijster. Microthruster characterization using thrust benches. Technical report, Delft University of Technology, Delft, 2013.
- [8] L. Bisi. *Upgrade of the data acquisition system of a 1N demonstrative model resistojet and analysis of its propulsive and thermal performance*. Master of science thesis, Delft University of Technology, 2005.
- [9] Timothy H. Boyer. The force on a magnetic dipole. *American Journal of Physics*, 56(8):688, 1988. ISSN 00029505. doi: 10.1119/1.15501. URL <http://link.aip.org/link/?AJP/56/688/1&Agg=doi>.
- [10] H. Brito, R. Garay, R. Duelli, and S. Maglione. A Compact, Low-Cost Test Stand for PPT Impulse Bit Measurements. In *36th AIAA/ASME/SAE/ASEE Joint Propulsion Conference*, Huntsville, Alabama, 2000. AIAA 2000-3435.
- [11] Bronkhorst. Mass flow meters & controllers for GAS, 2013. URL http://www.bronkhorst.com/en/products/gas_flow_meters_and_controllers/.
- [12] Brooks. Data Sheet DS-TMF-5800s-MFC-eng, 2008. URL <http://www.brooksinstrument.com/downloads/ProductDocumentation/ThermalMassFlowMetersControllersDigitalGas/DataSheets/ds-tmf-5800s-mfc-eng.pdf>.

- [13] Brooks. Thermal Mass Flow Controllers and Meters, 2013. URL <http://www.brooksinstrument.com/flow-pressure-level-measurement-technology/thermal-mass-flow.html>.
- [14] M.J. Burton, S.S. Wilson, and R.L. Bushman. A compact thrust stand for pulsed plasma thrusters. In *25th International Electric Propulsion Conference*, pages 765–772, Cleveland, Ohio, USA, 1997.
- [15] G. Cagnoli, L. Gammaitoni, J. Kovalik, F. Marchesoni, and M. Punturo. Eddy current damping of high Q pendulums in gravitational wave detection experiments. *Review of Scientific Instruments*, 69(7):2777, 1998. ISSN 00346748. doi: 10.1063/1.1149015. URL <http://link.aip.org/link/RSINAK/v69/i7/p2777/s1&Agg=doi>.
- [16] J. A. Cape and R.A. Young. Canted Helmholtz Coils for Constant-Gradient Faraday Balance Magnetometry. *Review of Scientific Instruments*, 42(7):1061, 1971. ISSN 00346748. doi: 10.1063/1.1685279. URL <http://link.aip.org/link/?RSI/42/1061/1&Agg=doi>.
- [17] Angelo Cervone. Propulsion System Requirements for the DelFFi Satellites (DelFFi/PROP/REQ/3.0), 2013.
- [18] Martin Connors and Farook Al-Shamali. The Magnetic Torque Oscillator and the Magnetic Piston. *The Physics Teacher*, 45(7):440, 2007. ISSN 0031921X. doi: 10.1119/1.2783155. URL <http://link.aip.org/link/PHTEAH/v45/i7/p440/s1&Agg=doi>.
- [19] E. A. Cubbin, J. K. Ziemer, E. Y. Choueiri, and R. G. Jahn. Pulsed thrust measurements using laser interferometry. *Review of Scientific Instruments*, 68(6):2339, 1997. ISSN 00346748. doi: 10.1063/1.1148116. URL <http://link.aip.org/link/RSINAK/v68/i6/p2339/s1&Agg=doi>.
- [20] F.M. Dekking, C. Kraaikamp, H.P. Lopuhaa, and L.E. Meester. *A Modern Introduction to Probability and Statistics: Understanding Why and How*. Springer-Verlag London Limited, 2005. ISBN 1-85233-896-2.
- [21] Brian C. D’Souza and Andrew D. Ketsdever. Investigation of time-dependent forces on a nano-Newton-second impulse balance. *Review of Scientific Instruments*, 76(1):015105, 2005. ISSN 00346748. doi: 10.1063/1.1834707. URL <http://link.aip.org/link/RSINAK/v76/i1/p015105/s1&Agg=doi>.
- [22] EOS. PA 2200, 2010. URL www.3dworknet.com/fileupload/Datasheets/Datasheet_PA2200.pdf.

- [23] P. Fernandes, G. Gessini, R. Marrega Sandonato, J. Toshiyuki Irita, G. Americo Neves, and Et Al. A Pendulum Target Balance for Ion Engine Thrust Measurement. In *30th International Electric Propulsion Conference*, pages 1–12, Florence, Italy, 2007.
- [24] Benjamin M.C. Friedman, Michael G. Abraham, Mark Paetkau, S. Richard Taylor, and Cynthia Ross Friedman. Use of a varying turn-density coil (VTDC) to generate a constant-gradient magnetic field and to demonstrate the magnetic force on a permanent magnet. *Canadian Journal of Physics*, 91(3):226–230, March 2013. ISSN 0008-4204. doi: 10.1139/cjp-2012-0405. URL <http://www.nrcresearchpress.com/doi/abs/10.1139/cjp-2012-0405>.
- [25] MI Ganef. *Lunar Transfer Optimization for OLFAR*. Msc. thesis, Delft University of Technology, 2013.
- [26] I.S. Grant and W.R. Phillips. *Electromagnetism*. John Wiley and Sons, Ltd., Bristol, 1975. ISBN 0 471 32246 6.
- [27] A.N. Grubišić and S.B. Gabriel. Development of an indirect measurement Micro-to-Milli-Newton thrust balance. In *International Space Propulsion Conference*, Crete, Greece, 2008.
- [28] A.N. Grubišić and S.B. Gabriel. Development of an indirect counterbalanced pendulum optical-lever thrust balance for micro- to millinewton thrust measurement. *Measurement Science and Technology*, 21(10):105101, 2010. ISSN 09570233. doi: 10.1088/0957-0233/21/10/105101. URL <http://stacks.iop.org/0957-0233/21/i=10/a=105101?key=crossref.0386ec76b8ed5fb614b3d01e56336eca>.
- [29] Jian Guo. Private conversation, 2013.
- [30] Thomas W. Haag. Thrust stand for pulsed plasma thrusters. *Review of Scientific Instruments*, 68(5):2060, 1997. ISSN 00346748. doi: 10.1063/1.1148097. URL <http://link.aip.org/link/RSINAK/v68/i5/p2060/s1&Agg=doi>.
- [31] C. Hartsuijker and J.W. Welleman. *Engineering Mechanics, Volume 2 - Stresses, Strains, Displacements*. Springer, Delft, 2007. ISBN 978-1-4020-4123-5.
- [32] Desmond J. Higham. *Financial Option Valuation*. Cambridge University Press, Cambridge, 1 edition, 2004. ISBN 978-0-521-54757-4.
- [33] D.L. Hitt, C.M. Zakrzewski, and M.A. Thomas. MEMS-based satellite micropropulsion via catalyzed hydrogen peroxide decomposition. *Smart Materials and Structures*, 10:1163–1175, 2001. URL http://iopscience.iop.org/0964-1726/10/6/305/pdf/0964-1726_10_6_305.pdf.

- [34] Jeff Hopkins. Skill: Applying PTFE tape to tapered pipe threads, 2012. URL <http://norcal.swagelok.com/blog/bid/88017/Skill-Applying-PTFE-tape-to-tapered-pipe-threads>.
- [35] IEST. FED STD 209E: AIRBORNE PARTICULATE CLEANLINESS CLASSES IN CLEANROOMS AND CLEAN ZONES. Technical report, Institute of Environmental Sciences and Technology, 1992. URL http://www.everyspec.com/FED-STD/FED-STD-209E_21739/.
- [36] Daniel J. Inman. *Engineering Vibrations*. Pearson Education International, New Jersey, USA, third edition, 2009. ISBN 978-0-13-136311-3.
- [37] ISO. ISO 5725-1:1994: Accuracy (trueness and precision) of measurement methods and results - Part 1: General principles and definitions. Technical report, International Organization for Standardization, Geneva, 1994.
- [38] ISO. ISO 14644-1, Cleanrooms and associated controlled environments - Part 1: Classification of air cleanliness. Technical report, International Organization for Standardization, Geneva, 1999.
- [39] S.M.J. Janssens. *Design of a micro propulsion test bench*. Msc. thesis, Delft University of Technology, 2009.
- [40] JCGM. International vocabulary of metrology - Basic and general concepts and associated terms (VIM). 2008. URL http://www.bipm.org/utils/common/documents/jcgm/JCGM_200_2008.pdf.
- [41] A.D. Ketsdever and B.C. D'Souza. Development of a Nano-Impulse Balance for Micropropulsion Systems. In *41st AIAA/ASME/SAE/ASEE Joint Propulsion Conference and Exhibit*, Tucson, AZ, USA, 2005. AIAA 2005-4080.
- [42] H Koizumi, K Komurasaki, and Y Arakawa. Development of thrust stand for low impulse measurement from microthrusters. *Review of Scientific Instruments*, 75(10):3185, 2004. ISSN 00346748. doi: 10.1063/1.1790568. URL <http://link.aip.org/link/RSINAK/v75/i10/p3185/s1&Agg=doi>.
- [43] Robert-Jan Koopmans. Test facilities in Europe and requirements on test facilities. Technical report, TNO, Rijswijk, 2006.
- [44] Johan Kuiper. GAIA-BE-RP-0019: PMT Thrust and Thrust Noise Characterization at the ONERA Thrust Test Facility. Technical report, Bradford Engineering B.V., 2008.
- [45] Johan Kuiper. GAIA-BE-RP-0018: PMT Thrust Characterization at ONERA: Test Report. Technical report, Bradford Engineering B.V., 2008.

- [46] Johan Kuiper. Private conversation, 2013.
- [47] J.W. Emhoff D.H. Simon H. Bruce Land. Progress in Thrust Measurements from Micro Pulsed Plasma Discharges. In *43rd AIAA/ASME/SAE/ASEE Joint Propulsion Conference & Exhibit*, Cincinnati, Ohio, USA, 2007.
- [48] Riki H. Lee, Brian C.D. Souza, and Taylor C. Lilly. Thrust Stand Micro-Mass Balance Diagnostic Techniques for the Direct Measurement of Specific Impulse Due to Mass Due to Impulse. *Mechanical Engineering*, (7), 2007.
- [49] T.C. Taylor C. Lilly, Andrew Ketsdever, Anthony P. Pancotti, and Marcus Young. Development of a Specific Impulse Balance for Capillary Discharge Pulsed Plasma Thrusters. *Journal of Propulsion and Power*, 25(3):823–826, May 2009. ISSN 0748-4658. doi: 10.2514/1.40261. URL <http://arc.aiaa.org/doi/abs/10.2514/1.40261>.
- [50] D. Di Cara L. Massotti S. Cesare F. Musso G. Castorina D. Feili B. Lotz. Performance verification of the uNRIT-2.5 thruster on the Nanobalance facility. In *32nd International Electric Propulsion Conference*, Wiesbaden, Germany, 2011.
- [51] Matbase. Polyamide 11 [PA 11], 2013. URL <http://www.matbase.com/material-categories/natural-and-synthetic-polymers/engineering-polymers/material-properties-of-polyamide-11-nylon-11-pa-11.html>.
- [52] Mettler-Toledo. Operating instructions METTLER TOLEDO AG balances. Technical report, Mettler-Toledo GmbH, 2004. URL http://us.mt.com/dam/mt_ext_files/Editorial/Generic/1/AG_03811812710212231_files/ag-ba-e-11780182.pdf.
- [53] Micro-Epsilon. capaNCDT: High resolution capacitive displacement sensors and systems, 2013. URL <http://www.micro-epsilon.com/download/products/cat--capaNCDT--en.pdf>.
- [54] Alessandro Migliaccio. How to Order a Nitrogen Storage Cylinder, 2010.
- [55] Michael J. Moloney. Strong Little Magnets. *The Physics Teacher*, 45(6):352, 2007. ISSN 0031921X. doi: 10.1119/1.2768691. URL <http://link.aip.org/link/PHTEAH/v45/i6/p352/s1&Agg=doi>.
- [56] J. Mueller, C. Marrese, J. Ziemer, A. Green, E. Yang, M. Mojarradi, T. Johnson, V. White, and D. Bame. JPL micro-thrust propulsion activities. In *AIAA Nanotech 2002*, Houston, TX, USA, 2002. AIAA. URL <http://hdl.handle.net/2014/10354>.

- [57] NASA. NASA Procedural Requirements NPR 7120.5D. Technical report, NASA Office of the Chief Engineer, 2007. URL http://fpd.gsfc.nasa.gov/NPR71205D/NPR_7120_5D.pdf.
- [58] National-Instruments. NI 622x Specifications. Technical report, National Instruments, 2007. URL <http://www.ni.com/pdf/manuals/371290g.pdf>.
- [59] National-Instruments. Troubleshooting Unexpected Voltages, Floating, or Crosstalk on Analog Input Channels, 2012. URL <http://digital.ni.com/public.nsf/allkb/B9BCDFD960C06B9186256A37007490CD>.
- [60] National-Instruments. How Do I Eliminate Ghosting From My Measurements?, 2012. URL <http://digital.ni.com/public.nsf/allkb/73CB0FB296814E2286256FFD00028DDF?OpenDocument>.
- [61] National-Instruments. Calibration Service for NI Data Acquisition Hardware, 2013. URL <http://sine.ni.com/nips/cds/view/p/lang/nl/nid/207957>.
- [62] Ron Noomen. Private conversation, 2013.
- [63] NorthwesternU. Regulator Installation, 2013. URL <http://www.youtube.com/watch?v=u0vwDbNDdWA>.
- [64] NPL. What do high vacuum and low vacuum mean?, 2010. URL [http://www.npl.co.uk/reference/faqs/what-do-high-vacuum-and-low-vacuum-mean-\(faq-pressure\)](http://www.npl.co.uk/reference/faqs/what-do-high-vacuum-and-low-vacuum-mean-(faq-pressure)).
- [65] Omega. PX209, PX219, PXM209, PXM219. URL <http://www.omega.com/manuals/manualpdf/M4085.pdf>.
- [66] D. Packan, J. Bonnet, and S. Rocca. Thrust Measurements with the ONERA Micronewton Balance. In *30th International Electric Propulsion Conference*, Florence, Italy, 2007. IEPC-2007-118.
- [67] D. Packan, J. Bonnet, and S. Rocca. The ONERA Micro-Newton Balance: Advances in thrust measurements and modeling. In *5th International Spacecraft Propulsion Conf. and 2nd International Symposium on Propulsion for Space Transportation*, Heraklion, Greece, 2008.
- [68] Daniel Perez-Grande. *Design and Development of a nano-propulsion thrust bench*. Msc. thesis, Universidad Politecnica de Madrid ; Delft University of Technology, 2010.
- [69] J. Perez Luna, C.H. Edwards, J. Gonzalez del Amo, and B. Hughes. Development Status of the ESA Micro-Newton Thrust Balance. In *32nd International Electric Propulsion Conference*, Wiesbaden, Germany, 2011.

- [70] Kurt A. Polzin, Thomas E. Markusic, Boris J. Stanojev, Amado DeHoyos, and Benjamin Spaun. Thrust stand for electric propulsion performance evaluation. *Review of Scientific Instruments*, 77(10):105108, 2006. ISSN 00346748. doi: 10.1063/1.2357315. URL <http://link.aip.org/link/RSINAK/v77/i10/p105108/s1&Agg=doi>.
- [71] R.J. Koopmans. *Improvement of the Delft Aerospace Rocket Test Stand*. Master of science thesis, Delft University of Technology, 2007.
- [72] K.J.A. Rycek. *Initial design and preliminary performance characterization of a 1N laboratory resistojet DUR-1*. Master of science thesis, Delft University of Technology, 2005.
- [73] Akihiro Sasoh and Yoshihiro Arakawa. A high-resolution thrust stand for ground tests of low-thrust space propulsion devices. *Review of Scientific Instruments*, 64(3):719, 1993. ISSN 00346748. doi: 10.1063/1.1144204. URL <http://link.aip.org/link/RSINAK/v64/i3/p719/s1&Agg=doi>.
- [74] Nathaniel P. Selden and Andrew D. Ketsdever. Comparison of force balance calibration techniques for the nano-Newton range. *Review of Scientific Instruments*, 74(12):5249, 2003. ISSN 00346748. doi: 10.1063/1.1623628. URL <http://link.aip.org/link/RSINAK/v74/i12/p5249/s1&Agg=doi>.
- [75] James Spanjers, Greg Lake, and Greg Cavallaro. Resonant Operation of a Micro-Newton Thrust Stand. In *38th AIAA/ASME/SAE/ASEE Joint Propulsion Conference & Exhibit*, Indianapolis, Indiana, USA, 2002. AIAA 2002-3821.
- [76] SSE. Facility Handbook 2.
- [77] Neil Storey. *Electronics - A systems approach*. Pearson Education Limited, Harlow, England, 4 edition, 2009. ISBN 978-0-273-71918-2.
- [78] O. Sutherland, M. Appolloni, S. O'Neil, J. Gonzalez del Amo, and B. Hughes. Advances with the ESA Propulsion Laboratory uN Thrust Balance. In *5th Int. Space Propulsion Conference*, Crete, Greece, 2008.
- [79] O. Sutherland, B. Benneke, S. Oberhollenzer, and J. Gonzalez del Amo. Standardization and Validation of a Test Harness for uN Thrust Measurement Using the Mettler-Toledo AX504. In *Proceedings of 6th ISPC*, Heraklion, Greece, 2008.
- [80] Haibin Tang, Chenbo Shi, Xin'ai Zhang, Zun Zhang, and Jiao Cheng. Pulsed thrust measurements using electromagnetic calibration techniques. *The Review of scientific instruments*, 82(3):

- 035118, March 2011. ISSN 1089-7623. doi: 10.1063/1.3567803. URL <http://www.ncbi.nlm.nih.gov/pubmed/21456799>.
- [81] Texas-Instruments. Application Note 31: Op Amp Circuit Collection. Technical report, Texas Instruments, 2002. URL <http://www.ti.com/ww/en/bobpease/assets/AN-31.pdf>.
- [82] M.F. van Bolhuis. *Delft Aerospace Space propulsion Test Facility*. Master of science thesis, Delft University of Technology, Delft, 2004.
- [83] W. Whyte, editor. *Cleanroom design*. John Wiley and Sons, Ltd., Chichester, West Sussex, England, 1991. ISBN 0471928143.
- [84] W.D. Willis III, C.M Zakrzwski, and S.M. Merkwowitz. Development of a Thrust Stand to Meet LISA Mission Requirements. In *38th AIAA/ASME/SAE/ASEE Joint Propulsion Conference & Exhibit*, Indianapolis, Indiana, USA, 2002. AIAA 2002-3820.
- [85] Andrea R Wong, Alexandra Toftul, Kurt A Polzin, and J Boise Pearson. Non-contact thrust stand calibration method for repetitively pulsed electric thrusters. *The Review of scientific instruments*, 83(2):025103, March 2012. ISSN 1089-7623. doi: 10.1063/1.3680557. URL <http://www.ncbi.nlm.nih.gov/pubmed/22380121>.
- [86] Kunning G. Xu and Mitchell L.R. Walker. High-power, null-type, inverted pendulum thrust stand. *The Review of scientific instruments*, 80(5):055103, May 2009. ISSN 1089-7623. doi: 10.1063/1.3125626. URL <http://www.ncbi.nlm.nih.gov/pubmed/19485530>.
- [87] A.H. Yan, B.C. Appel, and J.G. Gedrimas. MilliNewton Thrust Stand Calibration Using Electrostatic Fins. In *47th AIAA Aerospace Sciences Meeting Including The New Horizons Forum and Aerospace Exposition*, Orlando Florida, 2009. AIAA 2009-212.
- [88] V. Yuce. GAIA-BE-RP-0010: GAIA QM PMT Thrust Performance Test Report. Technical report, Bradford Engineering B.V., 2006.
- [89] S.M. Zakrzwski, P.G. Merkwowitz, C.M. Maghami, A. Willis, and W.D. Sharma. A microNewton thrust-stand for LISA. *Classical and Quantum Gravity*, 19:1745–1750, 2002. URL stacks.iop.org/CQG/18/1745.
- [90] B.T.C. Zandbergen. Leak analysis fundamentals (draft). Technical report, TU-Delft, Faculty of Aerospace Engineering, 2006.
- [91] B.T.C. Zandbergen. AE4S01: Thermal Rocket Propulsion (version 2.04), 2010.

- [92] B.T.C. Zandbergen. Private conversation, 2013.
- [93] B.T.C. Zandbergen, S. Janssens, F. Valente, D. Perez-Grande, and R. Koopmans. Test facility development for testing of micro-thrusters at TU-Delft. In *6th International Spacecraft Propulsion Conference, San Sebastian, Spain, 3-6 May 2010*, San Sebastian, Spain, 2010. URL <http://repository.tudelft.nl/view/ir/uuid:ec41e926-e040-4483-bb24-2a742cce0b4a/>.

HELMHOLTZ AND ANTI-HELMHOLTZ SETUPS

Using a combination of solenoids, the magnetic field between the coils can be shaped by changing the dimensions of the solenoids and their relative positioning. For several applications in physics, such as calibration of Gauss meters and cancellation of the Earth magnetic field, scientists and engineers utilize several arrangements to create homogeneous magnetic fields. One of those setups is the Helmholtz setup. In the following sections the Helmholtz setup and the Anti-Helmholtz setup will be discussed. The latter setup is used to create large magnetic field gradients in stead of homogeneous fields of constant field strength and are for example used in quantum physics experiments.

A.1 HELMHOLTZ

The Helmholtz setup is composed of two coaxial circular solenoids of radius R with their centers separated by a distance R . Using the Biot-Savart law, that describes the magnetic field around a wire element due to an electric current, the magnetic field strength B along the center line can be calculated[1]. For this it is assumed that both coils can be represented as single current loops. In this case the length of the coils and the number of windings layers are neglected. This simplified case can be used to represent field characteristics, while ignoring higher order effects. The magnetic field strength is given by

$$B = \frac{\mu_0 i R^2}{2} \left\{ \frac{1}{(R^2 + x^2)^{3/2}} + \frac{1}{(R^2 + (R - x)^2)^{3/2}} \right\} \quad (\text{A-1})$$

where μ_0 is the magnetic permeability of free space, i the electric current in A and x the coordinate along the center line in m. The conventions used can be found in [Figure A-1](#). The field gradient with respect to x can be found using partial differentiation.

$$\mu_0 = 4\pi \cdot 10^{-7} \text{ Vs A}^{-1} \text{ m}^{-1}$$

$$\frac{\partial B}{\partial x} = \frac{\mu_0 i R^2}{2} \left\{ \frac{-3x}{(R^2 + x^2)^{5/2}} + \frac{3(R - x)}{(R^2 + (R - x)^2)^{5/2}} \right\} \quad (\text{A-2})$$

The field strength and field gradient for a Helmholtz setup, calculated using (A-1) and (A-2), are plotted in [Figure A-2](#). As can be seen in the figure, the field strength is constant from approximately $-0.1 \frac{x}{R}$ to $0.1 \frac{x}{R}$.

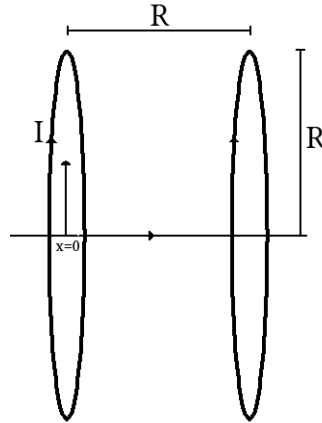


Figure A-1: Sketch of a Helmholtz setup.

A.2 ANTI-HELMHOLTZ

The geometry of the Anti-Helmholtz setup is equal to that of the normal Helmholtz setup. The current in one of the two solenoids, however, is reversed. The two opposing magnetic fields result in a field of steep gradients. The magnetic field strength and field gradient can be described with equations that are very similar to (A-1) and (A-2). The field strength B is given by

$$B = \frac{\mu_0 i R^2}{2} \left\{ \frac{1}{(R^2 + x^2)^{3/2}} - \frac{1}{(R^2 + (R-x)^2)^{3/2}} \right\} \quad (\text{A-3})$$

and the field gradient by

$$\frac{\partial B}{\partial x} = \frac{\mu_0 i R^2}{2} \left\{ \frac{-3x}{(R^2 + x^2)^{5/2}} - \frac{3(R-x)}{(R^2 + (R-x)^2)^{5/2}} \right\} \quad (\text{A-4})$$

The field strength and field gradient for an Anti-Helmholtz setup, calculated using (A-3) and (A-4), are plotted in Figure A-3. As can be seen in the figure, the gradients are steeper than for a normal Helmholtz setup.

REFERENCES

- [1] I.S. Grant and W.R. Phillips. *Electromagnetism*. John Wiley and Sons, Ltd., Bristol, 1975. ISBN 0 471 32246 6.

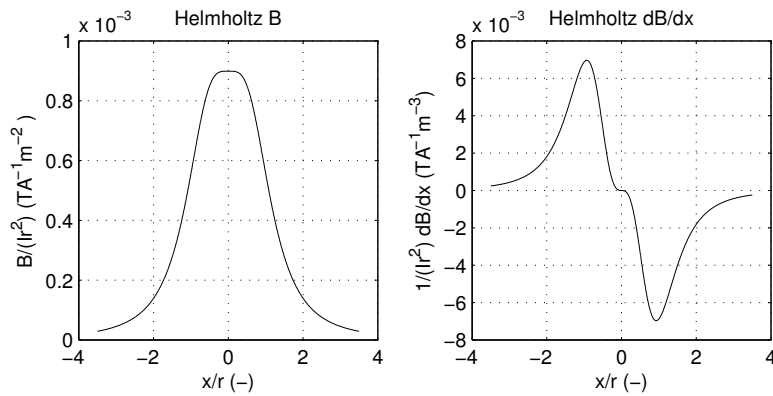


Figure A-2: Field strength and field gradient of a Helmholtz setup. The field strength B and gradient dB/dx have been made independent of coil radius and electric current. Reference has been moved to coincide with the centerpoint between the two coils.

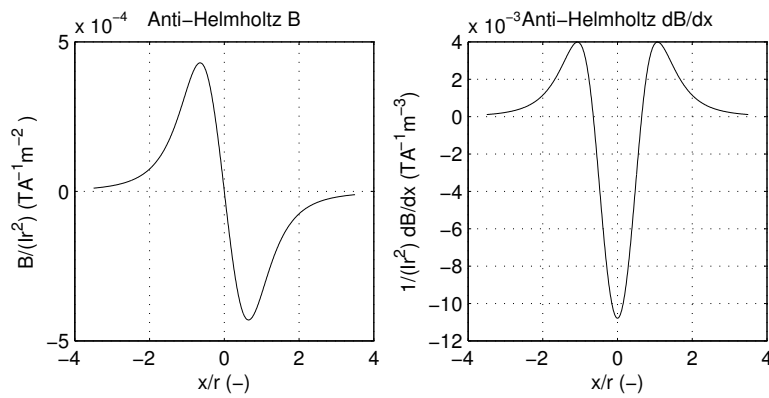


Figure A-3: Field strength and field gradient of an Anti-Helmholtz setup. The field strength B and gradient dB/dx have been made independent of coil radius and electric current. Reference has been moved to coincide with the centerpoint between the two coils.

DETERMINATION OF THE SPRING CONSTANT

For the TB-5m the rotational spring of the TB-2m design is reused. The TB-2m design used a spring constant of 0.3 N m rad^{-1} . The actual spring constant has to be known before new design activities can be undertaken, as this spring constant influences both the resolution and the full range of the new thrust stand. In this appendix, the measurement campaign for determining the spring constant of the available spring is described. The measurements are used to verify that the spring meets the design specifications of the TB-2m, as this has never been confirmed. The measurement setup and methods are described, followed by the accuracy analysis and results.

B.1 MEASUREMENT SETUP

The setup is composed of parts of the TB-2m thrust stand as it is depicted in [Figure B-1](#). The counter-mass, arm and gas canisters have been removed to reduce the effects of gravity. The cross-beam that supports the arm is left in place. A load is applied by suspending weights from one of the bolts, that fix the gas canister brackets to the cross-beam. A photo of the setup is presented in [Figure B-2](#). The masses are placed on an aluminium plate, that is suspended from the cross-beam using FireLine fishing line. The applied weight will cause the cross-beam to rotate. The rotation angle is measured by using a protractor to assess the angle between the bottom side and the wire.

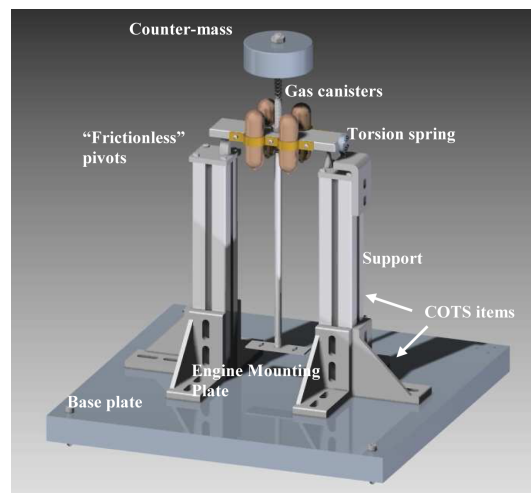


Figure B-1: 3D drawing of the TB-2m[1]

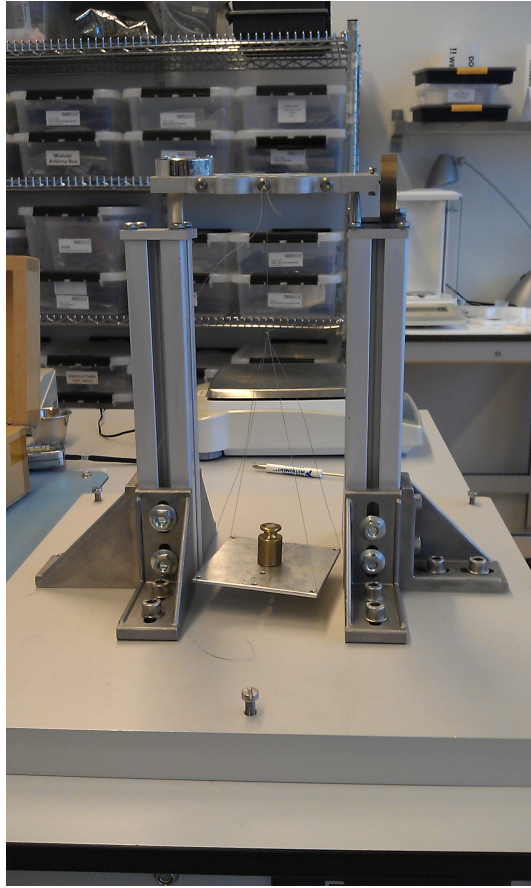


Figure B-2: Photo of measurement setup with mass suspended from cross-beam.

B.2 THEORETICAL MODEL

From the balance of moments around the pivot of the thrust stand, it can be derived that

$$K = \{(M_{\text{mass}} + M_{\text{basket}}) r + M_{\text{arm}} r_{\text{cg}}\} \frac{\cos \theta}{\theta} g \quad (\text{B-1})$$

where K is the spring constant in N m rad^{-1} , M_{mass} is the mass of the calibrated mass suspended from the string in kg, M_{basket} is the mass of the line and basket in kg, M_{arm} is the mass of the pendulum support arm in kg, r is the arm from pivot to line attachment location in m, r_{cg} is the arm from the pendulum support arm center of gravity to the pivot in m, θ is the rotation angle in rad and g is the gravitational acceleration in m s^{-2} .

The error in the estimation of the spring constant found in this way can be estimated using the following set of equations:

$$\Delta K = \left| \frac{\partial K}{\partial M_{\text{mass}}} \right| \Delta M_{\text{mass}} + \left| \frac{\partial K}{\partial M_{\text{basket}}} \right| \Delta M_{\text{basket}} + \left| \frac{\partial K}{\partial r} \right| \Delta r + \left| \frac{\partial K}{\partial M_{\text{arm}}} \right| \Delta M_{\text{arm}} + \left| \frac{\partial K}{\partial r_{\text{cg}}} \right| \Delta r_{\text{cg}} + \left| \frac{\partial K}{\partial \theta} \right| \Delta \theta + \left| \frac{\partial K}{\partial g} \right| \Delta g \quad (\text{B-2})$$

$$\left| \frac{\partial K}{\partial M_{\text{mass}}} \right| = \left| \frac{\partial K}{\partial M_{\text{basket}}} \right| = rg \frac{\cos \theta}{\theta} \quad (\text{B-3})$$

$$\left| \frac{\partial K}{\partial r} \right| = (M_{\text{mass}} + M_{\text{basket}}) \frac{\cos \theta}{\theta} g \quad (\text{B-4})$$

$$\left| \frac{\partial K}{\partial M_{\text{arm}}} \right| = r_{\text{cg}} \frac{\cos \theta}{\theta} g \quad (\text{B-5})$$

$$\left| \frac{\partial K}{\partial r_{\text{cg}}} \right| = M_{\text{arm}} \frac{\cos \theta}{\theta} g \quad (\text{B-6})$$

$$\left| \frac{\partial K}{\partial \theta} \right| = \{(M_{\text{mass}} + M_{\text{basket}}) r + M_{\text{arm}} r_{\text{cg}}\} \left(\frac{\sin \theta}{\theta} + \frac{\cos \theta}{\theta^2} \right) g \quad (\text{B-7})$$

$$\left| \frac{\partial K}{\partial g} \right| = \{(M_{\text{mass}} + M_{\text{basket}}) + M_{\text{arm}} r_{\text{cg}}\} \frac{\cos \theta}{\theta} \quad (\text{B-8})$$

B.3 MEASUREMENT PLAN

In this section, the conducted experiments are described, as well as the order in which steps are conducted and if necessary how they are conducted.

B.3.1 Test overview

The loads are suspended from either side of the cross-beam. The side of the thrust stand where the Electrostatic Discharge (ESD) connector is mounted on the baseplate, is labelled the ESD side to distinguish between both sides.

B.3.2 Procedure

Step 1: Level the cross-beam

The cross-beam has to be levelled before any loads are applied. To do this a wire and protractor are used. Loosen the center bolt that fixes the canister bracket to the cross-beam. Put the string between the bracket and the beam and re-fasten the bolt. Tie a small mass, such as a small nut or bolt, to the end of the wire. This will cause gravity to stretch the wire. Now loosen the two small bolts that fix the cross-beam to the axis of the spring. The cross-beam is now free to rotate, without loading the spring. Level the cross-beam by measuring the angle between the wire and the bottom side of the cross-beam. When the angle is 0° - within reading error of the protractor - tighten the bolts that fix the cross-beam to the spring. Remove the auxiliary string.

Step 2: Attach the basket and measure the arm length

The basket is attached in the same location as the auxiliary string. Use a capiler gauge to determine the arm length from the applied load to the pivot. As there is no marking on the cross-beam that indicates the rotation axis, measurement of the arm length is done by measuring the distance between the two brackets, that are used to mount to two gas canisters. The arm is then estimated as half the width, assuming that the rotation axis is aligned with the centerline of the cross-beam. This is depicted in [Figure B-3](#).

Step 3: Measure the angle of rotation

The rotation angle is measured using a protractor as indicated in [Figure B-4](#). The protractor origin is aligned with the location where the string and the bottom side of the cross beam intersect. This step is repeated for every applied load.

B.4 RESULTS AND DISCUSSION

Estimation of the spring constant and the corresponding uncertainty, using [Equation B-1](#) and [Equation B-2](#) requires knowledge of the basket mass, the arm mass and the used arm length. The basket mass and arm mass were measured using a Mettler Toledo AG245 scale to be $M_{\text{basket}} = 62.4160 \pm 0.0001 \text{ g}$ and $M_{\text{arm}} = 206.5803 \pm 0.0001 \text{ g}$, respectively. The arm was estimated to be $22.75 \pm 0.05 \text{ mm}$. It is assumed that the CoG of the cross-beam is located in the geometric center and that $r_{\text{cg}} = 0.000 \text{ m}$. The gravitational acceleration g is assumed 9.806 m s^{-2} in agreement with the value that is used in the calibration of the test masses. The accuracy of the mass of the basket and the cross-beam are $\Delta M = 1 \cdot 10^{-7} \text{ kg}$. The lengths and arms are

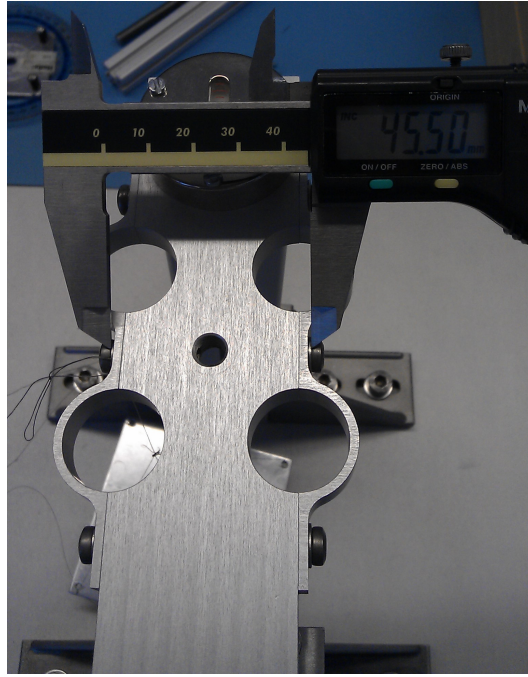


Figure B-3: Measurement of the distance between the retainers of the gas canisters to determine the arm length.

measured to an accuracy of $0.5 \cdot 10^{-3}$ m, the rotations to an accuracy of 0.5° and the gravitational acceleration is known to $5 \cdot 10^{-4}$ m s^{-2} . The accuracies of the used test masses can be found in the calibration sheet at the end of this appendix. These numbers, plugged in (B-2) to (B-8), yields the estimates of the spring constant in Figure B-5.

The measurements have been repeated multiple times on different dates to account for any variation in the environment. As can be seen in Figure B-5, the difference between the measurements is within the measurement accuracy and very repeatable. Two data points of series '14.05 ESD 2' can be considered outliers. It is speculated, that these outliers are caused by read-out errors when the rotation angle is measured. Other causes such as stick behavior of the spring are considered unlikely, because this should have occurred on multiple occasions. The derived spring constant is independent on the direction of rotation. The data points converge to a spring constant $K = 0.64 \pm 0.03$ N m rad^{-1} . This is considerably higher than the design spring constant of 0.3 N m rad^{-1} and will have to be taken into account in further design considerations. It also shows the importance of verification of delivered parts before installation.

B.5 CONCLUSIONS AND RECOMMENDATIONS

The spring constant is measured to be $K = 0.64 \pm 0.03$ N m rad^{-1} . This is considerably higher than the expected spring constant of 0.3 N m rad^{-1}

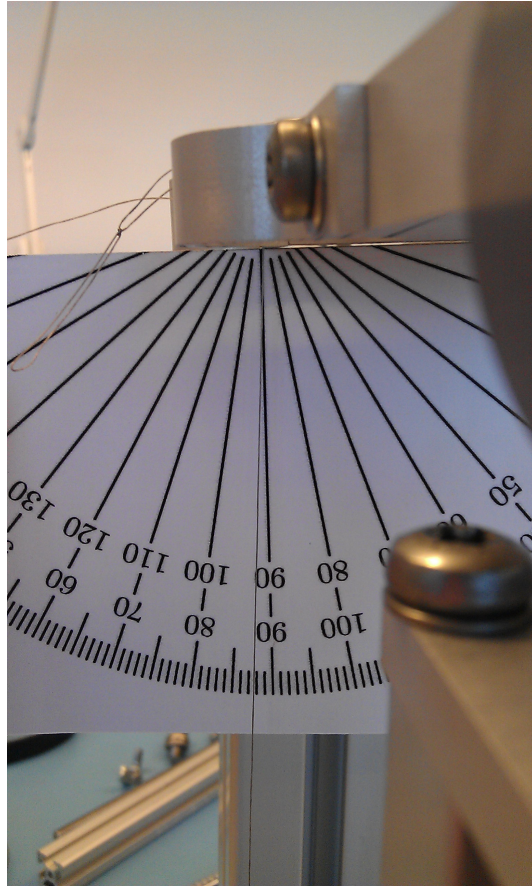


Figure B-4: Measurement of rotation angle.

and will have to be taken into account in further design considerations. The spring is linear - independent of the direction of rotation - and any hysteresis is within the measurement accuracy of this campaign.

REFERENCES

- [1] Daniel Perez-Grande. *Design and Development of a nano-propulsion thrust bench*. Msc. thesis, Universidad Politecnica de Madrid ; Delft University of Technology, 2010.

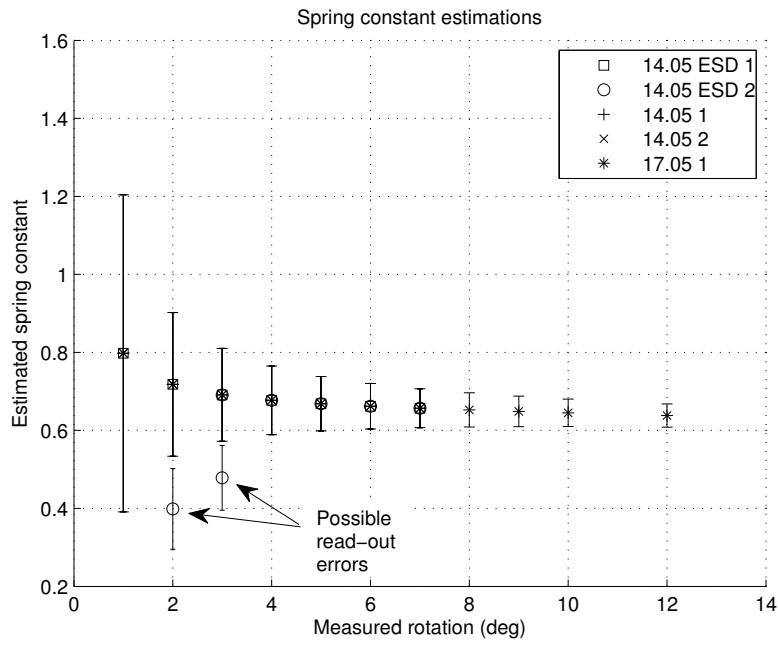


Figure B-5: Estimated spring constant based on given model and experimental data.

Aanvrager TU Delft
Kamer 08.07
Kluyverweg 1
2629HS DELFT

KALIBRATIE-CERTIFICAAT

Certificaatnummer: 8167/0410

Onderzocht 1 doos gewichten nr: 8167
Zie resultaat blad 2 van dit certificaat.

Wijze onderzoek Door weging en vergelijking met een (samengestelde) massastandaard is van elk massastuk de conventionele massa bepaald. Voor een gewicht met een temperatuur van 20°C is de conventionele massa gelijk aan de massa van een referentiegewicht met een dichtheid van 8000 kg/m³ waarmee eerstgenoemd gewicht in lucht van 1,2 kg/m³ in evenwicht is. De omgevingstemperatuur tijdens de kalibratie bedroeg (20 ± 5)°C.

Datum onderzoek 6 oktober 2004

Resultaat De massa van de gewichten bevindt zich inclusief de meetonzekerheid binnen de toleranties welke gelden voor gewichten klasse M1 EEG-ijkbeschikking precisiegewichten. Voor het resultaat wordt verwezen naar blad 2 van dit certificaat.

Onzekerheid De gerapporteerde onzekerheid is gebaseerd op een standaardonzekerheid, vermenigvuldigd met een dekkingsfactor $k = 2$, welke overeenkomt met een betrouwbaarheidsinterval van ongeveer 95 %.
De standaardonzekerheid is bepaald volgens EA-4/02.

Herleidbaarheid Metingen zijn uitgevoerd met standaarden (3002,3008) waarvan de herleidbaarheid naar (inter)nationale standaarden, ten overstaan van de Raad voor Accreditatie, is aangetoond.

Datum: 6 oktober 2004


G.P. Heezen
Hoofd weegkamer

Resultaat:

nummer doos	nominale massa	afwijking voor justeren	afwijking na justeren	onzekerheid
8167	200 g	+ 0,92 mg	--	3,00 mg
	200 g*	+ 1,02 mg	--	3,00 mg
	100 g	- 0,31 mg	--	1,50 mg
	50 g	- 0,86 mg	--	1,00 mg
	20 g	- 0,67 mg	--	0,80 mg
	20 g*	+ 0,39 mg	--	0,80 mg
	10 g	- 0,55 mg	--	0,60 mg
	5 g	+ 0,15 mg	--	0,50 mg
	2 g	+ 0,18 mg	--	0,40 mg
	2 g*	- 0,05 mg	--	0,40 mg
	1 g	+ 0,40 mg	--	0,30 mg

juiste massa = nominale massa + afwijking
 -- er heeft geen justering plaatsgevonden

Datum: 09 oktober 2004

Par: 

DETERMINATION OF THE MAGNETIC MOMENT USING A MAGNETIC PISTON

A number of small neodymium permanent magnets have been obtained in various sizes and associated strengths. The strength of the magnets is only known approximately. In this appendix, a simple and cheap method - referred to as the magnetic piston method - is used to determine the strength of the magnets. The method is described by Connors and Al-Shamali [1] and uses the repulsive force between two similar magnets and gravity to suspend one over the other. The separation distance can be modelled and compared to measurements to derive the magnetic moment.

C.1 MEASUREMENT SETUP

When similar poles (North-North or South-South) of two magnets are turned towards each other, the interaction of the magnetic fields results in a repulsive force between the magnets. Using this property, a magnetic piston can be created by levitating one magnet above another one. The interaction of the fields does not only create a repulsive force, it is also cause for a magnetic torque that forces the magnets fields to align with each other. When the rotary and side-to-side motion of the magnets are constrained, one magnet can be levitated above the other. A magnetic piston is easily constructed from a transparent cylindrical structure. The diameter of the cylinder should be chosen such that the levitated magnet is free to move vertically, but its motion is restricted in all other directions. For this measurement sequence, two cylinders were created using sturdy plastic foil. The foil was rolled into a tube with a diameter only slightly larger than the diameter of the magnets. A smaller semi-transparent tube was created from a $\varnothing 3$ mm drinking straw. Two photos of the setup can be found in [Figure C-1](#) and [Figure C-2](#).

C.2 THEORETICAL MODEL

Modern neodymium raw-earth magnets have strong magnetic fields. These fields are generally non-uniform and have a complex geometry. When the separation between two magnets is at least several times larger than their height, their fields can be approximated by dipoles. Along the axis of a dipole, the field strength can be given by [1]

$$B_z = \frac{\mu_0}{4\pi} \frac{2\mu_1}{z^3} \quad (\text{C-1})$$

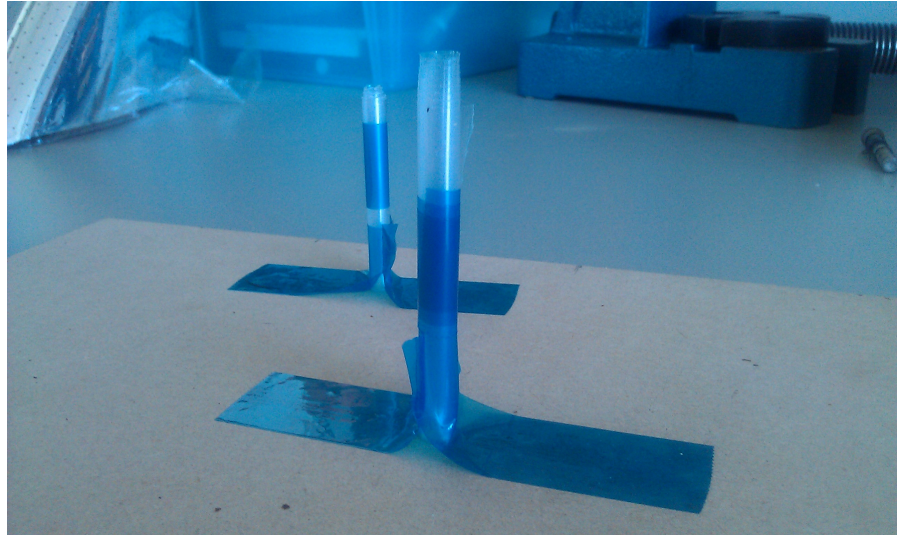


Figure C-1: Simple magnetic piston made of rolled plastic foil. The tubes were fixed in place using transparent tape.

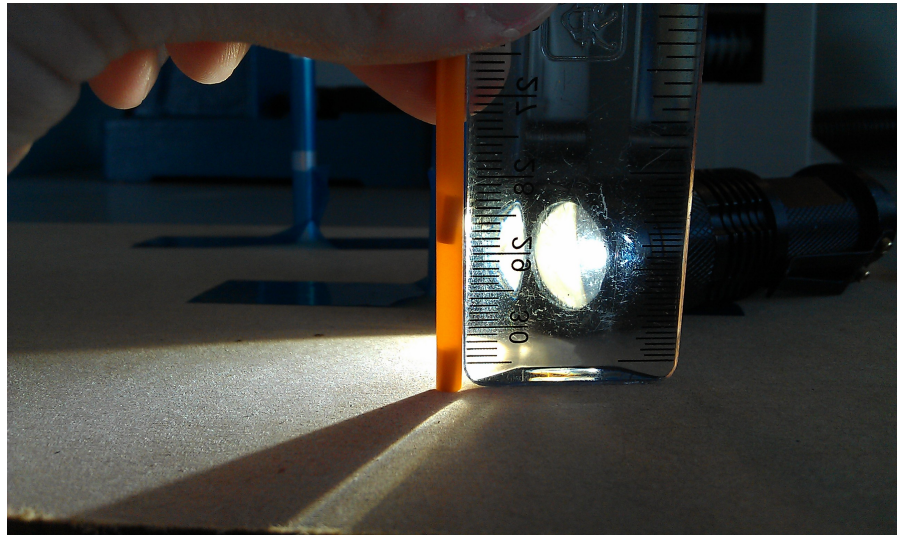


Figure C-2: Simple magnetic piston using a thin 3 mm drinking straw. A torch is used to increase the contrast and make the magnets visible. A ruler is used to measure the inner distance between the two stacks.

$$\mu_0 = 4\pi \cdot 10^{-7} \text{ V s A}^{-1} \text{ m}^{-1}$$

where μ_0 is the magnetic permeability of vacuum, μ_1 is the magnetic moment in A m and z is the distance from the origin of the dipole in m. The force between two magnets with a similar field is equal to the gradient of the field multiplied by the component of the magnetic moment μ_1 . For a pair of magnets of equal strength this can be given as

$$F_z = 3 \frac{\mu_0}{4\pi} \frac{2\mu_1^2}{z^4} \quad (\text{C-2})$$

Because the suspended magnet is considered to be in equilibrium, this magnetic force is equal in magnitude to the weight of the magnet:

$$nmg = 3 \frac{\mu_0}{4\pi} \frac{2(n\mu_1)^2}{z^4} \quad (\text{C-3})$$

where n is the number of magnets of each stack, m is the mass of a single magnet in kg, z is the separation distance between the centers of the two stacks in m and g is the gravitational acceleration in m s^{-2} . The latter is assumed to have a magnitude of 9.81 m s^{-2} . In this equation the Earth magnetic field is neglected. Solving (C-3) for μ_1 results in

$$\mu_1 = z^2 \sqrt{\frac{10^7}{6n} mg} \quad (\text{C-4})$$

By measuring the mass and separation distance of the magnets (from center to center) the magnetic moment can thus be estimated.

The accuracy of this estimation can be calculated using

$$\Delta\mu_1 = \left| \frac{\partial\mu_1}{\partial m} \right| \Delta m + \left| \frac{\partial\mu_1}{\partial g} \right| \Delta g + \left| \frac{\partial\mu_1}{\partial z} \right| \Delta z \quad (\text{C-5})$$

The partial differentials in this equation can be easily calculated to be

$$\frac{\partial\mu_1}{\partial m} = \frac{10^7}{12n} \left(\frac{10^7}{6n} mg \right)^{-1/2} z^2 g \quad (\text{C-6})$$

$$\frac{\partial\mu_1}{\partial g} = \frac{10^7}{12n} \left(\frac{10^7}{6n} mg \right)^{-1/2} z^2 m \quad (\text{C-7})$$

$$\frac{\partial\mu_1}{\partial z} = 2z \sqrt{\frac{10^7}{6n} mg} \quad (\text{C-8})$$

For the used magnets this results in a rule of thumb of an accuracy of 10% as will be shown in [Section C.4](#).

C.3 MEASUREMENT PLAN

In this section, the conducted experiments are described, as well as the order in which steps are conducted and if necessary how they are conducted.

C.3.1 Test overview

The magnetic moment of the S-06-06-N, S-04-04-N and S-02-02-N magnets has been determined. These magnets have a diameter equal to their height of 6 mm, 4 mm, 2 mm, respectively. Because of their small diameter, these measurements could not be performed for the

MAGNET	CLASS	$\varnothing \times H$ (mm)	MASS (g)	QUANTITY
S-1.5-0.5-N	N45	1.5 \times 0.5	0.0067	20
S-02-02-N	N48	2 \times 2	0.048	20
S-04-04-N	N45	4 \times 4	0.38	20
S-06-06-N	N48	6 \times 6	1.3	10

Table C-1: Specification of magnet magnetization class, dimensions, mass and quantity available.

S-15-05-N (1.5 mm diameter and 0.5 mm height). Alternative methods should be employed for these magnets. For the S-06-06-N five pairs of single magnets were used; for the S-04-04-N five pairs of two magnet high stacks were used and for the S-02-02-N five pairs of four magnet high stacks were used. These pairs were chosen randomly and after each measurement the pair was discarded and a new pair was picked from the remaining magnets. The available magnets and their specifications are given in [Table C-1](#).

C.3.2 Procedure

Step 1: Randomly select a pair of magnets

Randomly select a pair of magnets from the container and separate them. Because the magnets are strong and small, they may require pliers to get separated.

Step 2: Place the magnets in the tube

Place one of the magnet stacks in the tube. Place the second magnet stack in the tube, such that the magnets repel each other. Make sure the upper magnet can freely glide through the tube.

Step 3: Measure the distance between the magnets

When the upper magnet has reached an equilibrium position, measure the distance between the top side of the lower magnet and the bottom side of the levitated magnet, d_{inner} . The total distance d_{mid} is measured from the center of the magnets.

C.4 RESULTS AND DISCUSSION

The measured distances, the corresponding calculated magnetic moments and the calculated uncertainties are listed in [Table C-2](#), [Table C-3](#) and [Table C-4](#) for the S-06-06-N, S-04-04-N, S-02-02-N, respectively. The standard deviations of the measured distances are smaller

NO.	d_{inner} (mm)	d_{mid} (mm)	μ_1 (A m ²)	$\Delta\mu_1$ (A m ²)
1	30	36	0.19	0.014
2	29	35	0.18	0.014
3	31	37	0.20	0.015
4	29	35	0.18	0.014
5	30	36	0.19	0.014

Table C-2: Estimated magnetic moment for S-06-06-N magnets. Parameters: $m = 1.30$ g, $g = 9.81$ m s⁻², $h = 6$ mm, error in distance measurement $\Delta d = 1$ mm, $\Delta m = 5 \cdot 10^{-5}$ kg, $\Delta g = 0.005$ m s⁻², $\Delta z = 1 \cdot 10^{-3}$ m. The standard deviation of the measured distances d_{inner} is at 0.84 mm smaller than the resolution of 1 mm of the used scale. The resulting estimate of the magnetic moment of the S-06-06-N magnets is $\mu_1 = 0.19 \pm 0.014$ A m².

NO.	d_{inner} (mm)	d_{mid} (mm)	μ_1 (A m ²)	$\Delta\mu_1$ (A m ²)
1	24	32	0.059	0.0073
2	24	32	0.059	0.0073
3	23	31	0.055	0.0070
4	23	31	0.055	0.0070
5	23	31	0.055	0.0070

Table C-3: Estimated magnetic moment for S-04-04-N magnets. Parameters: $m = 0.40$ g, $g = 9.81$ m s⁻², $h = 4$ mm, error in distance measurement $\Delta d = 1$ mm, $\Delta m = 5 \cdot 10^{-5}$ kg, $\Delta g = 0.005$ m s⁻², $\Delta z = 1 \cdot 10^{-3}$ m. The standard deviation of the measured distances d_{inner} is at 0.55 mm smaller than the resolution of 1 mm of the used scale. The resulting estimate of the magnetic moment of the S-04-04-N magnets is $\mu_1 = 0.057 \pm 0.0071$ A m².

than the resolution of the used scale. With the standard deviation of the calculated magnetic moment smaller than the quoted uncertainties, the estimated values for the magnetic moments are taken as the average with an uncertainty equal to the average of the calculated uncertainties. The resulting estimate of the magnetic moment of the S-06-06-N magnets is $\mu_1 = 0.19 \pm 0.014$ A m². Similarly, the resulting estimate of the magnetic moment of the S-04-04-N magnets is $\mu_1 = 0.056 \pm 0.0071$ A m² and the estimate for the S-02-02-N magnets is $\mu_1 = 0.0073 \pm 0.0044$ A m². The relative error for the former two magnet types of 7% and 12% is acceptable for the intended design purpose. The relative error of the latter one is unacceptable at 60%. This estimate will have to be confirmed using alternative methods. Using this setup it can only be approved with more accurate separation measurements.

NO.	d_{inner} (mm)	d_{mid} (mm)	μ_1 ($A m^2$)	$\Delta\mu_1$ ($A m^2$)
1	15	23	0.0074	0.0045
2	15	23	0.0074	0.0045
3	15	23	0.0074	0.0045
4	15	23	0.0074	0.0045
5	14	22	0.0068	0.0041

Table C-4: Estimated magnetic moment for S-02-02-N magnets. Parameters: $m = 0.048$ g, $g = 9.81$ $m s^{-2}$, $h = 2$ mm, error in distance measurement $\Delta d = 1$ mm, $\Delta m = 5 \cdot 10^{-5}$ kg, $\Delta g = 0.005$ $m s^{-2}$, $\Delta z = 1 \cdot 10^{-3}$ m. The standard deviation of the measured distances d_{inner} is at 0.45 mm smaller than the resolution of 1 mm of the used scale. The resulting estimate of the magnetic moment of the S-02-02-N magnets is $\mu_1 = 0.0070 \pm 0.0044$ $A m^2$.

REFERENCES

- [1] Martin Connors and Farook Al-Shamali. The Magnetic Torque Oscillator and the Magnetic Piston. *The Physics Teacher*, 45(7):440, 2007. ISSN 0031921X. doi: 10.1119/1.2783155. URL <http://link.aip.org/link/PHTEAH/v45/i7/p440/s1&Agg=doi>.

SAMPLE CALCULATIONS

In the report, a large amount of calculations is presented for which the model is explained and the final results are given. This appendix supports these calculations by providing a step-by-step sample calculation.

D.1 SENSOR SYSTEM ACCURACY

In this section, the sensor system accuracy is calculated using the relations developed in [Section 4.1.2](#). The required equations and specifications are copied for clarity. This sample calculation is based on the Micro-Epsilon capaNCDT CS1 capacitive sensor, which is connected to a Micro-Epsilon capaNCDT DT6530 controller. The controller is in turn connected to a National Instruments PXI6229 [DAQ](#). The sensor has a [FSO](#) of 1 mm and a linearity of 0.05%. The controller has a resolution of 0.000075% [FSO](#), a linearity of 0.05% [FSO](#) and repeatability of 0.0003% [FSO](#).

A displacement sensor measures the real displacement d_{real} at the location of its target. The sensor and its controller add an uncertainty to the sensed value through nonlinearity and non-repeatability. This displacement is labelled d_{sens} and is composed as

$$d_{\text{sens}} = d_{\text{real}} + \Delta d_{\text{sens}} \quad (\text{D-1})$$

where Δd_{sens} is given as a percentage of the [FSO](#). From the sensor controller, the displacement is translated into a voltage U_{sens} , given by

$$U_{\text{sens}} = d_{\text{sens}} S \quad (\text{D-2})$$

where S is the sensitivity of the controller in V m^{-1} . The [DAQ](#) adds uncertainty in the form of a gain error and random noise.

$$U_{\text{DAQ}} = U_{\text{sens}} + U_{\text{sens}} G + \tilde{U} \quad (\text{D-3})$$

where G is the gain error and \tilde{U} is the random noise on the voltage signal in μVrms . The Gain Error G is calculated using

$$\begin{aligned} G = & \text{ResidualGainError} \\ & + \text{GainTempCo} \cdot (\text{TempChangeFromLastInternalCal}) \\ & + \text{ReferenceTempCo} \cdot (\text{TempChangeFromLastExternalCal}) \end{aligned} \quad (\text{D-4})$$

where $\text{TempChangeFromLastExternalCal} = 10 \text{ K}$ and $\text{TempChangeFromLastInternalCal} = 1 \text{ K}$ as specified by National Instruments [1]. The coefficients are listed in Table D-1 and depend on the voltage range setting of the DAQ. In data processing the measured

RANGE POSITIVE SCALE	V	RESIDUAL GAIN ER- ROR (PPM OF READING)	GAIN TEMPCO (PPM/C)	REFERENCE TEMPCO	RANDOM NOISE, σ (μVrms)
10		75	25	5	244
5		85	25	5	122
1		95	25	5	30
0.2		135	25	5	13

Table D-1: Accuracy parameters of the National Instruments PXI 6229 [1].

U_{DAQ} is converted back into a displacement. This is done by dividing U_{DAQ} by the controller sensitivity S . The total uncertainty in the measured displacement introduced through the sensor, controller and DAQ is given by combining (D-1) - (D-3)

$$\Delta d = d_{\text{meas}} - d_{\text{real}} = d_{\text{real}}G + (1 + G)\Delta d_{\text{sens}} + \frac{\tilde{U}}{S} \quad (\text{D-5})$$

The sensitivity of the sensor controller is easily found as the sensor FSO divided by the controller output voltage range. For the considered DT6530 controller the output voltage range is 0 V to 10 V. The DAQ voltage range is set to match this.

To calculate the accuracy of the complete sensor system, the parameters required in Equation D-5 need to be calculated. Following Equation D-4, the gain error is calculated. The required data is found in Table D-1.

$$\begin{aligned} G &= \text{ResidualGainError} \\ &+ \text{GainTempCo} \cdot (\text{TempChangeFromLastInternalCal}) \\ &+ \text{ReferenceTempCo} \cdot (\text{TempChangeFromLastExternalCal}) \\ &= 75 \cdot 10^{-6} + 25 \cdot 10^{-6} \cdot 1 + 3 \cdot 10^{-6} \cdot 10 = 1.5 \cdot 10^{-4} \end{aligned}$$

Three standard deviations are used to represent the random noise of the DAQ. For a full range of 10 V, the random noise is then $\tilde{U} = 3 \cdot 244 = 732 \mu\text{Vrms}$.

The resolution of the sensor system is dictated by the sensor controller. The controller has a resolution of 0.000075% FSO. With a FSO of 1 mm, this results in a resolution of $7.5 \cdot 10^{-10} \text{ m}$ or 0.75 nm. Using the FSO, the sensor sensitivity is also calculated easily.

$$S = \frac{\text{Full voltage range of DAQ}}{\text{FSO}} = \frac{10 \text{ V}}{1 \cdot 10^{-3} \text{ m}} = 10000 \text{ V m}^{-1}$$

Before the accuracy of the sensor system can be calculated, the inaccuracies introduced by the linearity and repeatability of the sensor head and the controller need to be calculated. This inaccuracy in sensor measurement Δd_{sens} is calculated as

$$\begin{aligned}\Delta d_{\text{sens}} &= \text{FSO} \left(\frac{\lambda_{\text{sensor linearity}} + \lambda_{\text{controller linearity}} + \lambda_{\text{controller repeatability}}}{100\%} \right) \\ &= 1 \cdot 10^{-3} \left(\frac{0.05\% + 0.0003\% + 0.05\%}{100\%} \right) = 1.0003 \cdot 10^{-6} \text{ m} \approx 1 \mu\text{m}\end{aligned}$$

The total accuracy is now calculated using Equation D-5, where $d_{\text{real}} = \text{FSO}/2$. Only half the FSO is used, to be able to measure a full oscillation of the pendulum.

$$\begin{aligned}\Delta d &= d_{\text{real}} G + (1 + G) \Delta d_{\text{sens}} + \frac{\tilde{u}}{S} \\ &= \frac{1 \cdot 10^{-3}}{2} \cdot 1.5 \cdot 10^{-4} + (1 + 1.5 \cdot 10^{-4}) 1.0003 \cdot 10^{-6} + \frac{732 \cdot 10^{-6}}{10000} \\ &\approx 1.149 \cdot 10^{-6} \text{ m} = 1.149 \mu\text{m}\end{aligned}$$

REFERENCES

- [1] National-Instruments. NI 622x Specifications. Technical report, National Instruments, 2007. URL <http://www.ni.com/pdf/manuals/371290g.pdf>.

STATISTICS: SUMMARY OF USED RELATIONS

Multiple measurements can be averaged to create one estimate for a specific parameter. In this appendix, the statistical relations used to estimate some of the parameters are explained. More information on statistical analysis can be found in ample text books on probability and statistics, e.g. Dekking et al. [1].

E.1 UNBIASED ESTIMATORS OF THE MEAN AND VARIANCE

Given a set of n draws X_i from an unknown random distribution, the mean \bar{X}_n is an unbiased estimator of the true value of the measured quantity.

$$\bar{X}_n = \frac{X_1 + X_2 + \cdots + X_n}{n} \quad (\text{E-1})$$

The uncertainty in this estimate is indicated by its variance σ^2 . With the distribution unknown, the variance is estimated using the unbiased estimator S_n^2 , which is normalized for $n - 1$ draws.

$$S_n^2 = \frac{1}{n-1} \sum_{i=1}^n (X_i - \bar{X}_n)^2 \quad (\text{E-2})$$

E.2 EXPECTATION AND VARIANCE OF AN AVERAGE

Using the law of large numbers, it can be shown that for n draws X_i from an independent and identically distributed sequence, the expected value of the mean is equal to the mean of the distribution.

$$E[\bar{X}_n] = \mu \quad (\text{E-3})$$

Also, the variance of the average approaches the variance of the distribution of each random variable inversely proportional to sample size n .

$$\text{Var}(\bar{X}_n) = \frac{\sigma^2}{n} \quad (\text{E-4})$$

E.3 CONFIDENCE INTERVALS FOR THE MEAN

Given n independent draws from an identically distributed sequence, it can be shown that

$$\frac{\bar{X}_n - \mu}{\sigma/\sqrt{n}} \quad (\text{E-5})$$

has a standard normal distribution. However, when the standard deviation is unknown, it can be shown that

$$\frac{\bar{X}_n - \mu}{S_n / \sqrt{n}} \quad (\text{E-6})$$

has a t-distribution with parameter m of which the probability density function equals

$$f(x) = k_m \left(1 + \frac{x^2}{m}\right)^{\frac{m+1}{2}} \quad (\text{E-7})$$

for $-\infty < x < \infty$. Parameter k_m is defined by

$$k_m = \Gamma\left(\frac{m+1}{2}\right) / \left(\Gamma\left(\frac{m}{2}\right) \sqrt{m\pi}\right) \quad (\text{E-8})$$

For a random sample X_1, \dots, X_n from an $N(\mu, \sigma^2)$ distribution, the studentized mean has a $t(n-1)$ distribution, regardless of the values of μ and σ . To construct a confidence interval from the obtained mean and estimated variance S_n^2 , the critical values of the t-distribution are used. These are dependent on the sample size n and the required confidence level. The critical values are listed by many sources Dekking et al. [1].

E.4 CORRELATION COEFFICIENT

The correlation coefficient r (or R) is the normalized coefficient of covariance for two random variables X and Y . It is used to determine if two random variables are dependent. It is given by

$$r_{XY} = \frac{\text{cov}(X, Y)}{\sigma_X \sigma_Y} = \frac{E[(X - \mu_X)(Y - \mu_Y)]}{\sigma_X \sigma_Y} \quad (\text{E-9})$$

where μ_i and σ_i are the mean and standard deviation of the random variable, respectively.

E.5 STANDARD ERROR OF ESTIMATION

The SEE for a regression based estimator is calculated using

$$\text{SEE} = \sqrt{\frac{\sum_i^n (X_i - f_i)}{n - m}} \quad (\text{E-10})$$

where X_i is the measured value, f_i the corresponding result of the regression, n the number of considered points and m the number of parameters estimated in the regression. For a linear regression, $m = 1$ when only the slope is estimated and the intercept is set to zero. In case also the intercept is estimated, $m = 2$.

E.6 COEFFICIENT OF DETERMINATION

The coefficient of determination R^2 determines how well a curve fits to the data based on the ratio of the total sum of squares and the residual sum of squares. Given a curve f with function values f_i and a data set of values y_i and mean \bar{y} , the aforementioned sums of squares are calculated as follows.

The *total sum of squares* is the square of the differences between each data point y_i and the mean value of the data set.

$$SS_{\text{total}} = \sum_i (y_i - \bar{y})^2 \quad (\text{E-11})$$

Equivalently, the *residual sum of squares* is the sum of squares of the differences between the data points y_i and the corresponding function values f_i

$$SS_{\text{residual}} = \sum_i (y_i - f_i)^2 \quad (\text{E-12})$$

From these two sum of squares, the coefficient of determination is easily calculated as

$$R^2 \equiv 1 - \frac{SS_{\text{residual}}}{SS_{\text{total}}} \quad (\text{E-13})$$

the value of which is on the interval $[0, 1]$.

E.7 UNCERTAINTY IN REGRESSION

For a linear regression function, or linear fit, of a set of data of the form

$$y = \beta x \quad (\text{E-14})$$

the slope β has a t -distribution with parameter $n - 1$ where n is the number of samples. The standard error of the slope, s_β is then given by [2]

$$s_\beta = \sqrt{\frac{\frac{1}{n-1} \sum_{i=1}^n (y_i - f_i)^2}{\sum_{i=1}^n (x_i - \bar{x})^2}} \quad (\text{E-15})$$

REFERENCES

- [1] F.M. Dekking, C. Kraaikamp, H.P. Lopuhaa, and L.E. Meester. *A Modern Introduction to Probability and Statistics: Understanding Why and How*. Springer-Verlag London Limited, 2005. ISBN 1-85233-896-2.
- [2] J.F. Kenney and E.S. Keeping. *Mathematics in Statistics, Pt. 1*. Van Nostrand, Princeton, 3rd edition, 1962.

SPACE PROPULSION 2014 - COLOGNE, GERMANY

ABSTRACT (ACCEPTED, DECEMBER 2013)

**Integration of a Variable Turn-Density Coil Actuator in a
Micropropulsion Thrust Stand**

R.J.F. Bijster

B.T.C. Zandbergen

Chair of Space Systems Engineering

Faculty of Aerospace Engineering

Delft University of Technology

Delft, The Netherlands

Thermal micropropulsion systems, such as cold gas thrusters, resistojets and arcjets, are widely used on spacecraft. Verification and validation of the performance of these low thrust engines requires a thrust stand that can be accurately calibrated. High calibration accuracy for a pendulum type thrust stand in open-loop measurements is achieved by using a calibration actuator that provides a force that is independent of the engagement distance between actuator and target. A Variable Turn-Density Coil (VTDC) based actuator was developed and integrated in the design of a micropropulsion thrust stand that allows thrust measurement in the 1 μN to 5000 μN range at a relative accuracy of 1% from 10 μN to 5000 μN and 10% in the 1 μN to 10 μN range.

The thrust stand is composed of a stable pendulum design with a removable torsional spring at its pivot. On the opposite side of the pendulum a counterweight is added to allow tuning of the thrust stand performance. The counterweight is composed of a set of five distinct masses to allow changes in the total counterweight. The arm that holds both the engine and the counterweight is partially threaded to allow changes in the arm ratio of engine and counterweight. These two design features allow tuning of the resolution for engines of different masses.

The rotation of the pendulum is measured using a capacitive sensor. The thrust can be derived from the pendulum rotation. The stand is calibrated using a VTDC actuator. This new actuator type is used to exert a force on a magnetic dipole which is independent of the along axis position of the dipole in the coil. This characteristic is achieved using a linearly varying turn-density along the coil. Having the calibration force independent from the along axis position of the dipole negates the necessity of a control loop.

The performance of the thrust stand is validated with hardware in the loop tests. The performance of the Bradford Engineering Proportional Micro-Thruster is known from prior measurements at ESA ESTEC and ONERA. Agreement between the three datasets shows that the thrust stand is capable of accurate measurements over the full required thrust range.

With the addition of the new thrust stand, the DARTS facility now has the capability of performing thrust measurements over six orders of magnitude: from 1 μN to 1 N. This allows for the design, verification and validation of a wide range of future (electro-)thermal spacecraft propulsion systems.

PROGRAM CODES

Listing 1: Calculation of the response of a RL network.

```

1  % Calculate response of coil under peak load.
  %
  % The actuator is modelled as a RL network of known resistance
  % and
  % inductance that are placed in series.
  %
6  % R.J.F. Bijster
  % 1506706
  % October, 2013

  clear all; close all; clc;

11 % Define electric parameters of coil
   R = 0.3;           % Ohm, resistance
   L = 27E-6;        % uH, inductance

16 % Transfer function
   num = 1;          % Numerator is 1
   den = [L R];      % Denominator is Ls + R
   H = tf(num, den);

21 % Define a step function of input voltage of 3 volts
   Vstep = 3;

   % Model for 15ms
   t = 0:0.0001:0.015;

26 % Allocate memory for two cases and set all to zero.
   u35 = zeros(1, length(t));
   u10 = zeros(1, length(t));

31 % Create two step functions of 3.5ms and 10ms respectively
   u35(t <= 0.0035) = Vstep;
   u10(t <= 0.0100) = Vstep;

   % Simulate reponses, output in time-domain

36 [I35,t] = lsim(H, u35,t);
   [I10,t] = lsim(H, u10,t);

   % Plot
   figure;
41 subplot(1,2,1);
   h1 = plot(t*1000,u10,'k-',t*1000,u35, 'k--');

```

```
ylabel('Supplied potential (V)', 'FontSize', 16);
xlabel('Time (ms)', 'FontSize', 16);
grid on;
46 axis square
   ylim([0 1.1*Vstep])
   xlim([0 max(t*1000)])

   set(gca, 'FontSize', 16)
51 subplot(1,2,2);
   h2 = plot(t*1000, I10, 'k-', t*1000, I35, 'k--');
   ylabel('Current (A)', 'FontSize', 16);
   xlabel('Time (ms)', 'FontSize', 16);
56 grid on;
   axis square
   ylim([0 1.1*Vstep/R])
   xlim([0 max(t*1000)])
   legend('10 ms', '3.5 ms')
61 set(gca, 'FontSize', 16)
```

VIRTUAL INSTRUMENTS

Most of the Virtual Instruments (VI) that were used to perform the measurements, share a lot of common components. In stead of listing all block diagrams (which are stored in DISC/Experiments/TEST-XXX/YYY, with YYY the test identifier), the base VI is given and dissected. For a full understanding of how the individual components work, the reader is directed to the LabVIEW manual [1] and the ample online resources [2].

The block diagram is given in [Figure H-3](#). As apparant from the figure, the program is composed of two phases, of which the latter can be split into three steps. The first stage creates the datafile and writes the length of each timestep to the first line.

In the second stage the measurements are taken. After creation of the data file, the interfaces to the data acquisition systems are setup. In case multiple hardware interfaces are used, such as for example a USB based system and a PXI/PCI based system, two different interfaces need to be created as shown in [Figure H-1](#). For each interface, several channels can be defined for sampling. Most of the used VIs also write a signal to a device, e.g. a voltage controlled power supply. For signal output, however, a seperate interface is required. The output signal is defined as a function of time in the 'Simulate Arbitrary Signal' block and written to the interface buffer. Each channel is sampled at the given rate and uses a hardware clock to trigger measurements. Once all interfaces have started, the while loop reads out the buffer every time a given amount of samples (typically 10 or 100) are obtained as shown in [Figure H-2](#). It converts the buffers, which are provided by the interfaces in the 'Waveform' datatype, to tabular data and writes them to the data file. After the set measurement length has passed, the VI waits for all current data acquisitions to finish, closes all interfaces and closes the data file. During the measurements, the data is also exported to a graph on the VI, such that the operator can see the data live during the campaign.

REFERENCES

- [1] National-Instruments. LabVIEW User Manual, 2003. URL <http://www.ni.com/pdf/manuals/320999e.pdf>.
- [2] National-Instruments. National Instruments Knowledgebase, 2013. URL <http://www.ni.com/kb>.

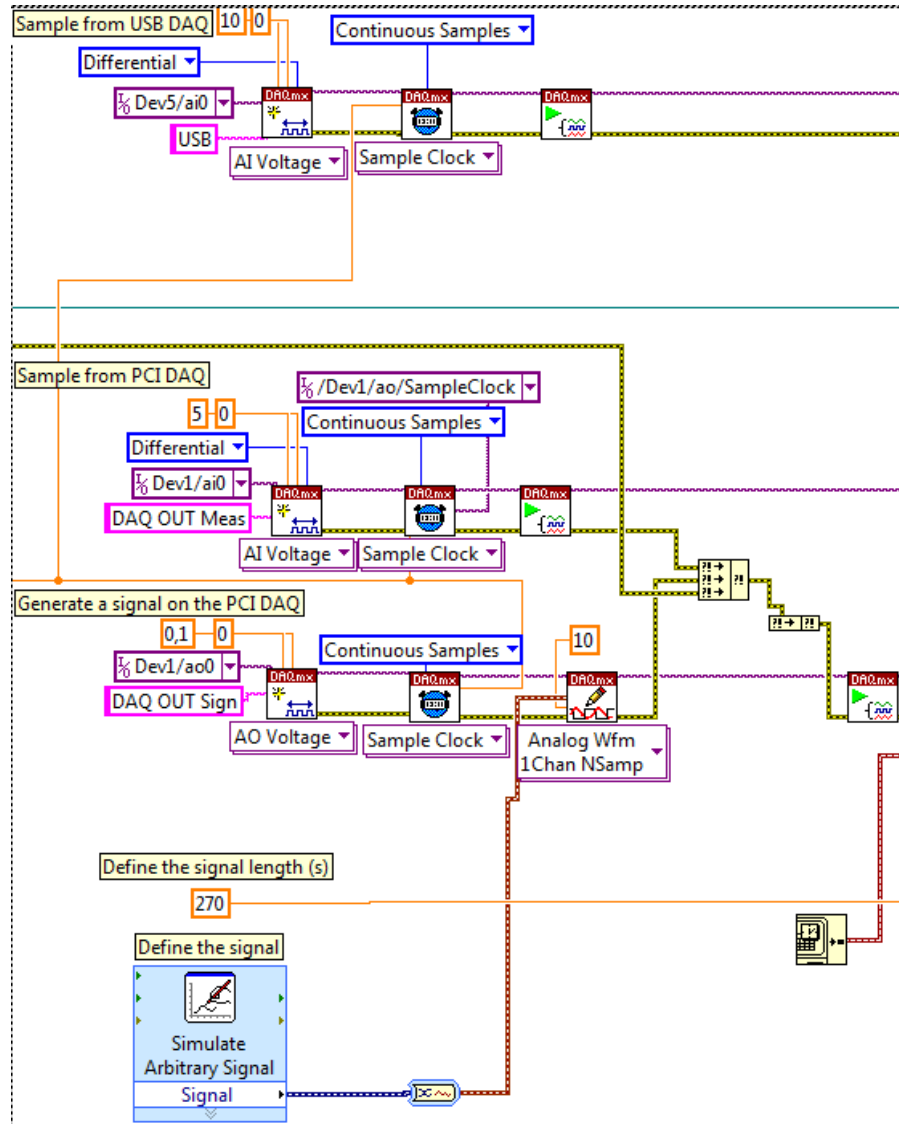


Figure H-1: Creation of data channels on the data acquisition systems.

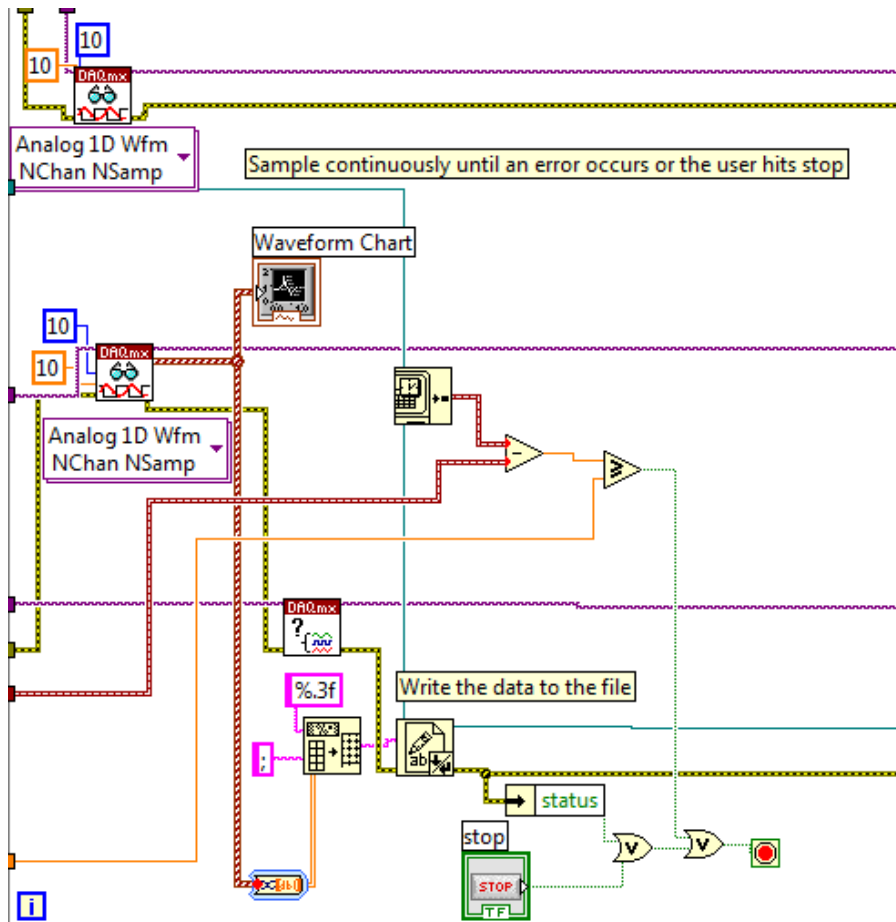


Figure H-2: Sampling of channels on the data acquisition systems.

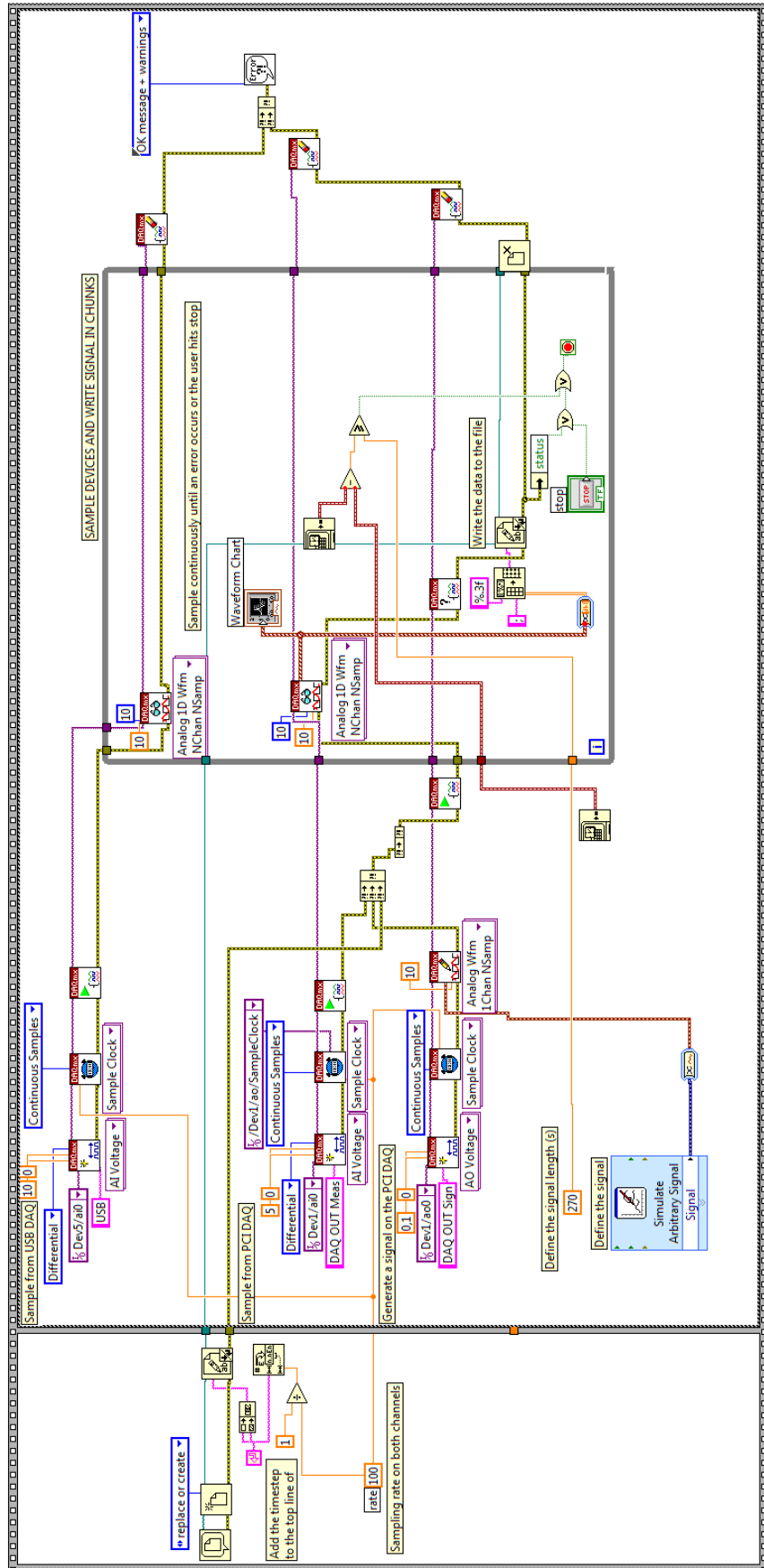
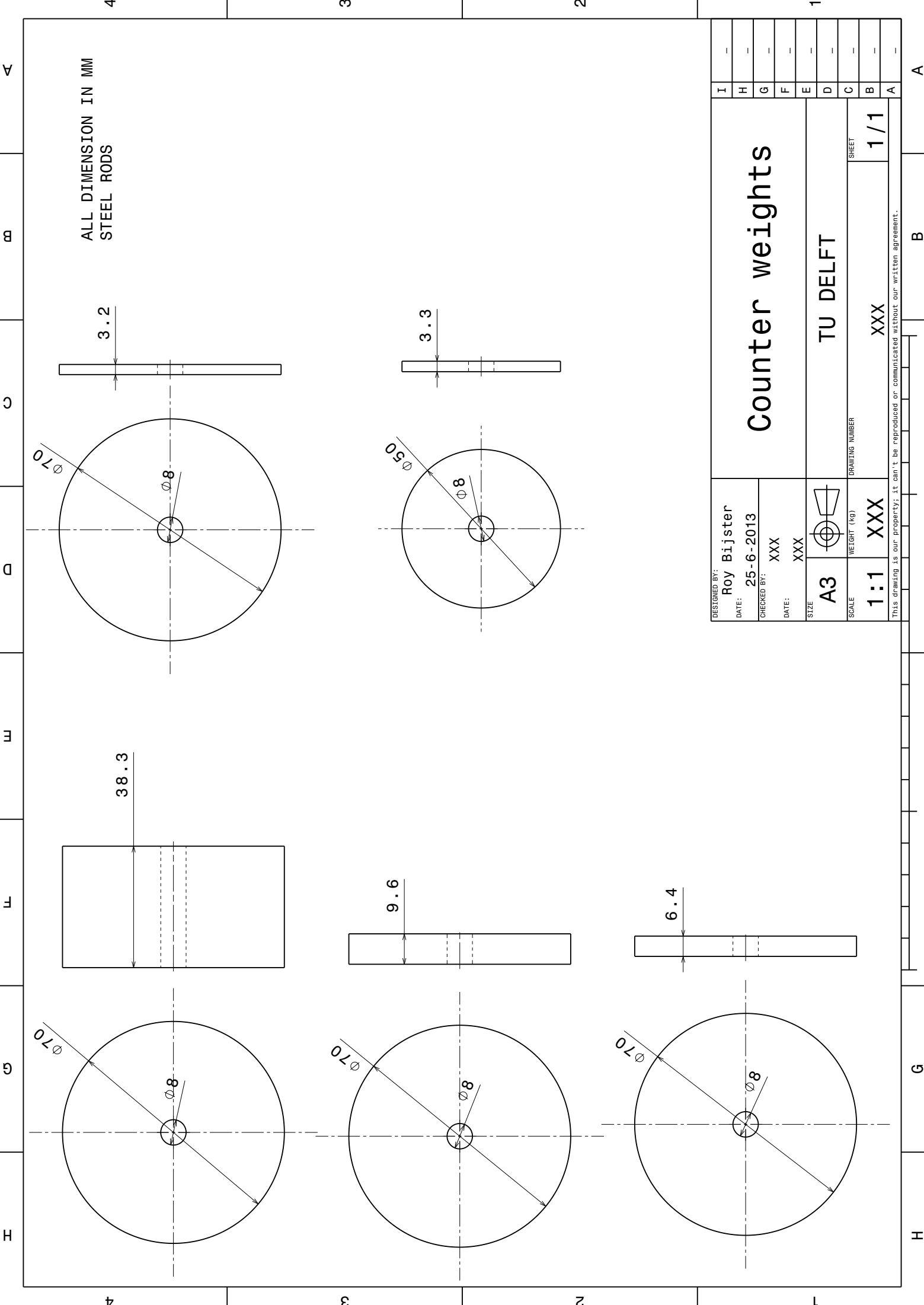


Figure H-3: Typical block diagram of the Labview Virtual Instruments used in the test campaign.



ALL DIMENSION IN MM
STEEL RODS

DESIGNED BY: Roy Bijster	DATE: 25-6-2013	CHECKED BY: XXX	DATE: XXX	SIZE A3	WEIGHT (kg) XXX	DRAWING NUMBER XXX	SHEET 1/1
Counter weights				TU DELFT			
This drawing is our property, it can't be reproduced or communicated without our written agreement.							

4
3
2
1

A
B
G
H

D

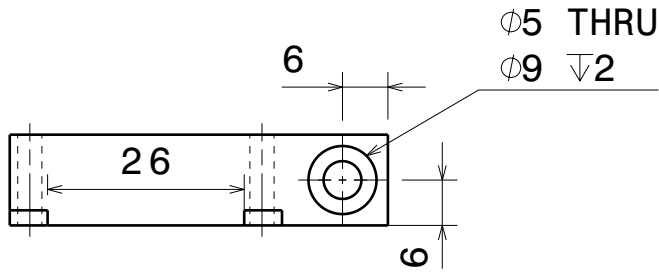
C

B

A

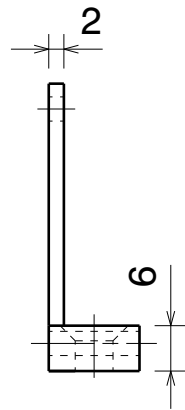
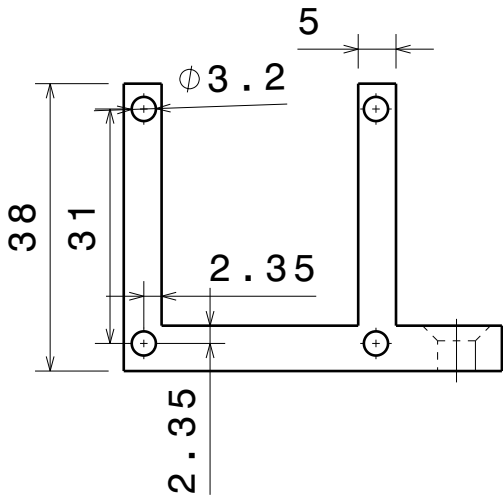
4

4



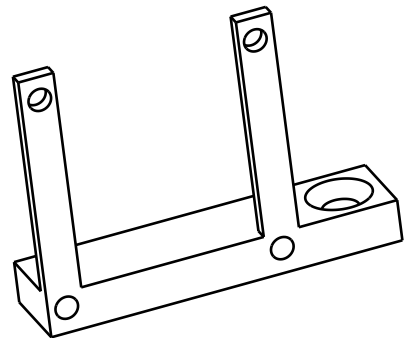
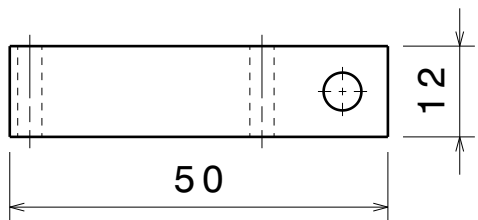
3

3



2

2



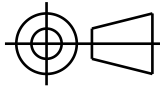
1

1

DESIGNED BY:
Roy Bijster
DATE:
24-6-2013

CHECKED BY:
XXX
DATE:
XXX

SIZE
A4



SCALE
1:1

WEIGHT (kg)
0,01

DRAWING NUMBER
PMTBracket2

SHEET
1 / 1

I	-
H	-
G	-
F	-
E	-
D	-
C	-
B	-
A	-

This drawing is our property; it can't be reproduced or communicated without our written agreement.

D

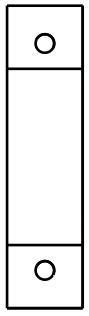
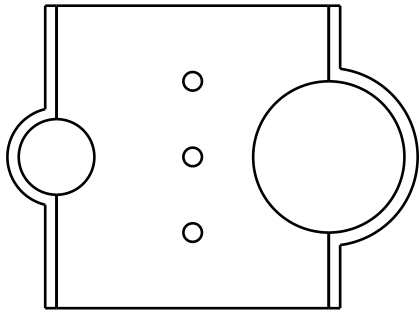
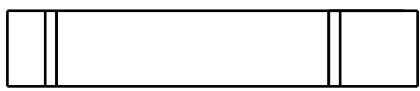
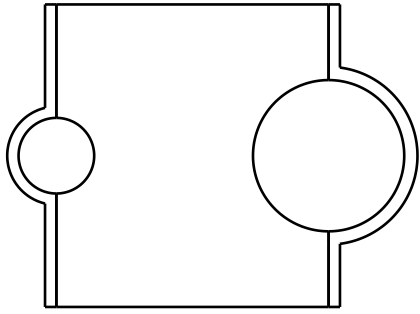
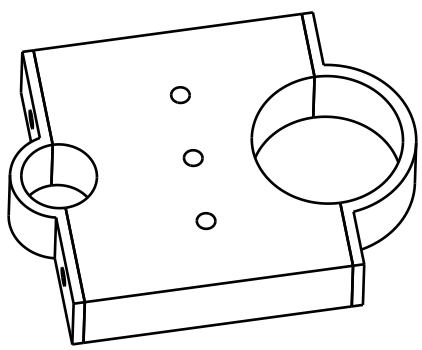
A

4 3 2 1

a

c

d



DESIGNED BY: Roy Bijster			SCALE 1:1	WEIGHT (kg) 0,00	DRAWING NUMBER 1/5	SHEET 1/5
DATE: 24-6-2013						
CHECKED BY: XXX	DATE: XXX	<h1>Sensor Bracket</h1>				
SIZE A4			TU DELFT			
SCALE 1:1			Assembly			
WEIGHT (kg) 0,00			DRAWING NUMBER 1/5			
This drawing is our property; it can't be reproduced or communicated without our written agreement.						

I -
H -
G -
F -
E -
D -
C -
B -
A -

4 3 2 1

A

D

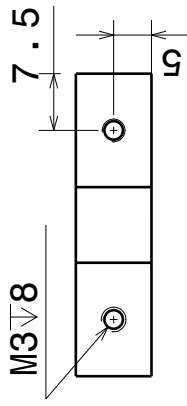
4 3 2 1

m

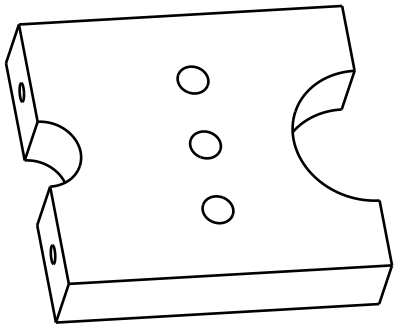
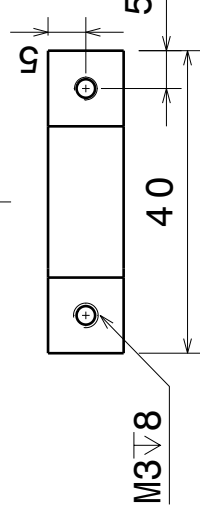
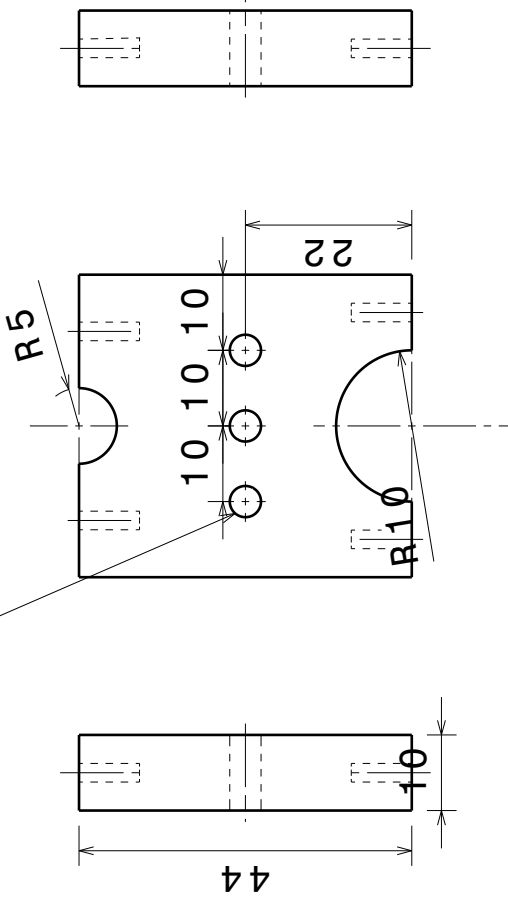
c

D

A



M5 THRU



DESIGNED BY: Roy Bijster	DATE: 24-6-2013
CHECKED BY: XXX	DATE: XXX
SIZE A4	WEIGHT (kg) 0,01
SCALE 1:1	DRAWING NUMBER SensorBracket
	SHEET 2/4

Sensor Bracket	
TU DELFT	
SensorBracket	
SHEET	
2/4	

I	-
H	-
G	-
F	-
E	-
D	-
C	-
B	-
A	-

This drawing is our property; it can't be reproduced or communicated without our written agreement.

D

A

4 3 2 1

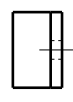
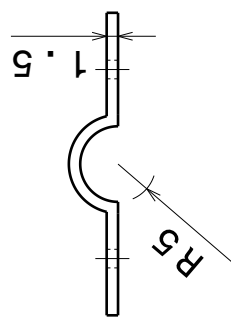
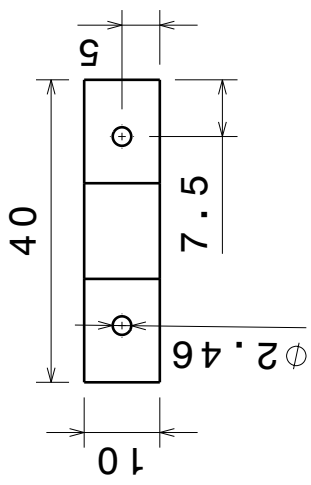
4 3 2 1

m

C

D

A



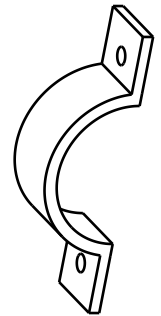
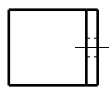
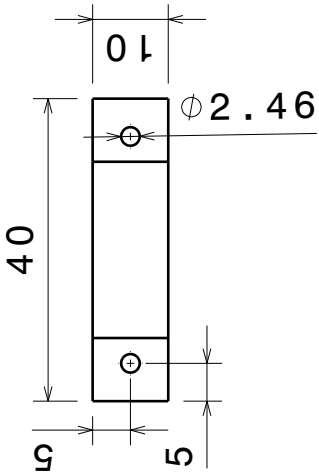
DESIGNED BY: Roy Bijster		DATE: 24-6-2013	
CHECKED BY: XXX		DATE: XXX	
SIZE: A4		DRAWING NUMBER: SensorBracketHolder10	
SCALE: 1:1	WEIGHT (kg): 0,00	SHEET: 3/5	
<h1>Sensor Bracket</h1>		I	-
		H	-
		G	-
		F	-
		E	-
TU DELFT		D	-
SensorBracketHolder10		C	-
SensorBracketHolder10		B	-
SensorBracketHolder10		A	-

This drawing is our property; it can't be reproduced or communicated without our written agreement.

4 3 2 1

D

A



DESIGNED BY: Roy Bijster		
DATE: 24-6-2013		
CHECKED BY: XXX		
DATE: XXX		
SIZE A4		
SCALE 1:1	WEIGHT (kg) 0,00	
DRAWING NUMBER SensorBracketHolder20		SHEET 4/5

Sensor Bracket		I	-
		H	-
TU DELFT		G	-
		F	-
		E	-
SensorBracketHolder20		D	-
		C	-
		B	-
		A	-

This drawing is our property; it can't be reproduced or communicated without our written agreement.

4 3 2 1

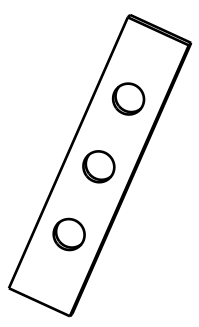
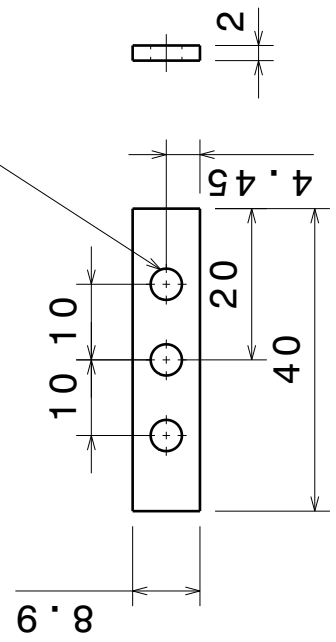
m

C

D

A

M5 THRU



DESIGNED BY:
Roy Bijster

DATE:
24-6-2013

CHECKED BY:
XXX

DATE:
XXX

SIZE
A4

WEIGHT (kg)
0,00

DRAWING NUMBER

1:1

5/5

Sensor Bracket

TU DELFT

FasteningPlate

I	-
H	-
G	-
F	-
E	-
D	-
C	-
B	-
A	-

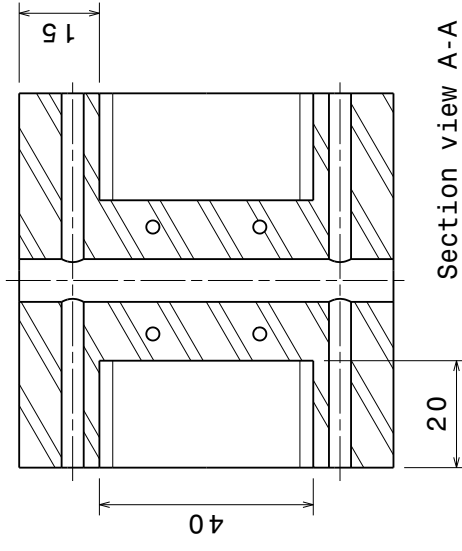
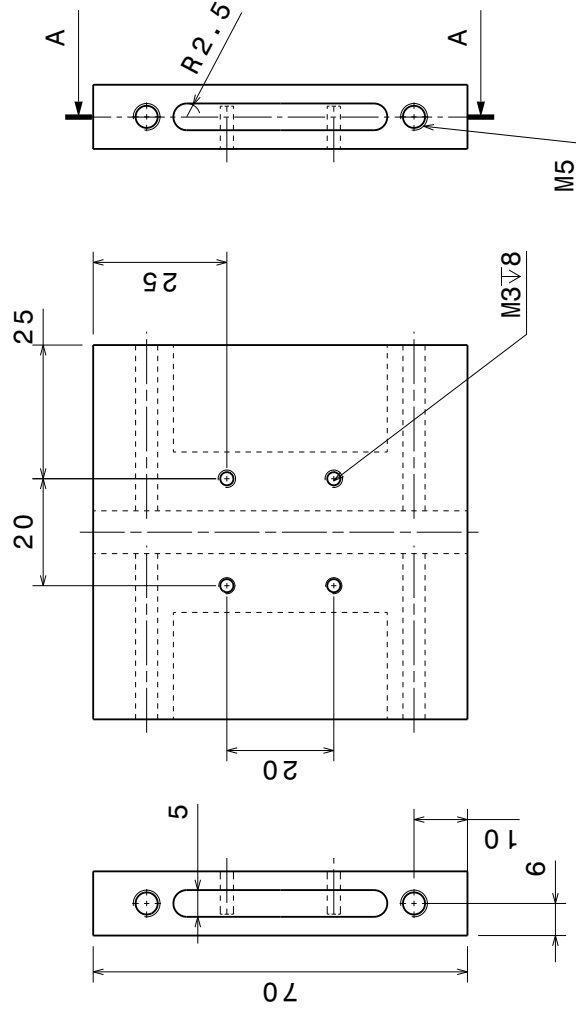
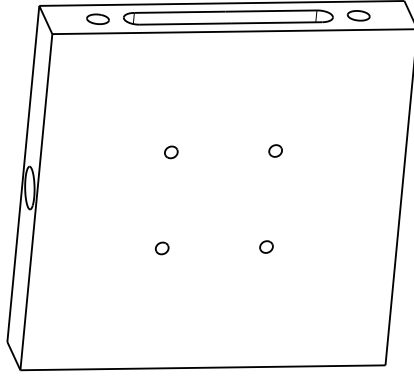
This drawing is our property; it can't be reproduced or communicated without our written agreement.

4 3 2 1

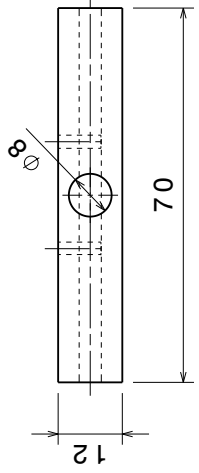
D

A

TOLERANCES: .01mm UNLESS NOTED
OTHERWISE

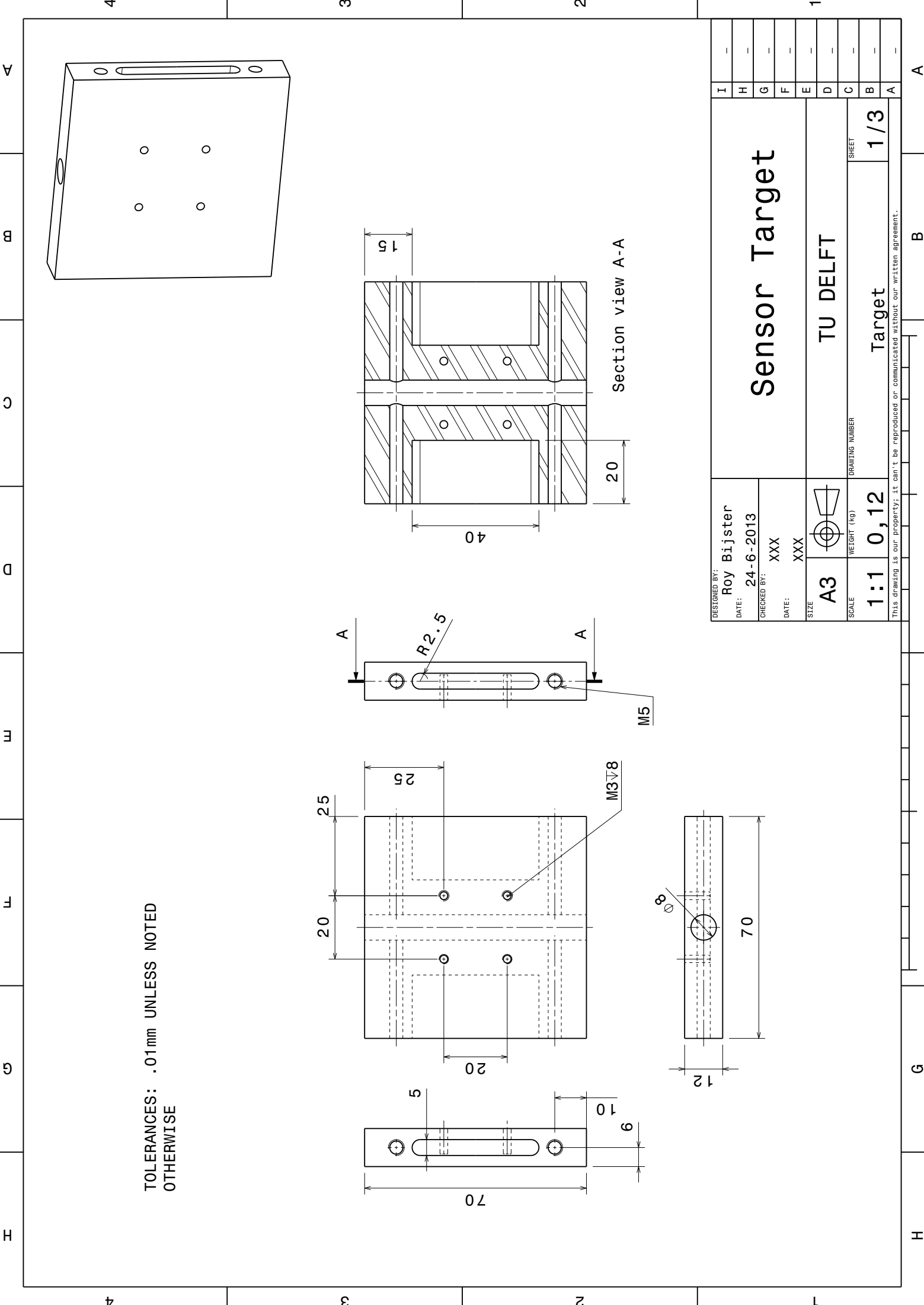


Section view A-A



DESIGNED BY: Roy Bijster	DATE: 24-6-2013	 TU DELFT Target	I
CHECKED BY: XXX	DATE: XXX		H
SCALE: 1:1	WEIGHT (kg): 0,12		G
SIZE: A3	DRAWING NUMBER: 0,12	F	E
SHEET		D	C
DRAWING NUMBER		B	A
SCALE		1/3	

This drawing is our property. It can't be reproduced or communicated without our written agreement.



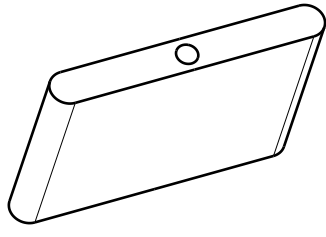
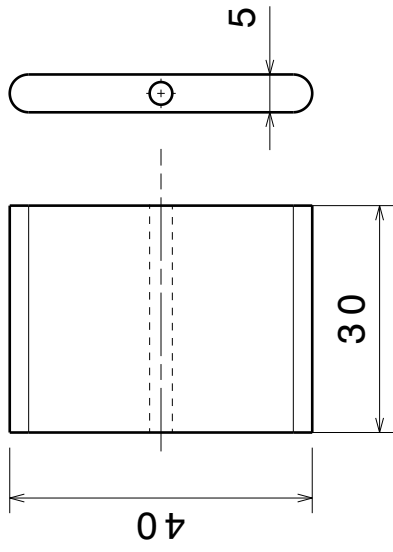
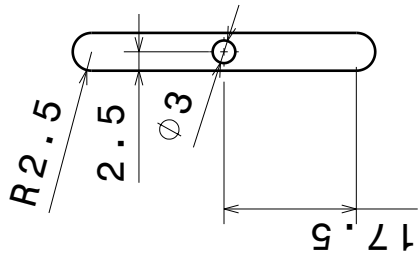
4 3 2 1

m

C

D

A



DESIGNED BY: Roy Bijster	
DATE: 24-6-2013	
CHECKED BY: XXX	
DATE: XXX	
SIZE A4	WEIGHT (kg) 0,05
SCALE 1:1	DRAWING NUMBER 0,05

Sensor Target		SHEET 2/3
TU DELFT		
CalibMass		
I	-	-
H	-	-
G	-	-
F	-	-
E	-	-
D	-	-
C	-	-
B	-	-
A	-	-

This drawing is our property; it can't be reproduced or communicated without our written agreement.

A

D

4 3 2 1

4

3

2

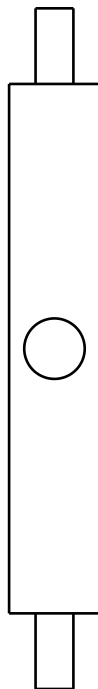
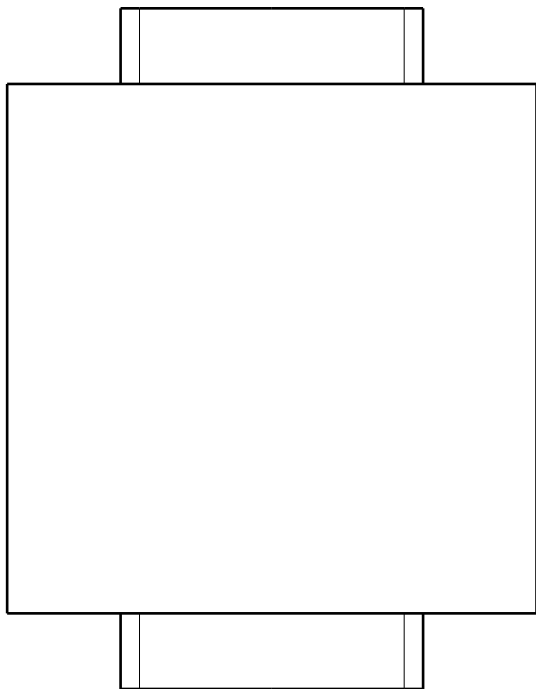
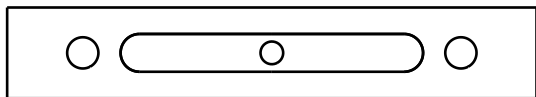
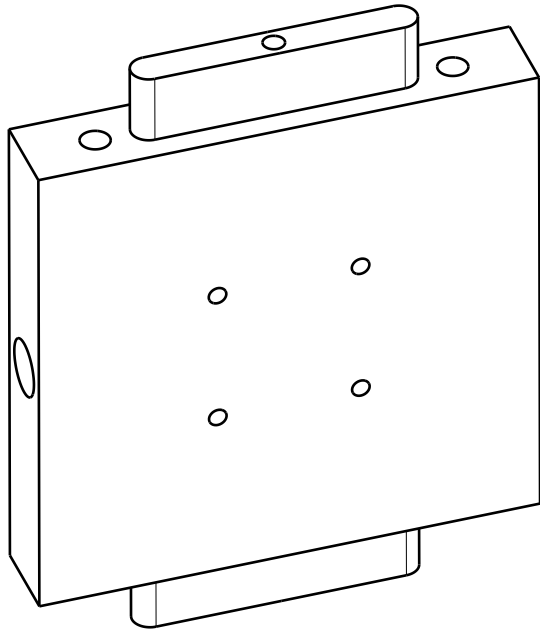
1

A

m

C

D



DESIGNED BY:

Roy Bijster

DATE:

24-6-2013

CHECKED BY:

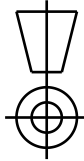
XXX

DATE:

XXX

SIZE

A4



WEIGHT (kg)

1:1 0,12

DRAWING NUMBER

SHEET

3/3

Sensor Target

TU DELFT

Target

I

-

H

-

G

-

F

-

E

-

D

-

C

-

B

-

A

This drawing is our property; it can't be reproduced or communicated without our written agreement.

D

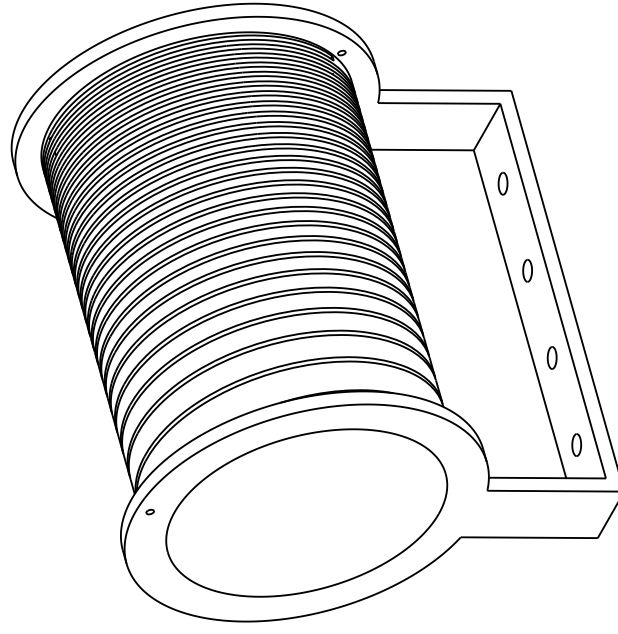
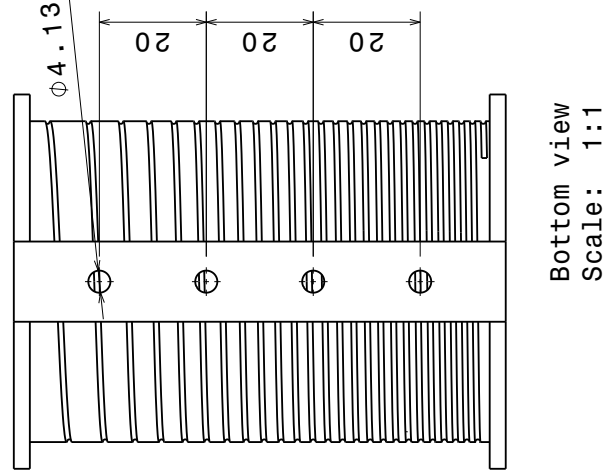
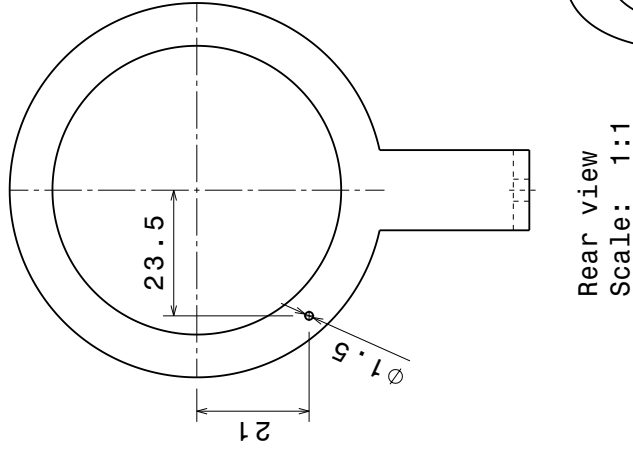
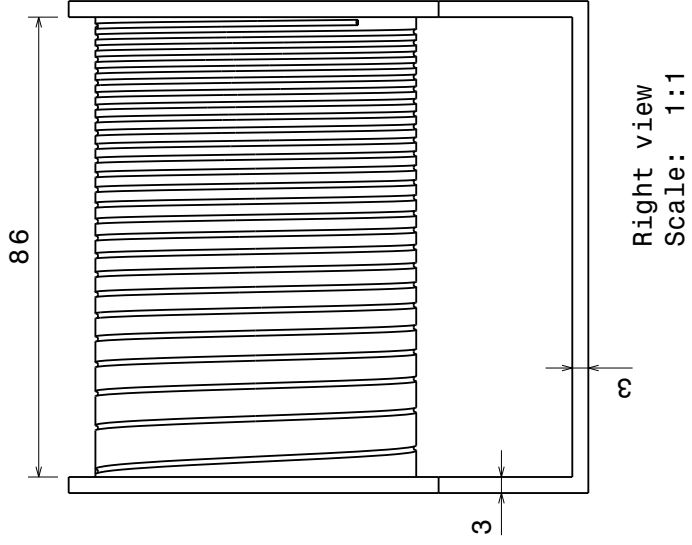
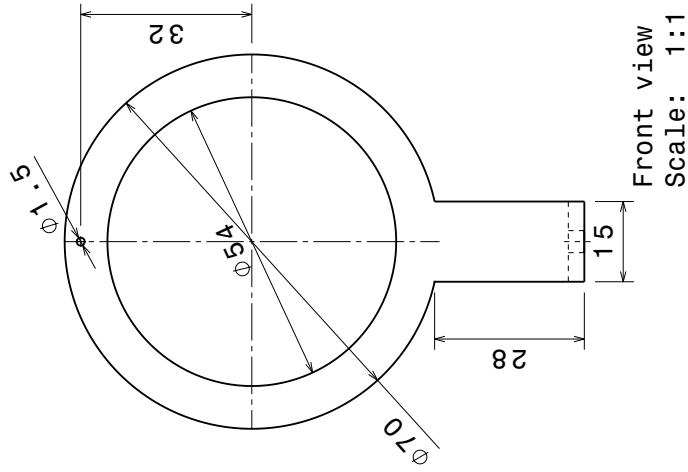
A

4

3

2

1



DESIGNED BY:
Roy.Bijster
DATE:
8-8-2013
CHECKED BY:
XXX
DATE:
XXX

SIZE
A3
SCALE
1:1
WEIGHT (kg)
0,06



DRAWING NUMBER
Coil Holder
SHEET
1/1

Coil Holder

DASSAULT SYSTEMES

Coil Holder

1/1

This drawing is our property. It can't be reproduced or communicated without our written agreement.

A B G H

4

3

2

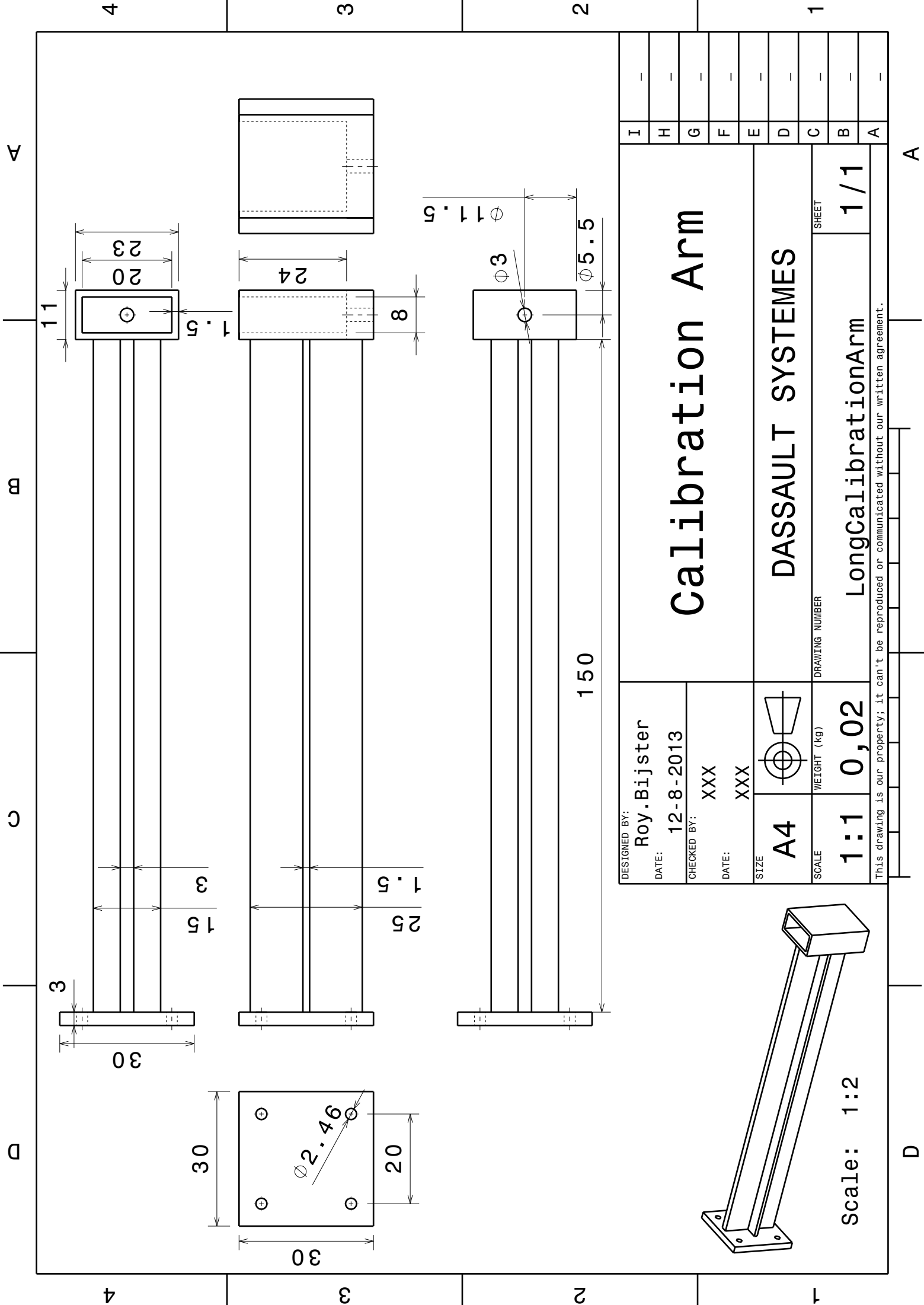
1

4

3

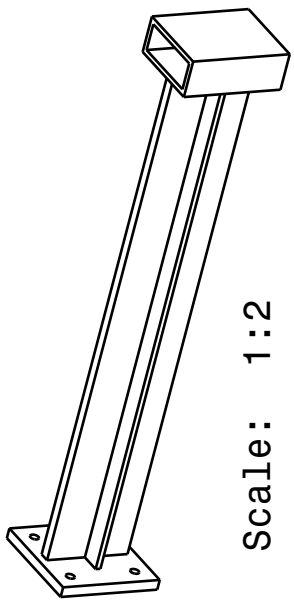
2

1



DESIGNED BY: Roy.Bijster	DATE: 12-8-2013
CHECKED BY: XXX	DATE: XXX
SIZE A4	WEIGHT (kg) 0,02
SCALE 1:1	DRAWING NUMBER LongCalibrationArm

Calibration Arm		SHEET 1				
DASSAULT SYSTEMES		1/1				
<table border="1"> <tr> <td>SCALE</td> <td>DRAWING NUMBER</td> </tr> <tr> <td>1:1</td> <td>LongCalibrationArm</td> </tr> </table>		SCALE	DRAWING NUMBER	1:1	LongCalibrationArm	
SCALE	DRAWING NUMBER					
1:1	LongCalibrationArm					



Scale: 1:2

This drawing is our property; it can't be reproduced or communicated without our written agreement.

A

B

C

D

A

4

3

2

1

4

3

2

1

A

D

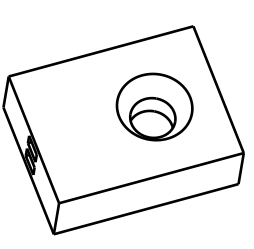
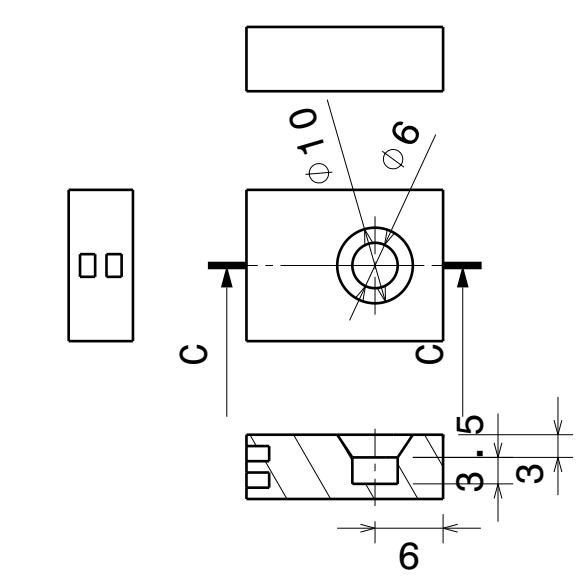
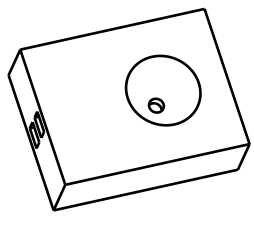
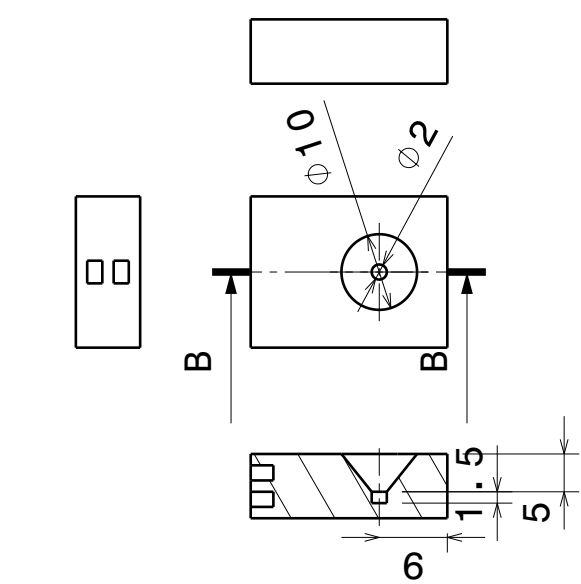
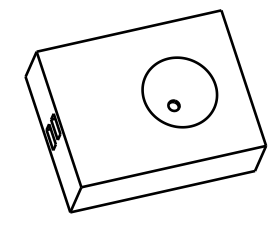
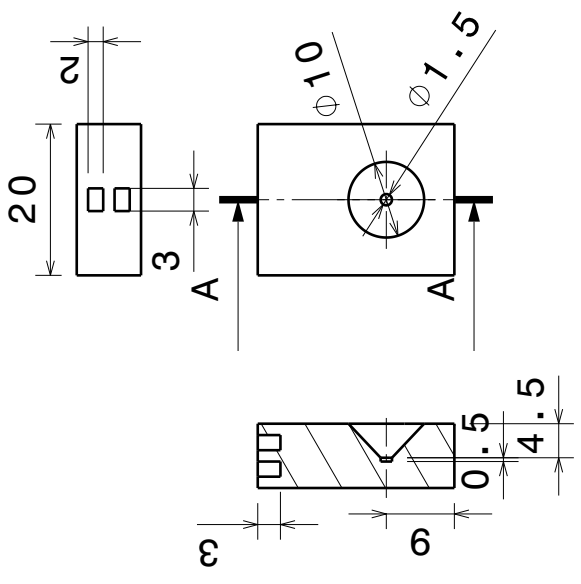
4 3 2 1

A

B

C

D



DESIGNED BY: Roy.Bijster		
DATE: 8-8-2013		
CHECKED BY: XXX		
DATE: XXX		
SIZE A4		
SCALE 1:1	WEIGHT (kg) 0,00	
DRAWING NUMBER MagnetHolder15, 20, 60		SHEET 1/1

I	-
H	-
G	-
F	-
E	-
D	-
C	-
B	-
A	-

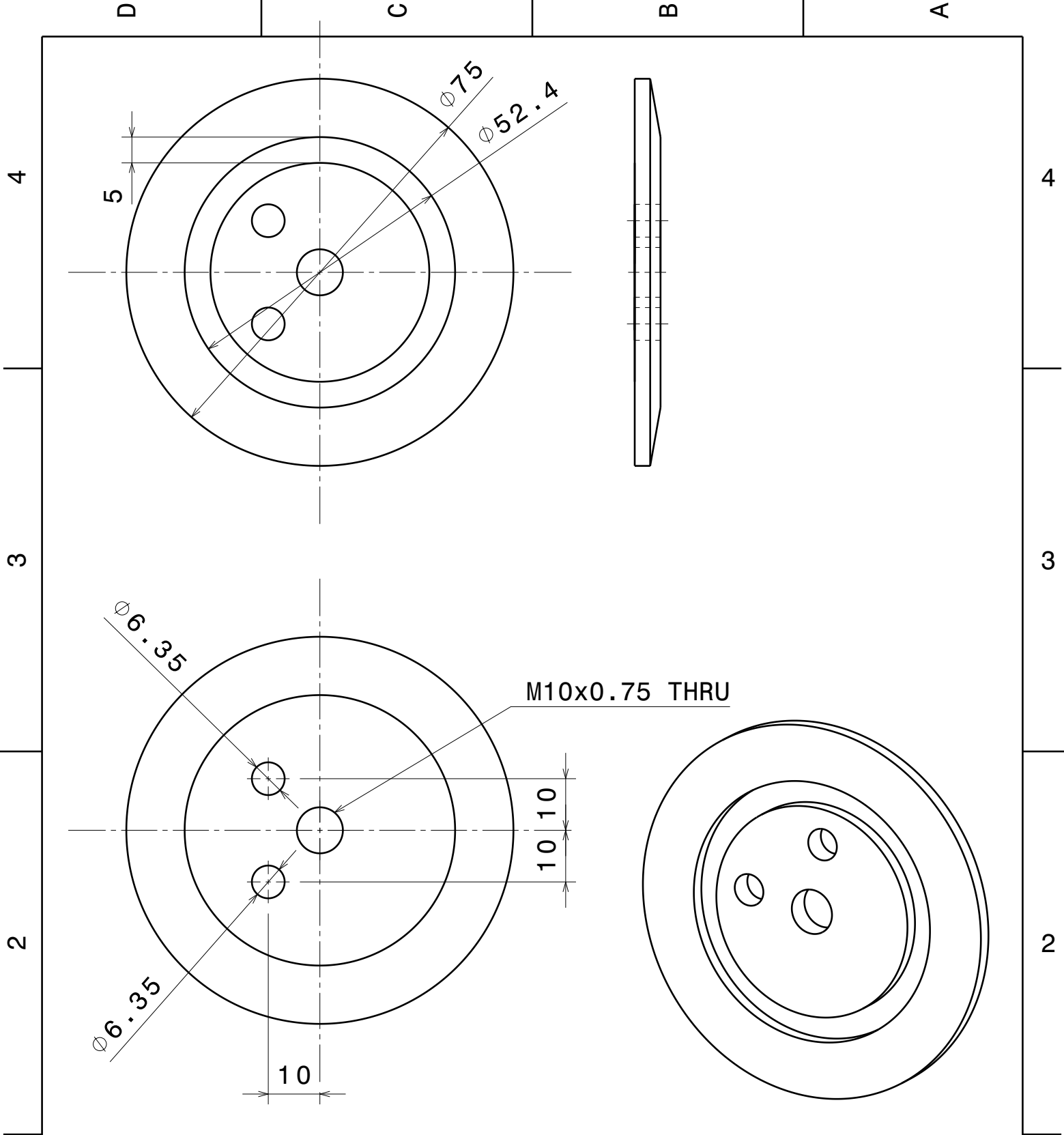
<h1>Magnet Holders</h1>	
<h2>DASSAULT SYSTEMES</h2>	

This drawing is our property; it can't be reproduced or communicated without our written agreement.

4 3 2 1

A

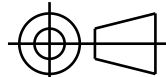
D



DESIGNED BY:
Roy Bijster
DATE:
23-10-2013

CHECKED BY:
XXX
DATE:
XXX

SIZE
A4



TU DELFT

SCALE
1:1

WEIGHT (kg)
0,02

DRAWING NUMBER
Flange

SHEET
1 / 1

I	-
H	-
G	-
F	-
E	-
D	-
C	-
B	-
A	-

This drawing is our property; it can't be reproduced or communicated without our written agreement.



LIST OF USED DATA FILES

In the table below, all used data files are listed. Main folder is /Experiments/TEST-XXX/.

TEST	DATE	FILE
110	11 Nov 2013	/110/20131111/TEST110_20131111.pdf
	22 Nov 2013	/110/20131122/TEST110_20131122.pdf
	04 Dec 2013	/110/20131122/TEST110_20131204.pdf
120	22 Oct 2013	/120/TEST DATA/TEST120_5.dat
310	14 Nov 2013	/310/DATA/TEST310-20131114-0953AM-Sideways-Vac.dat
	14 Nov 2013	/310/DATA/TEST310-20131114-1235PM-FrontToBack-Vac.dat
331	21 Nov 2013	/331/DATA/20131121/TEST311-20131121-310s_1.dat
	21 Nov 2013	/331/DATA/20131121/TEST311-20131121-310s_2.dat
	21 Nov 2013	/331/DATA/20131121/TEST311-20131121-310s_3.dat
	21 Nov 2013	/331/DATA/20131121/TEST311-20131121-310s_4.dat
	21 Nov 2013	/331/DATA/20131121/TEST311-20131121-310s_5.dat
	21 Nov 2013	/331/DATA/20131121/TEST311-20131121-310s_6.dat
	21 Nov 2013	/331/DATA/20131121/TEST311-20131121-310s_7.dat
	21 Nov 2013	/331/DATA/20131121/TEST311-20131121-310s_8.dat
	21 Nov 2013	/331/DATA/20131121/TEST311-20131121-310s_9.dat
	21 Nov 2013	/331/DATA/20131121/TEST311-20131121-310s_10.dat
411	13 Nov 2013	/411/DATA/20131113/TEST411-Trial20131311.dat
	13 Nov 2013	/411/DATA/20131113/TEST411-Trial20131311_2.dat

Continued on next page

Table J-1 – *Continued from previous page*

TEST	DATE	FILE
	13 Nov 2013	/411/DATA/20131113/TEST411-Trial20131311_3.dat
	14 Nov 2013	/411/DATA/20131114/TEST411-20131114-Orientation1-Vac_1.dat
	14 Nov 2013	/411/DATA/20131114/TEST411-20131114-Orientation1-Vac_2.dat
	14 Nov 2013	/411/DATA/20131114/TEST411-20131114-Orientation1-Vac_3.dat
	19 Nov 2013	/411/DATA/20131119/TEST411-20131119-Orientation1-Vacuum-PMT-Pressurized-Line.dat
	19 Nov 2013	/411/DATA/20131119/TEST411-20131119-Orientation1-Vacuum-PMT-Pressurized-Line2.dat
	19 Nov 2013	/411/DATA/20131119/TEST411-20131119-Orientation1-Vacuum-PMT-Pressurized-Line3.dat
	20 Nov 2013	/411/DATA/20131120/TEST411-20131120-Seq1_1.dat
	20 Nov 2013	/411/DATA/20131120/TEST411-20131120-Seq1_2.dat
	20 Nov 2013	/411/DATA/20131120/TEST411-20131120-Seq1_3.dat
	20 Nov 2013	/411/DATA/20131120/TEST411-20131120-Seq2_1.dat
	20 Nov 2013	/411/DATA/20131120/TEST411-20131120-Seq2_2.dat
	20 Nov 2013	/411/DATA/20131120/TEST411-20131120-Seq2_3.dat
	20 Nov 2013	/411/DATA/20131120/TEST411-20131120-Seq3_1.dat
	20 Nov 2013	/411/DATA/20131120/TEST411-20131120-Seq3_2.dat
	20 Nov 2013	/411/DATA/20131120/TEST411-20131120-Seq3_3.dat
	21 Nov 2013	/411/DATA/20131121/TEST411-20131121-PreTEST310_1.dat
	21 Nov 2013	/411/DATA/20131121/TEST411-20131121-PreTEST310_2.dat

Continued on next page

Table J-1 – *Continued from previous page*

TEST	DATE	FILE
	21 Nov 2013	/411/DATA/20131121/TEST411-20131121-PreTEST310_3.dat
	22 Nov 2013	/411/DATA/20131122/TEST411-20131122-Pre-Pulses-With-Current_1.dat
	22 Nov 2013	/411/DATA/20131122/TEST411-20131122-Pre-Pulses-With-Current_2.dat
	22 Nov 2013	/411/DATA/20131122/TEST411-20131122-Pre-Pulses-With-Current_3.dat
412	13 Nov 2013	/310/DATA/TEST310-20131113-0900PM-0800AM-Sideways-Ambient-Chamber-closed.dat
	20 Nov 2013	/450/DATA/20131120/TEST450-20131120-Seq2.dat
	20 Nov 2013	/450/DATA/20131120/TEST450-20131120-Seq2_2.dat
	20 Nov 2013	/450/DATA/20131120/TEST450-20131120-Seq2_3.dat
	20 Nov 2013	/450/DATA/20131120/TEST450-20131120-Seq2_4.dat
	20 Nov 2013	/450/DATA/20131120/TEST450-20131120-Seq2_5.dat
	20 Nov 2013	/450/DATA/20131120/TEST450-20131120-Seq2_6.dat
	20 Nov 2013	/450/DATA/20131120/TEST450-20131120-Seq2_7.dat
	20 Nov 2013	/450/DATA/20131120/TEST450-20131120-Seq2_8.dat
	20 Nov 2013	/450/DATA/20131120/TEST450-20131120-Seq2_9.dat
	20 Nov 2013	/450/DATA/20131120/TEST450-20131120-Seq2_10.dat
	20 Nov 2013	/450/DATA/20131120/TEST450-20131120-Seq1.dat
	20 Nov 2013	/450/DATA/20131120/TEST450-20131120-Seq1_2.dat
	20 Nov 2013	/450/DATA/20131120/TEST450-20131120-Seq1_3.dat
	20 Nov 2013	/450/DATA/20131120/TEST450-20131120-Seq1_4.dat

Continued on next page

Table J-1 – *Continued from previous page*

TEST	DATE	FILE
	20 Nov 2013	/450/DATA/20131120/TEST450-20131120-Seq1_5.dat
421	19 Nov 2013	/420/DATA/TEST420-20131119-Short-Range-Mag-Field.dat
	21 Nov 2013	/420/DATA/TEST420-20131121-Short-Range-Mag-Field.dat
430	19 Nov 2013	/420/DATA/TEST430-20131119-Long-Range-Grav-Field.dat
	21 Nov 2013	/420/DATA/TEST430-20131121-Long-Range-Grav-Field.dat
450	20 Nov 2013	/450/DATA/20131120/TEST450-20131120-Seq1.dat
	20 Nov 2013	/450/DATA/20131120/TEST450-20131120-Seq1_2.dat
	20 Nov 2013	/450/DATA/20131120/TEST450-20131120-Seq1_3.dat
	20 Nov 2013	/450/DATA/20131120/TEST450-20131120-Seq1_4.dat
	20 Nov 2013	/450/DATA/20131120/TEST450-20131120-Seq1_5.dat
	20 Nov 2013	/450/DATA/20131120/TEST450-20131120-Seq3_2.dat
460	22 Nov 2013	/460/DATA/20131122/DATA/TEST460-20131122-1mNs-6mm-magnet_1.dat
	22 Nov 2013	/460/DATA/20131122/DATA/TEST460-20131122-1mNs-6mm-magnet_2.dat
	22 Nov 2013	/460/DATA/20131122/DATA/TEST460-20131122-1mNs-6mm-magnet_3.dat
	22 Nov 2013	/460/DATA/20131122/DATA/TEST460-20131122-1mNs-6mm-magnet_4.dat
	22 Nov 2013	/460/DATA/20131122/DATA/TEST460-20131122-1mNs-6mm-magnet_5.dat
	22 Nov 2013	/460/DATA/20131122/DATA/TEST460-20131122-1muNs-6mm-magnet_1.dat
	22 Nov 2013	/460/DATA/20131122/DATA/TEST460-20131122-1muNs-6mm-magnet_2.dat
	22 Nov 2013	/460/DATA/20131122/DATA/TEST460-20131122-1muNs-6mm-magnet_3.dat

Continued on next page

Table J-1 – *Continued from previous page*

TEST	DATE	FILE
	22 Nov 2013	/460/DATA/20131122/DATA/TEST460-20131122-1muNs-6mm-magnet_4.dat
	22 Nov 2013	/460/DATA/20131122/DATA/TEST460-20131122-1muNs-6mm-magnet_5.dat
	22 Nov 2013	/460/DATA/20131122/DATA/TEST460-20131122-1muNs-6mm-magnet_6.dat
	22 Nov 2013	/460/DATA/20131122/DATA/TEST460-20131122-1muNs-6mm-magnet_7.dat
	22 Nov 2013	/460/DATA/20131122/DATA/TEST460-20131122-1muNs-6mm-magnet_8.dat
	22 Nov 2013	/460/DATA/20131122/DATA/TEST460-20131122-1muNs-6mm-magnet_9.dat
	22 Nov 2013	/460/DATA/20131122/DATA/TEST460-20131122-1muNs-6mm-magnet_10.dat

K

HARDWARE QUOTATIONS AND INVOICES

During the thesis hardware was procured either through in-house manufacture, purchase or rental. An overview of the incurred costs is listed in [Table K-2](#) on the next page. The related invoices are added to the end of this appendix.

DESCRIPTION	FROM	COST (€, FY2013)	NOTES
Manufactured components	AE Workshop	≈ 600	BAAN L10 L13882
Sensor rental, capaNCDT 6530 + CS1 + CS10 + Vacuum transition	Micro-Epsilon	377	Two weeks rental. Invoice included.
Shipment of sensor back to manufacturer	UPS Standard	≈ 110	Based on estimate from UPS. Actual costs unknown.
Bottle of 10 L gaseous Nitrogen, 5.0	TU Delft	?	Bottle not emptied, available in clean room. BAAN L10 L13882
Vacuum flange KF-50 for vacuum transition	Pfeiffer Vacuum Benelux B.V.	9.00	Paid for by clean room facility. Invoice included.
Various small components for the feed system.	Swagelok	46.63	
Super magnets S-1.5-0.5-N, S-02-02-N, S-04-04-N and S-06-06-N	Supermagnete	23.00	Spares available. Invoice included.
Calibration arm, magnet holders and coil holder	3D Worknet	136.62	
Small hoseclamps	IQ-Parts	9.05	Used to mount thermocouples on the pendulum.
K-type thermocouple wire	RS-Online	17.80	Ordered via the AE Instrumentation lab.
Proportional Micro Thruster	MOOG Bradford Engineering	0.00	Provided free of charge for educational purposes.
Total		€1329.10	

Table K-2: Costs incurred during project.

Delft University Of Technology
 Materials Science & Engineering
 Mekelweg 2
 2628 CD Delft
 NIEDERLANDE

Order Confirmation

Order no.:	Date:
K125969	21-Oct-2013
Blanket order no.:	Project no.:
	P030562
Customer no.:	Your VAT no.:
106796	NL001569569B01

Your reference:	Date:	Your contact person:	Contact person:	Representative:
/your e-mail	21-Oct-2013	Mr. M. Sc. Roy Bijster	Stelzl Stefan Tel. +49 8542 168-418	Aarts Patrick Tel. +31 162 510400
Our supplier no.:	Delivery date:		Our reference:	
	20-Nov-2013		SSt	

We thank you for your order for the products and services indicated below which we will execute in accordance with the General Terms of Sale of MICRO-EPSILON.

++++
 "The listed goods are subject to export controls. For the export of these goods from the European community an export license is necessary."
 ++++

capaNCDT SERIES 6500
 Non-contact capacitive displacement
 measuring system
 - lending fees -

Item	Part-no./Part description	Quant.	Units	Unit price	Discount	Total EUR
0001	2101009 DT6530 8-channel desktop cabinet 19 inch Eurocard cabinet with aluminium- frame and steel sheated cover; height 3 units, width 84 units, integral power supply (connection to 90 - 265 VAC mains); built-in oscillator for up to 8 channels in synchronous mode in the cabinet; integral digital display (resolution 0.01 % of full scale) for all measuring channels; 37-pole front subD connector with analog output signals of all channels (0 ... 10 V	1.000	pc.	169.70		

Order Confirmation

K125969 from 21-Oct-2013
Page 2/4



Item	Part-no./Part description	Quant.	Units	Unit price	Discount	Total EUR
	and 4 ... 20 mA), 21 bit Ethernet/Ethercat interface; blind front panels for free plug-in positions included; Customs tariff no./HS: 9031 80 34					
0002	2303013 DL6530 Demodulator with internal preamplifier front connector for sensor cable; internal switch for metal / insulator target; front trimmers for zero, sensitivity and linearity adjustment for the analog output signal (0 ... 10 Volt on front BNC connector with 8.5 kHz / 4th order low pass filter); 7 units wide plug-in board; Customs tariff no./HS: 9031 80 34	1.000	pc.	147.10		
0003	6610054 CS1 Capacitive Sensor measuring range: 0-1mm; target: metal, also applicable for insulator target material; sensor diameter: 10mm; replaces former S600-1; Customs tariff no./HS: 9031 80 34	1.000	pc.	11.55		
0004	6610057 CS10 Capacitive Displacement Sensor measuring range: 0-10mm: target: metal, also applicable for insulator target material; sensor diameter: 60mm; Customs tariff no./HS: 9031 80 34	1.000	pc.	23.65		
0005	2903177 CC1,0B Sensor cable capaNCDT 1,0m long with two straightline connectors, for sensor models with measuring ranges of 1mm and more; triaxial cable, 3.2mm diameter ; Customs tariff no./HS: 9031 80 34	2.000	pc.	10.30		
0006	0323050 Vacuum tight triaxial transition (female / female) Mounting thread M10 x 0.75 / Length 34 mm, wall thickness for the mounting maximum 17 mm Customs tariff no./HS: 9031 80 34	1.000	pc.	3.65		

Order Confirmation

K125969 from 21-Oct-2013
Page 3/4



Item	Part-no./Part description	Quant.	Units	Unit price	Discount	Total EUR
0007	9960106	1.000	WO	376.25		376.25
	LENDING FEE capaNCDT for system consists of item 0001-0006 per week					

Total: 376.25
Insurance: 0.75
Net value: 377.00

Courier: UPS-Standard
Delivery terms: EXW ex factory Micro-Epsilon GmbH acc. Incoterms® 2010
Payment terms: 30 days net

Delivery address:

TU Delft
B.T.C. Zandbergen
Office B62-8.10
Kluyverweg 1
2629 HS Delft
NIEDERLANDE

Invoice address:

TU Delft, Faculteit L&R
SSC-F&C Crediteuren (160)
Postbus 5024
2600 GA Delft
NIEDERLANDE

Order Confirmation

K125969 from 21-Oct-2013
Page 4/4



Period of loan: 2 weeks after receipt of goods

When extending the period of loan we need to invoice 2.5 % per week of the total value of goods.
Please return the goods within above period or contact us before the end of the period.

For the period up to we receive the equipment you are liable for the goods.
Please insure goods when you return them and send it back free of costs
for MICRO-EPSILON.

We herewith certify this proforma-invoice to be correct and true.

Micro-Epsilon expressly points out that the test equipment is only provided for the purpose for making possible the test of the function required by you.

Hereby, Micro-Epsilon only warrants the technical data specified in the product documentation (in particular in the data sheet, in the quotation, in the operating manual) under the condition of compliance with the boundary conditions stated there.

Micro-Epsilon does not warrant that the test equipment is suitable for the purpose required by you and/or for any specific application unless Micro-Epsilon has expressly issued a warranty for this. The same applies, if you decide after the test measurements to purchase a product from Micro-Epsilon for this purpose/for this application. It is your responsibility to perform the test run while observing the usual care and under the real usage conditions and to check the suitability of the test equipment for your application and your required purpose.

Otherwise, we refer you to our General Terms and Conditions which you can request from us or download directly from our website under www.micro-epsilon.de/verkaufsbedingungen.

Please indicate on all correspondence our order number and customer number!

With Best Regards

MICRO-EPSILON MESSTECHNIK
GmbH & Co. KG

Dipl.-Ing. Stefan Stelzl
Produktmanager Sensorik



supermagnete

Order no. 1-571888

Order confirmation

Page 1 of 1

Roy Bijster

Stuttgartstraat 34

3047 AS Rotterdam

Niederlande / Netherlands

Date:	05/07/2013	Date of order:	05/07/2013
Date of shipment:	08/07/2013	Order no.:	1-571888
Our BTW- identificatienummer:	NL823261670B01	Delivery address:	TU Delft Space Systems Engineering Debby van der Sande Kluyverweg 1 Kamer 8.14; t.a.v. R. Bijster 2629 HS Delft Netherlands

Article ID	Description	Quant.	Unit price gross EUR	Total gross EUR
S-02-02-N	Disc magnet Ø 2 mm, height 2 mm, ndFeB, N48, nickel-plated	20	0,20	4,00
S-04-04-N	Disc magnet Ø 4 mm, height 4 mm, ndFeB, N45, nickel-plated	20	0,22	4,40
S-06-06-N	Disc magnet Ø 6 mm, height 6 mm, ndFeB, N48, nickel-plated	10	0,41	4,10
S-1.5-0.5-N	Disc magnet Ø 1,5 mm, height 0,5 mm, ndFeB, N45, nickel-plated	20	0,20	4,00
<small>All items are free of harmful substances according to RoHS Directive 2002/95/EC.</small>				
			Value of goods (gross)	16,50
			Shipping Costs (gross)	6,50
This order was paid on 05/07/2013 via iDEAL.			Total incl. VAT EUR	23,00
			21% VAT EUR	3,99
			Total excl. VAT EUR	19,01

Principle Location:
Webcraft GmbH
Industriepark 206
78244 Gottmadingen
Germany

Distributing Warehouse:
Webcraft GmbH
Industriepark 206
78244 Gottmadingen
Germany

Registration Office:
Freiburg i.Br.
HRB 706014
Chief Executive Officers:
Matthias Ackermann
Reto Heygel

Contact:
support@supermagnete.nl
Phone: +49 7731 939 839 2
Fax: +49 7731 939 839 9
www.supermagnete.nl

Pfeiffer Vacuum Benelux BV
 Newtonweg 11
 NL 4104 BK Culemborg
 Phone +31 0345 - 478400
 Fax +31 0345 - 531076
 www.pfeiffer-vacuum.nl
 office@pfeiffer-vacuum.nl

Pfeiffer Vacuum Benelux BV · Newtonweg 11 · NL 4104 BK Culemborg

TU Delft
 Fac / TNW / DCT
 T.a.v. Financiële Adm.
 Mr. Roy Bijster
 Julianalaan 136
 NL 2628BL Delft

Customer: 138728

Delivery address:
 TU Delft Fac. L&R / SSE
 t.a.v. Balthazar Santos
 Gebouwnummer 62
 Kluyverweg 1
 NL 2629HS Delft
 Mr. Roy Bijster

Our offer: 11002749 / 04.10.2013
Purchase order No.: 160000677, 16.10.2013

We confirm your order according to our general terms
 and conditions of sale and supply:

Order Acceptance
 12004813 N - 16.10.2013

Market Team PV-NL	
Contact:	Christel Pothuizen
Phone:	+31 0345 478 401
Fax:	+31 0345 531 076
Email:	Christel.Pothuizen@pfeiffer-vacuum.nl
Sales	
Contact:	Heidema, Pieter
Phone:	+31 6 20604433
Email:	Pieter.Heidema@pfeiffer-vacuum.nl

Item	Description	Tariff / Origin	Quantity	Price in EUR	
				per unit	total
1.0	Blank Flange, DN 50 ISO-KF Aluminum EN AW-6082/3.2315 Part No.: 110FBL050 Delivery week: 42/13	7609 00 00 / TW	12	9,00	108,00
				Value of goods	108,00
				Surcharges	0,00
				VAT	21,00% 22,68
				Total amount	130,68

Costs of carriage and insurance:
CIP - carriage/insurance will be charged

This Order Acceptance is machinemade and valid without any signature!

Pfeiffer Vacuum Benelux BV

Terms of payment and delivery:

Delivery: CIP - carriage/insurance will be charged
 Payment: 30 days after invoice date, net
 Ship via: D P D

Net weight: 0,660 kg

 Vacuum Solutions from a single Source

Complete range of products for vacuum technology!

– Anzeige / Advert–

